Universidade de Aveiro
2017

Departamento de Física

João Vasco Silvestres Vidal

Efeito magnetoelétrico em compósitos baseados em piezoelétricos monocristalinos

Magnetoelectric effect in composites based on single crystalline piezoelectrics

Universidade de Aveiro
2017

Departamento de Física

João Vasco Silvestres Vidal

Efeito magnetoelétrico em compósitos baseados em piezoelétricos monocristalinos

Magnetoelectric effect in composites based on single crystalline piezoelectrics

Tese apresentada à Universidade de Aveiro para cumprimento dos requisitos necessários à obtenção do grau de Doutor em Engenharia Física, realizada sob a orientação científica do Doutor Nikolai Andreevitch Sobolev, Professor Associado do Departamento de Física da Universidade de Aveiro, e co-orientação do Doutor Andrei Leonidovitch Kholkin, Investigador Coordenador da Universidade de Aveiro.

Apoio financeiro da Fundação para a Ciência e tecnologia (FCT) através da bolsa SFRH/BD/89097/2012.

FCT
Fundação para a Ciência e a Tecnologia
MINISTÉRIO DA CIÊNCIA, TECNOLOGIA E ENSINO SUPERIOR

o júri

Presidente

Prof. Doutor António Manuel Rosa Pereira Caetano
professor catedrático do Departamento de Matemática da Universidade de Aveiro

Prof. Doutor Mikhail Igorevich Vasilevskiy
professor catedrático do Departamento de Física da Universidade do Minho

Prof. Doutor Pedro Manuel de Melo Bandeira Tavares
professor associado do Departamento de Química da Universidade de Trás-os-Montes e Alto Douro

Prof. Doutor Manuel Almeida Valente
professor associado do Departamento de Física da Universidade de Aveiro

Prof. Doutor Nikolai Andreevitch Sobolev
professor associado do Departamento de Física da Universidade de Aveiro

Prof. Doutor João Pedro Esteves de Araújo
professor associado da Faculdade de Ciências, Departamento de Física da Universidade do Porto

agradecimentos

Agradeço primeiro que tudo aos meus pais e familiares próximos, embora sejam uns chatos do caraças, por me terem mudado as fraldas e essas cenas todas. Agradeço também ao meu orientador e colegas de laboratório. Não é toda a gente que me consegue aturar durante tantos anos. No futuro irei ver o que posso fazer para que sejam nomeados para o prémio Nobel da Paz. Por fim agradeço aos meus melhores amigos destes últimos 4 anos: Liberdade Individual, Wikipédia, Atum Enlatado, Café, Paracetamol, Paroxetina e Alprazolam. Sem vocês nunca teria conseguido!

palavras-chave

Efeito magnetoelétrico, Piezoeletricidade, Magnetostrição, Compósitos, Estruturas laminadas, Monocristais, Anisotropia, Bimorfos, Resonância eletromecânica, Sensores magnéticos, Captação de energia, Metglas, Niobato de lítio, Ortofosfato de gálio, PMN-PT.

Resumo

Este trabalho expõe um estudo teórico e experimental das propriedades anisotrópicas magnetoelétricas (ME) em diferentes compósitos contendo monocristais piezoelétricos (PE), maioritariamente sem chumbo na sua composição, com vista a diversas aplicações multifuncionais. Uma descrição linear do efeito ME em termos de campos elétricos, magnéticos e elásticos e constantes materiais é apresentada. Um modelo fenomenológico quasi-estático é usado para ilustrar a relação entre as constantes materiais, sua anisotropia e os coeficientes MEs transversais de tensão e carga. Subsequentemente, este modelo é empregue para estimar o máximo coeficiente ME direto de tensão expectável numa série de compósitos tri-camadas de Metglas/Piezocristal/Metglas em função da orientação do cristal PE. Demonstra-se assim como os efeitos MEs são fortemente dependentes da orientação cristalina, o que suporta a possibilidade de se gerarem coeficientes MEs de tensão elevados em compósitos contendo monocristais PEs sem chumbo como o niobato de lítio ($LiNbO_3$; LNO), tantalato de lítio ($LiTaO_3$), ortofosfato de gálio ($GaPO_4$; GPO), quartzo (SiO_2), langatato ($La_3Ga_{5.5}Ta_{0.5}O_{14}$) e langasite ($La_3Ga_5SiO_{14}$) através da otimização da orientação cristalina.

Uma técnica experimental dinâmica de lock-in para a medição da impedância e efeito ME direto é exposta. O formalismo descritivo desta técnica, assim como um arranjo experimental desenvolvido para o efeito são apresentados. O esquema e características deste, assim como diferentes formas de reduzir o ruído e a indesejável indução mútua são exploradas.

Um estudo comparativo do efeito ME direto em compósitos tri-camadas de Metglas e monocristais de LNO e PMN-PT conectados de forma simples é exposto. Embora o PMN-PT possua piezocoeficientes de carga muito superiores aos do LNO, o coeficiente ME direto de tensão demonstrou-se comparável entre ambos os compósitos devido a uma muito menor permitividade dielétrica do LNO. Cálculos teóricos indicam aínda que as propriedades MEs poderão ser significativamente melhoradas (até 500 V/(cm.Oe)) através da otimização do ângulo de corte do LNO, espessura relativa entre camadas ferroelétrica/ferromagnética e uma melhor colagem entre o Metglas e o LNO. Vantagens da utilização do material ferroelétrico LNO em compósitos MEs são discutidas.

Num estudo subsequente, as propriedades dinâmicas anisotrópicas de impedância e MEs em compósitos tri-camadas de Metglas e monocristais PEs sem chumbo de LNO e GPO são exploradas. Medições foram realizadas em função do corte de cristal, magnitude e orientação do campo magnético de polarização e frequência do campo de modulação. Coeficientes MEs altamente intensos em certos modos de ressonância são explorados, e a sua relação com as propriedades materiais dos cristais e geometria dos compósitos é investigada. Um coeficiente ME de até 249 V/(cm.Oe) foi aqui observado num compósito com um cristal de LNO com corte 41ºY a 323.1 kHz. Mostramos assim

que compósitos multicamadas contendo cristais sem chumbo de LNO e GPO podem exibir efeitos MEs anisotrópicos relativamente elevados. Demonstramos também que o controlo da orientação dos cristais PEs pode em princípio ser usado na obtenção de propriedades MEs anisotrópicas desejáveis para qualquer aplicação. Características únicas como elevada estabilidade química, piezoeletricidade linear e robusteza térmica abrem verdadeiras perspetivas para a utilização de compósitos baseados no LNO e GPO em diversas aplicações.

Eventualmente, compósitos bi-camadas contendo lâminas PEs com bidomínios de LNO com corte 127ºY foram estudados tanto teoricamente como experimentalmente. Estas lâminas de LNO possuem uma estrutura de bidomínios com vetores de polarização espontânea opostos ao longo da direção da sua espessura (i.e. uma estrutura de macrodomínios ferroelétricos "*head-to-head*" ou "*tail-to-tail*") Medições de impedância, efeito ME e densidade de ruido magnético equivalente foram realizadas nos compósitos operando sob condições quasi-estáticas e de ressonância. Coeficientes MEs de até 578 V/(cm.Oe) foram obtidos a ca. 30 kHz sob ressonâncias de dobramento usando cristais PEs com 0.5 mm de espessura. Medições de densidade de ruído magnético equivalente demosntraram valores de até 153 $pT/Hz^{1/2}$ a 1 kHz (modo quasi-estático) e 524 $fT/Hz^{1/2}$ sob condições de ressonância. É de esperar que uma otimização adicional das técnicas de fabrico, geometria dos compósitos e circuitos de detenção possa permitir reduzir estes valores até pelo menos 10 $pT/Hz^{1/2}$ e 250 $fT/Hz^{1/2}$, respetivamente, e a frequência de ressonância em pelo menos duas ordens de grandeza. Estes sistemas poderão assim no futuro ser usados em sensores vetoriais de campo magnético simples e sensíveis, passivos e estáveis e operáveis a elevadas temperaturas.

Keywords Magnetoelectric effect, Piezoelectricity, Magnetostriction, Composites, Laminates, Single-crystals, Anisotropy, Bimorphs, Electromechanical resonance, Magnetic sensing, Energy harvesting, Metglas, Lithium niobate, Gallium orthophosphate, PMN-PT.

Abstract

This work presents a theoretical and experimental study of the anisotropic magnetoelectric (ME) properties of differently structured composites featuring piezoelectric (PE) single-crystals, mainly lead-free, for diverse multifunctional applications. A linear description of the ME effects in terms of electric, magnetic and elastic fields and material constants is offered. An averaging quasi-static phenomenological model is used to illustrate the relation between the material constants, their anisotropy and the transversal direct ME voltage and charge coefficients. Subsequently, the aforementioned model is employed in the calculation of the maximum expected direct ME voltage coefficient for a series of tri-layered Metglas/Piezocrystal/Metglas composites as a function of the PE crystal orientation. The ME effects are shown to be strongly dependent on the crystal orientation, which supports the possibility of inducing large ME voltage coefficients in composites comprising lead-free PE single crystals such as lithium niobate ($LiNbO_3$; LNO), lithium tantalate $LiTaO_3$, gallium phosphate ($GaPO_4$; GPO), quartz (SiO_2), langatate ($La_3Ga_{5.5}Ta_{0.5}O_{14}$) and langasite ($La_3Ga_5SiO_{14}$) through the optimization of the crystal orientation.

An experimental dynamic lock-in technique for the measurement of the impedance and direct ME effect is presented. The formalism describing this technique and an implemented custom-made setup are introduced. The scheme and characteristics of the latter as well as ways to reduce the noise and the undesirable mutual induction are explored.

A comparative study of the direct ME effect in simply bonded tri-layered laminates of Metglas and LNO and PMN-PT crystals is exposed. Though PMN-PT has much larger charge piezocoefficients than LNO, the direct magnetoelectric voltage coefficient is found to be comparable in both trilayers due to the much lower dielectric permittivity of LNO. Calculations show that the ME properties can be significantly improved (up to 500 V/(cm·Oe)) via an optimization of the cut angle of LNO, relative thickness ratio of the ferroelectric/ferromagnetic layers and a better bonding between Metglas and LNO. Advantages of using the LNO ferroelectric in ME composites are discussed.

In a subsequent study, the dynamic impedance and ME anisotropic properties of tri-layered composites of Metglas and single-crystalline lead-free PE of LNO and GPO are explored. Measurements have been performed as a function of the crystal-cut, magnitude and orientation of the magnetic bias field and frequency of the modulated field. Greatly enhanced ME coefficients in certain resonance modes are explored, and their relation to the material properties of the crystals and the geometry of the composites is investigated. The largest ME coefficient of up to 249 V/(cm·Oe) was observed for a composite with a 41ºY-cut LNO crystal at 323.1 kHz. We thus show that multilayers comprising lead-free LNO and GPO crystals can exhibit relatively large anisotropic ME effects. We also demonstrate that the control of the PE crystal's

orientation can in principle be used to obtain almost any desired quasi-static and resonant anisotropic ME properties for any given application. Such unique features as chemical stability, linear piezoelectricity and thermal robustness open up a real perspective of using lead-free LNO and GPO based ME tri-layers in various applications.

Eventually, bi-layered composites comprising PE bidomain plates of 127ºY-cut LNO were studied both theoretically and experimentally. The LNO plates possessed an engineered bidomain structure with opposite spontaneous polarization vectors along the thickness direction (i.e. a “head-to-head” or “tail-to-tail” ferroelectric macrodomain structure). Impedance, ME effect and equivalent magnetic noise density measurements have been performed on the composites operating under quasi-static and resonant conditions. ME coefficients of up to 578 V/(cm·Oe) were obtained at ca. 30 kHz at the bending resonance using 0.5 mm thick piezoelectric crystals. Equivalent magnetic noise density measurements yielded values down to 153 $pT/Hz^{1/2}$ at 1 kHz (quasi-static mode) and 524 $fT/Hz^{1/2}$ under resonant conditions. A further optimization of the fabrication techniques, laminate geometry and detection circuit is expected to allow reducing these values down to at least 10 $pT/Hz^{1/2}$ and 250 $fT/Hz^{1/2}$, respectively, and the resonance frequency by at least two orders of magnitude. Such systems may in future thus find use in simple and sensitive, passive and stable, low-frequency and high-temperature vector magnetic field sensors.

“In the South Seas there is a cargo cult of people. During the war they saw airplanes land with lots of good materials, and they want the same thing to happen now. So they've arranged to imitate things like runways, to put fires along the sides of the runways, to make a wooden hut for a man to sit in, with two wooden pieces on his head like headphones and bars of bamboo sticking out like antennas—he's the controller—and they wait for the airplanes to land.”

–Richard Feynman

“"Just to give you a general idea," he would explain to them. For of course some sort of general idea they must have, if they were to do their work intelligently–though as little of one, if they were to be good and happy members of society, as possible. For particulars, as every one knows, make for virtue and happiness; generalities are intellectually necessary evils.”

–Aldous Huxley, *Brave New World*

“When did mediocrity and banality become a good image for your children ... I want my rockstars DEAD!”

–Bill Hicks

“And now for something completely different”

Contents

List of Publications

T. T. Carvalho, J. R. A. Fernandes, J. Perez de la Cruz, J. V. Vidal, N. A. Sobolev, F. Figueiras, S. Das, V. S. Amaral, A. Almeida, J. Agostinho Moreira, P. B. Tavares, "Room temperature structure and multiferroic properties in Bi0.7La0.3FeO3 ceramics", *J. Alloy. Compd.*, **554**(0), 97-103, (2013).

A. A. Timopheev, J. V. Vidal, A. L. Kholkin, N. A. Sobolev, "Direct and converse magnetoelectric effects in Metglas/LiNbO3/Metglas trilayers", *J. Appl. Phys.*, **114**(4), 044102-044108, (2013).

J. V. Vidal, A. A. Timopheev, A. L. Kholkin, N. A. Sobolev, "Anisotropy of the magnetoelectric effect in tri-layered composites based on single-crystalline piezoelectrics", *Vacuum*, **122**, Part B 286-292, (2015).

J. V. Vidal, A. A. Timopheev, A. L. Kholkin, N. A. Sobolev, *Chapter 6, Engineering the Magnetoelectric Response in Piezocrystal-Based Magnetoelectrics: Basic Theory, Choice of Materials, Model Calculations.* In: I. Tiginyanu, P. Topala, V. Ursaki, editors. *Nanostructures and Thin Films for Multifunctional Applications: Technology, Properties and Devices*. Cham: Springer International Publishing; (2016). p. 189-226.

J. V. Vidal, A. A. Timopheev, A. L. Kholkin, N. A. Sobolev, *Chapter 7, Dynamic Measurements of Magnetoelectricity in Metglas-Piezocrystal Laminates*. In: I. Tiginyanu, P. Topala, V. Ursaki, editors. *Nanostructures and Thin Films for Multifunctional Applications: Technology, Properties and Devices*. Cham: Springer International Publishing; (2016). p. 227-265.

J. V. Vidal, A. V. Turutin, I. V. Kubasov, M. D. Malinkovich, S. P. Kobeleva, A. L. Kholkin, N. A. Sobolev, “Equivalent magnetic noise in bi-laminates comprising bidomain $LiNbO_3$ crystals”, to be published in 2017.

List of Abbreviations

Abbreviation	Name
ME	Magnetoelectric
ME_H	Direct magnetoelectric effect
ME_E	Converse magnetoelectric effect
PE	Piezoelectric
MS	Magnetostriction/Magnetostrictive
EM	Electromechanical
FMR	Ferromagnetic resonance
MAR	Magnetoacoustic resonance
LNO	Lithium niobate ($LiNbO_3$)
GPO	Gallium orthophosphate ($GaPO_4$)
SEH	Stationary external heating
DA	Diffusion annealing
EMND	Equivalent magnetic noise density

List of Symbols

Symbol	Name	Common units
E_i	Electric field strength	$V \cdot m^{-1}$
P_i	Electric polarization density	$C \cdot m^{-2}$
D_i	Electric displacement field ($= \varepsilon_0 E_i + P_i$)	$C \cdot m^{-2}$
H_i	Magnetic field strength	Oe ($= 1/4\pi \times 10^3$ $A \cdot m^{-1}$)
M_i	Magnetization density	$A \cdot m^{-1}$
B_i	Magnetic induction field ($= \mu_0(H_i + M_i)$)	T
T_{ij}	Stress tensor	$N \cdot m^{-2}$
S_{ij}	Strain tensor	–
u_i	Displacement field	m
ϕ	Electric potential	V
ε_0	Electric permittivity of free space ($= 8.854... \times 10^{-12}$ $F \cdot m^{-1}$)	$F \cdot m^{-1}$
μ_0	Magnetic permeability of free space ($= 4\pi \times 10^{-7}$ $H \cdot m^{-1}$)	$H \cdot m^{-1}$
${}^{e}\chi_{ij}$	Electric susceptibility	–
ε_{ij}	Electric permittivity ($= \varepsilon_0(1 + {}^{e}\chi_{ij})$)	$F \cdot m^{-1}$
${}^{m}\chi_{ij}$	Magnetic susceptibility	–
μ_{ij}	Magnetic permeability ($= \mu_0(1 + {}^{m}\chi_{ij})$)	$H \cdot m^{-1}$
d_{ijk}	Piezoelectric coefficient	$pC \cdot N^{-1}$ ($= 10^{-12}$ $m \cdot V^{-1}$)
q_{ijk}	Piezomagnetic coefficient	$ppm \cdot Oe^{-1}$ ($= 10^{-6}$ Oe^{-1})
s_{ijkl}	Compliance tensor	10^{-12} m^2/N
λ_s	Saturation magnetostriction	ppm ($= 10^{-6}$)

α_{ij}	Linear magnetoelectric (ME) susceptibility tensor	$s \cdot m^{-1}$
α_{Eij}	Direct ME voltage coefficient ($= \partial E_i / \partial H_j$)	$V \cdot cm^{-1} \cdot Oe^{-1}$
α_{Qij}	Direct ME charge coefficient ($= \partial D_i / \partial H_j$)	$C \cdot cm^{-2} \cdot Oe^{-1}$
ρ	Mass density	$g \cdot cm^{-3}$
σ	Electrical conductivity	$S \cdot m^{-1}$
k_{33}^{l}	Electromechanical coupling factor	–
Q	Mechanical quality factor	–
T_C	Curie temperature	^oC
k_c	Coupling factor	–
V	Voltage;	V
I	Current;	A
Z	Electrical impedance	**Ω**
Y	Electrical admittance ($= 1/Z$)	S
f	Frequency	Hz
ω	Angular frequency ($= 2\pi f$)	rad·Hz
t	Time / Thickness	s / m
w	Width	m
l	Length	m
A	Area ($= wl$)	m^2
v_n	Noise spectral density	$V_{rms} \cdot Hz^{-1/2}$

List of Tables

List of Figures

Chapter 1

1. Introduction

1.1. The magnetoelectric effect

The linear magnetoelectric effect (ME), according to the original definition outlined by Debye in 1924–1926 [1], is described as the linear induction of a polarization, $\boldsymbol{P}$, in a material, in response to an applied magnetic field, $\boldsymbol{H}$. This corresponds to the direct ME effect also designated by the acronym ME_H. In the same way, the converse ME effect (ME_E) is defined as the induction of a magnetization, $\boldsymbol{M}$, in a material as a result of an applied electric field, $\boldsymbol{E}$. These two relations can be expressed to the first order in the following form (in SI units) [2-5]:

$$P_i = \alpha_{ij} H_j \,, \tag{1.1}$$

$$\mu_0 M_i = \alpha_{ji} E_j \,, \tag{1.2}$$

where $\boldsymbol{\alpha}$ indicates the linear ME susceptibility tensor (rank-2 tensor with units of s/m), and μ_0 is the magnetic permeability of empty space. We note that the summation of the repeated index variables (i and j) over all of their integer values in tridimensional space is implicit in the above equations following the Einstein notation. Symbols in bold, on the other hand, represent vector or tensor fields.

The ME effect has given rise to a lot of interest in the scientific community over the past two decades being driven by the possibility of new and promising multifunctional device paradigms and also by the demand for a greater understanding of the fundamental physics associated with solid materials. This interest is evidenced by the large number of review articles and books related to developments in the field of the ME effect published in recent times [4-41]. Figure 1.1 further shows the manifest increase in the number of scientific papers related to the ME effect published along the last decade (2006-2016).

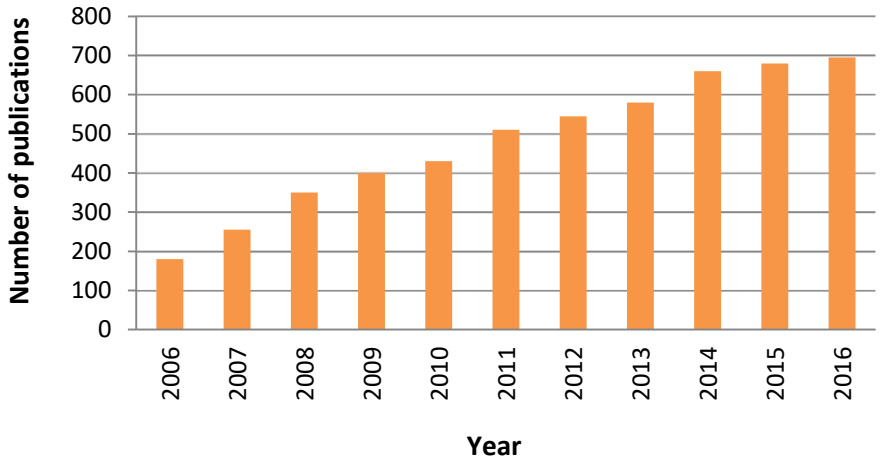

Figure 1.1 Publications registered under the keyword "ME effect" in the last decade according to the Web of Science.

Theoretical physical models are highly important because they allow us to draw valuable conclusions and predictions about the nature of the ME effect. Since early times, an important inequality for the ME single-phase materials has been drawn from a thermodynamic treatment. It states that [42, 43]:

$$\alpha_{ij} < \left({}^{e}\chi_{ii}\,{}^{m}\chi_{jj}\right)^{\frac{1}{2}}, \tag{1.3}$$

where ${}^{e}\chi_{ii}$ and ${}^{m}\chi_{jj}$ are the electric and magnetic susceptibility tensor coefficients, respectively. The inequality (1.3) indicates the existence of a well-defined upper bound for all components of the $\boldsymbol{\alpha}$ tensor. Although this limit is much higher than the experimentally measured values for all known ME materials [44], it still represents a severe limitation on the magnitude of the linear ME response in single-phase materials [45, 46]. This is due to a chemical contraindication to the simultaneous occurrence of a high permittivity and permeability in the same material and results in part from a large intrinsic difficulty in electrically polarizing magnetic ions [47]. Furthermore, by arguments from the group theory, it can also be shown that the static linear ME effect may only be observed in media that are neither symmetrical with respect to the space inversion operation (i.e., systems without a center of symmetry) nor with respect to the time reversal (i.e. systems with a magnetic ordering) [45, 46, 48]. Therefore, the ME effect is allowed only in 58 out of the 122 magnetic point groups [49]. A more general approach to the ME coupling may include higher-order contributions

(describing the so-called secondary ferroics), parameterized by tensors such as β (ME effect induced by the $\boldsymbol{H}$ field) or γ (ME effect induced by the $\boldsymbol{E}$ field), both of rank-3, as can be seen by the general electromagnetic Helmholtz free energy expansion of a material [5, 50]:

$$F(\boldsymbol{E},\boldsymbol{H}) = F_0 - P_i^S E_i - M_i^S H_i - \frac{1}{2}\varepsilon_{ij}E_iE_j - \frac{1}{2}\mu_{ij}H_iH_j - \alpha_{ij}E_iH_j - \frac{1}{2}\beta_{ijk}E_iH_jH_k - \frac{1}{2}\gamma_{ijk}H_iE_jE_k, \quad (1.4)$$

where P_i^S and M_i^S are the spontaneus polarization and magnetization, respectively. However, the linear term α_{ij} is generally the dominant contribution to the ME effect, and thus much of the current research in this area is directed towards the study of this linear effect.

Up to date, the ME effect has already been observed in several different types of materials [6, 8]. Two major classes of ME compounds can, however, be distinguished: single-phase ME materials (mostly ME multiferroics) and ME composites materials which combine both piezoelectric (PE) and magnetostrictive (MS) materials in some manner. These composites may also integrate non-electric and non-magnetic compounds such as organic polymers and even multiferroic materials. Only the magnetoelectric composites will be explored in detail in this Thesis, with the single-phase ME compounds standing outside of its scope.

1.2. Magnetoelectric composites

The ME composite materials constitute a class of structures that incorporate both PE and MS compounds [5, 6, 45]. The demand for these types of materials is essentially guided by the prospect of being able to control their internal charge distribution through the action of an applied magnetic field or, alternatively, their spin distribution by an electric field, thus allowing the development of new forms of multifunctional devices [21]. A ME coupling of large magnitude is therefore essential in order for them to find use in effective practical applications. Some of their most promising applications include [6, 8-10, 24]: *DC* and *AC* magnetic field sensors, electric current sensors, energy harvesters, MEMS devices, multiple-state memories, RAM-like magnetic memories, micro-sensors in read-heads, transformers, gyrators, spinners, diodes, inductors, optical devices that generate spin waves and electrically tunable microwave devices having the potential to offer several advantages in relation to other technologies such as a more compact size, faster operation, better sensitivity, energy efficiency, thermal and chemical stability, linearity of operation, availability, simplicity and finally a lower commercial price.

For the particular case of single-phase multiferroic compounds it has been known that the ME coupling constitutes a very rare phenomenon, usually being only observable at very low temperatures (low Curie and/or Néel temperatures for the electric and magnetic ordering) [6, 8, 22]. Furthermore, these materials are commonly characterized by low values of the ME coupling coefficient ($\alpha_E \approx 0.4 - 20$ mV/(cm·Oe)) [14, 17], in part due to the limits imposed by inequality (1.3). On the other hand, composite materials generally exhibit orders of magnitude stronger ME responses, even at room temperature, and therefore are currently much closer to being used in commercial applications [6, 10]. Another major advantage of this configuration is associated with its extended manufacture flexibility. In fact, in order to manipulate the ME behavior of a composite, several parameters may be individually tuned. These include [6, 8, 10, 19]:

(i) The properties of the constituent phases (e.g. PE and piezomagnetic coefficients, permittivity, permeability, elastic constants, electric resistivity, loss tangents, etc.); *(ii)* the volume and geometrical arrangement of the various phases (e.g. particulate or laminate structures, volume fraction between phases, layer thickness, grain size, rod diameter, etc.); *(iii)* the quality of the coupling between interfaces (e.g., structural compatibility between materials; synthesis techniques employed such as sintering, sol-gel method, hot-pressing, tape-casting, solid-state reaction or other physical/chemical deposition techniques; binding substances used such as epoxy, polymeric matrix, cyanoacrylate glue, etc.); *(iv)* the modes of operation (i.e. relative orientation between the applied/measured electric and magnetic fields, static or dynamic fields, charge, i.e. short-circuit, or voltage, i.e. open-circuit, measurements, frequency of the magnetic or electric modulation fields, etc.); *(v)* the processing techniques (e.g., pre-poling, pre-magnetizing, pre-stressing, heat treatments, etc.); and *(vi)* the use of bulk phases or nanostructures such as thin films (which can give rise to new exotic effects).

To better understand the origin of the ME effect in PE/MS composite systems, we first take a look at the concept of physical properties resulting from the combination of distinct single-phase compounds. Here, it is known that composite systems may exhibit properties similar to those of their constituent phases but also give rise to completely new ones, absent in the parent compounds. The sum and scaling properties are part of the first class, while the product properties are associated with the former [8, 14, 51]. Thus, the ME effect in composite materials is in fact an extrinsic product property resulting from the interaction between PE and MS constituent phases [14, 18, 52]. As shown in Figure 1.2, the physical mechanism of the direct ME (ME_H) effect is as follows: the MS material is strained (***S***) as a result of the application of an external magnetic field (***H***) due to the magnetostrictive effect. Part of this strain is then transferred to the PE phase through the stress (***T***) driven elastic coupling between phases leading to the induction of a macroscopic electric polarization (***P***) due to the piezoelectric effect. It is clear that the reciprocal effect may also take place (i.e. the

converse ME effect or ME_E effect). In this case, an external electric field ($\boldsymbol{E}$) induces a deformation of the PE component elongating or contracting it. This strain is then transmitted to the MS phase through a mechanical coupling between components. Thus, the magnetic phase experiences a magnetization ($\boldsymbol{M}$) change indirectly induced by the electric field. In summary, we just saw how a composite material can be characterized by a new property, the ME coupling, which is manifested by the appearance of a polarization/magnetization in response to an externally applied magnetic/electric field. Roughly speaking, the direct and converse ME effects may then be written under the form of the products [53]:

$$\mathrm{ME_H}\ effect = \frac{Electrical}{Mechanical} \times \frac{Mechanical}{Magnetic}; \qquad \mathrm{ME_E}\ effect = \frac{Magnetic}{Mechanical} \times \frac{Mechanical}{Electrical},$$

where $Electrical/Mechanical$ and $Mechanical/Magnetic$ represent, respectively, the generation of PE charge ($d_{ij} = \partial D_i/\partial T_j$) and the MS deformation ($q_{ij} = \partial S_j/\partial H_i$), while $Magnetic/Mechanical$ and $Mechanical/Electrical$ represent the piezomagnetic induction ($q_{ij} = \partial B_i/\partial T_j$) and the PE deformation ($d_{ij} = \partial S_j/\partial E_i$). With this concept of product properties in mind, the effective short-circuit ($E_i = 0$) ME coefficient can then be approximately expressed as [6, 15]:

$$\alpha_{Qij} = \partial D_i/\partial H_j = (\partial D_i/\partial T_k)(\partial T_k/\partial S_l)(\partial S_l/\partial H_j) = k_c d_{ik} s_{kl}^{-1} q_{jl}\,, \tag{1.5}$$

where k_c is a coupling factor ($0 \leq |k_c| \leq 1$) that quantifies the efficiency of the transference of strain between phases (i.e. the ratio between the strain transferred to the PE/MS phase and the strain generated in the MS/PE phase by the external field) [54]. This expression indicates that the ME coupling should be favored by large PE coefficients (d_{ij}), piezomagnetic coefficients (q_{ij}), the inverse of averaged effective elastic compliances (s_{ij}^{-1}) and coupling factors (k_c). Consequently, the ME effect in composite materials is a coupling between electrical and magnetic fields mediated by an elastic interaction, and is therefore an extrinsic property generated from separate compounds which do not exhibit any ME behavior by themselves.

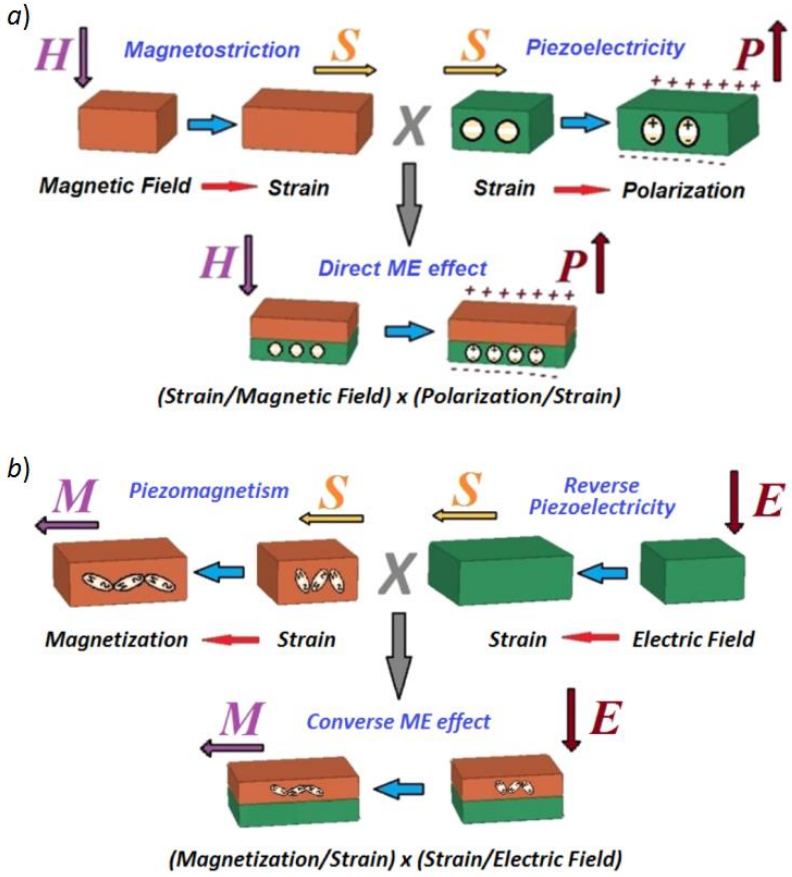

Figure 1.2 Schematic illustration of the elastically mediated ME effect in a two-phase composite consisting of a magnetostrictive (in red) and a piezoelectric (in green) layers. *a)* Direct ME effect; *b)* Converse ME effect.

Since the ME interaction between different phases is a complex process, in composites the ME effect is effectively a dynamic effect and a large response can generally only be observed as a linear function of an *AC* field (electric or magnetic) oscillating in the presence of a given *DC* field [8, 10]. In addition to the nonlinear response with the *DC* field, due to the quadratic effect of magnetostriction, generally the ME coupling in composites also displays an hysteretic nature [14]. Therefore, a dynamic direct ME voltage coefficient $\alpha_{Eij} = \partial E_i/\partial H_j$, measured under open-circuit conditions ($D_i = 0$) is almost always used as a figure of merit for practical applications. In traction-free composite the relation $\alpha_{ik} = -\varepsilon_0 \varepsilon_{rij} \alpha_{Ejk}$ can be proven [15, 55, 56], where α_{ij} represents its effective dynamic ME susceptibility, ε_{rij} the effective relative dielectric permittivity and ε_0 the permittivity of empty space. α_{Eij} is typically specified in technical units of V/(cm·Oe) which can be converted to SI units (V/m)/(A/m) through a multiplication by a factor of 4π/10. This coefficient is usually obtained for a given magnetic *AC* modulation field ($\delta H_i(t) = \delta H_i \cdot \sin(\omega t)$) with small

amplitude (δH up to approximately 1 Oe) and a frequency ($f = \omega/2\pi$) of up to about 1 MHz, superimposed on a larger (up to, say, 20 kOe) magnetic *DC* bias field ($\boldsymbol{H}$) [8]. The amplitude of the ME induced *AC* voltage (δV_i) measured between two electrodes in the sample should then be proportional to the amplitude of the *AC* magnetic field in any detection circuit, thus establishing an analogy with the linear ME susceptibility. Finally, in order to quantify the dynamic ME coefficients, one measures the ME voltage induced in a sample by the magnetic field and then uses the relation $\alpha_{Eij} = \delta V_i/(t \cdot \delta H_j)$, which is valid for small enough δH_j [57] and where t is the effective distance between electrodes generally equal to the thickness of the PE. In practice, two particular cases of this coefficient are commonly studied in the literature [6, 8, 10, 43]: *(i)* the longitudinal T-T (i.e. transversal magnetization and transversal polarization) ME voltage coefficient (α_{E33}), and *(ii)* the transversal L-T (i.e. longitudinal magnetization and transversal polarization) ME voltage coefficient (α_{E31} or α_{E32}). Additionally to α_E, another ME coefficient can be used to describe the direct ME effect in composites. This is the so called charge ME coefficient (α_Q), measured under short-circuit conditions ($E_i = 0$), and it quantifies the amount of charge generated as a function of the applied magnetic field, i.e. $\alpha_{Qij} = \partial D_i/\partial H_j \propto -C\alpha_{Eij}$, where C is the low-frequency capacitance of the composite [58-60]. This coefficient can be measured directly by an electrometer or ammeter or indirectly as a voltage from the output of a charge amplifier and is particularly important for applications in low-noise (< 5 pT/Hz$^{1/2}$) and low-frequency (< 1 Hz) magnetic field sensors [59, 61, 62]. Alternatively, a less common converse ME coefficient, $\alpha_{Bij} = \partial B_i/\partial E_j$, can also be quantified by measuring the magnetic response of a sample when an electric field is applied to it (e.g., through a change in the amplitude of the magnetization induced by an applied voltage, a variation in hysteretic magnetization curves, a change in the magnetic anisotropy or a shift of ferromagnetic resonance absorption peaks) [11]. The analysis of this parameter can be important, e.g., for applications in inductances and electrically controlled microwave devices [9].

Composite materials can be manufactured with a variety of geometries and compositions. Here, a certain phase may take the shape of particles, fibers/rods, layers or three-dimensional arrays which, in the Newnham notation, can be denoted by the indices 0, 1, 2 and 3, respectively [63]. In this way, the notation 2-2, for example, indicates a two-phase composite consisting of alternating layers of different materials. As for its composition, bi-phasic composites contain a PE phase, usually $BiFeO_3$ (BFO), $BaTiO_3$ (BTO), $PbTiO_3$ (PTO), $Pb(Zr,Ti)O_3$ (PZT), $(1–x)[PbMg_{1/3}Nb_{2/3}O_3]–x[PbTiO_3]$ (PMN-PT) or $(1–x)[PbZn_{1/3}Nb_{2/3}O_3]–x[PbTiO_3]$ (PZN-PT), and a MS phase, generally consisting of ferrites or magnetic alloys such as $NiFe_2O_4$ (NFO), $CoFe_2O_4$ (CFO), Fe_3O_4, $La_{1–x}Sr_xMnO_3$ (LSMO), $Y_3Fe_5O_{12}$ (YIG), $Tb_xDy_{1–x}Fe_2$ (Terfenol-D), Metglas (Fe–Ni–Co–B–Si–Mo), Permendur (Fe–Co–V) or Galfenol (Fe–Ga) [6, 7]. Table 1.1 summarizes some of the most important

properties from the point of view of the ME coupling, of some of the most thoroughly investigated PE materials. PE ceramics, PZT in particular, have been extensively studied and shown to provide a strong ME coupling thanks to their relatively large PE and electromechanical coupling coefficients [64-66]. Other compounds commonly used as the PE phase in ME composite materials are PMN-PT and PZN-PT [7, 12, 66]. These materials have PE and electromechanical characteristics superior to those of PZT but, on the other side of the coin, are associated with lower Curie temperatures and lower fracture toughness, which severely limits their practical applications [7]. The polymer PVDF is another common material, less attractive from the point of view of the PE accumulation of charge (though it has a relatively large PE strain coefficient), but which has the advantages of being elastically soft and having a high electrical resistivity and resistance to solvents [7]. Some early research also has pointed out to the possibility of using single-crystalline PE materials exhibiting considerably better performances [12]. Nevertheless, the PE ceramics based on PZT, PMN-PT and PZN-PT still possess the strongest known PE properties and thus are in the prime position for future applications in actuators, sensors and resonators [7, 12, 64-66].

Table 1.1 Main physical properties, relevant to the ME effect, of some common Z-cut piezoelectrics. Here, d_{31} and d_{33} represent the PE strain coefficients, ε_{r33}^{T} is the dielectric relative permittivity, T_C the Curie temperature, ρ the mass density, Q the mechanical quality factor (i.e. 2π times the energy stored divided by the energy dissipated per cycle for a given fundamental resonance mode expressed as $\sqrt{L_1/C_1}/R_1$, where L_1, C_1 and R_1 are respectively the series inductance, capacitance and resistance of the equivalent electrical circuit of the PE vibrator [67]) and k_{33}^{l} the electromechanical coupling factor for a longitudinal oscillation (i.e. the square-root of the ratio between delivered mechanical or electrical energy and total absorbed energy, in this case given by $d_{33}/\sqrt{s_{33}^{E}\varepsilon_{33}^{T}}$ [67]).

	$BaTiO_3$	$LiNbO_3$	$GaPO_4$	PZT–5	PZT–4	PZN-PT	PMN-PT	PVDF	NKN
d_{31} (pC/N)	–33	–0.85	-1.58 (d_{14})	–175	–109	–1280	≈ 700	16.5	–
d_{33} (pC/N)	94	6	4.37 (d_{11})	400	300	2000–2500	2000	–33	158
ε_{r33}^{T}	132	85.2	5.38 (ε_{r11}^{T})	1750	1350	7200	5000	10	–
T_C (°C)	152	1210	900	360	320	163	80	129	415
ρ (g/cm^3)	6	4.63	3.57	7.7	7.6	8.2	7.8	1.78	–
Q	–	–	–	80	500	–	–	4	234
k_{33}^{l}	0.63	0.17	0.15 (k_{11}^{l})	0.72	0.68	0.94	≈ 0.9–0.94	0.19	0.46
Ref.	[68, 69]	[70]	[71, 72]	[7]	[7]	[7, 73, 74]	[7, 75]	[7]	[13]

However, lead (Pb) featured in these compounds represents a serious environmental problem, and therefore a great deal of current research is focused on identifying lead-free PE compounds which could serve as alternatives to the former [13, 76]. In recent times, many developments have been made in this direction with the appearance of a series of new "clean" piezoelectrics. Among these, ceramics based on the compound $(Na,K)NbO_3$ (NKN) have received considerable attention for two main reasons [13]: *(i)* their PE properties stay unchanged over a wide temperature range and *(ii)* there are numerous possibilities of chemical substitution in the compounds.

Similarly, the main properties of the most attractive MS materials are summarized in Table 1.2. Here, one can identify the greatest advantage of ferrites with respect to metallic alloys when employed in particulate ME composites, viz., its high electrical resistivity. This is critical when one seeks to obtain MS phases capable of withstanding an electric displacement field on 0-3 particulate or 1-3 fiber/rod composites because, otherwise, there would be a large leakage of current through the compound thus nullifying the charge built-up. $NiFe_2O_4$, in particular, is the ferrite with the largest saturation magnetostriction (λ_s) currently known, while also possessing good mechanical properties. Despite its small magnetostriction in relation to alloys, $NiFe_2O_4$ is still widely used in ME composites and could find applications, e.g., in microwave devices [7]. However, in 2-2 laminate composites, layers of the MS phase tend to be interspersed by layers of the PE phase, commonly associated with a large electrical resistivity. In this case the leakage of current through the thickness of the composite is minimized, so that the MS phases are no longer required to have high resistivities. Therefore, the research on ME composites in the last decade has been strongly focused on composite laminates containing the MS alloy Terfenol-D ($Tb_{0.3}Dy_{0.7}Fe_{1.92}$/$Pb(Zr_{0.52}Ti_{0.48})O_3$) [10, 77-81]. Among all known magnetic materials, Terfenol-D is still the one with the highest saturation magnetostriction [6]. On the other hand, this compound is very expensive and brittle, as well as exhibiting high losses at high frequencies ($\gtrsim$ 100 kHz) caused by eddy currents. As in all alloys, it also has a low electrical resistivity and cannot be co-sintered with ferroelectric oxides [7]. Also, its low magnetic permeability ($\mu_r \approx 3$–10) and large saturation field require high magnetic fields (typically above 1 kOe) in order to maximize the ME coupling coefficients, making it unsuitable for low-field applications [6, 9]. Consequently, the study of other lower-cost magnetic alloys such as Permendur (Fe-Co-V), Galfenol (Fe-Ga) or Metglas (Fe-Ni-Co-B) is of great interest [64, 82-84]. Currently, one of the most promising MS alloys is Metglas, mainly because of its huge relative magnetic permeability ($\mu_r > 10\,000$), large piezomagnetic coefficient ($q_{33} \approx 4.0$ ppm/Oe) and reasonable saturation magnetostriction (λ_s = 40 ppm) [7]. Different types of this compound consist of soft Fe-, Co- or Fe–Ni-based amorphous alloys, also containing small quantities of B and in some cases Si and Mo, fabricated by a rapid solidification process [85]. This process provides it with unique magnetic properties such as a very high permeability and a very low coercivity and magnetic anisotropy. Despite its smaller

saturation magnetostriction when compared to Terfenol-D, ME composites of Metglas can still display very large ME couplings. This is because, as will be shown later, the ME dynamic coefficients are proportional to the linear piezomagnetic constants ($q_{ij} = \partial S_j/\partial H_i = \partial \lambda_j/\partial H_i$) and not to the saturation magnetostriction (λ_s). In fact, Metglas constitutes the material with the largest known piezomagnetic coefficient, $q_{33} \approx 4$ ppm/Oe (in the case of the 2605SA1 alloy) [82, 86], being approximately twice the one observed for Terfenol-D [65]. It also has a high transversal coefficient of $q_{11} + q_{12} \approx 1.5$ ppm/Oe [87]. Additionally, it's very high permeability ensures a high concentration of magnetic flux and, therefore, a saturation of the magnetization and magnetostriction at very low magnetic fields of ca. 10 Oe. Consequently, its piezomagnetic and ME coefficients, when incorporated into a ME composite, generally attain maximum values at low magnetic fields.

Table 1.2 Main physical properties, relevant to the ME effect, of some important MS materials. Here, λ_s is the saturation magnetostriction, q_{33} the piezomagnetic coefficient, μ_{r33}^T the relative magnetic permeability, ρ the mass density, σ the electrical conductivity and T_C the Curie temperature.

	$NiFe_2O_4$	Terfenol-D	Permendur	Galfenol	Metglas 2605
λ_s (ppm)	27	1400	70	200	40
q_{33} (ppm/Oe)	≈ 0.18	≈ 1–2	≈1	≈ 1.5	≈ 4.0
μ_{r33}^T	20	≈ 6–10	2300	20	> 40 000
T_C (ºC)	535	380	940	670	395
ρ (g/cm^3)	5.37	7.8	8.2	7.7	7.18
σ (S/m)	1.00×10^{-6}	1.72×10^{6}	2.38×10^{6}	1.67×10^{6}	7.69×10^{5}
Ref.	[7, 88]	[7, 65, 86, 89]	[90-92]	[7, 93, 94]	[7, 82, 86]

Since its initial development and until this day, the ME laminate composites have attracted a particularly large interest because of their large ME coefficients, due to a good mechanical coupling between phases and an absence of current leakage, which have paved the way to several promising applications. Thus, a wide variety of laminar geometries [80, 81, 95-97], synthesis/binding techniques [96-98] and operation modes [77-80, 99, 100] have already been studied in detail. With regard to their geometry, the most frequently employed laminate composites are based on simple structures of only two or three rectangular or disk-shaped layers (i.e. sandwich structures) [6]. These structures are the most investigated primarily for their ease of manufacture and for exhibiting, in general, very intense ME effects with coefficients usually in the range from 0.05 to 45 V/(cm·Oe) in the quasi-static regime (i.e. far from any resonance conditions) [16, 18, 22, 23, 26]. Figure 1.3 sums up some of the recent progress made in the development of the various types of ME composites.

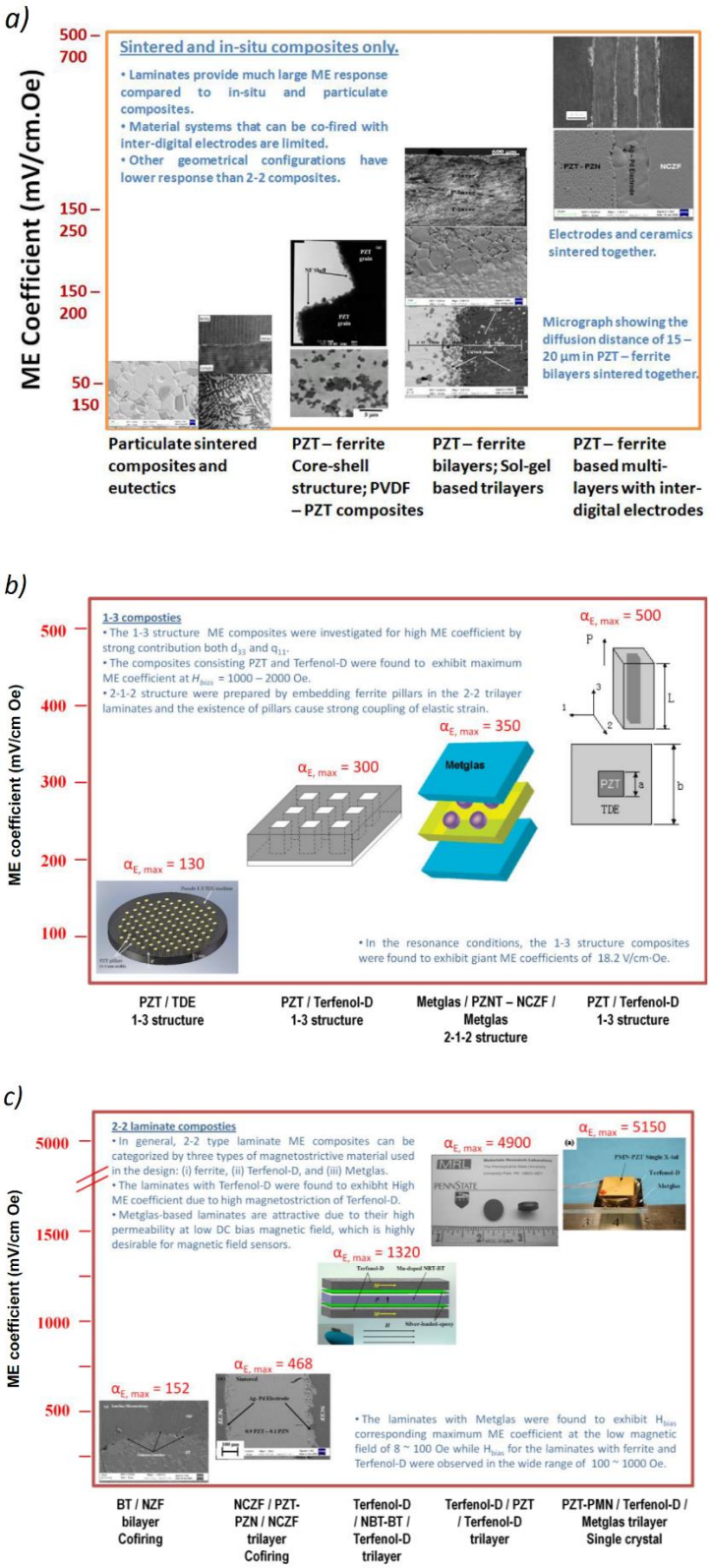

Figure 1.3 Evolution of the ME effect in terms of the amplitude of the quasi-static ME coefficient in various ME composites: *a) in situ* and sintered 3-0 particulate composites; *b)* 1-3 rod/matrix composites and *c)* 2-2 laminate composites. Adapted from [13].

When an oscillating *AC* magnetic field is applied to a ME composite, its ME response oscillates with the fundamental frequency and higher harmonics of this field. In particular, a large increase in the magnitude of the ME effect is expected whenever the frequency matches one of the natural electrical, magnetic or mechanical modes of resonance of the structure [11, 101-103]. Both phases of the composite can exhibit these phenomena. These are known as electromechanical (EM) resonance, for the case of the PE phase, and ferromagnetic resonance (FMR), for the case of the magnetic phase.

The EM resonance occurs when a characteristic mechanical eigenmode of the PE phase is indirectly excited by the varying magnetic field [102]. This field produces a periodic strain in the MS phase which is then transferred to the PE phase. A conventional mechanical resonance of the PE can then be observed when the elastic vibration frequency coincides with a natural frequency (or one of its harmonics) of the system. This frequency depends on the effective material parameters and geometry of the PE. Thus, a large oscillation amplitude of the standing wave in this layer will also give rise to a large polarization/voltage through the PE effect. Theoretical models based on equivalent circuits for the composites have shown that the ME coefficient at resonance is approximately Q_m times larger than that observed off resonance, where Q_m is the effective mechanical quality factor of the composite [12]. It is also possible to show that the extensional length-resonance frequencies of a traction-free laminate composite with the shape of a long bar (i.e., with a length much larger than its width and thickness) can be given by $f_{ln} = (2n-1)/2\ell\sqrt{\rho s_{11}}$ [104], where $n \in \mathbb{N}$ is the harmonic number, ℓ the length of the PE bar, ρ its mass density and s_{11} the longitudinal elastic compliance along the length direction [7]. For laminate composites with lengths of about 1 cm and thicknesses of about 1 mm, fundamental in-plane extensional EM resonances are generally observed in the range of 100 – 500 kHz, while fundamental thickness extensional EM resonances are commonly found in the range of 2 – 8 MHz [105-107]. For the case of a PE with a more complex geometry, however, additional types of EM modes are expected to be found including shear and flexural modes, mainly in the case of symmetrical laminate composites, and bending modes, mainly in the case of asymmetrical laminate composites. As in the extensional case, for a traction-free long-bar shaped PE the n first bending resonant modes should be observed at $f_{bn} = \beta_n^2 t/2\pi\ell^2\sqrt{12\rho s_{11}}$ (with $\beta_1 \approx 4.730$, $\beta_2 \approx 7.853$, $\beta_3 \approx 10.996$, $\beta_4 \approx 14.137$, etc.) [104], where t is the thickness of the PE. The fundamental bending modes are typically observed in the range from 40 – 80 kHz in PE plates with lengths of approximately 1 cm and thicknesses of about 1 mm. Under bending EMR conditions, ME voltage coefficients as large as 737 V/(cm·Oe) have thus already been detected at low frequencies in ME thin film layered composites [108] and up to 20 kV/(cm·Oe) in specially designed ME ferromagnetic-elastic-PE cantilever structured composites [109-112].

The FMR phenomenon involves the resonant absorption of a microwave by the ferromagnetic component of the composite when subjected to some magnetic bias field. An electric field applied to the composite thus straining the ferromagnetic phase may consequently shift this resonant magnetic field [102, 113]. A very large ME coupling has additionally been predicted for a superposition of EM resonance and FMR, in which case it is called magnetoacoustic resonance (MAR) [102]. In general, one expects to observe EM resonance for frequencies of the order of 100 kHz, FMR of the order of 10 GHz and antiferromagnetic resonances of the order of 100 GHz [6, 8, 10, 23]. The latter two make the ME laminates very promising from the point of view of microwave devices.

1.3. Thesis outline

This thesis follows the work carried out mostly in the Department of Physics of the University of Aveiro related to the ME effect in composites ca. in chronological order. Starting with a detailed analysis of the existing literature we thus tried to find the most attractive compositions, structures and modes of operations from the point of view of practical applications. A simple quasi-static phenomenological model was then used to predict the ME coefficient in such composites. Various laminate composites were prepared afterwards by bounding commercial layers of PE crystals and MS Metglas and an experimental apparatus was developed in order to study its ME, impedance and noise properties. The three studies that followed comprised the comparative investigation of the direct and converse ME effects in tri-layered composites with PMN-PT and LNO single-crystals, the anisotropic ME effect in tri-layered composites with LNO and GPO single-crystals and the equivalent magnetic noise in bi-laminates comprising bidomain LNO crystals. The first study allowed us to identify LNO as a very promising alternative to PMN-PT for ME applications offering among other advantages a lead-free nature, a very large chemical and thermal stability, a linear operation and a much lower commercial price. In the second study we found strongly anisotropic ME effects in differently oriented crystals of LNO and GPO and showed how the control of this orientation could be useful e.g. in the development of desirable anisotropic properties for some given application. Finally, in the last part we present bilayered composites containing bidomain LNO plates as a strong candidate for future sensitive, passive and thermally stable ME-based vector magnetic field sensors operating at low frequencies in the bending resonant regime.

Chapter 2

2. Phenomenological modeling of the magnetoelectric effect

Abstract

This chapter presents a simple quasi-static model of the anisotropic ME effect in tri-layers of Metglas and PE single-crystals. The properties of various common PE and MS substances are discussed, and arguments for the choice of the most appropriate materials are made. A linear description of the ME effects in terms of electric, magnetic and elastic material fields and material constants is presented. An averaging quasi-static method is used to illustrate the relation between the material constants, their anisotropy and the transversal direct ME voltage and charge coefficients.

Subsequently, the aforementioned model is employed in the calculation of the maximum expected direct ME voltage coefficient for a series of tri-layered Metglas/Piezocrystal/Metglas composites as a function of the PE crystal orientation. The ME effects are shown to be strongly dependent on the crystal orientation, which supports the possibility of inducing large ME voltage coefficients in composites comprising lead-free PE single crystals such as $LiNbO_3$, $LiTaO_3$, α-$GaPO_4$, α-quartz, langatate and langasite through the optimization of the crystal orientation.

2.1. Piezoelectricity and magnetostriction

The phenomena of piezoelectricity and magnetostriction can be mathematically described by a model derived from thermodynamics, electrodynamics and continuum mechanics. The set of equations that governs the material includes the Maxwell's equations, conservation of linear momentum, angular momentum, energy and mass (in the non-relativistic approximation). The approximate form of the phenomenological constitutive relations for each phase can be derived from these first principles and depends on the choice of the thermodynamic potential. Thus, starting with a PE system and considering isothermal and adiabatic conditions and ignoring higher-order effects, the system's Gibbs free energy may be described by [67, 114-116]:

$$G(\boldsymbol{E},\boldsymbol{T}) = -\frac{1}{2}{}^{p}s_{ijkl}^{E}\,{}^{p}T_{ij}\,{}^{p}T_{kl} - d_{kij}\,{}^{p}E_{k}\,{}^{p}T_{ij} - \frac{1}{2}(\varepsilon_{kl}^{T} - \varepsilon_{0}\delta_{kl})\,{}^{p}E_{k}\,{}^{p}E_{l}\,, \tag{2.1}$$

where the Einstein summation convention is used. Here, ${}^{p}s_{ijkl}^{E}$ is an element of the elastic compliance tensor (a rank-4 tensor), d_{kij} the PE strain coefficient (a rank-3 tensor), ε_{kl}^{T} the dielectric permittivity (a rank-2 tensor), ${}^{p}T_{ij}$ the elastic stress (a rank-2 tensor), and ${}^{p}E_{k}$ the electric field (a vector). The superscripts E and T in the material constants indicate that those are defined under the conditions of a constant electric field or stress, respectively. Throughout the rest of this thesis, the subscripts i, j, k and l will range over the integers 1, 2 and 3, whereas the subscripts a, b, c and d over just 1 and 2. The superscript p on the constants and variables is meant to remind us that we are dealing with a PE medium. Through the partial differentiation of the G potential, the linear constitutive equations of piezoelectricity are obtained as [67, 114-116]:

$${}^{p}D_{k} = \varepsilon_{0}\,{}^{p}E_{k} - \frac{\partial G}{\partial\,{}^{p}E_{k}} = \varepsilon_{kl}^{T}\,{}^{p}E_{l} + d_{kij}\,{}^{p}T_{ij}\,; \tag{2.2}$$

$${}^{p}S_{ij} = -\frac{\partial G}{\partial\,{}^{p}T_{ij}} = {}^{p}s_{ijkl}^{E}\,{}^{p}T_{kl} + d_{kij}\,{}^{p}E_{k}\,, \tag{2.3}$$

where ${}^{p}D_{k}$ is the electric displacement (a vector) and ${}^{p}S_{ij}$ is the elastic strain (a rank-2 tensor).

All of the tensor parameters for a given property of the material mentioned so far are mathematical objects that change with the coordinate system in a predictable way and obey certain symmetry relations, which considerably reduces the number of their independent components. Those symmetry relations have three basic sources [117]: the symmetry of the partial differential equation (PDE) that defines the property, the symmetry of the tensor variables which determine the property, and the symmetry of the material that exhibits the property (i.e., its point group). The first kind of symmetry limits the number of independent elements of the tensor properties which are defined by repeated differentiation. An example of this is the PE coefficient, where $d_{kij} = d_{kij}^{E} = \left(\partial D_{k}/\partial T_{ij}\right)_{E} = -\partial^{2}G/\partial T_{ij}\partial E_{k} = -\partial^{2}G/\partial E_{k}\partial T_{ij} = \left(\partial S_{ij}/\partial E_{k}\right)_{T} = d_{kij}^{T}$, the dielectric permittivity $\varepsilon_{kl}^{T} = (\partial D_{k}/\partial E_{l})_{T} = \varepsilon_{0}\delta_{lk} - \partial^{2}G/\partial E_{l}\partial E_{k} = \varepsilon_{0}\delta_{kl} - \partial^{2}G/\partial E_{k}\partial E_{l} = (\partial D_{l}/\partial E_{k})_{T} = \varepsilon_{lk}^{T}$, and the compliance $s_{ijkl}^{E} = \left(\partial S_{ij}/\partial T_{kl}\right)_{E} = -\partial^{2}G/\partial T_{ij}\partial T_{kl} = -\partial^{2}G/\partial T_{kl}\partial T_{ij} = s_{klij}^{E}$. The theory of linear elasticity yields $S_{ij} = (1/2)\cdot(\partial u_{i}/\partial x_{j} + \partial u_{j}/\partial x_{i})$, where u_{i} are the displacement vectors along the x_{i} Cartesian directions, so that $S_{ij} = S_{ji}$, thus reducing the number of independent variables to six. Furthermore, the conservation of angular momentum also implies

that $T_{ij} = T_{ji}$. Consequently, taking into account this symmetry of the tensor variables that determine the properties $d_{kij} = \left(\partial D_k/\partial T_{ij}\right)_E$ and $s^E_{ijkl} = \left(\partial S_{ij}/\partial T_{kl}\right)_E$, one further identifies the following symmetry relations: $d_{kij} = d_{kji}$ and $s^E_{ijkl} = s^E_{jikl} = s^E_{ijlk} = s^E_{jilk}$. In summary, it follows from these two sources of intrinsic symmetry that the dielectric permittivity has a maximum of 6 independent constants, whereas the dielectric coefficient and compliance have a maximum of 18 and 21, respectively. To simplify the manipulation of these expressions, a special notation known as Voigt's notation is commonly used in literature. Here, the $\boldsymbol{\varepsilon^T}$, $\boldsymbol{d}$ and $\boldsymbol{s^E}$ tensors are represented as 3×3, 3×6 and 6×6 matrices, where the ij subscripts are reduced to a single subscript (m or n) using the substitutions $ij = 11 \rightarrow 1$, $ij = 22 \rightarrow 2$, $ij = 33 \rightarrow 3$, $ij = 23{,}32 \rightarrow 4$, $ij = 13{,}31 \rightarrow 5$, $ij = 12{,}21 \rightarrow 6$. Other rules of conversion in this matrix notation, which must be taken into account, are [67, 118]: $S_m = S_{ij}$, when m = 1, 2 or 3; $S_m = 2S_{ij}$, when m = 4, 5 or 6; $s^E_{mn} = s^E_{ijkl}$, when both m and n are = 1, 2 or 3; $s^E_{mn} = 2s^E_{ijkl}$, when m or n are = 4, 5 or 6; $s^E_{mn} = 4s^E_{ijkl}$, when both m and n are = 4, 5 or 6; $d_{km} = d_{kij}$, when m = 1, 2 or 3; and $d_{km} = 2d_{kij}$, when m = 4, 5 or 6. The values of these coefficients are frequently presented in literature in this notation. Taking all these symmetry considerations into account, we see that the constitutive equations (2.2) and (2.3) can be written in the general matrix form [67, 114]:

$$\begin{bmatrix} S_m \\ D_i \end{bmatrix} = \begin{bmatrix} {}^p s^E_{mn} & d^t_{mj} \\ d_{in} & \varepsilon^T_{ij} \end{bmatrix} \begin{bmatrix} T_n \\ E_j \end{bmatrix}, \tag{2.4}$$

where the superscript t indicates the transpose of the $\boldsymbol{d}$ Voigt matrix. Finally, it should be noted that the symmetry of the material is also an important source of additional constrains on its tensor properties. From the physical symmetry of a system we know that there are a set of symmetry operations which will not change the material in any observable way, so that the material properties will be invariant under such operations. These operations are the ones that define the point group of the system. Thus, one sees that the material properties are in part governed by the point group symmetry of the material. More precisely, the Neumann principle states that [119] *the symmetry elements of any physical property of a crystal must include all the symmetry elements of the point group of the crystal*. In other words, the components of a tensor representing a property must remain invariant under any transformation of coordinates governed by a symmetry operation valid for the point group of the crystal. This also implies that a given physical property may only possess a higher or equal symmetry than that of the crystal. Therefore, a physical property must have a symmetry at least as high as one of the 32 conventional point groups or one of the 122 magnetic points groups to

which the crystal belongs. Taking, e.g., the PE $LiNbO_3$ crystal corresponding to the point group *3m*, it is possible to show that it will be associated with at most 2 independent dielectric constants (ε_{11}^T and ε_{33}^T), 4 PE constants (d_{31}, d_{33}, d_{22} and d_{15}) and 6 compliance constants (s_{11}^E, s_{12}^E, s_{13}^E, s_{14}^E, s_{33}^E and s_{44}^E) [70]. A listing of all the 32 point groups and associated tensor properties can be found, e.g., in [119-121].

Most of the discussion mentioned above for PE materials can also be applied to piezomagnetic materials. The difference resides in the fact that, because magnetic fields are pseudovectors generated by currents and change sign under the time inversion operation, magnetic properties will necessarily have more complex symmetries [117]. In fact, there is a whole set of additional point group symmetries for the magnetic properties as a consequence of current reversal. Therefore, while the simplest magnetic properties, such as the magnetic permeability and susceptibility, have the forms that are required by the basic crystallographic point group of the material, more complex properties, such as the ferromagnetic moment and the MS coefficients, do not. Those will instead have the form required by one of the 122 magnetic point groups. Assuming the same conditions as in the case of the PE material, the elastic Gibbs function for the MS material can also be derived. From it, the linear piezomagnetic constitutive relations follows [56, 122]:

$$ {}^mB_k = \mu_0 {}^mH_k - \frac{\partial G}{\partial {}^mH_k} = {}^mB_{0k}(\boldsymbol{H_0}) + \mu_{kl}^T(\boldsymbol{H_0}){}^mH_l + q_{kij}(\boldsymbol{H_0}){}^mT_{ij} \; ; \tag{2.5} $$

$$ {}^mS_{ij} = -\frac{\partial G}{\partial {}^mT_{ij}} = {}^mS_{0ij}(\boldsymbol{H_0}) + {}^ms_{ijkl}^E {}^mT_{kl} + q_{kij}(\boldsymbol{H_0}){}^mH_k \; , \tag{2.6} $$

where ${}^mB_k$ is the magnetic induction (a vector) and ${}^mH_k$ the magnetic field strength (a vector). Also, ${}^mB_{0k}(\boldsymbol{H_0}) = {}^mB_k(\boldsymbol{H_0}) - \mu_{kl}^T(\boldsymbol{H_0}){}^mH_{0l}$ and ${}^mS_{0ij}(\boldsymbol{H_0}) = \lambda_{ij}(\boldsymbol{H_0}) - q_{kij}(\boldsymbol{H_0}){}^mH_{0k}$ where $\mu_{kl}^T(\boldsymbol{H_0})$ is the magnetic permittivity (a rank-2 tensor), $q_{kij}(\boldsymbol{H_0})$ the piezomagnetic coefficient (a rank-3 tensor), ${}^mB_k(\boldsymbol{H_0})$ the magnetic induction and $\lambda_{ij}(\boldsymbol{H_0})$ the magnetostriction all obtained at a bias $\boldsymbol{H_0}$ magnetic field. The superscript m indicates the MS nature of the material to which equations (2.5) and (2.6) apply. It should be noted that, when obtaining these equations, the pseudo-piezomagnetic approximation was taken. This is because magnetostriction is approximately a quadratic effect (${}^mS_{ij} = b_{ijkl}M_kM_l$, where $\boldsymbol{b}$ is the 6×6 magnetoelastic tensor), whereas piezomagnetism is a linear effect (${}^mS_{ij} = q_{kij}H_k$). However, for small variations of the applied $\boldsymbol{H}$ field close to a bias field $\boldsymbol{H_0}$, the slope $\partial S_{ij}^m/\partial H_k(\boldsymbol{H})$ of the magnetostriction curve is approximately constant in a small interval around $\boldsymbol{H_0}$. Therefore the Taylor expansion of the magnetostriction curve

around $\boldsymbol{H_0}$ may be truncated to first order as follows: ${}^{m}S_{ij}(\boldsymbol{T}=0,\boldsymbol{H}) = \lambda_{ij}(\boldsymbol{H}) = \lambda_{ij}(\boldsymbol{H_0}) + \partial\lambda_{ij}/\partial H_k(\boldsymbol{H_0}).(H_k - H_{k0}) + (1/2)\partial^2\lambda_{ij}/\partial H_k\partial H_l(\boldsymbol{H_0}).(H_k - H_{k0})(H_l - H_{l0}) + \ldots \approx \lambda_{ij}(\boldsymbol{H_0}) + \partial\lambda_{ij}/\partial H_k(\boldsymbol{H_0}).(H_k - H_{k0})$, and thus the magnetostriction can be approximated in this region as a piezomagnetic effect with $q_{kij}(\boldsymbol{H_0}) = \partial\lambda_{ij}/\partial H_k(\boldsymbol{H_0})$ [43, 123]. In practical applications, the magnetostriction is often used in this linear piezomagnetic regime with small applied *AC* magnetic fields. Similarly, a pseudo-paramagnetic approximation, where $\mu_{kl}^{T}(\boldsymbol{H_0}) = \partial B_k/\partial H_l(\boldsymbol{H_0})$, is also assumed for the ferromagnetic material. Having taken this into consideration, one can therefore assume the validity of equations (2.5) and (2.6). Before advancing any further, we note that the assumption that the material coefficients in the constitutive equations are constants dependent only on the spatial coordinates and magnetic fields produces a much idealized model. In a more accurate description these coefficients should be complex functions of space, material fields, frequency, time and temperature, thus taking into account the non-linearities, dispersion, losses, current state (e.g. remanent polarization/magnetization of the PE/MS phase, aging effects, etc.) and temperature dependence of the material's properties. A listing of all the linear dielectric, PE and elastic constants of the different piezoelectrics, measured under standard ambient conditions, can generally be easily found in the literature.

2.2. Averaging quasi-static method

In this Section we are going to estimate the maximum expected magnitude of the ME voltage coefficient for a series of tri-layered geometries of the type Metglas/PE/Metglas, where different single crystals are employed as the PE phase. To do this, a standard averaging low-frequency model (i.e., in the quasi-static regime), based on the constitutive equations, will be used [124]. Being quasi-static it will naturally neglect high frequency effects such as electromechanical resonances, material dispersion and losses as well as eddy currents generated in the conductive phases.

The simultaneous resolution of the constitutive equations (2.2)–(2.3) and (2.5)–(2.6), taking into account the boundary conditions for the material interfaces, allows one to obtain the ME voltage coefficient of the composite depending on its composition, microstructure, operating mode, etc. Currently, a number of analytical and numerical techniques are known which may be employed in solving these equations. In general, they allow estimations in terms of mean fields and are based on the formalism of Green's functions [53] (multiple-scattering approach in the many-body theory) or on micromechanical methods [125]. More sophisticated models may include the quadratic effect of

magnetostriction [126] and pyroelectric or pyromagnetic phenomena [125] in the constitutive equations.

In the quasi-static model, a square shaped tri-layered structure like the one shown in Figure 2.1 *a)* is considered. Its constitutive elastostatic and electrostatic equations are solved assuming that all of the material fields are averaged constants in each layer up to the leading order. This limits the model to the study of purely extensional deformations thus excluding any kind of bending deformations which, however, are only significant for the case of asymmetrical composites such as bilayers. As we see, this composite is designed to operate in its L–T mode, i.e., with a magnetic field ($\delta H_j(t)$) applied along its longitudinal length direction (L) and with the voltage ($\delta V_3(t)$) measured across its transversal thickness direction (T). This L-T mode is generally associated with larger ME coefficients than the transversally magnetized and transversally poled (T-T) mode mainly because of the absence of the demagnetization effect (for thin enough layers) and also because the piezomagnetic coefficients tend to be larger for parallel magnetic and strain fields (q_{ii}), so that the in-plane strain component, which is transmitted to the PE phase, will be larger.

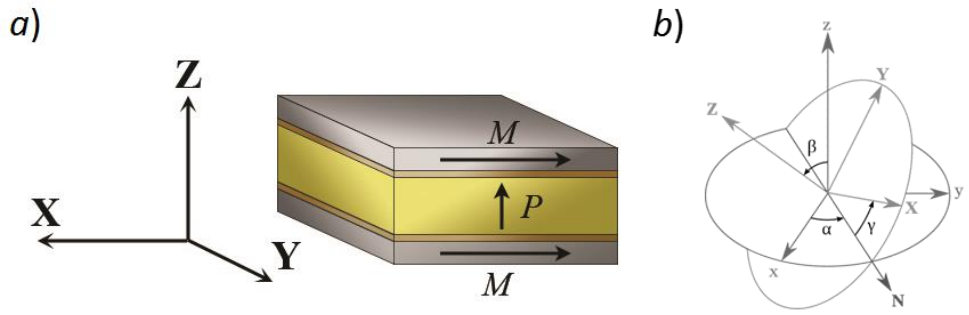

Figure 2.1 *a*) Representation of a tri-layered ME composite operating in the transversal L–T mode (i.e. longitudinal or in-plane magnetization, ***M***, of the MS layers and transversal or out-of-plane polarization, ***P***, of the PE layer). *b*) Euler angles scheme used in the rotation of the crystallographic frame of a single crystal to the laminate frame of figure *a)*.

To set the boundary conditions, we start by assuming that there is no external traction applied to the system (i.e. $t_i = n_i T_{ij} = 0$ on the surfaces of the material, where n_i is the unit surface normal). Thus, the average tractions on the top and bottom surfaces of the system (${}^{m}T_{3i}$), as well as the average tractions on the lateral surfaces (${}^{p}T_{ab}\,{}^{p}v + {}^{m}T_{ab}\,{}^{m}v$), are null. These two relations are expressed as [56, 122]:

$$ {}^{m}T_{3i} = {}^{p}T_{3i} = 0 \; ; \tag{2.7} $$

$$ {}^{p}T_{ab}\,{}^{p}\nu + {}^{m}T_{ab}\,{}^{m}\nu = 0 \; , \tag{2.8} $$

where ${}^{p}\nu$ and ${}^{m}\nu$ are the volume fractions of the PE and MS phases, respectively. Taking into account that all layers have a square shaped surface with the same area, these fractions can be given by ${}^{p}\nu = {}^{p}t/({}^{p}t + 2\,{}^{m}t)$ and ${}^{m}\nu = 2\,{}^{m}t/({}^{p}t + 2\,{}^{m}t)$, where ${}^{p}t$ is the thickness of the PE crystal and ${}^{m}t$ is the thickness of each one of the two magnetic layers. The continuity conditions at the interfaces between layers guarantees that ${}^{m}T_{3i} = {}^{p}T_{3i}$. Furthermore, a parameter known as the coupling coefficient, $k_c = ({}^{p}S_{ab} - {}^{p}S_{0\,ab})/({}^{m}S_{ab} - {}^{p}S_{0\,ab})$, is introduced [55]. This parameter describes the coupling quality at the interface between the PE and MS materials. In the expression of k_c, ${}^{p}S_{0\,ab}$ indicates the component of the strain tensor in the PE phase that appears when the friction between layers is null (i.e. ${}^{p}T_{ab} = 0$, so that ${}^{p}S_{0\,ab} = \; d_{kab}\,{}^{p}E_k$ by equation (2.3)), and ${}^{p}S_{ab}$ and ${}^{m}S_{ab}$ are the strains in the PE and MS phases, respectively. The coupling parameter consequently defines the ratio between the induced strains in the PE and MS layers. For an ideal interface we then have k_c = 1, whereas for an interface without any friction between layers (i.e. without mechanical coupling between them) we have k_c = 0. The boundary conditions for the strain components on the lateral surfaces of the composite are therefore [72]:

$$ {}^{p}S_{ab} = \; k_c\,{}^{m}S_{ab} + (1 - k_c)\,{}^{p}S_{a0} \; . \tag{2.9} $$

It is further assumed that the interface is perfectly electromechanically bound. Consequently, the in-plane electric and magnetic fields will be continuous along the composite, the change in the normal displacement fields across the interfaces will be equal to the surface charge density (σ) and the normal magnetic induction will be continuous [56, 122]:

$$ {}^{p}E_1 = {}^{m}E_1, \;\; {}^{p}E_2 = {}^{m}E_2, \;\; {}^{p}D_3 - {}^{m}D_3 = \sigma \; ; \tag{2.10} $$

$$ {}^{p}H_1 = {}^{m}H_1, \;\; {}^{p}H_2 = {}^{m}H_2, \;\; {}^{p}B_3 = {}^{m}B_3 \; . \tag{2.11} $$

We now seek to find the expression for the direct ME voltage coefficient given by $\alpha_{Eij} = \partial\,{}^{p}E_i/\partial\,{}^{m}H_j$, or the electric field induced in the PE when the MS layers are subjected to an external

magnetic field. By substitution of the constitutive equations (2.3) and (2.6) into equation (2.9) we get:

$$ {}^{p}s^{E}_{abkl}\,{}^{p}T_{kl} + k_c d_{km}\,{}^{p}E_k = \; k_c\,{}^{m}s^{E}_{abkl}\,{}^{m}T_{kl} + k_c({}^{m}S_{0ab}(\boldsymbol{H_0}) + q_{kab}(\boldsymbol{H_0})\,{}^{m}H_k)\,. \qquad (2.12) $$

Now adding the stress boundary conditions (2.7) and (2.8) to this expression and converting its parameters to the Voigt notation yields:

$$ s_{mn}\,{}^{p}T_n + k_c d_{km}\,{}^{p}E_k = \; k_c({}^{m}S_{0m}(\boldsymbol{H_0}) + q_{km}(\boldsymbol{H_0})\,{}^{m}H_k)\,, \text{ for } m, n = 1, 2, 6, \qquad (2.13) $$

where $s_{mn} = {}^{p}s^{E}_{mn} + k_c f\,{}^{m}s^{E}_{mn}$ is an effective compliance and f is the ratio between the volume fractions of the PE and MS phases (${}^{p}v/{}^{m}v$). The rank-three square s_{mn} matrix in this expression can thus be inverted in order to write the PE stress ${}^{p}T_n$ explicitly as a function of the electric and magnetic fields. Subsequently, substituting this stress in the PE constitutive equation (2.2) and taking into account the elastic boundary conditions (2.7) one arrives at (in Voigt's notation):

$$ {}^{p}D_k = (\varepsilon^{T}_{kl} - k_c d_{km} s^{-1}_{mn} d_{ln})\,{}^{p}E_l \; + k_c d_{km} s^{-1}_{mn}({}^{m}S_{0n}(\boldsymbol{H_0}) + q_{jn}(\boldsymbol{H_0})\,{}^{m}H_j)\,, \qquad (2.14) $$

where s^{-1}_{mn} is the inverse of the s_{mn} effective compliance matrix. Taking now into account that the magnetic layers consist of the electrically conductive Metglas alloy, the electric and displacement fields (${}^{m}D_i = \varepsilon_0\,{}^{m}E_i$) in this layer should be approximately null and its top and bottom surfaces equipotential. Therefore one has [56, 122]:

$$ {}^{m}E_1 = {}^{m}E_2 = \; {}^{m}D_3 = 0\,. \qquad (2.15) $$

By a substitution of the above relations in equation (2.10) the following additional conditions are obtained:

$$ {}^{p}E_1 = {}^{p}E_2 = \; 0\,;\, {}^{p}D_3 = \sigma\,. \qquad (2.16) $$

Replacing this conditions in equation (2.14) one can finally write the ${}^{p}D_3$ component of the dielectric displacement as a function of the ${}^{p}E_3$ electric field and the magnetic fields in the MS layer:

$$ {}^{p}D_3 = (\varepsilon_{33}^{T} - k_c d_{3m} s_{mn}^{-1} d_{3n}) {}^{p}E_3 + k_c d_{3m} s_{mn}^{-1} ({}^{m}S_{0n}(\boldsymbol{H_0}) + q_{jn}(\boldsymbol{H_0}) {}^{m}H_j) . \quad (2.17) $$

Supposing a magnetic field ${}^{m}H_k$ is applied to the composite along one of the three possible directions k = 1, 2 or 3, one can therefore rearrange the expression above in order to obtain the variable ${}^{p}E_3$ explicitly as a linear function of this field as well as the ${}^{p}D_3$ field. Starting by considering an open circuit situation ($I = \int_{Area} {}^{p}\dot{D}_3 \, dA = 0$, where I is the current in the Z direction), in which ${}^{p}D_3$ equals an initial constant surface charge σ, as shown in equation (1.16), which is assumed to be null (${}^{p}D_3 = 0$), and differentiating ${}^{p}E_3$ with respect to ${}^{m}H_k$, one finally arrives at the desired direct ME voltage coefficient. From this it follows that for $\boldsymbol{H} \to \boldsymbol{H_0}$ the general ME voltage coefficient can be written as a function of this field by the compact expression:

$$ \alpha_{E3k}(\boldsymbol{H}) = \frac{\partial {}^{p}E_3}{\partial {}^{m}H_k}(\boldsymbol{H}) = \frac{-k_c d_{3m} s_{mn}^{-1} q_{kn}(\boldsymbol{H})}{\varepsilon_{33}^{T} - k_c d_{3m} s_{mn}^{-1} d_{3n}} . \quad (2.18) $$

In the special case of a uniaxial PE (such as PZT ceramic with ∞m symmetry) which has only 2, 3 and 5 independent dielectric, PE and elastic constants, respectively, and a MS material, such as Metglas, with a normal orientation (∞m symmetry), this yields the result [19, 56]:

$$ \alpha_{E3k}(\boldsymbol{H}) = \frac{\partial {}^{p}E_3}{\partial {}^{m}H_k}(\boldsymbol{H}) = \frac{-k_c d_{31}(q_{k1}(\boldsymbol{H}) + q_{k2}(\boldsymbol{H}))}{\varepsilon_{33}^{T}[({}^{p}s_{11}^{E} + {}^{p}s_{12}^{E}) + k_c f({}^{m}s_{11}^{E} + {}^{m}s_{12}^{E})] - 2k_c d_{31}^2} , \quad (2.19) $$

which shows the tendency of the direct ME effect to be larger in composites containing PE phases with a large transverse piezocoefficient (d_{31}), small out-of-plane dielectric permittivity (ε_{33}^{T}) and small longitudinal and transverse compliance or flexibility (${}^{p}s_{11}^{E} + {}^{p}s_{12}^{E}$). Additionally, the MS phase should have large longitudinal and transverse piezomagnetic coefficients ($q_{k1}(\boldsymbol{H}) + q_{k2}(\boldsymbol{H})$) and small compliances (${}^{m}s_{11}^{E} + {}^{m}s_{12}^{E}$). The curves of this ME coefficient as a function of the external magnetic field are known to follow those of the piezomagnetic coefficients [123]. The ME coefficient

is thus proportional to the first derivative of the magnetostriction curve, increasing with the H field up to a given point, where the derivative of the magnetostriction is maximum, and decreasing progressively to zero afterwards, as the straining of the magnetic phase eventually saturates. Consequently, the piezomagnetic coefficients presented in literature often correspond to their maximum values for a given magnetic field, and the ME coefficients estimated by solving equation (2.18) will then be associated with the maximal expected coefficients for this field. Expression (2.19) additionally shows that, in order to maximize the ME effect, it is extremely important to obtain a good mechanical coupling between phases (i.e. a large k_c), thus guarantying an efficient transference of strain between them. Also, the thickness ratio between the PE and the MS layers should be as small as possible (i.e. small f), thus maximizing the in-plane normal tensile/compressive stress ${}^{p}T_n$ applied to the PE phase by the MS phase in the direction of the applied magnetic field, as seen by equation (2.13), while at the same time nullifying the compressive/tensile stress ${}^{m}T_n$ felt by the MS phase, as seen by equation (2.8). However, since the voltage measured in any real detection circuit associated with some input noise is proportional to the thickness of the PE layer, the maximal signal-to-noise ratio should be observed for a finite PE thickness. On the other hand, minimizing f by infinitely increasing the thickness of the MS layers would lead to unpractically large samples, so that some compromise has to be achieved for any given application.

The model shown in this part also permits the estimation of the quasi-static charge ME coefficient through a simple change in the electrical boundary conditions. For this case we consider a short-circuited composite ($V = -\int_{p_t} {}^{p}E_3 \, dZ = 0$, where V is the voltage developed across the PE) in such a way that we have ${}^{p}E_3 = 0$ instead of ${}^{p}D_3 = 0$ in (2.16). Subsequently equation (2.17) is differentiated in relation to ${}^{m}H_k$, thus yielding:

$$\alpha_{Q3k}(\boldsymbol{H}) = \frac{\partial {}^{p}D_3}{\partial {}^{m}H_k}(\boldsymbol{H}) = k_c d_{3m} s_{mn}^{-1} q_{kn}(\boldsymbol{H}) \, . \tag{2.20}$$

Comparing the general equations (2.18) and (2.20), one sees that both the charge and voltage coefficients can be directly related by the expression $\alpha_{Q3k}(\boldsymbol{H}) = -(\varepsilon_{33}^{T} - k_c d_{3m} s_{mn}^{-1} d_{3n})\alpha_{E3k}(\boldsymbol{H})$, where $C = (\varepsilon_{33}^{T} - k_c d_{3m} s_{mn}^{-1} d_{3n})A/{}^{p}t$ represents the low frequency capacitance of the composite as it will be shown later. This capacitance tends to decrease with increasing k_c (i.e. better coupling between layers) and decreasing f (i.e. thicker MS layers in relation to the PE ones). For the case of uniaxial PE and MS materials, expression (2.20) is simplified to:

$$\alpha_{Q3k}(\boldsymbol{H}) = \frac{\partial {}^{p}D_3}{\partial {}^{m}H_k}(\boldsymbol{H}) = \frac{k_c d_{31}(q_{k1}(\boldsymbol{H})+q_{k2}(\boldsymbol{H}))}{({}^{p}s_{11}^{E}+{}^{p}s_{12}^{E})+k_c f({}^{m}s_{11}^{E}+{}^{m}s_{12}^{E})}, \tag{2.21}$$

which shows that, when compared to the α_{E3k} coefficient in equation (2.19), the charge coefficient is generally associated with a change of sign and no longer depends on the dielectric permittivity ε_{33}^{T} of the PE. Apart from this, all of the observations made before remain valid.

As mentioned before, up to this point the demagnetization effects on the MS layers have been neglected. For the special case of uniformly magnetized ellipsoids (with magnetization M_j) subjected to an uniform external magnetic field H_k', the uniform field developed inside the material H_k can be given by $H_k = H_k' - N_{kj}M_j$, where N_{kj} is a demagnetization factor which depends on the shape of the ellipsoid [127]. In the case of an infinite plane with a normal pointing in the *Z* direction this demagnetization factor is given by $N_{33} = 1$ and $N_{kj} = 0$ otherwise [127]. Therefore, for thin enough MS layers the demagnetization fields can be neglected for H_k' applied in the *X* or *Y* directions (i.e. $H_k' = H_k$). However, in the case of thick MS phases, such that $N_{aa} \neq 0$, or of the ME longitudinal geometry where $H_3 \neq 0$, this effect can become quite substantial. The ME coefficients given by equations (2.18-2.21) can be corrected to take this effect into account. To do this, one starts by writing the external magnetic field H_k' as a function of the internal magnetic field H_k. Taking the demagnetization equation for some N_{kj} and making the substitution ${}^{m}M_j = {}^{m}B_j/\mu_0 - {}^{m}H_j$, one obtains ${}^{m}H_k'$ as a function of ${}^{m}H_j$ and the magnetic induction ${}^{m}B_j$ given by equation (2.5). Subsequently, through a series of substitutions involving equations (2.7), (2.8) and (2.13) one arrives at the final result:

$${}^{m}H_k' = \overline{H_{0k}}(\boldsymbol{H_0}) + \overline{\mu_{kl}}(\boldsymbol{H_0}){}^{m}H_l + \overline{\alpha_{Qk3}}(\boldsymbol{H_0}){}^{p}E_3\,, \tag{2.22}$$

where $\overline{H_{0k}}(\boldsymbol{H_0}) = (N_{kj}/\mu_0)({}^{m}B_{0j}(\boldsymbol{H_0}) - k_c f q_{jm}(\boldsymbol{H_0}) s_{mn}^{-1}{}^{m}S_{0n}(\boldsymbol{H_0}))$, $\overline{\alpha_{Qk3}}(\boldsymbol{H_0}) = (N_{kj}/\mu_0)k_c f q_{jm}(\boldsymbol{H}) s_{mn}^{-1} d_{3n}$, $\overline{\mu_{kl}}(\boldsymbol{H_0}) = \delta_{kl} - N_{kl} + \mu_{kl}(\boldsymbol{H_0}) - k_c f q_{km}(\boldsymbol{H_0}) s_{mn}^{-1} q_{ln}(\boldsymbol{H_0})$.and ${}^{p}E_3$ is related to ${}^{m}H_j$ and ${}^{p}D_3$ through equation (2.17). The corrected ME voltage coefficients written as a function of the known external magnetic fields $\boldsymbol{H'} \rightarrow \boldsymbol{H_0'}$ can therefore be given as $\alpha_{E3k}'(\boldsymbol{H'}) = \partial {}^{p}E_3/\partial {}^{m}H_k'(\boldsymbol{H'}) = \partial {}^{p}E_3/\partial {}^{m}H_j(\boldsymbol{H}(\boldsymbol{H'}))\,.\,\partial {}^{m}H_j/\partial {}^{m}H_k'(\boldsymbol{H'})$, which reduces to:

$$\alpha_{E3k}'(\boldsymbol{H'}) = \alpha_{E3j}(\boldsymbol{H}(\boldsymbol{H'}))\left[\overline{\mu_{jl}}^{-1}(\boldsymbol{H}(\boldsymbol{H'}))\left[\delta_{lk} - \overline{\alpha_{Ql3}}(\boldsymbol{H}(\boldsymbol{H'}))\alpha_{E3k}(\boldsymbol{H}(\boldsymbol{H'}))\right]\right], \tag{2.23}$$

where $\overline{\mu_{jl}}^{-1}(\boldsymbol{H}(\boldsymbol{H}'))$ is the inverse of the $\overline{\mu_{kl}}(\boldsymbol{H_0})$ function, $\alpha_{E3j}(\boldsymbol{H}(\boldsymbol{H}'))$ is given by equation (2.18) and $\boldsymbol{H}(\boldsymbol{H}')$ is determined by solving the implicit expression (2.22). In summary, this shows that the maximum ME effects of composites subjected to demagnetization effects tend to be smaller and to appear at higher applied magnetic fields [6].

The aforementioned ME coefficients were defined for ideal open-circuit or short-circuit conditions. However, in experiment the ME composites are operated under non-ideal conditions, in which case the parameters of the external measuring circuits have to be taken into account. Therefore it is useful to model the composites as equivalent electrical circuits. In this regard, assuming harmonic fields of the type ${}^{m}H_k = {}^{m}H_{0k} + \delta H_k e^{j\omega t}$, where ${}^{m}H_{0k}$ is a bias field, δH_k a complex amplitude, j the imaginary unit, ω the angular frequency and t the time, and differentiating equation (2.17) with respect to time and integrating it over the volume of the composite (i.e. $\int_{p_t}\int_{Area} {}^{p}\dot{D}_3\, dAdZ$), one can derive the relation:

$$\delta V_3 = (-\alpha_{E3k}(\boldsymbol{H_0})^{p}t)\delta H_k - (1/j\omega C)\delta I_3\ , \tag{2.24}$$

where $\delta V_3 = -\int_{p_t} \delta^{p}E_3\, dZ$ is the *AC* voltage measured between the top and bottom of the composite and $\delta I_3 = j\omega \int_{Area} \delta^{p}D_3\, dA$ is the *AC* current flowing through it in the *Z* direction. This expression thus shows that the composite can be modeled as a Thévenin equivalent circuit consisting of an equivalent voltage source of $\delta V_3 = (-\alpha_{E3k}(\boldsymbol{H_0})^{p}t)\delta H_k$ connected in series with an equivalent impedance given by $Z = 1/j\omega C$ which represents a capacitor with capacitance $C = (\varepsilon_{33}^{T} - k_c d_{3m} s_{mn}^{-1} d_{3n})A/{}^{p}t$. Equivalently, the composite can also be modeled as a Norton equivalent circuit composed of a current source of $\delta I_3 = (j\omega\alpha_{Q3k}(\boldsymbol{H_0})A)\delta H_k$ connected in parallel with the same impedance. More precisely, by taking into account the important effects of dielectric dispersion ($\varepsilon_{33}^{T}(\omega)$), dielectric losses ($\varepsilon_{33}^{T''}(\omega)$) and conductivity ($\sigma$) of the PE through the introduction of the complex dielectric coefficient $\varepsilon_{33}^{T}(\omega) = \varepsilon_{33}^{T\prime}(\omega) - j\varepsilon_{33}^{T''}(\omega) + \sigma/j\omega = \varepsilon_{33}^{T'}(\omega) - j\varepsilon_{33}^{T'}(\omega)\tan(\delta)$, where $\omega\varepsilon_{33}^{T'}(\omega)\tan(\delta)$ is the so called dissipation factor, the equivalent impedance of the composite can be given by $Z = 1/(1/R' + j\omega C')$ which corresponds to a capacitor with $C' = \left(\varepsilon_{33}^{T'}(\omega) - k_c d_{3m} s_{mn}^{-1} d_{3n}\right)A/{}^{p}t$ connected in parallel with a resistor with $R' = {}^{p}t/A\omega\varepsilon_{33}^{T'}(\omega)\tan(\delta)$. In conclusion, when measuring for example the ME voltage coefficient, the finite input impedance of the measuring circuit should always be taken into account. Assuming e.g. an input impedance of

$Z_{in} = 1/(1/R_{in} + j\omega C_{in})$ as in the case of a lock-in amplifier, the measured voltage in such a device as a function of the magnetic fields will be given by $\delta V_{in} = (Z_{in}/(Z + Z_{in}))\delta V_3$. Thus, the circuit will generally behave as a high-pass filter with a small input amplitude $|\delta V_{in}| = (R_{in}/(R' + R_{in}))|\delta V_3|$ being measured at zero frequency (because R' usually takes a much larger value than R_{in} in a lock-in amplifier) and a larger input amplitude $|\delta V_{in}| = (C'/(C' + C_{in}))|\delta V_3|$ measured at high frequencies (because C_{in} is normally much smaller than C'). An important application of this circuit model is in the development of sensitive low-noise magnetic field sensors based on the ME effect [60, 62].

ME composites comprising PE single crystals have been the subject of a few recent studies including PMN-PT [61, 128-130], PZN-PT [131], barium titanate ($BaTiO_3$) [132], lithium niobate ($LiNbO_3$) [128, 133], gallium phosphate ($GaPO_4$) [134], quartz (SiO_2) [135], aluminum nitride (AlN) [108], zinc oxide (ZnO) [136], langatate ($La_3Ga_{5.5}Ta_{0.5}O_{14}$, LGT) [137, 138] and langasite ($La_3Ga_{5.5}SiO_{14}$, LGS) [138]. These have promised further enhancement of the ME coupling. Since single crystals are highly anisotropic, their electric and elastic properties sensitively depend on their crystallographic orientation. Therefore, the optimization of the orientation could lead to greatly enhanced ME coefficients in composites. To study this dependency of the ME coupling on the crystal orientation, we have to subject the material tensors to a passive transformation of coordinates. Equations (2.1)–(2.24) contain the material coefficients and fields defined in the laminate *XYZ* frame of Figure 2.1 *a)*. However, the material properties are usually described in the crystallographic *xyz* frame (or [100]×[010]×[001]), and that is why we have to transform them to the laminate frame before applying the equations. To do so, the rotation matrix a_{ij} is introduced, where the Euler angles $Z_1X_2Z_3$ scheme (see Figure 2.1 *b)*) is employed [139]:

$$\boldsymbol{a} = \begin{bmatrix} \cos(\gamma)\cos(\alpha) - \cos(\beta)\sin(\alpha)\sin(\gamma) & \cos(\gamma)\sin(\alpha) + \cos(\beta)\cos(\alpha)\sin(\gamma) & \sin(\gamma)\sin(\beta) \\ -\sin(\gamma)\cos(\alpha) - \cos(\beta)\sin(\alpha)\cos(\gamma) & -\sin(\gamma)\sin(\alpha) + \cos(\beta)\cos(\alpha)\cos(\gamma) & \cos(\gamma)\sin(\beta) \\ \sin(\beta)\sin(\alpha) & -\sin(\beta)\cos(\alpha) & \cos(\beta) \end{bmatrix} \tag{2.25}$$

This matrix describes a sequence of three direct elemental rotations, the first around the Z axis by an angle α, the second around the X axis by an angle β, and the third again around the Z axis by an angle γ. In this case, after applying the rotation matrix to the crystal, the angles α and β will identify the vector normal to the plane of the laminate, and the angle γ will determine the orientation of the side faces of the laminate in this plane (and consequently the direction of the applied in-plane magnetic fields). Upon changing the frame of reference, the material parameters follow the specific tensor transformation rules which also define the second-, third- and fourth-rank tensors [119]:

$$\varepsilon_{ij} = a_{im}a_{jn}\varepsilon'_{mn}\,;\quad d_{ijk} = a_{im}a_{jn}a_{ko}d'_{mno}\,;\quad s_{ijkl} = a_{im}a_{jn}a_{ko}a_{lp}s'_{mnop}\,, \tag{2.26}$$

where the constants with an apostrophe denote the material properties in the initial crystallographic frame, and those without the properties in the new frame of reference described by the transformation $\boldsymbol{a}$.

2.3. Estimation of the quasi-static transversal ME voltage coefficients in magnetostrictive/piezocrystalline/magnetostrictive tri-layers

We are now in possession of all the tools we need in order to estimate the transversal ME response (α_{E3i}, with i = 1 or 2) in a series of tri-layered composites containing two layers of Metglas bonded to a PE single crystal of some sort. To do so, we create a fine grid of Euler angles in steps of 1° and subsequently analyze the calculations for these angles. The composites we investigated had the shape of a square plate like the one shown in Figure 2.1 *a*), where we considered 10 × 10 mm^2 sheets of Metglas with 29 μm of thickness bonded to opposite sides of a 10 × 10 mm^2 PE crystal with a thickness of 0.5 mm. A perfect coupling between interfaces was assumed (k_c = 1). In a traction-free Metglas layer a maximum q_{11} value of ca. 4 ppm/Oe and q_{12} of ca. –1.7 ppm/Oe are attained at a bias field of ca. 10 Oe [140-143]. These were therefore taken as our piezomagnetic coefficients. All of the dielectric, piezoelectric, piezomagnetic (for Metglas [140-143]) and elastic material parameters needed for these calculations where obtained from the literature and are presented in the Appendix. The lead-free piezoelectrics studied here thus have included: $LiNbO_3$ [70, 144], α-$GaPO_4$ [71, 72], α-quartz [145, 146], langatate [147, 148], langasite [149, 150], AlN [151, 152], $LiTaO_3$ [153-155] and $BaTiO_3$ [68, 69], and also the lead-based ones, viz., PZT-2 [156], PMN-33%PT ([111] poled) [157], PMN-30%PT ([011] poled) [75], PMN-33%PT ([001] poled) [158], PZN-9%PT ([011] poled) [159] and PZN-8%PT ([001] poled) [160].

The results obtained by solving equation (2.18) are summarized in Table 2.1 which shows the maximum expected direct ME coefficients for each composite and respective optimal crystallographic orientations of the PE phase. From these estimations we confirmed the possibility of generating large quasi-static ME effects in ME composites comprising lead-free PE single crystals. Here, coefficients as large as 35.6 V/(cm·Oe) are expected. These ME effects are particularly attractive for the tri-layers comprising $LiNbO_3$, $GaPO_4$, quartz, PMN–33%PT ([111] poled) and

PZN–9%PT ([011] poled) originating from a particularly good combination of relatively large PE coefficients and low dielectric constants. Also, because the maximum expected ME effects are of the same order of magnitude in both lead-based and lead-free PEs, such exclusive features as chemical stability, linear piezoelectricity and high Curie temperature (in the range of 570–1475ºC) open up a real perspective to use these lead-free PE-based magnetoelectric tri-layers in practical applications.

The selection of crystals with an appropriate cut is a very important step in the development of ME composites. The engineering of these cuts should in principle allow one to develop materials with specific anisotropic properties desired for each type of practical application. Large ME effects are particularly important in applications requiring enhanced efficiencies and sensitivities. Figure 2.2 thus shows the maximum absolute transversal ME coefficients (in the range of all spanned γ angles) estimated as a function of the α and β angles for all considered tri-layers. From these figures we notice the great sensitivity of the ME effect to the orientation of the piezocrystal. The shape of the figures depends on the point group symmetry of the PE mainly through the term $|g_{31} - g_{32}|$ which indicates the difference between PE voltage coefficients ($g_{ij} = -\partial E_i/\partial T_j = \varepsilon_{ik}^{-1} d_{kj}$) for stresses directed along both lateral surfaces of the crystal, since the elastic term varies much less with the orientation of the crystal.

We note at this point that, alongside the dispersion and losses of the material's properties not taken into account, a much more important limitation of the model is the fact that the piezomagnetic coefficients of Metglas are also strongly dependent on the bias magnetic fields and stress tensors. A more complex model for the soft MS phase shows for example that the large compressive pre-stress produced by the PE substrate in the MS sheets tends to decrease the maximum value of q_{kn} and at the same time increase the bias field at which it is attained [161]. Therefore, the maximum ME coefficients predicted in this part should be somewhat overestimated. Nonetheless, the relation between ME coefficients obtained for the composites with different PE crystals still remains valid. Furthermore, we point out that the thickness ratio between the MS and PE layers in the composites was not optimized for a maximum ME response. Thicker MS layers are expected to produce a larger effective strain on the PE crystal and thus increase the amplitude of the ME effect by up to one order of magnitude. In this calculations, 29 μm thick layers of Metglas were used because, in practice, some peculiarities associated with the fabrication of these alloys (i.e. a melt spinning rapid solidification process) restricts their thickness to just a few of tens of μm. Also, commercial PE crystals are generally found with thicknesses no smaller than 0.2 mm.

In the next paragraphs we are going to discuss the results of the calculations in greater detail. Starting with the case of the $LiNbO_3$ crystal, which belongs to the trigonal *3m* symmetry point group, we see that the estimated ME coefficient could be as large as 27.24 V/(cm·Oe) for a crystal with a

(*ZXl*) 39º-cut (α = 0º, β = 39º and γ = 90º), commercially commonly referred to as 129ºY-cut, and five other cuts equivalent by symmetry. We also see that this effect stays within 90% of its maximum value for cut deviations, in relation to its optimal orientation, of approximately $\Delta\alpha$ = ±20º and $\Delta\beta$ = ±10º. $LiTaO_3$ has the same symmetry as $LiNbO_3$, but we calculated in this case an expected coefficient of 11.40 V/(cm·Oe), being about 3 times smaller than that in the former material. This is mainly because of its characteristically smaller PE coefficients (especially its d_{15} and d_{22} components), as well as comparable dielectric constants. The maximum effect should be observed in a (*ZXl*) 45º-cut crystal (α = 0º, β = 45º and γ = 90º) and also other five equivalent cuts. This coefficient decreases by less than 10% for cut deviations of about $\Delta\alpha$ = ±25º and $\Delta\beta$ = ±10º. $BaTiO_3$ single crystals belong to the tetragonal *4mm* point group and have much larger PE and dielectric coefficients than $LiNbO_3$. The largest expected ME coefficient here is just of 10.74 V/(cm·Oe) and is only observed in the Z-cut crystal, decaying very rapidly as we move away from this optimal orientation. AlN piezocrystals exhibit a hexagonal *6mm* symmetry and relatively small dielectric and PE coefficients. The maximum coefficient for a composite containing this phase was calculated as 13.06 V/(cm·Oe) for the (*ZXl*) 60º-cut ($0º \leq \alpha < 360º$, β = 60º and γ = 90º) and (*ZXl*) 120º-cut crystals. As in $BaTiO_3$, this effect is axially symmetric and stays within 90% of its maximum value for cut deviations of approximately $\Delta\beta$ = ±10º.

Table 2.1 Estimation of the maximum expected transversal direct ME voltage coefficients for a series of 10 × 10 mm^2 ME tri-layered composites consisting of two 29 μm thick layers of Metglas and one central 0.5 mm thick PE crystal of some kind. The optimal crystallographic orientations and corresponding crystal cuts according to the IEEE standard [67] are also presented. Here, the optimal orientations are given as a set of Euler angles (α, β and γ in deg.), where the first column indicates the possible combinations of angles (equivalent by symmetry) corresponding to the same absolute maximum positive ME effect, whereas the second column gives the combination of angles for the same absolute maximum but negative ME effect (i.e., with an inversion in the sign of the ME coupling coefficient). The frame of reference in each case corresponds to the crystallographic frame except in PZT, PMN-PT and PZN-PT, where it corresponds to their respective poled multidomain frames with the Z axis directed along their poling directions.

PE crystal	**$LiNbO_3$**			**α–$GaPO_4$**			**α–Quartz**			**Langatate (LGT)**			**Langasite (LGS)**			**AlN**		**$LiTaO_3$**			**$BaTiO_3$**		
Maximum $\lvert\alpha_{E3a}\rvert$ (V/(cm·Oe))	27.24			35.62			23.77			16.68			16.59			13.06		11.40			10.74		
Z-cut crystal α_{E3a} (V/(cm·Oe))	1.23			0			0			0			0			8.16		2.89			10.74		
Optimal orientation	α	0 120 240	60 180 300	α	90 210 330	30 150 270	α	90 210 330	30 150 270	α	30 150 270	90 210 330	α	30 150 270	90 210 330	α	0 – 360	0 – 360	α	0 120 240	60 180 300	α	0 – 360	0 – 360
	β	39	141	β	90	90	β	90	90	β	90	90	β	90	90	β	120	60	β	45	135	β	0	180
	γ	90	90	γ	12	168	γ	169	11	γ	156	24	γ	160	20	γ	90	90	γ	90	90	γ	0 – 360	0 – 360
Crystal cut	(*ZXl*) 39º			(*XYt*) 12º			(*XYt*) 11º			(*XYt*) 24º			(*XYt*) 20º			(*ZXl*) 60º		(*ZXl*) 45º			Z		

PE crystal	PZT–2			PMN–33%PT ([111] poled)			PMN–30%PT ([011] poled)			PMN–33%PT ([001] poled)			PZN–9%PT ([011] poled)			PZN–8%PT ([001] poled)		
Maximum $\lvert\alpha_{E3a}\rvert$ (V/(cm·Oe))	7.47			27.11			12.50			10.80			23.04			8.30		
Z-cut crystal $\lvert\alpha_{E3a}\rvert$ (V/(cm·Oe))	5.41			5.78			12.50			6.29			23.04			7.66		
Optimal orientation	α	0 – 360	0 – 360	α	0 120 240	60 180 300	α	0 – 360	0 – 360	α	45 135 225 315	45 135 225 315	α	0 – 360	0 – 360	α	45 135 225 315	45 135 225 315
	β	37	143	β	42	138	β	0	180	β	116	64	β	0	180	β	38	142
	γ	90	90	γ	90	90	γ	90–α	90–α	γ	90	90	γ	90–α	90–α	γ	0	0
Crystal cut	(*ZXl*) 37º			(*ZXl*) 42º			Z			(*ZXtl*) 45º/64º			Z			(*ZXtl*) 45º/38º		

a)

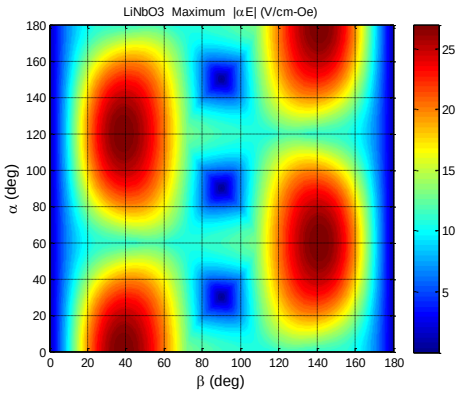
LiNbO3 Maximum |αE| (V/cm-Oe)
α (deg)
β (deg)

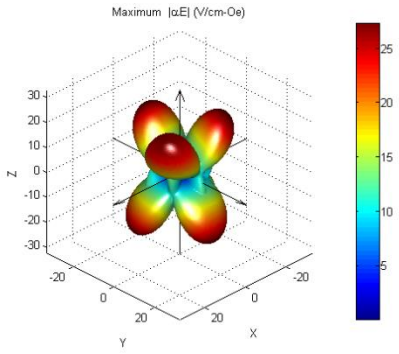
Maximum |αE| (V/cm-Oe)
Z
Y
X

b)

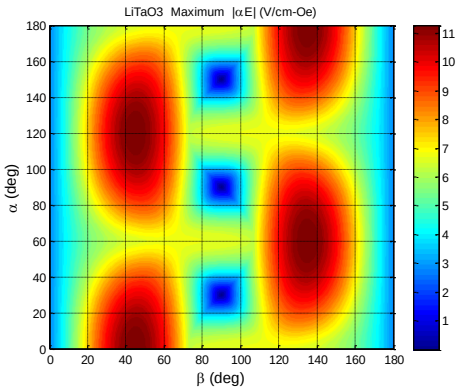
LiTaO3 Maximum |αE| (V/cm-Oe)
α (deg)
β (deg)

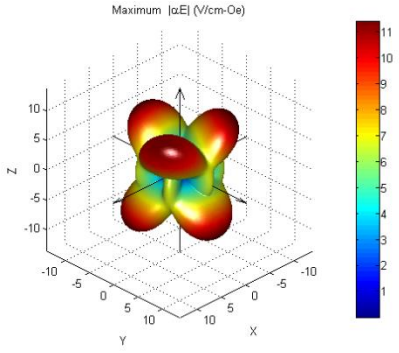
Maximum |αE| (V/cm-Oe)
Z
Y
X

c)

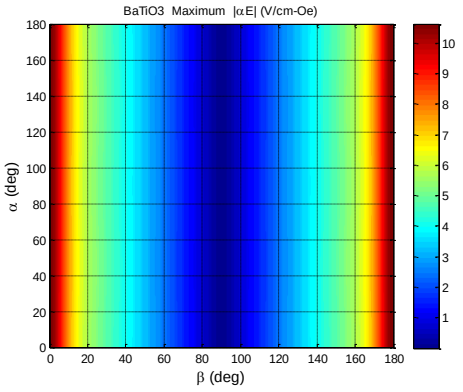
BaTiO3 Maximum |αE| (V/cm-Oe)
α (deg)
β (deg)

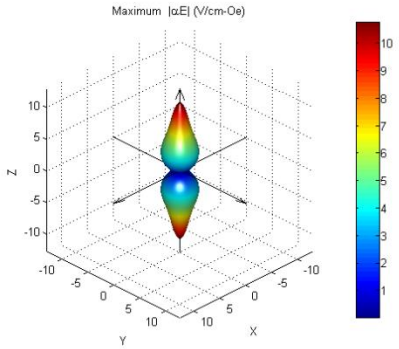
Maximum |αE| (V/cm-Oe)
Z
Y
X

d)

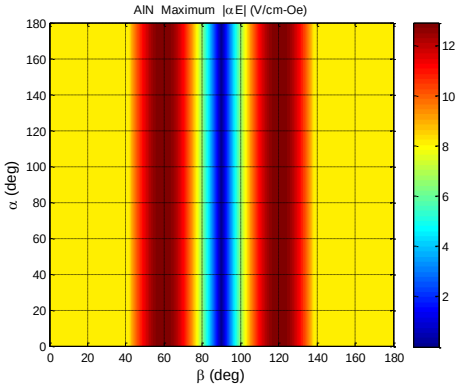
AlN Maximum |αE| (V/cm-Oe)
α (deg)
β (deg)

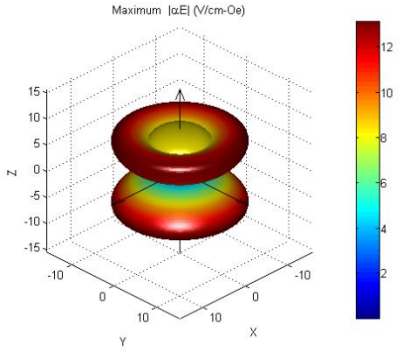
Maximum |αE| (V/cm-Oe)
Z
Y
X

e)

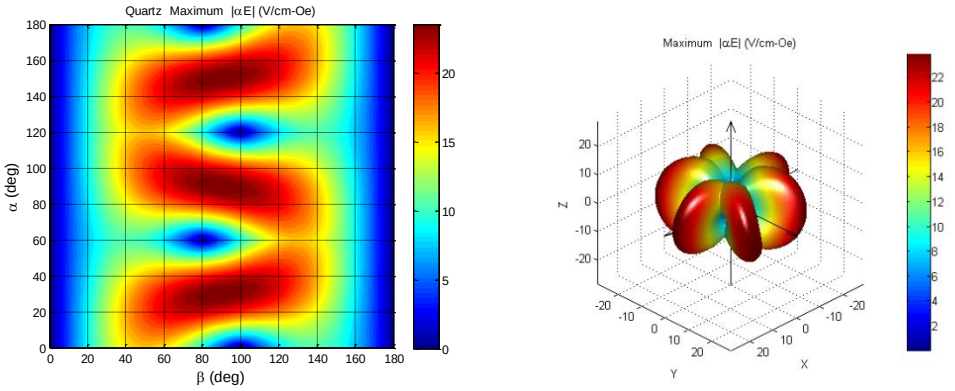
Quartz Maximum |αE| (V/cm-Oe)
α (deg)
β (deg)
Maximum |αE| (V/cm-Oe)
Z
Y
X

f)

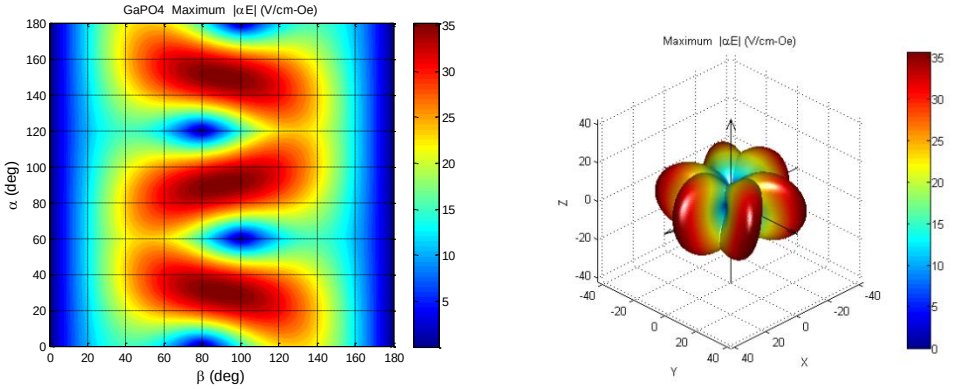
GaPO4 Maximum |αE| (V/cm-Oe)
α (deg)
β (deg)
Maximum |αE| (V/cm-Oe)
Z
Y
X

g)

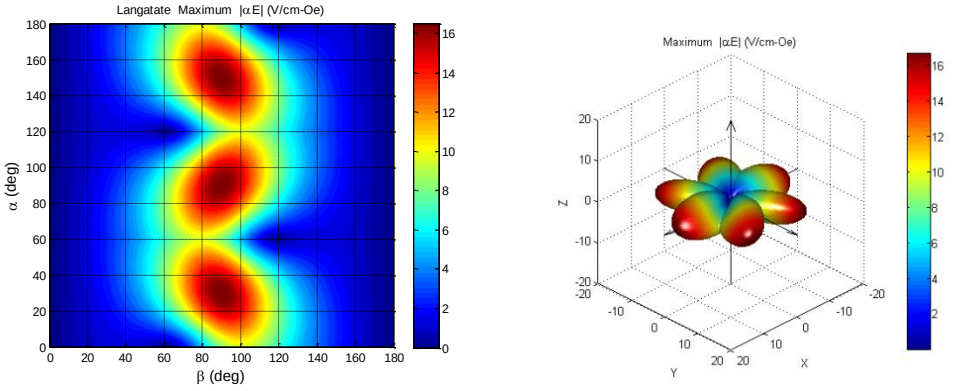
Langatate Maximum |αE| (V/cm-Oe)
α (deg)
β (deg)
Maximum |αE| (V/cm-Oe)
Z
Y
X

h)

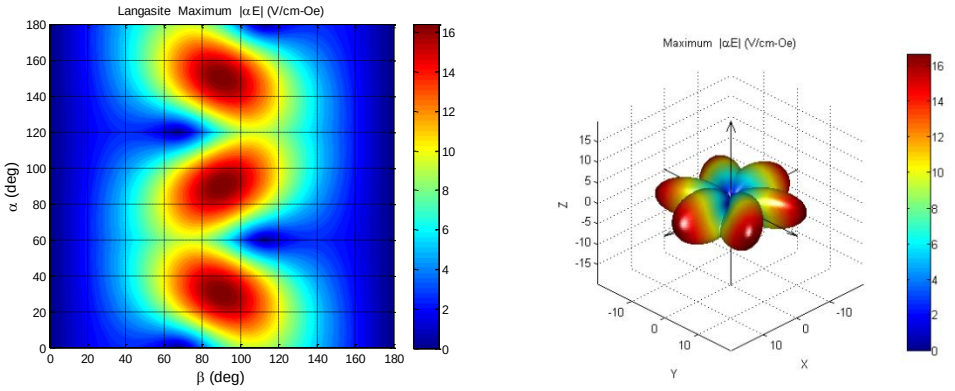
Langasite Maximum |αE| (V/cm-Oe)
α (deg)
β (deg)
Maximum |αE| (V/cm-Oe)
Z
Y
X

i)

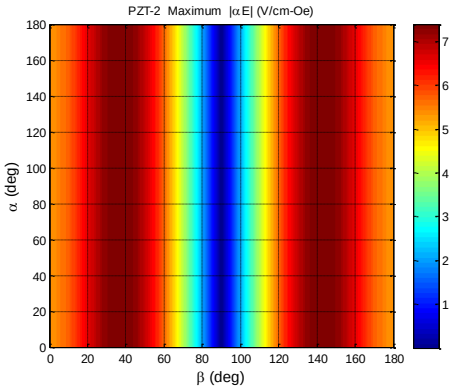
PZT-2 Maximum |αE| (V/cm-Oe)
α (deg)
β (deg)

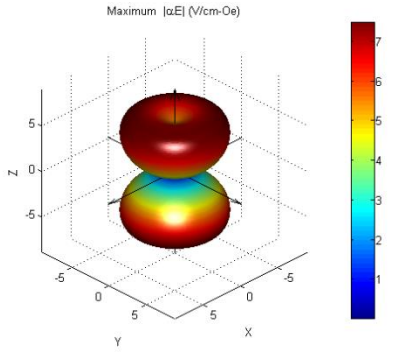
Maximum |αE| (V/cm-Oe)
Z
Y
X

j)

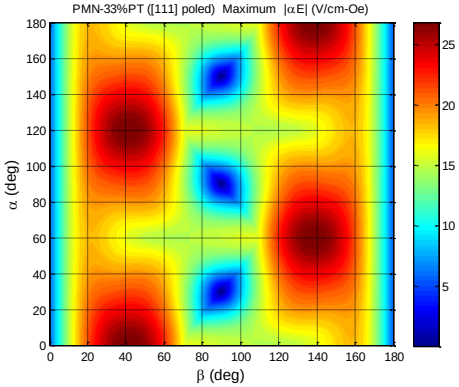
PMN-33%PT ([111] poled) Maximum |αE| (V/cm-Oe)
α (deg)
β (deg)

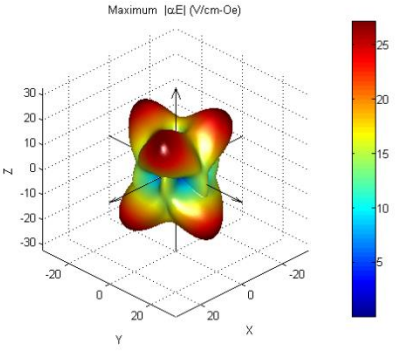
Maximum |αE| (V/cm-Oe)
Z
Y
X

k)

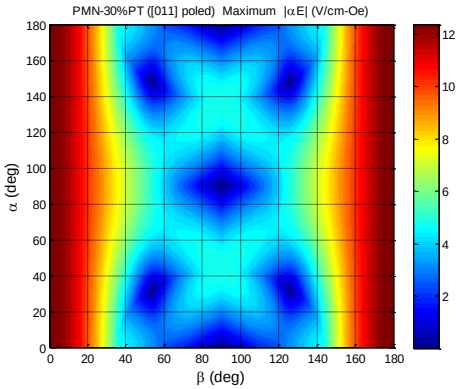
PMN-30%PT ([011] poled) Maximum |αE| (V/cm-Oe)
α (deg)
β (deg)

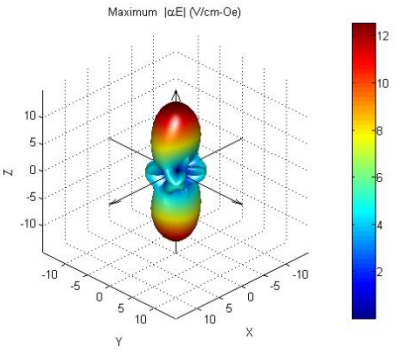
Maximum |αE| (V/cm-Oe)
Z
Y
X

l)

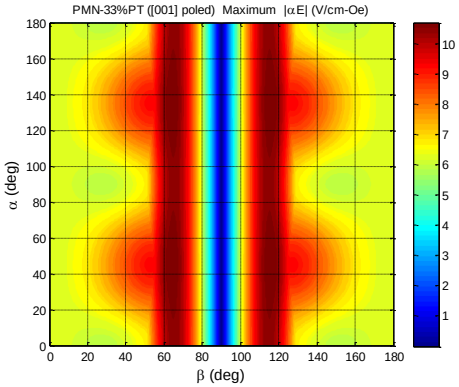
PMN-33%PT ([001] poled) Maximum |αE| (V/cm-Oe)
α (deg)
β (deg)

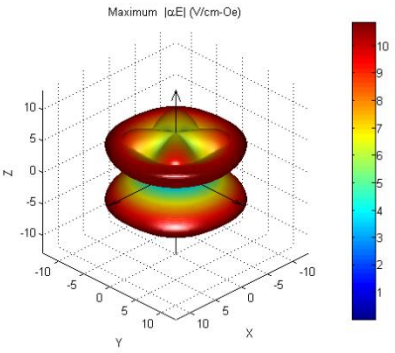
Maximum |αE| (V/cm-Oe)
Z
Y
X

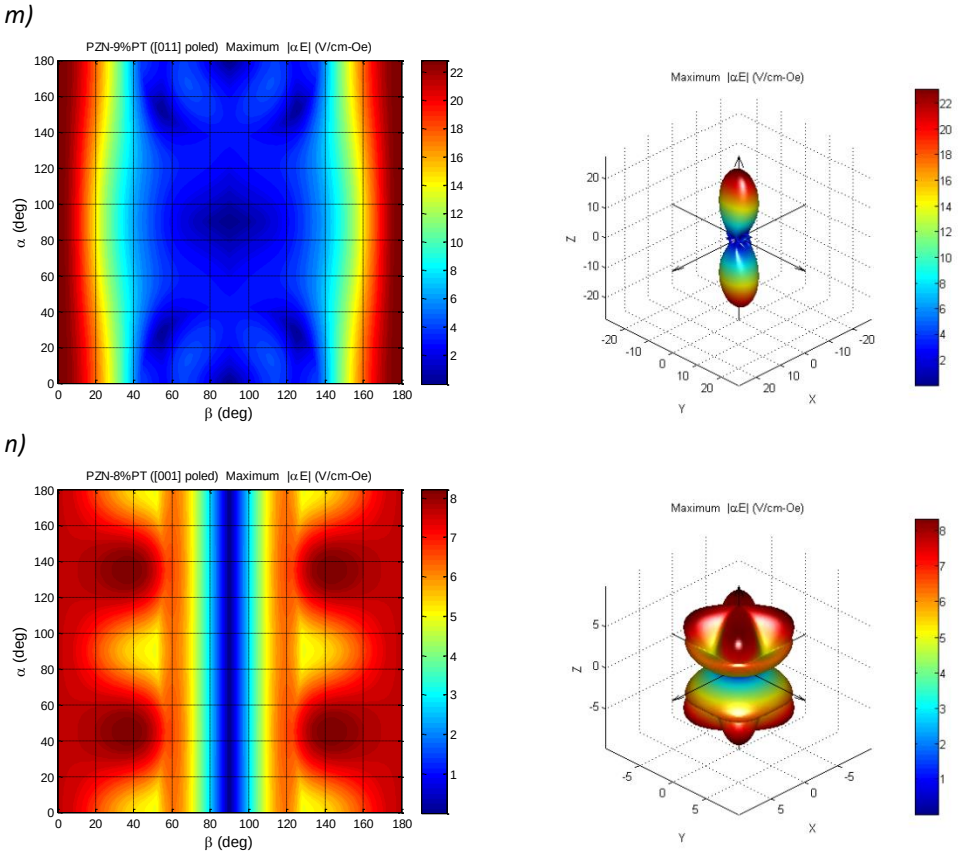

Figure 2.2 Contour plots (left panels) and $|\alpha_{E3i}|$ representation surfaces (right panels) depicting the maximum estimated absolute values of the transversal ME voltage coefficient α_{E3i} (across $0 < \gamma < 180^{o}$) as a function of the crystal-cut orientation (α and β angles) for the tri-layered ME composites of Metglas/PE/Metglas, where the PE phase is a single crystal of: *a*) $LiNbO_3$; *b*) $LiTaO_3$; *c*) $BaTiO_3$; *d*) AlN; *e*) α-quartz; *f*) α-$GaPO_4$; *g*) langatate; *h*) langasite; *i)* PZT-2; *j)* PMN-33%PT ([111] poled); *k)* PMN-30%PT ([011] poled); *l)* PMN-33%PT ([001] poled); *m)* PZN-9%PT ([011] poled) and *n)* PZN-8%PT ([001] poled).

The α-quartz and α-$GaPO_4$ PE crystals are another class of lead-free piezoelectrics which, like $LiNbO_3$, exhibit relatively large ratios between PE and dielectric constants. They both belong to the trigonal *32* point group. The most noticeable differences between them are related to the PE coefficients, which are approximately twice as large for the case of $GaPO_4$, as well as the dielectric coefficients which are about 20% larger in $GaPO_4$ as compared to quartz. Even though they have some of the smallest piezoconstants among the piezocrystals studied in this chapter, their dielectric permittivities are also comparatively small, which therefore gives rise to large PE/dielectric ratios and consequently opens the possibility for large ME responses in the composites. Indeed, following the model described above we calculated maximum ME coefficients of 35.62 and 23.77 V/(cm·Oe)

for the $GaPO_4$ and quartz crystals, respectively. These values are quite high and may be observed in (*XYt*) 12º-cut (α = 90º, β = 90º and γ = 12º) crystals of $GaPO_4$ and in (*XYt*) 11º-cut (α = 90º, β = 90º and γ = 11º) crystals of quartz, as well as in other five cut directions equivalent by symmetry. We also note that these cuts are quite near the X-cut direction. In this case, the ME coefficient decreases by less than 10% for cut deviations from the maximum direction of about $\Delta\alpha = \pm 10^o$ and $\Delta\beta = \pm 25^o$.

Langatate and langasite are other two piezoelectrics belonging to the trigonal *32* point group. They are characterized by PE coefficients comparable to the ones of $GaPO_4$, but also exhibit considerably larger dielectric coefficients. Their maximum expected ME coefficients where calculated as 16.68 V/(cm·Oe) for an (*XYt*) 24º-cut crystal (α = 90º, β = 90º and γ = 24º), in the case of langatate, and 16.59 V/(cm·Oe) for an (*XYt*) 20º-cut crystal (α = 90º, β = 90º and γ = 20º), in the case of langasite. Furthermore, the maximum ME effect is more sensitive to the cut angle in these two crystals. We observe that the effect stays within 90% of its maximum value for cut deviations of just about $\Delta\alpha = \pm 10^o$ and $\Delta\beta = \pm 10^o$.

In the class of the lead-based piezoelectrics we start by looking at the PZT-2 uniaxial ceramic having an ∞mm symmetry. As we know, its PE and dielectric properties are quite distinguished. Still, the maximum direct ME coefficient of just about 7.47 V/(cm·Oe) was calculated for the (*ZXl*) 37º-cut direction ($0^o \leq \alpha < 360^o$, β = 37º and γ = 90º) and another equivalent direction. Even though this compound constitutes one of the piezoelectrics most commonly employed in practice, we note that its maximum expected ME response is the smallest among all piezo-crystals studied in this chapter. This fact underlines the importance of the dielectric properties of the materials employed in ME composites. Thus, we see that compounds with merely large PE coefficients do not necessarily yield large direct ME effects. We also observe that for this PZT-2 ceramic the maximum ME coefficient changes little for cut angles in the range $0^o \leq \beta < 60^o$ and $120^o \leq \beta < 180^o$. Therefore, common commercially available Z-cut ceramics still could exhibit a maximum 5.41 V/(cm·Oe) ME response.

PMN-PT crystals are a family of lead-based macrosymmetric multidomain engineered piezoelectrics [162]. Here we studied the ME effect in composites featuring the following compositions: [111] poled PMN-33%PT, [011] poled PMN-30%PT and [001] poled PMN-33%PT. The first compound has a trigonal *3m* symmetry, while the second and third have an orthorhombic *mm2* and tetragonal *4mm* macrosymmetry, respectively. From a general point of view, the [011] poled crystal exhibits the largest dielectric coefficients, followed by the [001] poled and the [111] poled ones. The largest piezocoefficients in each crystal are d_{15} = 4100 pC/N, d_{15} = 3262 pC/N and d_{33} = 2820 pC/N in the [111], [011] and [001] poled compounds, respectively. In the calculations we identified a relatively large maximum direct ME coefficient of 27.11 V/(cm·Oe) in the [111]

poled and (*ZXl*) 42º-cut PMN-PT crystal (α = 0º, β = 42º and γ = 90º), and five other equivalent directions, although this is just of 5.78 V/(cm·Oe) in the Z-cut crystal. The maximum coefficient decays by more than 10% of its highest value for angle deviations larger than $\Delta\alpha$ = ±10º and $\Delta\beta$ = ±10º from the optimal orientation. In the [011] poled crystal, the largest expected value is of 12.50 V/(cm·Oe), and it is observed in the Z-cut crystal. This coefficient changes only slightly for $\Delta\beta$ = ±10º. In the [001] poled PMN-PT crystal the maximum is of 10.80 V/(cm·Oe) and should be attained in the crystal with a (*ZXtl*) 45º/64º complex cut (α = 45º, β = 64º and γ = 90º), and seven other directions. The most common Z-cut could exhibit a ME response of up to 6.29 V/(cm·Oe). By symmetry considerations, an almost maximized ME effect could, nonetheless, be observed in the range of 60º ≤ β < 70º and 110º ≤ β < 120º, for any α angle.

Finally, we also studied PZN-PT piezocrystals with engineered domain structures. Those where the [011] poled PZN-9%PT, with an orthorhombic *mm2* macrosymmetry, and the [001] poled PZN-8%PT, with a tetragonal *4mm* macrosymmetry. The first crystal has a large difference between transversal PE coefficients $|d_{31} - d_{32}|$ = 2181 pC/N, which therefore explains its large calculated maximum direct ME coefficient of 23.04 V/(cm·Oe) in the Z-cut crystal. As in the [011] poled PMN-PT, this coefficient changes only slightly for β = ±10º. In the [001] poled PZN-8%PT, the maximum effect was estimated as 8.30 V/(cm·Oe) for the (*ZXtl*) 45º/38º-cut (α = 45º, β = 38º and γ = 0º), and seven other directions. In the Z-cut crystal, this decays just to 7.66 V/(cm·Oe). Mainly, the maximum coefficient decreases by less than 10% of its largest value for cut deviations of approximately $\Delta\alpha$ = ±10º and $\Delta\beta$ = ±10º.

In summary, using an averaging model based on the constitutive equations, we have predicted the possibility of producing large ME responses in tri-layered composites employing suitably cut PE crystals. Especially strong ME effects are expected for single crystals of $LiNbO_3$, α-$GaPO_4$, α-quartz, [111] poled PMN-33%PT and [011] poled PZN-9%PT. Even so, in practice the use of the first three in ME composites still remains largely unexplored.

2.4. Conclusions

A theoretical model of the anisotropic quasi-static direct ME effect in tri-layered composites of Metglas and PE single crystals has been used in the quantitative estimation of the ME coupling as a function of the crystallographic orientation (i.e. PE cut plane). First, a description of the PE and linear MS (in the pseudo-piezomagnetic approximation) effects in terms of electric, magnetic and elastic material fields and constants has been given. An averaging quasi-static method was

subsequently used together with specific boundary conditions in order to derivate the relation between the material constants and the transversal (T-L) direct ME voltage (α_{E3a}) and charge coefficients (α_{Q3a}). The method consisted of the solution of the elastostatic and electrostatic equations taking into account the linear constitutive relations of the two phases. The properties of some common PE and MS materials (the latter with emphasis on the Metglas alloy exhibiting giant magnetostriction) have been discussed, and their influence on the ME coupling has been explored. It has been demonstrated that large ME voltage coefficients tend to be favored by large transversal piezoelectric coefficients, transversal and longitudinal piezomagnetic coefficients and coupling constants as well as small out-of-plane dielectric and compliance constants and the volume ratio between the PE and MS phases. On the other hand, it has also been shown that the ME charge coefficients do not depend on the dielectric constants of the PEs and thus tend to be much larger in lead-based crystals with very large piezoelectric constants such as PMN-PT and PZN-PT. The effects of the demagnetization fields on the attenuation of the ME coefficients were briefly explored. A description of the ME composites as equivalent Thévenin/Norton circuits composed of a magnetically driven voltage/current source in series/parallel with a characteristic impedance of the composite has also been exposed.

After that, we used the quasi-static model for the calculation of the maximum expected direct transversal ME voltage coefficients in a series of tri-layered composites of the type Metglas/Piezocrystal/Metglas, as a function of the PE crystal orientation. The PE single crystals studied in this chapter included lead-free lithium niobate, α-galium phosphate, α-quartz, langatate, langasite, aluminum nitride, lithium tantalate and barium titanate, as well as the lead-based PZT-2, PMN-33%PT ([111] poled), PMN-30%PT ([011] poled), PMN-33%PT ([001] poled), PZN-9%PT ([011] poled) and PZN-8%PT ([001] poled). The estimations revealed a strong dependence of the ME effects with the crystal orientation. They also supported the possibility of generating large quasi-static ME voltage coefficients in composites comprising lead-free PE single-crystals through the optimization of the crystal orientation. These ME effects were found to be particularly attractive for the case of lithium niobate, α-galium phosphate, quartz, [111]-poled PMN-33%PT and [011]-poled PZN-9%PT. The enhanced effects were found to be originated from a particularly good combination of relatively large PE coefficients and low dielectric constants. We thus have revealed that the choice of crystals with an appropriate cut is a vital step in the development of ME composites valuable for practical applications.

Chapter 3

3. Experimental techniques for the measurement of the ME effect

Abstract

This chapter describes an experimental technique, developed experimental setup and respective study of the dynamic direct magnetoelectric (ME) effect measured in Metglas/piezocrystal laminates. Various techniques used in the measurement of the ME effect are explored, with special emphasis on the dynamic lock-in technique employed in our experiments. In this technique the sample is subjected to two magnetic fields, a *DC* bias and an *AC* modulation field. The *AC* voltage generated across the sample is subsequently measured in a lock-in amplifier. This measurements can then be performed as a function of the magnetic bias field or the frequency of the modulation field. The formalism describing this technique is presented, and we show how the different order ME coefficients can be extracted from the measurements of the voltages synchronized with the fundamental and harmonic frequencies of the magnetic exciting signal. Subsequently we present a custom-made setup used by us to measure the dynamic ME effect. Its scheme and characteristics as well as ways to reduce the noise and the undesirable induced electromotive force are explored.

3.1. Introduction

In the experimental quantification of the direct ME effect a dynamic direct ME voltage coefficient $\alpha_{Eij} = \partial E_i/\partial H_j$ (where E_i is the component of the electric field in the i direction and H_j is the component of the magnetic field in the j direction) is generally used as a figure of merit under open-circuit conditions (i.e. with a displacement field D_i = 0). Also, a large enhancement in the magnitude of the ME effect is expected whenever the frequency of an applied modulation magnetic field with amplitude (δH) matches one of the natural electrical, magnetic or mechanical modes of resonance of the composite [11, 101-103]. For the case of the PE phase this is known as electromechanical (EM) resonance and it occurs whenever a characteristic elastic eigenmode of the

PE phase is indirectly excited by the time varying magnetic field [102]. Thus, a large oscillation amplitude of the standing wave in this phase gives rise to a large polarization/voltage through the PE effect. The frequency of these important EM resonances then depends on the effective material parameters and geometry of the PEs.

From the point of view of the constituent phases, large transversal direct voltage ME effects (α_{E3a}, where a and b are the direction indexes equal to 1 or 2) tend to be favored by MS phases with large longitudinal pseudo-piezomagnetic coefficients ($q_{ab} = \partial\lambda_b/\partial H_a$, where λ_b is the H dependent MS strain) and PE phases with a large ratio between transversal piezoelectric (d_{3a}) and longitudinal dielectric constants (ε_{33}), as well as an efficient stress transfer between layers [6, 8]. A very promising class of MS materials are the Metglas® (Ni-Fe-Mo-B, Fe-Si-B, Co-Fe-Si-Ni-B, etc.) amorphous alloys. As for the PE phase, ferroelectric ceramics of PZT ($Pb(Zr,Ti)O_3$) have been extensively studied and tend to provide a strong ME coupling due to their relatively large piezoelectric and electromechanical (EM) coupling coefficients [64-66]. Nonetheless, the use of highly anisotropic single-crystalline ferroelectrics, poled and cut along desirable crystallographic directions, constitutes an alternative way to achieve large but also anisotropic ME effects [108, 135]. The current research on ME composites has therefore been remarkably focused on lead-based compounds such as PMN-PT or PZN-PT [6, 9, 163, 164]. Nevertheless, some lead-free PE single-crystals have been recently explored and shown to potentially yield a comparably large direct ME effect in composites.

In the present chapter, we report the development of a dynamic lock-in setup and subsequent simple study of the anisotropic direct ME properties of bulk tri-layered structures of Metglas/$LiNbO_3$/Metglas, Metglas/$GaPO_4$/Metglas and Metglas/PMN-PT/Metglas using different cuts of the crystalline PEs and under quasi-static and EM resonance conditions.

3.2. Magnetoelectric measurement techniques

In general, the experimental measurement of the direct ME effect has proven to be a simpler and more accurate method for the quantification of the ME effect when compared to the measurement of the converse ME effect. The advantages of the first technique include the relative easiness of producing large magnetic fields used to excite the samples and the fact that magnetic fields can generate higher energy densities than electric fields [48]. Also, the possibility of destructive dielectric breakdown, which could be caused by excessively high voltages applied during the measurement of the reverse effect, is avoided. The direct voltage and charge ME effects, quantified by the respective

coefficients $\alpha_{Eij} = \partial E_i/\partial H_j$ and $\alpha_{Qij} = \partial D_i/\partial H_j$, with indexes i and j equal to 1, 2 or 3, can be experimentally measured via three fundamental methods [15, 48]:

(i) The static method, where the sample is subjected to a uniform magnetic bias field (H), and the voltage ($V = E_i \cdot t$, where t is the thickness of the PE phase) or charge ($Q = D_i \cdot A$, where A is the area of the electrodes placed on the PE) developed across its electrodes is measured with an electrometer in voltage (high-input-impedance) or charge (low-input-impedance) mode, respectively. In the charge mode, the input of the electrometer is a virtual ground, and therefore the measurement of charge instead of voltage should be less affected by the problem of leakage currents flowing through the sample due to an eventually small PE conductivity. By applying different magnetic fields, the induced ME voltage can therefore be quantified as a function of *H*;

(ii) The quasi-static method, where a voltage or charge generated across the sample's electrodes is measured using an electrometer as a function of time simultaneously with a slow variation of the applied *DC* magnetic field (with a rate of ca. 0.05 – 0.5 T/min). Here, the magnetic field is generally increased from zero up to a maximum value, stabilized at this value and subsequently decreased back to zero. A baseline can be subsequently used to correct for an eventual time drift of the voltage / charge due, e.g., to the pyroelectric effect;

(iii) The dynamic method, where a modulation magnetic field with frequency *f* and a small amplitude δH is superimposed on a comparatively large magnetic *DC* bias field H. Using a lock-in amplifier, the *AC* ME voltage generated across the sample or the current flowing through it is then measured as a function of *H* or *f*. This dynamic method presents a series of advantages in comparison to the static and quasi-static methods [57, 165]. The first one is a very efficient reduction of the electronic noise thanks to the phase-sensitive detection of the lock-in amplifier. Here, signals with a frequency distinct from the frequency of a reference signal are rejected and filtered by the unit. This method also allows one to eliminate the problem of charge accumulation, observed for certain ceramics, where the charge generated during polarization of the sample accumulates at its grain boundaries. These charges can move towards the electrodes during the measurements, thus disturbing the experimental results. The relatively high speed of measurement in this method thus allows a minimization of the accumulation of charge. Another advantage is that the ME response may be studied in different modes of operation, e.g., with different values of the magnetic bias field or at different time scales by changing the frequency of the modulation field. However, some negative

aspects and special cautions should also be noted. These include [9, 18, 57, 59]: the leakage of charge under periodic conditions, which may occur through the Ohmic resistance of the samples at low frequencies of the *AC* field, or through the capacitance formed between the two surfaces at higher frequencies. Some undesirable mutual inductance will also exist between the source of the magnetic field and the system composed of the sample and cables connected to its electrodes. A frequency-proportional voltage will therefore always be induced across the electrodes by the applied time-changing magnetic field due to the effect of electromagnetic Faraday induction. Furthermore, we may also have the induction of eddy currents in the system, thus decreasing the effective modulated magnetic field felt by the sample. For high enough frequencies, these effects might even be more significant than the voltage generated by the ME effect in the samples. Some external sources of synchronized noise can also be especially harmful to this technique, including, e.g., the thermal noise, introduced by pyroelectric currents, and, more importantly, external vibrational or acoustic noises (microphony) which can be coupled to the sample via the piezoelectric effect.

In addition to the aforementioned techniques that can be used to measure the direct ME effect, several others have also been tested [15]. Some of those include: *(i)* active modes of analysis, where a test current is passed through the sample, and subsequently dielectric and polarization measurements are performed in various applied magnetic fields [9]; *(ii)* techniques using a pulsed magnetic field, which are ideal for the study of EM resonance phenomena [106], and *(iii)* ME measurements based on the PE effect making use of a microwave microscope or a magnetic cantilever [11].

3.2.1 Dynamic magnetoelectric technique

From this point onwards we will mainly focus on the dynamic lock-in technique since this is the method in which we are most experienced. Thus we begin by presenting a formalism describing this technique and consequently show how the different order ME coefficients can be extracted from the measurements of the voltages synchronized with the fundamental and harmonic frequencies of the magnetic exciting signal. Assuming that the non-linear ME voltage ($V = E \cdot t$) induced across a ME composite as a function of an applied magnetic field (H) can be expanded in a Taylor series centered at a bias field H_0, it follows that [57]:

$$V(H) = \sum_{n=0}^{\infty} \alpha_n (H - H_0)^n \text{, with } \alpha_n = \frac{1}{n!}\frac{\partial^n V}{\partial H^n}(H_0) \ . \tag{3.1}$$

When a bias and a modulated *AC* magnetic field with frequency $f = \omega/2\pi$, given by $H = H_0 + \delta H cos(\omega t)$, where t stands for time, are applied to this composite, the output voltage thus becomes:

$$V = \sum_{n=0}^{\infty} \alpha_n \cdot \delta H^n \cos(\omega t)^n \ . \tag{3.2}$$

Next, taking into account that:

$$\cos(\omega t)^n = \begin{cases} \frac{1}{2^{n-1}} \sum_{j=0}^{\frac{n-1}{2}} \binom{n}{j} \cos\big((n-2j)\omega t\big), & \text{if } n \subset \mathbb{N} \text{ is odd} \\ \frac{1}{2^n}\binom{n}{\frac{n}{2}} + \frac{1}{2^{n-1}} \sum_{j=0}^{\frac{n}{2}-1} \binom{n}{j} \cos\big((n-2j)\omega t\big), & \text{if } n \subset \mathbb{N} \text{ is even} \end{cases} , \tag{3.3}$$

where $\binom{n}{j}$ are the binomial coefficients and substituting this expression in equation (3.2), one gets:

$$V = \sum_{l=0}^{\infty} \frac{1}{2^{2l}} \binom{2l}{l} \cdot \alpha_{2l} \cdot \delta H^{2l} + \sum_{n=1}^{\infty} \frac{1}{2^{n-1}} \cdot \alpha_n \cdot \delta H^n \sum_{j=0}^{\left\lfloor \frac{n-1}{2} \right\rfloor} \binom{n}{j} \cos\big((n-2j)\omega t\big) \ , \tag{3.4}$$

where $\lfloor ... \rfloor$ indicates the nearest lower integer. Introducing the new variable $k = n - 2j$ and changing the order of summation allows us to collect the cosine terms in the last part of the equation:

$$V = \sum_{l=0}^{\infty} \frac{1}{2^{2l}} \binom{2l}{l} \cdot \alpha_{2l} \cdot \delta H^{2l} + \sum_{k=1}^{\infty} \left[\sum_{j=0}^{\infty} \frac{1}{2^{k+2j-1}} \binom{k+2j}{j} \cdot \alpha_{k+2j} \cdot \delta H^{k+2j} \right] \cos(k\omega t) \ , \tag{3.5}$$

which shows that this voltage will be a combination of sinusoidal functions of time with frequencies equal to the frequency of the applied modulation field and its harmonics. The amplitudes associated with each of these harmonic signals will therefore be given by the parameter in brackets:

$$\delta^k V = \sum_{j=0}^{\infty} \frac{1}{2^{k+2j-1}} \binom{k+2j}{j} \cdot \alpha_{k+2j} \cdot \delta H^{k+2j} \ . \tag{3.6}$$

For example, the amplitudes of the fundamental signal and its first two harmonics are then:

$$\begin{aligned} \delta^1 V &= \alpha_1 \delta H + \frac{3}{4}\alpha_3 \delta H^3 + \frac{10}{16}\alpha_5 \delta H^5 + \cdots ; \\ \delta^2 V &= \frac{1}{2}\alpha_2 \delta H^2 + \frac{1}{2}\alpha_4 \delta H^4 + \frac{15}{32}\alpha_6 \delta H^6 + \cdots ; \\ \delta^3 V &= \frac{1}{4}\alpha_3 \delta H^3 + \frac{5}{16}\alpha_5 \delta H^5 + \frac{21}{64}\alpha_7 \delta H^7 + \cdots . \end{aligned} \tag{3.7}$$

Assuming that the partial derivatives in expansion (3.1) decrease fast enough and δH is sufficiently small, so that $\sum_{j=1}^{\infty} \frac{1}{2^{2j}} \binom{k+2j}{j} \cdot \frac{\alpha_{k+2j}}{\alpha_k} \cdot \delta H^{2j} \ll 1$ for all $k \in \mathbb{N}$, then all higher-order terms in the expansion (3.6) may be neglected, and one can arrive at the commonly made approximation:

$$^k\alpha_E = \frac{1}{t} \cdot \frac{\partial^k V}{\partial H^k} \simeq 2^{k-1} k! \frac{\delta^k V}{t \cdot \delta H^k} \ , \tag{3.8}$$

where $^k\alpha_E$ is the k-th order H_0 dependent voltage ME coefficient and t is the effective thickness of the PE phase. This expression shows that the amplitude of the k-th harmonic of the voltage ($\delta^k V$) as measured in the lock-in should be approximately proportional to the k-th power of the amplitude of the applied modulation field (δH^k) and to the k-th derivative of the V vs. H curve at some bias H_0 field. Therefore we see that in the first order this ratio will be related to the direct voltage ME coefficient through: $\alpha_E = \delta^1 V/(t \cdot \delta H)$.

More generally, to take into account the dispersion in the response of the ME coefficients α_n in expansion (3.1) we assume that the output voltage in (3.4) can be described by the convolution relation:

$$V(t) = V_0 + \sum_{k=1}^{\infty} \int_{-\infty}^{t} \delta^k V(t - t') \cdot \cos(k 2\pi f t')\, dt' \ , \tag{3.9}$$

where t and t' represent the time. Making use of the convolution theorem, the Fourier transform of the above expression will then be:

$$V'(f') = V_0\delta(f') + \sum_{k=1}^{\infty} \delta^k V'(f') \cdot \frac{1}{2}[\delta(f' - kf) + \delta(f' + kf)] \ , \tag{3.10}$$

where $V'(f')$ and $\delta^k V'(f')$ represent the Fourier transforms of $V(t)$ and $\delta^k V(t)$, respectively, f' the frequency of the output voltage signal, f the frequency of the modulated H field and $\delta(x)$ the Dirac delta function. Therefore, all complex coefficients $\delta^k V'(f')$ in the expansion are now described as functions of the frequency f'. As before, this expression shows that the amplitude of the output voltage signal measured in a lock-in amplifier should only be nonzero at integer multiple frequencies of f. As an example, supposing that all the factors $\delta^k V'(f')$ in this expression, which depend on the complex ME coefficients ${}^n\alpha'_E(f') = \alpha'_n(f') \cdot n!/t$ corresponding to the Fourier transforms of the ME coefficients ${}^n\alpha_E$ in expression (3.6), given by:

$$\delta^k V'(f', H_0) = \sum_{j=0}^{\infty} \frac{1}{2^{k+2j-1} j!(k+j)!} \cdot t \cdot {}^{k+2j}\alpha'_E(f', H_0) \cdot \delta H^{k+2j} \ , \tag{3.11}$$

are associated with a ME resonance peak at an arbitrary frequency $f' = f_R$. Then, in the ME measurements (with some constant applied bias H_0) this peak will be observed at $f = f_R$ in the fundamental frequency mode having an amplitude given by $|\delta^1 V'(f_R)| = \sqrt{\delta^1 V'(f_R)^* \cdot \delta^1 V'(f_R)}$. Furthermore, for the 1st and 2nd harmonic frequency detection with $f' = 2f$ and $f' = 3f$, this peak should appear at lower frequencies, $f = f_R/2$ and $f = f_R/3$, with amplitudes $|\delta^2 V'(f_R)|$ and $|\delta^3 V'(f_R)|$, respectively. This last general expression thus allows us to relate the output voltage measured in any detection circuit with the magnetic bias and modulated fields, frequency and characteristic ME voltage coefficient of a particular composite.

3.3. Experimental dynamic magnetoelectric measurement setup

As implied in the previous section, the basic blocks needed to perform dynamic measurements of the direct ME effect are a magnetic field source (usually one or two electromagnets), capable of producing constant and *AC* magnetic fields which are applied to the

sample, and a lock-in amplifier, whose purpose is to measure the *AC* voltage generated on the sample through the ME effect. Since commercial systems are still unavailable at this point, as an example Figure 3.1 shows schematically an experimental setup built by our group in order to measure the dynamic direct and converse ME effects [128]. Here, the samples are placed in the center of a plastic box containing a Helmholtz coil capable of generating *AC* magnetic fields with amplitudes δH of up to 100 Oe as well as constant bias fields H of up to the same value. A *DC* bias field, in the range of 0 – 15 kOe, can also be produced by an external electromagnet (Bruker® ESP 300E) collinear with the Helmholtz coil and directed along the *X* direction. This bias field is stabilized by a Hall-sensor-based regulating feedback loop. The Helmholtz coil can be driven by a power amplifier (AE Techron®, model 7224) with a gain between 1 and 20 and low output impedance (28 mOhm in Series with 1 μH). The current flowing through the coil is stabilized by a current control loop or by taking into account the complex impedance of the whole circuit. The amplitude and frequency of the *AC* current are set either by an external function generator (SRS®, model DS345) or by the internal generator of the lock-in amplifier (Zurich Instruments®, model HF2LI). The *AC* current passing through the Helmholtz coil can be continuously measured directly by a multimeter (Agilent®, model 34401A) or has voltage drop across the 50 Ω input of the lock-in. The second method has the advantage of allowing the determination of not only the amplitude but also the phase of this current. The measured current is then used to calculate the previously calibrated magnetic *AC* field amplitude δH. This current can be measured with the multimeter directly, using its ammeter mode, up to a frequency of only ca. 10 kHz due to accuracy limitations of the device, and indirectly, using its voltmeter mode, for frequencies larger than 10 kHz by making use of the known complex impedance of the Helmholtz coil or a known reference resistor. Using an *AC* field of δH = 0.1 Oe the power-amplifier was found to operate stably up to a frequency of about 600 kHz. A gaussmeter (DSP®, model 475) is used to measure the exact value of the bias field produced by the external electromagnet. The amplitude and phase of the transverse voltage δV induced across the sample by the applied in-plane *AC* magnetic field δH is measured with the lock-in. Higher harmonics of the ME signal can also be measured simultaneously in this way by using multiple independent demodulators. The measuring system as a whole can be synchronized by a TTL output signal from the function generator or alternatively by the internal oscillator of the lock-in, depending on the source of the *AC* signal. The entire setup is autonomously driven by a home-made data acquisition software based on LABview®. The direct ME measurements are consequently presented as the direct ME coefficient given by equation $\alpha_E = \partial E/\partial H = \delta V/(t \cdot \delta H)$ as a function of the magnetic bias field *H*, with an applied constant-frequency modulation field, or as a function of the frequency *f* of the *AC* field, with an applied constant bias field. We also point out that, since most lock-in amplifiers have an input impedance of just about between 1 and 10 MΩ, the use of a high input impedance

voltage pre-amplifier is usually required in this system, at least at low frequencies (ca. <10 kHz), in order to achieve the open-circuit condition specified by the definition of the ME voltage coefficient (α_E). Otherwise, the circuit parameters of the sample and measuring device should be taken into account in the calculation of α_E.

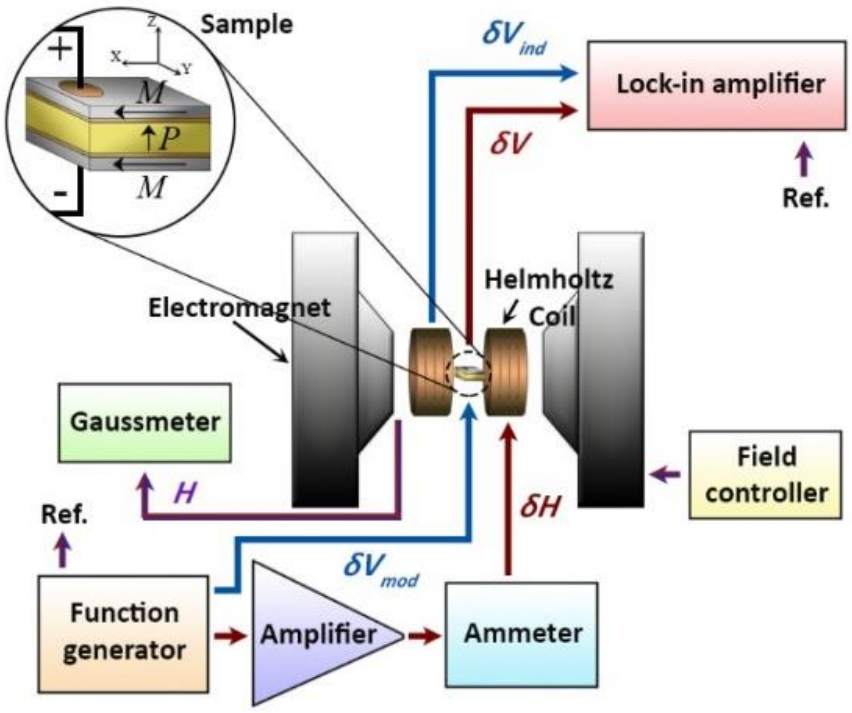

Figure 3.1 Schematic representation of the experimental setup used to perform the ME measurements. Red and blue arrows are associated with the measurements of the direct and converse ME effects, respectively. Here, the lock-in amplifier can by itself take up the role of the detection circuit, function generator and ammeter. Furthermore, the gaussmeter and amplifier may be dropped in some cases.

Although not optimized for this purpose, we note that this system may also be used to measure the converse ME effect. This measurements are performed by applying an *AC* voltage (δV_{mod}), produced by a function generator, to the sample and using the Helmholtz coil (although too far away) to pick up the small induced voltage due to the magnetic flux produced by the sample. The amplitude and phase of the voltage induced on the coil (δV_{ind}) as a function of either the driving frequency, at a constant *DC* magnetic bias field, or of the swept magnetic field, at a constant excitation frequency, are then detected by the lock-in. The resulting ME effect can then be represented as a ratio between the *AC* voltage detected on the Helmoltz coil and the voltage applied

to the sample ($\delta V_{ind}/\delta V_{mod}$) or as the traditionally used converse ME coefficient $\alpha_B = \partial B/\partial E$, in units of G·cm/kV, after properly calibrating the pickup coil. The accessible frequency range for this type of measurements goes from several Hz up to several tens of MHz.

Figure 3.2 displays a picture of the complete developed setup with its components labeled. A plastic box is used to house the sample and contains the Helmholtz coil which produces the *AC* magnetic field. It consists of a $60 \times 55 \times 68$ mm^3 container built with non-conductive and non-ferromagnetic materials (mostly PVC and Teflon) in order to avoid losses at large frequencies due to eddy currents and a concentration of the field lines away from the center of the coil. The two modulation coils are fixed on opposed interior side walls. This box can then be connected to a goniometer and used in sync with a helium flow or a nitrogen flow cryostat, thus allowing measurements from cryogenic temperatures up to about 600 K. The Helmholtz coil scheme was adopted for the modulation because of its simplicity and high uniformity of the generated field in the center of the coils with variations of less than 1% of its central value inside a central cube with a side length of about ½ the radius of the coil. Both coils were electrically connected in parallel between themselves and into the output of the power amplifier. This type of connection minimizes the equivalent inductance of the coil circuit and thus allows one to produce higher currents with the same voltage for higher frequencies of operation. In order to magnetically calibrate the Helmholtz coil, we calculated and experimentally measured the magnetic field generated in the center of the coil using a gaussmeter, as a linear function of the *DC* driven current, as measured by the ammeter, having obtained a relation of $H \approx 32 \cdot I$. In order to generate a constant *AC* field over a wide range of frequencies, the complex impedance of the circuit of the Helmholtz coil should be known. This impedance was measured with the help of the lock-in amplifier having obtained a resistance of ca. R = 0.9 Ω and an inductance of L = 0.47 mH. With this information we are thus able to calculate the amplitude of the voltage signal (δv) that has to be applied to the coil at any given frequency (f) in order to generate a desired current amplitude ($\delta i \propto \delta H$) through the simple relation: $\delta v/\delta i = \sqrt{R^2 + (2\pi f L)^2}$. All of the aforementioned steps were integrated into the measurement program written in LabVIEW. We note that, beside the *AC* field, the Helmholtz coil may also simultaneously be used to produce a bias field of up to 100 Oe, thus allowing direct ME measurements to be performed independently without any external electromagnet.

Figure 3.2 Photo of the setup used in the ME measurements. The labeled components are: *1)* electromagnet (from the Bruker® ESP 300E spectrometer); *2)* box containing the Helmholtz coil; *3)* sample support and goniometer; *4)* PC; *5)* lock-in amplifier (Zurich Instruments®, model HF2LI); *6)* function generator (SRS®, model DS345); *7)* multimeter (Agilent®, model 34401A); *8)* power amplifier (AE Techron®, model 7224) and *9)* gaussmeter (DSP®, model 475).

An important component in this kind of systems is the electrical contact and support for the samples. This support must be able to fix the samples in place while taking into account that a large enough stress applied by the support may negatively affect the sensitive ME effects under resonant conditions. The support must also ensure a good electrical contact to the sample's top and bottom electrode surfaces. The ME voltage signal produced between the electrodes must then be carried by a cable to the input of the lock-in. A very short low-noise coaxial cable or twisted pair cable are ideal

in this case. These cables can also be enclosed by a conductive shield thus functioning as triaxial cables where the external conductor provides an electromagnetic shielding of the inner conductors mainly from the *AC* magnetic field. The voltage difference between the inner conductors of the signal cable can subsequently by measured by the lock-in amplifier operating in differential mode.

There are several issues that should be taken into account in the measurements of the dynamic direct ME effect. One of the most important is the generation of an electromotive force in the cables connected to the sample induced by the time changing *AC* magnetic flux due to the effect of Faraday induction [9]. This magnetically generated signal, having the same frequency as the modulation field, will thus be detected by the lock-in and can easily pass as a ME signal. From the Faraday law of induction we known that the amplitude of the induced signal is proportional to the amplitude of the modulation field (δB), the area of the "loop" formed by the electrodes and the frequency of the field. It should also be shifted by 90º with respect to the modulated field. Since the phase of an eventual ME signal obtained in the lock-in is generally measured relatively to the phase of the voltage applied to the power amplifier that drives the coil, this fact can be used to our advantage in order to obtain the phase of this ME signal relatively to the modulated field. The expression of the induced electromotive force shows that this effect in principle can be minimized by using relatively small frequencies of operation and reducing the area normal to the magnetic field of the electric wires. The effective area between wires can be minimized by using coaxial cables or especially twisted pairs of thin wires with a large number of loops per unit of length and by carefully orienting these wires in relation to the applied time-varying magnetic field. Even so, test measurements using a non-ME reference sample with dimensions of approximately 10×10×0.5 mm^3 in our support in the frequency range of up to 600 kHz have shown linear output voltages with slopes of up to ca. 873 mV/(Oe·MHz) (see Figure 3.3 *a)*). This value of the induced voltage was obtained for the case of the single-mode detection of the lock-in. On the other hand, in the differential detection mode of the lock-in with the signal being measured between the inner conductors in a triaxial cable, the induced voltage was found to be 467 mV/(Oe·MHz). Finally, the use of the lock-in in the differential detection mode together with a grounded outer thick conductive shield was shown to reduce the Faraday induced voltage in the support by up to ten times down to ca. 81 mV/(Oe·MHz). This is the case because of the ability of the conductive outer tube to effectively shield the interior signal-carrying conductors from the external modulated field. Nonetheless, in most laminate and particulate bulk ME composites this effect is not an issue at low frequencies (up to ca. 1 kHz) because they usually yield ME responses of the order of some tens or hundreds of mV/(cm·Oe) [6-8, 12, 17]. However, for the case of single-phase multiferroics and thin-film composites this induction can become noteworthy because of the weak nature of the ME coupling. Indeed, in the first case maximum direct ME coefficients of the order of only some mV/(cm·Oe) [16, 17] tend to be observed,

while in the second even smaller signals of the order of tens or hundreds of μV/Oe [9, 16] can be detected due to the small thickness of the thin films (even though the direct coefficients can still be comparable to the ones observed in bulk composites). Also, the eventual generation of eddy currents in the wires may also take an important part in this last case [166]. For samples associated with a weak ME effect a simple method can be used to correct the data from the induction effects. Here, a preceding reference measurement is carried out with a non-ME reference sample with about the same dimensions as the ME sample (e.g. a tri-layered composite of Metglas and Teflon) and using the same parameters as in the subsequent ME measurement. The complex in-phase (X) and out-of-phase (Y) components of the induced signal can posteriorly be subtracted from the second ME measurement. An example of this procedure is illustrated in Figure 3.3 *b)*.However, for the case of samples with a large conductivity or magnetic permeability, the mutual inductance between the Helmholtz coil and sample support may depend significantly on this parameters because of the concentration of magnetic field lines close to the wires. Thus a better method might employ two measurements using the same sample, a first one with the sample oriented in some direction and a second with the sample rotated by 180º around the central axis of the Helmholtz coil. In this last case the voltage produced by the ME effect is expected to be shifted by 180º while the voltage due to the induced effect should stay the same. Subsequently, the results of these two measurements can be subtracted.

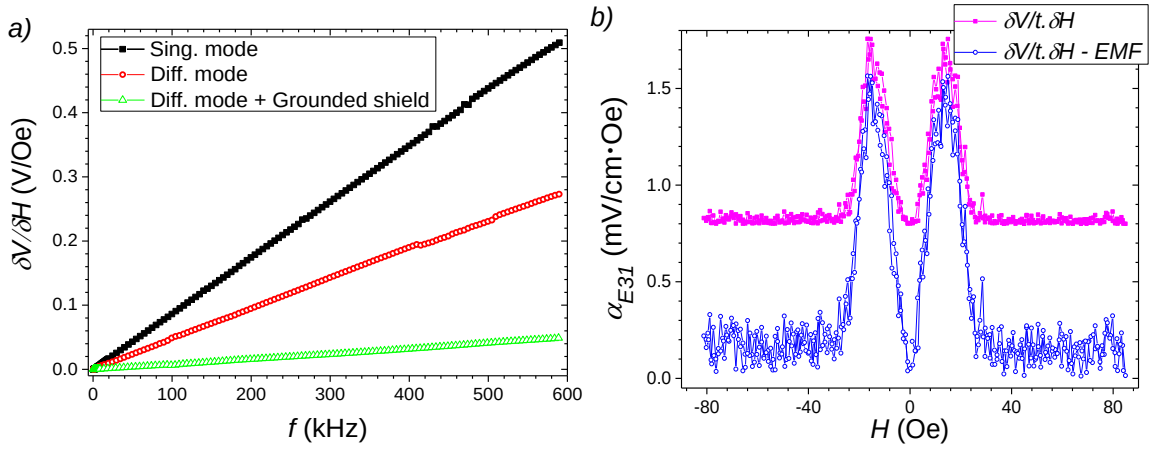

Figure 3.3 *a)* Test dynamic ME measurements performed in a reference non-ME sample while operating the lock-in in its single or differential mode with a grounded or not grounded exterior conductive shield. The observed voltages increase linearly with the frequency of the modulated field (δH = 0.1 Oe) and are induced between the electrodes by the Faraday effect. *b)* Small transversal direct ME effect (α_{E31}) measured in a bi-layered composite of Metglas/Z-cut $LiNbO_3$ (1 mm thick) with f = 10 kHz and δH = 1 Oe. The originally measured signal $\delta V/t.\delta H$ represents the amplitude

of the voltage due to the ME effect superimposed on that generated by the Faraday induction (*EMF*), of about 0.81 mV/(cm·Oe), which is independent of the bias field. The second curve shows the corrected ME effect obtained by subtracting this second known component.

In addition to the electromagnetic induction and intrinsic noise sources such as Johnson, shot and 1/*f* noise, various other extrinsic sources of synchronous noise may negatively influence the results of the experiment. They can be originated, e.g., by capacitive, inductive or resistive coupling between components of the system. The use of balanced lines between instruments can offer some considerable common mode rejection of such noise sources. The capacitive coupling can be reduced by the use of short cables connected to the samples and by placing such cables far away from eventual sources of stray electric fields (e.g., power amplifiers). Coaxial or twisted cables can be used to minimize the inductive coupling. A grounded electromagnetic shield (i.e. Faraday cage) with high conductivity and permeability may also be used to enclose the system containing the sample, Helmholtz coil and lock-in in order to shield it from stray external *DC* and time changing electric and magnetic fields. Ground loops can also give rise to a synchronous voltage and are avoided by grounding all of the instruments to the same physical point. Microphonic noise can be minimized by properly fixing the cables and sample support. In our case we also noted the existence of a 50 Hz harmonic noise from the power line, and so measurements at multiple frequencies of 50 Hz were avoided at least up to about 800 Hz, after which this effect is no longer noticeable. The value of the spectral noise density at 1 kHz was estimated as 31 $\mu V_{rms}/Oe\cdot\sqrt{Hz}$, and therefore, in order to obtain a single-to-noise ratio of 100 at 1 kHz with a bandwidth of 1 Hz, a signal of only about 0.44 mV/Oe should be required.

In order to demonstrate the capabilities of this system and the applicability of equations (3.6) and (3.8), we present an example of a direct ME measurement performed on a tri-layered composite. In this case, two sheets of the magnetostrictive alloy Metglas were bonded with epoxy to both surfaces of square shaped piezoelectric single crystals of $LiNbO_3$. Y- and 41ºY-cut crystals were employed here. Using the setup described above, we first measured the direct ME response of the Y-cut sample as a function of the in-plane magnetic bias field using a modulation field with an amplitude of 1 Oe and a frequency of 1 kHz. The fundamental-frequency voltage signal ($\alpha_{ME1}= \delta V/t \cdot \delta H$), as well as its 1st ($\alpha_{ME2} = \delta^2 V/t \cdot \delta H^2$) and 2nd ($\alpha_{ME3} = \delta^3 V/t \cdot \delta H^3$) harmonics, for k = 2 and k = 3, respectively, as in equation (3.8), were measured simultaneously relative to the applied modulated field. These correspond to the component of the generated voltage in phase with the applied modulated field (i.e. the real part of $\delta^k V'(f', H_0)$ as in equation (3.11)). Figure 3.4 shows the results obtained in this way. The uppermost graph depicts the real part (i.e. in-phase with the

modulated field) of the direct ME coefficient (α_{E31}) in units of mV/(cm·Oe) as a function of the bias field. Here we can see that a coefficient as large as 946 mV/(cm·Oe) was generated for a field of just about 24 Oe. In general, the shape of the ME curves tend to follow the first derivative of a typical magnetostrictive curve for the Metglas alloy (i.e. $\alpha_{ME1} \simeq \alpha_E = (1/t) \cdot \partial V/\partial H \propto q = \partial\lambda/\partial H$) since the corresponding piezoelectric curve of the PE crystal is highly linear in this range of coupled strains. The second graph, on the other hand, depicts the measured 1st harmonic (at 2 kHz) of the ME output signal in units of mV/(cm·Oe^2). In particular, this signal is shown to be relatively large even for a null bias field. The superimposed red line in this graph represents 1/4 times the numerical field derivative of the fundamental response in the above graph. This derivative perfectly fits the measured data as predicted by equation (3.8), where we have: $\alpha_{ME2} = \delta^2 V/t \cdot \delta H^2 \simeq (1/(4 \cdot t)) \cdot \partial^2 V/\partial H^2 \simeq (1/4) \cdot \partial(\delta V/t \cdot \delta H)/\partial H = (1/4) \cdot \partial\alpha_{ME1}/\partial H$. The third graph shows the measured 2nd harmonic (at 3 kHz) of the ME response in units of mV/(cm·Oe^3) as a function of the bias field. Superimposed on this response is a line which represents 1/6 times the numerical derivative of the 1st harmonic response. Yet again we see that this derivative fits well the measured signal as predicted by equation (3.8): $\alpha_{ME3} = \delta^3 V/t \cdot \delta H^3 \simeq (1/(24 \cdot t)) \cdot \partial^3 V/\partial H^3 \simeq (1/6) \cdot \partial(\delta^2 V/t.\delta H^2)/\partial H = (1/6) \cdot \partial\alpha_{ME2}/\partial H$. In conclusion, in this measurement we have proven experimentally the validity of equation (3.8). In practice these ME curves are generally closely related to the non-linear magnetostrictive curves of the MS phase as shown by: $\alpha_{MEk} \simeq (1/2^{k-1}k!) \cdot {}^k\alpha_E \propto {}^k q = \partial^k\lambda/\partial H^k$, where ${}^k q$ are the k-th order piezomagnetic coefficients.

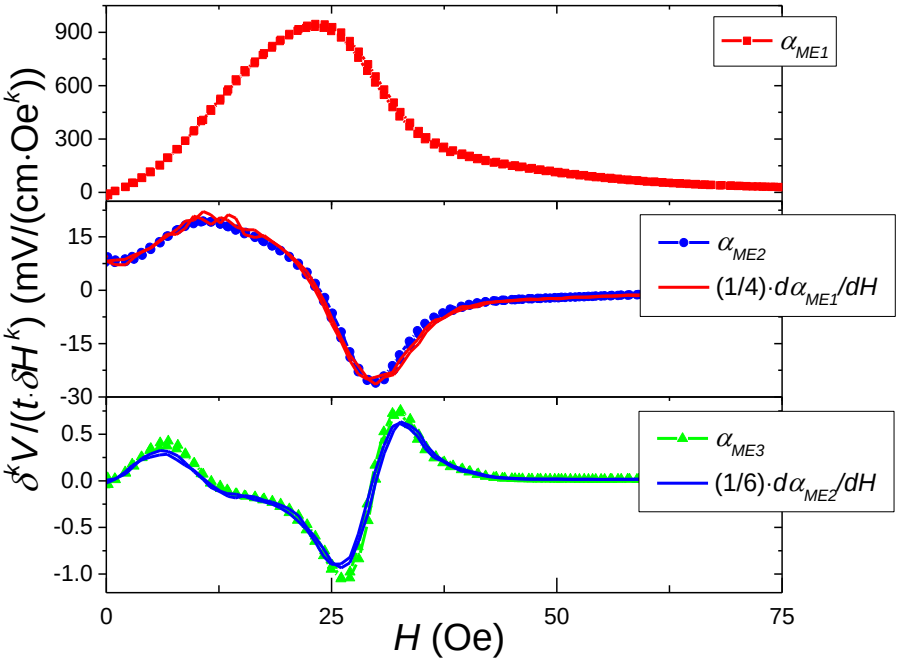

Figure 3.4 Direct ME effect measurements of a Metglas/Y-cut $LiNbO_3$/Metglas sample as a function of the bias field at 1 kHz and with δH = 1 Oe. The uppermost graph shows the ME response detected at its fundamental frequency (α_{ME1}) equal to the frequency of the applied modulated field. The second and third graphs show the 1st (α_{ME2}) and 2nd (α_{ME3}) harmonic response functions, respectively. Superimposed on them are lines representing the numerical derivatives of the previous lower-order harmonic responses.

The aforementioned setup also allows the measurement of the ME response as a function of the frequency of the modulated field (f) for a fixed bias field. Figure 3.5 shows an example of this measurement for the case of a Metglas/41ºY-cut $LiNbO_3$/Metglas composite. This measurement was made in the T-L mode (in-plane magnetic field and out-of-plane voltage detection), using a bias field of 25 Oe and a modulated field with an amplitude of 0.1 Oe. The fundamental response (α_{ME1}) as well as its 1st (α_{ME2}) and 2nd (α_{ME3}) harmonics were recorded. In the fundamental mode we note the existence of a single in-plane contour EM resonance mode at a frequency of ca. f_R = 323.1 kHz. At this frequency, a coefficient as large as 250 V/(cm·Oe) has therefore been measured. As predicted by equation (3.10), we also see that this same resonance mode is also excited by modulated fields with frequencies of 161.5 kHz ($\simeq f_R/2$) and 107.7 kHz ($\simeq f_R/3$) in the 1st and 2nd harmonic measurements, respectively, through the non-linear MS effect (i.e. $\alpha_{MEk} \propto {}^kq = \partial^k\lambda/\partial H^k$). The amplitudes of these peaks are of approximately 37.1 V/(cm·Oe^2) and 4.7 V/(cm·Oe^3), respectively. Furthermore, we can also observe the existence of another resonance peak at 323.1 kHz in the 2nd

harmonic detection. This resonance peak should correspond obviously to the first harmonic mode of the fundamental contour mode observed at 323.1 kHz, since it is observed at an odd integer multiple of this frequency, and therefore should be strongly excited by a modulated field frequency of 969.3 kHz. This frequency is larger than the maximum modulated field frequency of 600 kHz which can be attained with the equipment due to technical limitations. Thus, we note that higher-harmonic detection can be useful, e.g., in the study of resonance modes of vibration at frequencies larger than the ones which can be achieved in a given Helmholtz coil. The resonance peak observed at 442.3 kHz and 294.7 kHz in the 1st and 2nd harmonic detection, respectively, corresponds to another contour mode of resonance which in the fundamental frequency detection should be observed at ca. 884.4 kHz. In summary, three distinct contour modes of EM resonance of the composite were identified using the aforementioned technique as seen in the 2nd harmonic detection. We finally note that these non-linear resonant ME effects may be found to be very useful in future e.g. for the development of highly sensitive and low-power wideband *AC* magnetic field sensors [92, 148].

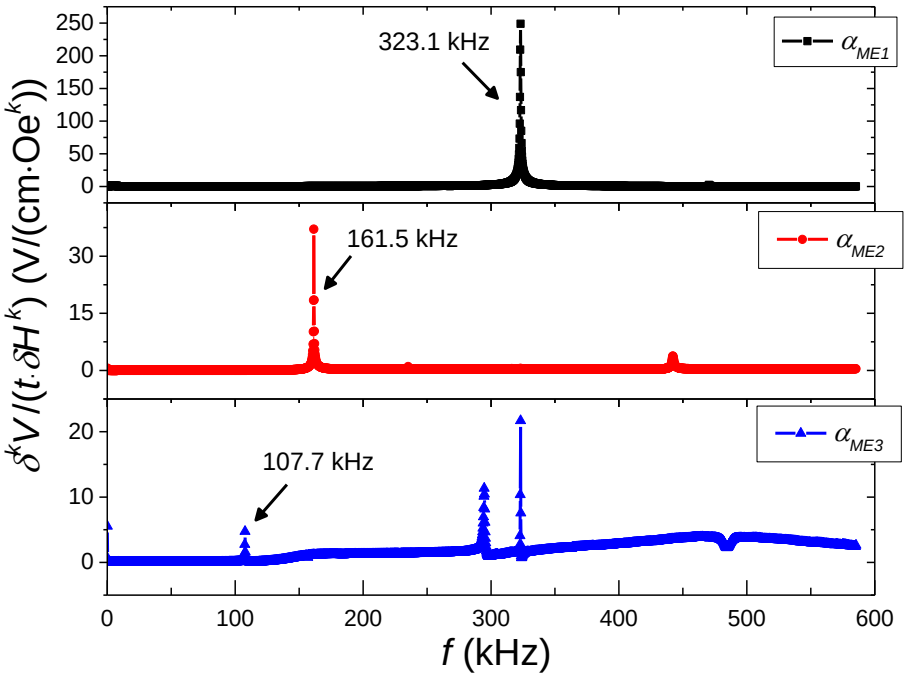

Figure 3.5 Direct ME effect measurements of a Metglas/41°Y-cut $LiNbO_3$/Metglas sample as a function of the modulated field frequency with δH = 0.1 Oe and H = 25 Oe. Here, the fundamental frequency detection (α_{ME1}) is plotted in the top graph, whereas the 1st (α_{ME2}) and 2nd (α_{ME3}) harmonic detections are plotted next. The single peak observed in the fundamental mode corresponds to an electromechanical resonance of the composite.

Chapter 4

4. Comparative study of the direct and converse magnetoelectric effects in tri-layered composites of Metglas with $LiNbO_3$ and PMN-PT single crystals

Abstract

In this chapter we present a comparative study of the direct magnetoelectric (ME) effect in simply bonded Metglas-piezocrystal tri-laminates. Electromechanical and magnetoelectric properties of Metglas/$LiNbO_3$/Metglas trilayers were studied in the frequency range from 1 kHz to 0.4 MHz. A trilayer of Metglas/PMN-PT/Metglas prepared in the same way was used as a reference for comparison. Though PMN-PT has much larger charge piezocoefficients than $LiNbO_3$ (LNO), the direct magnetoelectric voltage coefficient is found to be comparable in both trilayers due to the much lower dielectric permittivity of LNO. A magnitude of the direct magnetoelectric effect in the LNO trilayers is about 0.4 V/(cm·Oe) in the quasi-static regime and of about 90 V/(cm·Oe) at the electromechanical resonance. Calculations show that the magnetoelectric properties can be significantly improved (up to 500 V/cm·Oe) via controlling the cut angle of LNO, relative thickness ratio of the ferroelectric/ferromagnetic layers and bonding between Metglas and LNO. Advantages of using $LiNbO_3$ ferroelectric in magnetoelectric composites are discussed.

4.1. Introduction

As we noted in the introduction, since the estimated magnitude of the direct ME effect is approximately proportional to the product of the magnetostrictive and piezoelectric properties of the MS and PE phases, carefully engineered composites can in principle exhibit a remarkable ME coupling, orders of magnitude larger than the ones observed in single-phase multiferroics [6, 8]. The same behavior is expected in the case of the converse ME effect. While the former can find applications in the electric detection of magnetic fields [167-169], the latter could be useful in the electrical control of magnetism [25, 170].

For laminated composites operating in the L-T mode, necessary requirements for a large voltage ME effect (α_{E3a}) include a PE phase with large transversal PE coefficients (d_{3a}), small thickness dielectric permittivity (ε_{33}^{T}) and small longitudinal and transversal compliance (s_{ab}^{E}). Although $Pb(Zr,Ti)O_3$ (PZT) ceramics do not satisfy these requirements from a general point of view, the fabrication of PZT-based ME composites is still commonplace [100, 171]. The use of single-crystalline PEs, poled and cut along desirable crystallographic directions, is another possible approach to achieve large ME effects [108, 128, 135]. Among the commercially available single crystals, lead magnesium niobate - lead titanate (PMN-PT) [172] and lead zinc niobate - lead niobate (PZN-PT) exhibit the largest known piezocoefficients and are thus frequently employed in laminate ME structures [80, 81, 130, 163, 164, 169]. Nonetheless, both of them are characterized by some notorious drawbacks which include their low Curie and depolarization temperatures (ca. 100ºC), large chemical and electrical instabilities, non-linear hysteretic behavior, uneasy growth of high-quality crystals and consequently a very high price.

Due to these factors, other single crystalline piezoelectrics are being tested at present [13, 108, 128, 135-137]. Those have included so far lead-free crystals such as barium titanate ($BaTiO_3$) [132], lithium niobate ($LiNbO_3$) [128, 133], gallium phosphate ($GaPO_4$) [134], quartz (SiO_2) [135], aluminum nitride (AlN) [108], zinc oxide (ZnO) [136], langatate ($La_3Ga_{5.5}Ta_{0.5}O_{14}$, LGT) [137, 138] and langasite ($La_3Ga_{5.5}SiO_{14}$, LGS) [138]. $LiNbO_3$ (LNO), a uniaxial PE with a very high Curie temperature (~1210ºC), in particular could be proven to be a very promising choice. Although the PE coefficients of LNO are up to three orders of magnitude smaller than those of PMN-PT and PZN-PT, its dielectric coefficients also are, and therefore a comparable ME voltage coefficient can be anticipated in composites featuring this compound. Even in the weakly PE quartz [135], the induced ME coefficient has been found to be very large (ca. 175 V/(Oe·cm)) under EM resonance conditions. Optimization of the LNO-based structures is therefore believed to yield comparable or even larger ME coefficients. Among other attractive features of LNO, one can highlight its relatively low price, high chemical, thermal and mechanical stability, availability of large crystals of high quality and its lead-free nature [128]. Its multifunctionality could also bring new opportunities for devices based on a coupling between optical, magnetic and electric properties. LNO and a closely related PE $LiTaO_3$ have already been widely used in surface and bulk acoustic wave devices, optical modulators, waveguides, filters, transducers, acoustic microscopes, etc. [173-177]. Experimentally, magnetically tunable surface wave devices were already tested in doped LNO [178, 179]. However, as a PE layer in ME laminate structures, LNO has been considered only in a few studies [122, 133, 180]. A theoretical estimation of the ME effect in a structure of Terfenol/LNO/Terfenol was made in [122] and an experimental study, in [133]. A very significant tunability of the magnetic properties of a polycrystalline nickel film deposited over a LNO single crystal has also been shown [180].

4.2. Experimental details

Several tri-layered ME composites of the 2-2 connectivity type were fabricated by bonding thin foils of the amorphous Metglas (Ni-Fe-Mo-B) MS alloy to opposite sides of square shaped $10 \times 10 \times 0.5$ mm^3 PE single crystals of LNO and PMN-31%PT poled in the [011] direction. Commercially available 29 μm thick sheets of 2826MB type Metglas® (Hitachi Metals Europe GmbH) were cemented to opposite surfaces of LNO single-crystals (Roditi International Corporation Ltd.) and PMN-PT (H.C. Materials Corp.) using a commercial cyanoacrylate-based glue. Both PE crystals were poled by the suppliers after growth. In this study we used Y-cut and 41ºY-cut crystals of LNO. The LNO crystal has a trigonal symmetry (belonging to the point group *3m*), and its polarization vector lies along the c-axis. The corresponding anisotropic PE, dielectric and elastic constants of the substrates can be calculated by rotating the crystallographic frame of the system, for which the coefficients can be obtained from the literature [70], with respect to their respective laminate frames [122]. The in-plane PE coefficients of the Y-cut LNO substrate were therefore calculated as d_{31} = –20.8 pC/N and d_{32} = 0, while an out-of-plane dielectric constant of ε_{r33}^{T}= 85.2 was obtained. On the other hand, the 41ºY-cut crystal has PE constants d_{31} = – 16.3 pC/N and d_{32} = –17.5 pC/N and a relative permeability of ε_{r33}^{T}= 60.9. The PMN-PT crystals used were poled along their thickness direction (i.e. along [011]), so that a *mm*2 multidomain symmetry was engineered [162, 172] with effective in-plane extensional PE constants $d_{31} \approx -1750$ pC/N and $d_{32} \approx 564$ pC/N and relative dielectric out-of-plane constant of $\varepsilon_{r33}^{T} \approx 4600$ [162, 172].

In order to study the EM and ME properties of the samples, impedance spectroscopy, as well as direct and converse ME effect measurements were carried out. The impedance measurements were performed in the frequency range of 100 Hz – 10 MHz. In this case a simple I-V circuit was used with a reference resistor connected in series with the piezocrystal, with gold electrodes deposited on each surface, and the frequency of a constant voltage signal generated by and internal source of the lock-in was swept. The amplitudes and phases of the voltage developed across the reference resistor were then detected by the lock-in amplifier, and, using a simple equivalent circuit model, the active and reactive parts of the sample impedance were subsequently obtained. The whole measuring procedure was controlled by a home-made LabVIEW® based program. This technique was used mainly in order to determine the quasi-static dielectric constant of the tri-layers and observe their characteristic EM resonances.

4.3. Results and discussion

The results of the impedance measurements are shown in Figure 4.1 in the form of the absolute admittance, $|Y|$, as a function of the frequency. Here we can distinguish a series of characteristic EM resonance and anti-resonance peaks. The sound velocity for longitudinal waves in $LiNbO_3$ propagating along the principal axes is ($v_s = 1/\sqrt{s_{11}^E \rho}$): for the *Z* direction, 7.271×10^5 cm/s; for the *Y* direction, 6.549×10^5 cm/s; and for the *X* direction, 6.580×10^5 cm/s [70, 181, 182]. Applying these values to the case of a $10 \times 10 \times 0.5$ mm^3 Y-cut LNO crystal, we see that the thickness extensional mode should roughly appear at ca. 6.58 MHz. The closest observed peak is centered at a slightly lower frequency of 6.34 MHz. The calculated length extensional resonances along the *X* and *Z* directions (327.5 kHz and 363.5 kHz, respectively) can be associated with the peaks observed at 281 kHz, 314 kHz and 355 kHz. The remaining peak centered at 3.65 MHz should be attributed to a shear thickness mode. This mode could be mediated by the relatively large d_{34} coefficient (– 69.2 pC/N). In the case of the 41ºY-cut LNO crystal, the thickness shear mode is much less intense because of a much smaller d_{34} = 3.83 pC/N [181, 182]. Also, in this case the two largest peaks observed at 323.9 kHz and 6.71 MHz must correspond to contour and thickness modes of vibration, respectively.

In order to exactly identify the in-plane contour acoustic vibrational modes of the LNO crystals observed in the impedance measurements, we implemented a simple model capable of predicting the dynamic electrical behavior of the crystals. More precisely, we numerically solved the thickness-averaged linear elastic and quasi-electrostatic equations of the crystals using a two-dimensional finite element-method (FEM). In the two-dimensional approximation [183, 184], where the thickness of the crystal is assumed to be much smaller than its length, we end up with a system of partial differential equations (PDEs) that can be solved numerically after prescribing the elastic displacements or stresses and electric potentials or electric displacements on the boundary surfaces of the media (i.e. the boundary conditions). Setting the appropriate material constants for each orientation of the crystal and assuming a grounded bottom electrode and a harmonic homogenous potential on the upper electrode ($\delta V_3 e^{j\omega t}$), as well as a null electric displacement field normal to the side surfaces and a null traction over all boundaries, the admittance at each frequency was calculated. To do this, the current flowing through a transverse section of the crystal was obtained by integrating the time derivative of the harmonic displacement field over this surface (i.e. $\delta I_3 = j\omega \int_{Area} \delta D_3 \, dA$).

The results of these simulations for the Y-cut and 41ºY-cut crystals are plotted in Figure 4.1 *a)* along with the experimental data. Here we observe a good agreement between the

simulated and experimental results and can perfectly identify a correspondence between the resonance and anti-resonance peaks in each type of Y-cut crystal. Therefore, we confirm the existence of three contour modes of resonance in the Y-cut crystal, situated at approximately 278, 314 and 358 kHz, and a single mode for the 41°Y-cut crystals at ca. 324 kHz. By setting the frequency of the applied voltage in the model to a value corresponding to some characteristic resonance mode and plotting the amplitude of the spatial distribution of the in-plane displacement fields, we can analyze and identify the contour resonance modes associated with each peak. The modes thus found are labeled and represented in Figure 4.1 *a)* which shows the absolute value of the displacements along the plane of the PE in a color scale (from blue for a null displacement to pink for large displacements) and the directions of these displacements as red arrows. Thus, the three resonance modes observed in the Y-cut crystal correspond to the three contour acoustic modes labeled as: *1)*, *2)* and *3)*. All of those are non-trivial modes because of the relatively complex geometry of the system. The mode *1)* is comparable to an extensional mode of type I, as labeled by the IRE standard [121], just like the mode *3)*. In summary, the mode *1)* is characterized by oscillatory displacements mainly along the central region of each face, while the central and vertex regions stay almost still. In mode *2)* there is a periodic bending of the vertexes to the sides. The *3)* mode is associated with a periodic displacement of the vertex regions of the plane along the radial direction. Since the *1)* and *3)* modes are associated with larger displacements over larger areas, they naturally produce larger variations of the current flowing through the crystals and consequently larger resonant peaks. The single large resonant mode observed in the 41°Y-cut crystal labeled *4)*, on the other hand, corresponds to a symmetric contour mode of the type III [121] where the crystal periodically expands and contracts almost isotopically in both in-plane directions and is generated due to the almost in-plane isotropic nature of the material constants in this case.

For the case of the PMN-PT based tri-layer, two low-frequency modes (67 kHz and 111 kHz) and one high-frequency mode (4.87 MHz) are observed, as shown in Figure 4.1 *b)*. According to [185],the sound velocity for the longitudinal mode propagating along the *Z* direction is 4.727×10^5 cm/s, which yields for a thickness extensional resonance a frequency of about 4.73 MHz that is close to the experimentally observed value. Using the same model as in the aforementioned case, we identified the contour resonance modes responsible for the two observed low-frequency peaks. Those are labeled *5)* and *6)* and are shown in Figure 4.1 *b)*. The first of these modes therefore corresponds to a simple extensional mode, while the second exhibits a behavior similar to the one observed in the mode *2)*. When compared to the electrically excited contour resonant modes of the LNO crystals, the resonant admittance peaks measured in the PMN-PT crystal are shown to be one order of magnitude larger, which should be a result of a much stronger PE effect in this crystal.

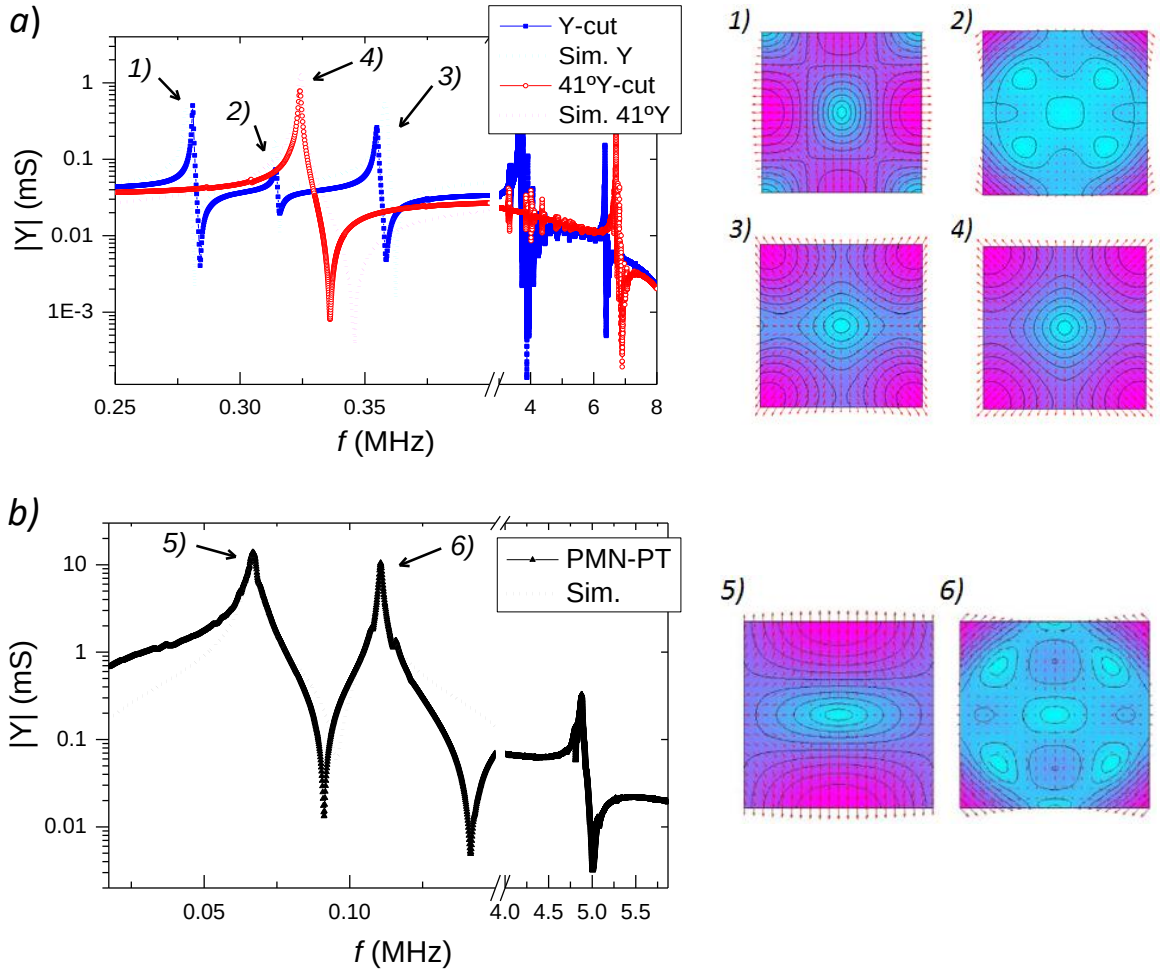

Figure 4.1 On the left: experimental and simulated impedance spectra of *a*) LNO and *b*) [011]-poled PMN-PT PE single crystals depicting its various characteristic EM resonance ($|Y| \to \infty$) and anti-resonance ($|Y| \to 0$) modes. On the right: spatial distribution of the in-plane relative displacement fields associated with each type of observed contour EM resonance mode labeled as *1) – 6)*. Here, more purple regions correspond to larger relative displacement amplitudes while more cyan regions are associated with small displacements. The superimposed small red arrows depict the direction of such displacements.

Measurements of the direct ME effect were carried out at room temperature and at a frequency of 5 kHz in the quasi-static regime, i.e. far enough from any observed EM resonances. The modulation amplitude of the *AC* field was fixed at δH = 1 Oe, while the transversal ME voltage coefficients α_{E31} and α_{E32} (given by equation 3.8 for k = 1) were measured in two orthogonal in-plane orientations. Thus, α_{E31} was measured with the bias field H oriented along the X direction in

the laminate frame, while α_{E32} was measured with H oriented along the Y direction. Figure 4.2 shows the experimental results obtained. In the general case we start by noting that the soft magnetic properties of the Metglas alloy are responsible for the appearance of the maximum ME effect in magnetic fields as low as 25 Oe. The region where the ME effect is not null corresponds to the field range where the magnetization vector of the MS phase increases by the rotation of magnetic domains and by domain wall motion. The saturation of the ferromagnetic foil occurs at $H \approx 50$ Oe, after which any further increase of the external bias field does not lead to any substantial increase of the strain in the thin foil (i.e. the magnetostriction attains its saturation value λ_S), and consequently the ME effect vanishes. Furthermore, as it was expected, we see that the samples demonstrate an anisotropy of their in-plane ME properties due to the anisotropy of the PE properties. The sample containing the Y-cut LNO crystal exhibits a difference between α_{E31} and α_{E32} of more than an order of magnitude. The respective measured values were α_{E31} = 0.46 V/(cm·Oe) and α_{E32} = 0.024 V/(cm·Oe). In this crystal we have d_{31} = – 20.8 pC/N and d_{32} = 0 and, consequently, the small observed α_{E32} coefficient is exclusively generated by the transversal Poisson stress of the magnetostriction acting on the d_{31} component. In the latter case, the magnitude of the ME induced voltage was comparable to the parasitic electromagnetic induction voltage, so that the corresponding correction has been applied. On the other hand, in the 41ºY-cut LNO crystal sample an almost isotropic in-plane behavior has been observed with $\alpha_{E31} \approx \alpha_{E32} \approx$ 0.42 V/(cm·Oe), which is due to almost equivalent values of the d_{31} and d_{32} piezocoefficients (– 16.3 pC/N and – 17.5 pC/N, respectively). For the case of the PMN-PT composite, the d_{31} piezoconstant is twice as large as d_{32} and has a different sign. As a result, the maximum of α_{E31} corresponds to 1.15 V/(cm·Oe), while the maximal amplitude of α_{E32} equals – 0.41 V/(cm·Oe). Following the procedure described in [122] and using the Metglas and PMN-PT material parameters measured by the suppliers and by independent sources [162, 172], we calculated the maximum expected quasi-static values of α_{E31} and α_{E32} for our specific sample to be α_{E31} = 23.2 V/(cm·Oe) and α_{E32} = – 7.2 V/(cm·Oe). These values are more than one order of magnitude larger than the experimental ones. This may be mainly due to a weak coupling between interfaces, where the intermediate glue layers absorb part of the tensile stress being transferred from the MS to the PE phase, and a non-optimized PE/MS thickness ratio between phases, where composites with much thicker MS phases are expected to generate considerably larger effects due to a minimal compressive stress produced by the thin PE substrate on the MS phases [56]. Nevertheless, as both of these factors should result in an identical reduction of the ME effect in the PMN-PT and LNO based composites, further discussion shall be more focused on the relation between the measured coefficients rather their absolute values.

A very important point can be drawn from the quasi-static direct ME measurements. The maximum amplitudes of the observed ME voltage coefficients for the LNO tri-layers are only about

three times lower than those for the PMN-PT composite. The maximal ME voltage coefficient for the PMN-PT tri-layer is 1.16 V/(cm·Oe), while for the LNO tri-layers employing Y-cut and 41°Y-cut crystals it is 0.47 V/(cm·Oe) and 0.42 V/(cm·Oe), respectively. Comparable magnitudes are mainly explained by the fact that the dielectric constant of PMN-PT is more than 60 times larger than that of LNO. Consequently, the same amount of charge generated by piezoelectricity gives rise to a 60 times lower voltage in PMN-PT. Therefore, the huge piezoelectric coefficients of PMN-PT are effectively nullified by its also huge dielectric coefficients in terms of the open-circuit ME effect.

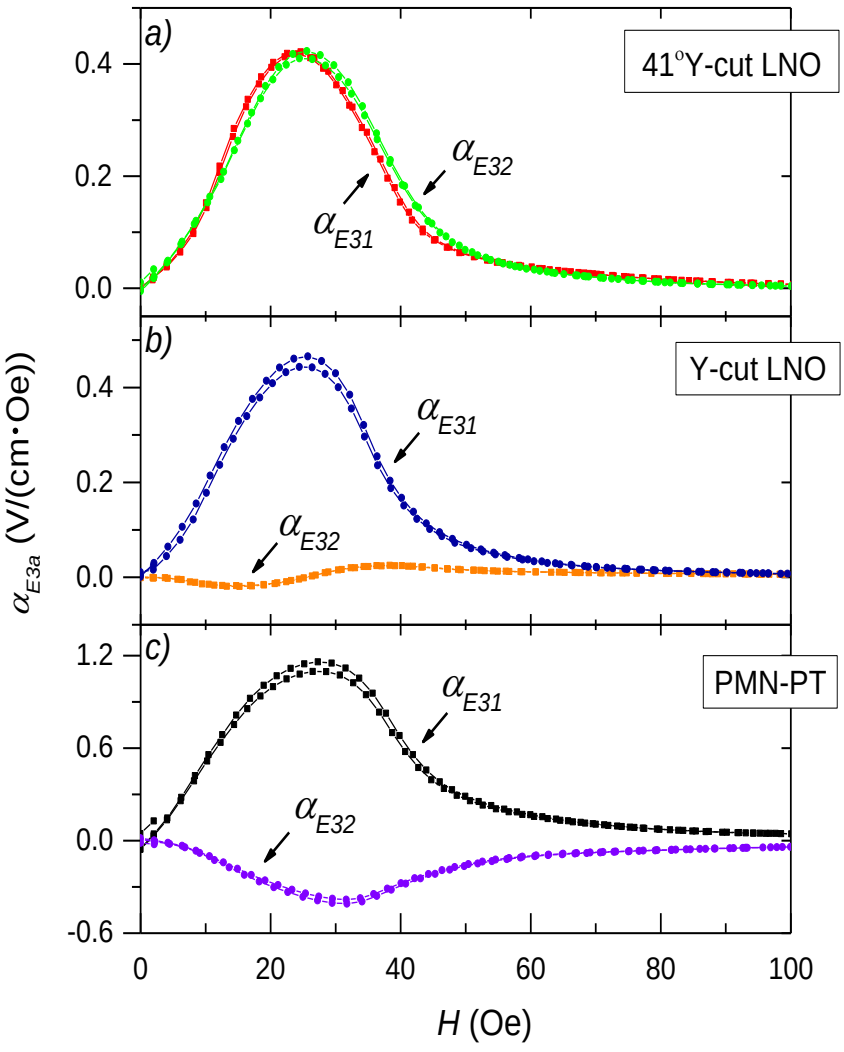

Figure 4.2 Direct voltage ME effects measured in the tri-layered composites of Metglas/PE/Metglas with PE single-crystals of *a)* 41°Y-cut LNO; *b)* Y-cut LNO and *c)* [011]-poled PMN-PT (with f = 5 kHz and δH = 1 Oe).

As we have seen, the magnitude of the direct ME voltage coefficient can be comparable in LNO- and PMN-PT-based composites because this response is approximately proportional to the ratio between the PE coefficients and dielectric constants. However, this concurrent influence on the composite's performance is no longer favorable for the case of the converse ME effect because this effect is independent of the dielectric constants ($\alpha_B = \partial B/\partial E = (\partial B/\partial T)(\partial T/\partial S)(\partial S/\partial E) = qs^{-1}d$) [124, 186-188]. Thus, in this regime, the huge difference in piezoelectric coefficients between PMN-PT and LNO becomes crucial, and the PMN-PT composites should exhibit much stronger converse ME responses. To show this, we performed converse ME measurements on the three composites. Figure 4.3 shows the converse magnetoelectric response represented as the ratio between the electromotive force induced on the sensing Helmholtz coil, δV_{ind}, and the voltage applied to the tri-layered composite, δV_{mod} = 10 V. This effect is associated with a change in the effective permeability of Metglas when under a stress, which is transferred from the PE substrate. As expected, the dependences of the converse ME effect as a function of the external magnetic bias field are shown to be qualitatively similar to those observed in the direct ME effect measurements, diverging between the different composites only in terms of amplitude. In fact, the composite with the 41ºY-cut LNO exhibits a two orders of magnitude lower response than the one with PMN-PT. Beyond any doubt, the large difference between PE coefficients becomes crucial in this mode. In conclusion, even though the direct ME voltage response is comparable in both composites, the benefits of using PMN-PT crystal for the converse ME effect as well as the direct short-circuit ME charge response in such laminate structures remains indisputable.

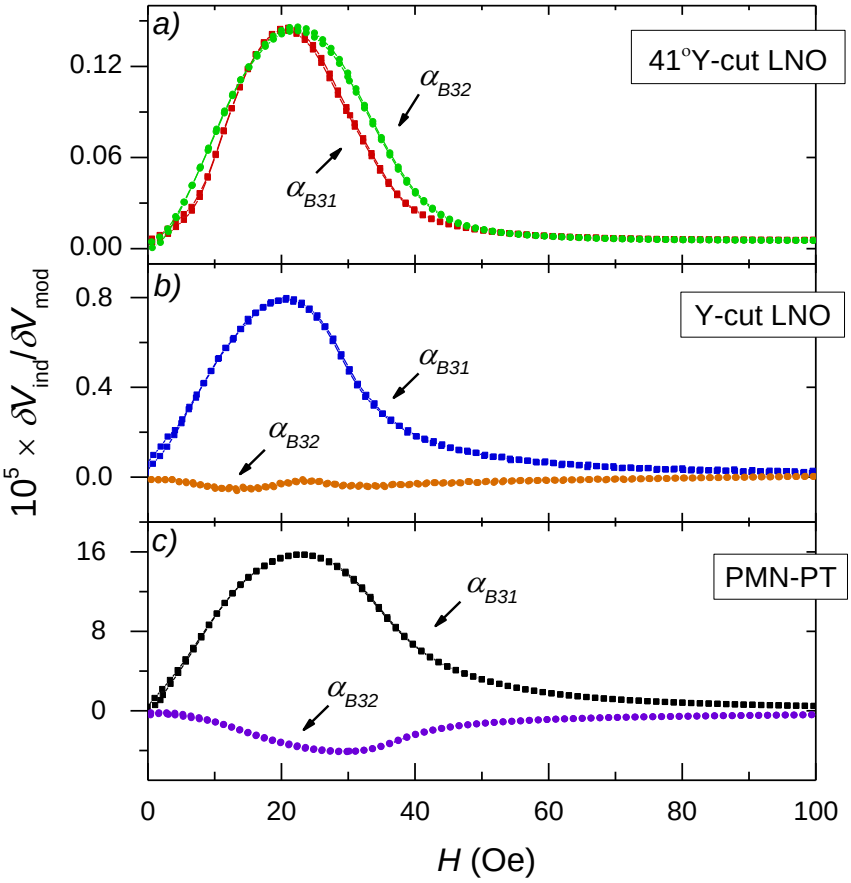

Figure 4.3 Converse ME effects measured (given by the ratio between the voltage induced in the sensing coil, δV_{ind}, and the voltage applied to the composites, δV_{mod} = 10 V) in the tri-layered composites of Metglas/PE/Metglas with PE single-crystals of *a)* 41ºY-cut LNO; *b)* Y-cut LNO and *c)* [011]-poled PMN-PT.

Returning to the direct ME effect measurements, the benefits of PMN-PT already do not look so convincing. The three times greater ME voltage coefficient hardly seems to justify an order of magnitude higher price and lower Curie temperature of the PMN-PT crystal. When measured as a function of the *AC* magnetic field frequency, f, the EM resonance modes observed in the impedance measurements can also be detected in the direct ME effect. These measurements were performed in the range of 1 kHz – 600 kHz (with a fixed bias field H = 25 – 30 Oe and an *AC* field amplitude δH = 0.5 Oe). The results depicted in Figure 4.4 show the characteristic large increase in the direct response of the composites under such resonance conditions (more precisely the impedance anti-resonance conditions). Surprisingly, the system with the 41ºY-cut LNO crystal yielded the largest effect of ca. 88 V/(cm·Oe) at the largely symmetric resonant mode *4)* shown in Figure 4.1 , while in

the PMN-PT system the maximum was only of 66 V/(cm·Oe). We also note that the EM resonance is situated in a very suitable frequency range. From the point of view of possible sensor applications, a full implementation could be done using standard low-cost electronic components.

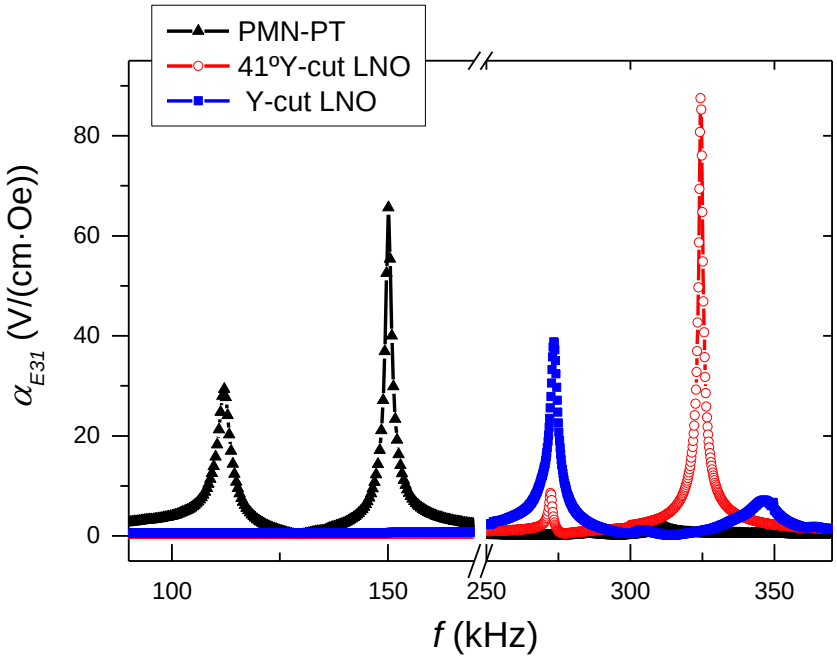

Figure 4.4 Direct transversal ME effects (α_{E31}) measured in the tri-layered Metglas/PE/Metglas composites as a function of the modulated field frequency *f* with H = 25 Oe and δH = 0.5 Oe.

4.4. Conclusions

In summary, in this part we introduced a comparative study between the direct and converse ME effects in tri-layered composites of the type Metglas/PE/Metglas based on single crystals of $LiNbO_3$ (LNO) and [011]-poled PMN-PT bonded with a cyanoacrylate glue. Due to the simplified preparation method, the amplitude of the observed ME effect was rather modest. In the quasi-static regime, although the highly piezoelectric PMN-PT-based composite has exhibited an orders of magnitude stronger converse ME effect, the measurements of the direct ME effect have shown comparable magnitudes for both types of systems, mainly due to comparable ratios between piezoelectric and dielectric coefficients of both crystals. The converse ME effects, on the other hand, were shown to be much stronger in the sample with the PMN-PT crystal since, according to the theory, this effect depends only on the piezoelectric constants which are much larger in this case. We

also presented the results of the direct ME measurements in the resonant regime. Here we found an even larger ME effect peak in the composite with the 41ºY-cut LNO than in the one with PMN-PT. The largest direct ME voltage coefficient of about 88 V/(cm·Oe) has been obtained for the 41ºY-cut LNO composite, while this was only of 66 V/(cm·Oe).for the PMN-PT-based structure Therefore, in this study we identified crystalline LNO as a valuable alternative to lead-based PEs in ME applications with the potential to form its own field of ME-based low-cost high-temperature magnetic-field sensors.

Chapter 5

5. Anisotropic magnetoelectric effect in tri-layered composites of Metglas with $LiNbO_3$ and $GaPO_4$ single crystals

Abstract

This chapter describes an experimental study of the dynamic impedance and magnetoelectric anisotropic properties in tri-layered composites of Metglas and single-crystalline lead-free piezoelectrics. We have prepared a variety of different magnetoelectric laminates by bonding magnetostrictive Metglas foils onto single-crystalline substrates of $LiNbO_3$ and $GaPO_4$. The measurements have been performed as a function of the crystal cut, magnitude and orientation of the magnetic bias field and the frequency of the modulation field. Greatly enhanced ME coefficients in certain resonance modes are explored and their relations to the material properties of the crystals and the geometry of the composites are investigated. The largest ME coefficient of up to 249 V/(cm·Oe) was observed for a composite with a 41°Y-cut LNO crystal at 323.1 kHz. In summary, we show that crystalline lead-free LNO and GPO can exhibit relatively large anisotropic ME effects in multilayers. We also demonstrate that control of the PE crystal's orientation can be successfully used in order to obtain almost any desired quasi-static and resonant anisotropic ME properties for some given application. Such unique features as chemical stability, linear piezoelectricity, thermal robustness open up a real perspective to use lead-free $LiNbO_3$ and α-$GaPO_4$ based ME tri-layers, e.g., as vector magnetic field sensors working in a wide range of temperatures.

5.1. Introduction

In the previous section we showed how the use of highly anisotropic single crystalline LNO in ME tri-layered composites can yield very remarkable quasi-static and resonant ME effects. Besides LNO, a noteworthy piezocrystal for ME applications is gallium orthophosphate ($GaPO_4$, GPO) a commercially available piezoelectric crystal with a trigonal structure (point group *32*) and excellent high-temperature properties [71]. As a crystal homotypic to quartz, it possesses many

properties similar to the latter. Characteristic of this material are its larger piezoelectric coefficients when compared to quartz (ca. 1.2 times larger e_{11} and 2.5 times larger e_{14}) [71]. Other desirable properties of the compound are its high thermal stability, with its piezoelectric coefficients and most of its properties barely changing up to a cristobalite transition at 933ºC, large ratio between PE and dielectric constants (d_{3a}/ε_{33}), the absence of ferroelectricity and pyroelectricity, a higher EM coupling as compared to quartz, and a high purity of the as-grown crystals [71, 72]. In the present part, we report a study of the anisotropic direct ME properties of enhanced bulk tri-layered composites of Metglas/LNO/Metglas and Metglas/GPO/Metglas, making use of differently oriented crystalline PEs and under quasi-static and EM resonance conditions [134]. The maximum expected quasi-static ME coefficients in each case were numerically estimated as a function of the crystal orientation and compared with the experimental results. The physical origin of the in-plane directional ME response was therefore uncovered.

5.2. Theoretical calculations

In order to numerically investigate the nature of the anisotropic ME coupling in tri-layered composites of amorphous Metglas and piezocrystals of LNO and GPO, the maximum direct transversal ME voltage coefficients, $\alpha_{E3a} = \partial E_3/\partial H_a$, were numerically estimated for a series of such structures. A standard averaging linear quasi-static micromechanical method based on coupled constitutive equations for each layer was used for this purpose [56, 122]. Here, a square shaped 10 × 10 mm^2 ME tri-layered structure composed of two 29 μm thick foils of Metglas and one central 0.5 mm thick piezoelectric crystal, operating in the L-T mode, like the one shown in Figure 2.1, was considered. Its constitutive elastostatic, electrostatic and magnetostatic equations were then solved assuming averaged homogeneous tensor fields in each perfectly elastically coupled layer (k_C = 1) and under unclamped and open circuit boundary conditions. The required linear anisotropic electric, magnetic and elastic material constants were obtained from the literature (Metglas [140-142], LNO [70], and α-GPO [71, 72]).

Since the material properties of single crystals are highly anisotropic, the optimization of the piezocrystal orientation (crystal-cut) can in principle lead to significantly enhanced ME coefficients in composites. To investigate the dependence of the maximum ME coupling coefficient with the crystal orientation, the material tensors were transformed from the crystalline frame to the frame of the laminate using the classic Euler angles $Z_1X_2Z_3$ corresponding to a sequence of three rotations each denoted by the angles α, β and γ [122, 139, 162]. The results obtained in this way are shown in Figure

5.1 as representation surfaces of $|\alpha_{E3a}|$ maximized in the range of all γ angles between 0º and 180º and as a function of the α and β angles for the composites containing LNO and GPO. A very large variation of the magnitude of the transversal ME effect with the orientation of the piezocrystal, whose symmetry coincides with the symmetry of the corresponding crystal's point group, can be observed. As strong ME effects are particularly important in applications requiring high efficiencies and sensitivities, we conclude that the selection of a crystal with an appropriate cut is a very important step in the development of ME sensors. For the case of the LNO crystal, we see that the calculated ME coefficient could potentially be as large as 27.24 V/(cm·Oe) for a crystal with a (*ZXl*) 39º-cut (α = 0º, β = 39º and γ = 90º) and five other cuts equivalent by symmetry. In commercially available crystals this orientation is commonly denoted as 129ºY-cut. An even larger maximum coefficient of 35.62 V/(cm·Oe) was predicted for the GPO crystal with a (*XYt*) 12º-cut (α = 90º, β = 90º and γ = 12º) and five other equivalent orientations. This cut is very close to the commonly available X-cut crystals (α = 90º, β = 90º and γ = 0º).

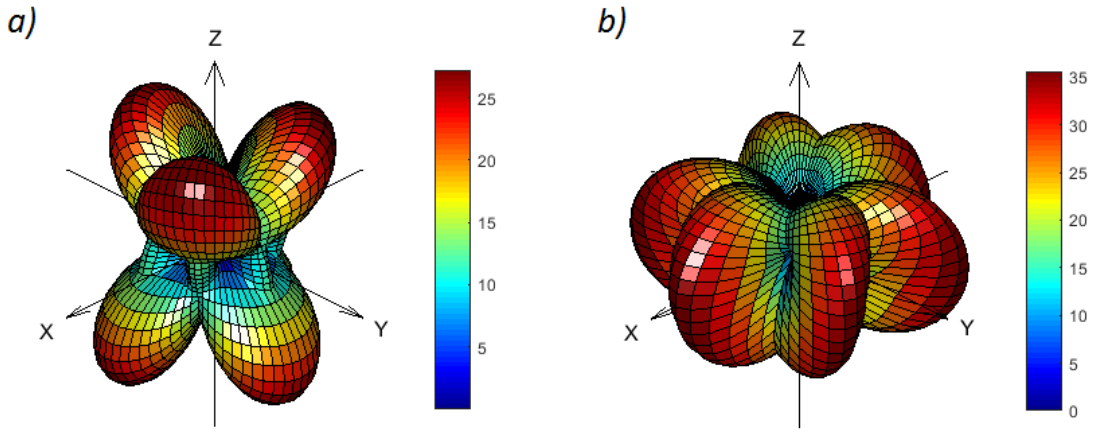

Figure 5.1 Representation surfaces depicting the maximum estimated absolute values of the transversal ME voltage coefficient $|\alpha_{E3a}|$ (across $0 < \gamma < 180$º) as a function of the crystal orientation (normal to the plane of the laminate associated with the rotation angles α and β for the tri-layered ME composites of Metglas/Piezocrystal/Metglas, with piezocrystals of: *a*) $LiNbO_3$; and *b*) α-$GaPO_4$.

For comparison we also used the model described above in order to calculate the transversal ME coefficients for the particular case of the piezocrystals employed in the experimental part. Those consisted of Y-cut (α = 0º, β = –90º and γ = 0º) and 41ºY-cut (α = 0º, β = –49º and γ = 0º) LNO as well as X-cut (α = 90º, β = 90º and γ = 0º) GPO. The results thus obtained indicate, for the 41ºY-cut

crystal, maximum values of α_{E31} and α_{E32} in-phase and with approximately the same magnitude (α_{E31} = 11.2 V/(cm·Oe) and α_{E32} = 11.9 V/(cm·Oe)), which is due to almost equivalent d_{31} and d_{32} PE coefficients (–16.5 pC/N and –17.5 pC/N, respectively). In the composite containing the Y-cut crystal, on the other hand, there should be a very large anisotropy in its transversal ME effect (α_{E31} = 11.6 V/(cm·Oe) and α_{E32} = -1.3 V/(cm·Oe)). This is the case because the transversal piezoelectric coefficients are very different: d_{31} = –20.8 pC/N and d_{32} = 0. Consequently, the small α_{E32} coefficient is generated only by the traction component perpendicular to the magnetic field, which originates from the Poisson effect, acting on the d_{31} PE component. In the system with X-cut GPO a behavior similar to the aforementioned one was also predicted (α_{E31} = 34.0 V/(cm·Oe) and α_{E32} = -3.8 V/(cm·Oe)), since the PE constants are similarly given by d_{31} = –4.37 pC/N and d_{32} = 0.

5.3. Experimental details

To experimentally investigate the direct ME effect we prepared tri-layered structure containing two 29 μm layers of 2826MB Metglas (Hitachi Metals Europe GmbH) bonded on both faces of $10 \times 10 \times 0.5$ mm^3 square-shaped commercial PE single crystals of congruent LNO and GPO (Roditi International Corporation Ltd.) cut along desirable crystallographic directions. These consisted of substrates of Y-cut, 41°Y-cut LNO and X-cut GPO bounded to Metglas using a commercial epoxy resin which was cured for 24 h. This type of adhesive is commonly used in the preparation of ME layered composites [6-12, 14, 16, 20] and is well known for its good mechanical, thermal and chemical properties. Their anisotropic ME and EM properties were subsequently studied.

5.4. Results and discussion

Using the setup described in chapter 3, we measured the direct ME effect in the quasi-static regime in each of the three composites. The tri-layered structures were subjected to a fixed *AC* magnetic field with amplitude δH = 1 Oe and a frequency of 1 kHz. The magnetic bias field H was then applied in the X and Y directions in relation to the samples and swept in such a way so as to measure the hysteretic in-plane α_{E31} and α_{E32} ME coefficients (i.e., with the field increasing from zero up to its maximum value followed by a decrease down to a minimum value and an increase back to zero). The results of these measurements are plotted in Figure 5.2. As in the previous comparative

study, we see that the maxima of the ME effects are attained at magnetic fields as low as 25 Oe, which is due to the soft magnetic properties of Metglas. We also note an almost complete absence of a hysteretic response, which confirms the linear nature of the piezoelectric properties of both LNO and GPO. An imperative observation is that, as expected, all of the samples exhibit a significant anisotropy of their in-plane ME properties ($\alpha_{E31} \neq \alpha_{E32}$). Such noticeable differences are mostly related to the anisotropic nature of the material constants of the piezocrystals, mainly their piezoelectric d_{3a} coefficients. In the case of the tri-layered composite with the 41ºY-cut LNO crystal, maximum effects of α_{E31} = 0.83 V/(cm·Oe) and α_{E32} = 0.92 V/(cm·Oe) were obtained. This response corresponds to an almost in-plane isotropic ME behavior with $\alpha_{E32} \approx \alpha_{E31}$ in agreement with the predictions made in the preliminary calculations. This behavior contrasts with the structure containing the Y-cut LNO crystal which exhibits a difference between maximum absolute values of α_{E31} and α_{E32} by almost an order of magnitude. This is the case because the d_{32} PE coefficient happens to be null in this orientation. The obtained values here were α_{E31} = 0.95 V/(cm·Oe) and α_{E32} = –0.10 V/(cm·Oe). We also note that both maximum coefficients have a different sign. The positive value defines an in-phase dependence between the applied *AC* magnetic field and the induced *AC* voltage and the negative value indicates an out-of-phase relation between these fields. Finally, we see that the sample with the X-cut GPO piezocrystal equivalently yields an almost anisotropic unipolar response with maximum ME coefficients of α_{E31} = 0.24 V/(cm·Oe) and α_{E32} = –0.03 V/(cm·Oe), as was already predicted by our calculations.

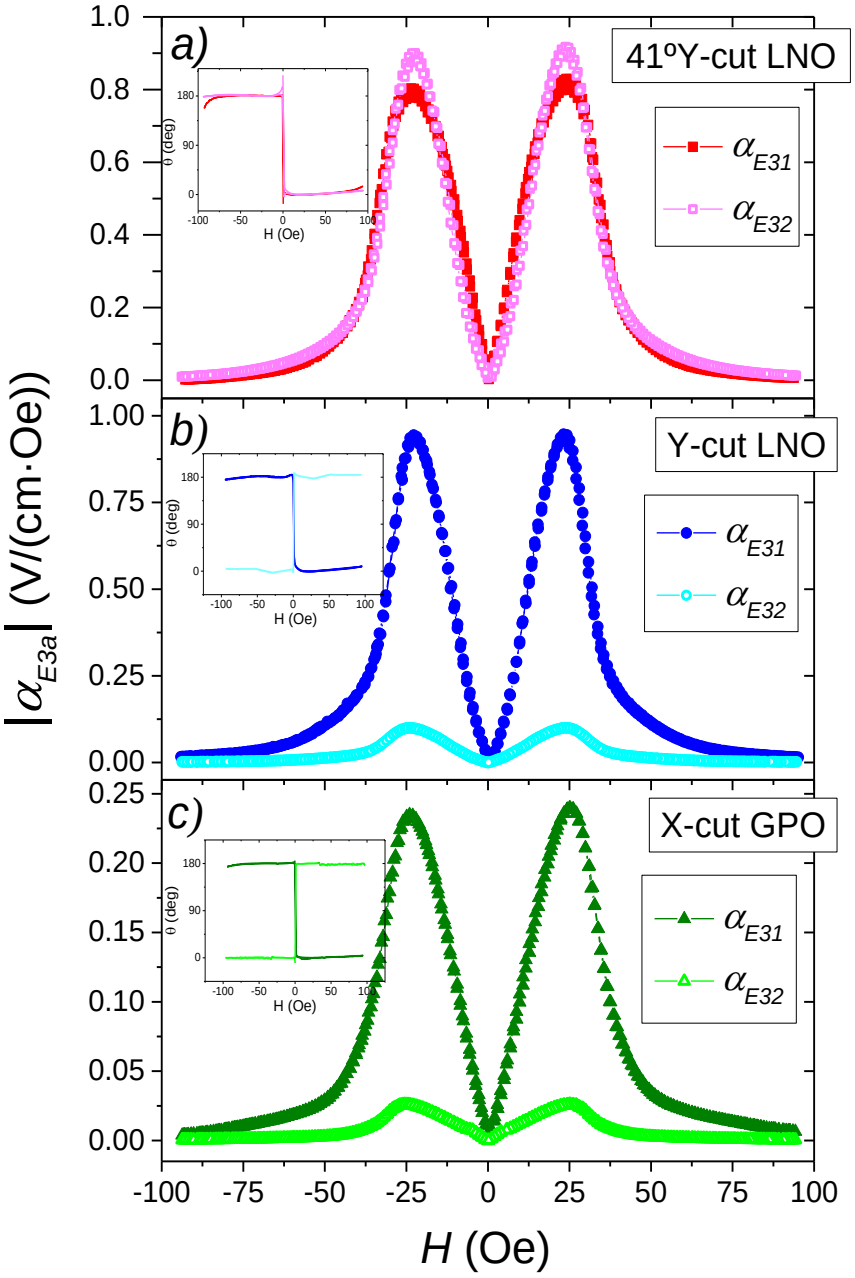

Figure 5.2 Direct quasi-static transversal ME effect measurements ($|\alpha_{E31}|$ and $|\alpha_{E32}|$) of the tri-layered composites of Metglas and *a)* 41ºY-cut LNO, *b)* Y-cut LNO, or *c)* X-cut GPO, with f = 1 kHz and δH = 1 Oe. The insets depict the phase (in degrees) corresponding to each ME coefficient.

Considering again the preliminary calculations, we conclude that all of the experimental results are in a good qualitative agreement with the theoretically estimated effects. However, in quantitative terms, the obtained coefficients were still one order of magnitude smaller than the

maximum calculated ones. The main reasons for this should be attributed to a far from optimal thickness ratio between the PE and MS phases and elastic coupling between phases. Additionally, because the magnetostrictive response of the MS alloy is highly non-linear, its pseudo-piezomagnetic q_{ki} coefficients change abruptly with the bias field and stress tensor. In fact, a more sophisticated model for the MS phase [161] shows that the large compressive pre-stress produced by the thick PE in the direction of the applied bias field tends to decrease the maximum value of q_{ki} and increase the bias field at which it is attained. Also, our calculations predicted a three times larger effect in the system with GPO in relation to the one with Y-cut LNO. Since all samples were prepared in the same manner, this seems to be in disagreement with the experiment. A likely explanation is the existence of a large discrepancy between piezoelectric and dielectric coefficients of GPO as the ones found in the literature due to variations in the growth and poling techniques [71, 72, 189]. It may also be related to limitations of the model which, e.g., does not take into account possible stress relaxation occurring along the thickness of the piezoelectric layer nor the properties of the interfaces between the piezoelectric crystals and the layers of epoxy with a finite thickness.

To investigate the dynamic properties of the composites we again started by performing impedance measurements of the PE crystals alone. Figure 5.3 shows the results thus obtained in the form of *a)* the absolute impedance $|Z|$.as a function of the frequency and *b)* the corresponding Nyquist plots of the impedance (-Z'' *vs* Z', where Z' is the real and Z'' the imaginary parts of Z, respectively). These figures clearly illustrate a multitude of EM resonances (where $|Z|$ attains a minimum value) and anti-resonances (where $|Z|$ attains a maximum value) in the frequency range between 150 kHz and 390 kHz. The amplitude and frequency of the anti-resonance modes is particularly interesting because, as we shall see later, these modes are strongly linked with the resonant peaks observed in the dynamic ME measurements. Of notice is the fact that the X-cut GPO crystal was shown to produce four different resonant modes which are nonetheless much weaker than those found in the LNO substrates and appear at smaller frequencies, due to ca. 3 times larger compliance coefficients in the former [70-72]. Another important observation is that the difference between the anti-resonant and resonant frequencies of the 41ºY-cut LNO is much larger than in the other crystals which indicate an enhanced effective EM coupling factor (k_{eff}) and consequently a more efficient conversion of energy [67]. The Nyquist plots show us how the real and imaginary parts of the impedance of the PEs change with the frequency close to a certain resonance mode. Thus we see that, as the frequency increases, the imaginary part of Z starts to increase up to a maximum value where the resonance frequency is ca. attained. After this, the imaginary part starts to drop to zero while the real part of Z starts to increase from a very low positive value up to a maximum close to the anti-resonance frequency. After this frequency, the real part returns to its initial positive value while the imaginary part decreases down to a negative minimum and subsequently returns to its

initial value. Each of these resonance modes therefore form a closed loop in the Nyquist plot. More intense resonances in general thus give rise to wider loops and larger resonance peaks.

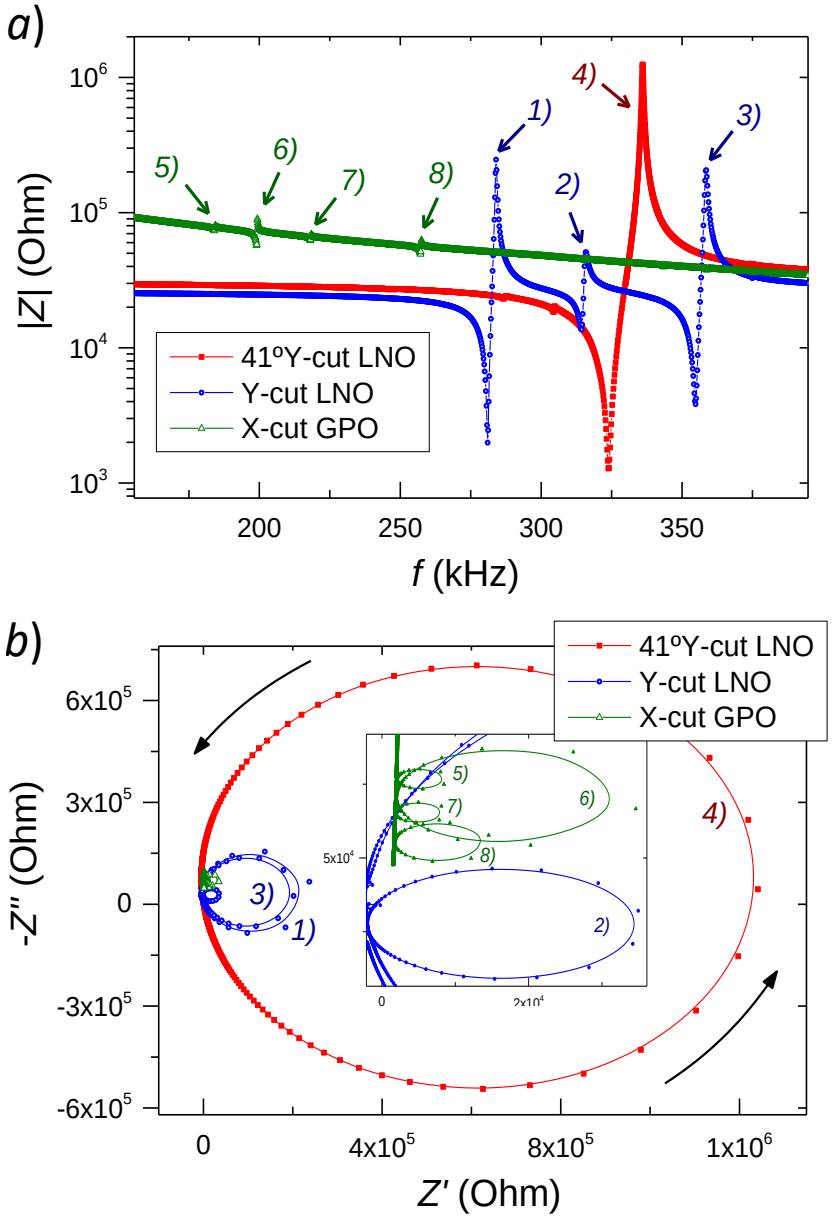

Figure 5.3 Impedance spectra of the 41ºY-cut LNO, Y-cut LNO and X-cut GPO single-crystals showing its characteristic EM resonance ($|Z| \rightarrow 0$) and anti-resonance ($|Z| \rightarrow \infty$) modes labeled as *1) – 8)* and depicted as: *a)* the absolute value of the impedance $|Z|$ *vs* f and; *b)* Nyquist plots of the impedance ($-Z''$ *vs* Z'). In the last case, the arrows indicate the direction of the increasing frequency and the inset shows in detail the small loops associated with the weak resonance modes of the Y-cut LNO and X-cut GPO crystals.

To identify each acoustic resonant mode we again implemented in Matlab® a two-dimensional finite element-method in order to simulate the results [183, 184]. These calculations clearly proved that the resonant peaks observed correspond to different types of in-plane contour resonance modes. The obtained modes are thus labeled in Figure 5.3 as *1) – 8)* and depicted in Figure 5.4 *c)*. To summarize this part, the frequency and $|Z|$ amplitude associated with each anti-resonant mode is listed next: *1)* f = 284.0 kHz; $|Z|$ = 246 kOhm; *2)* f = 315.8 kHz; $|Z|$ = 51 kOhm; *3)* f = 358.6 kHz; $|Z|$ = 205 kOhm; 4*)* f = 336.1 kHz; $|Z|$ = 1.25 MOhm; *5)* f = 184.8 kHz; $|Z|$ = 80 kOhm; *6)* f = 199.3 kHz; $|Z|$ = 90 kOhm; *7)* f = 218.4 kHz; $|Z|$ = 69 kOhm; *8)* f = 257.5 kHz; $|Z|$ = 63 kOhm.

The dynamic ME effects (α_{E31} and α_{E32} components) were subsequently measured for the three composites as a function of the frequency of the *AC* magnetic field. The measurements were performed in the range from 1 kHz–600 kHz, with a fixed bias field of H = 25 Oe and a modulation field amplitude of δH = 0.1 Oe. The obtained results are depicted in Figure 5.4 *a)* and *b)*. Here, we can again identify the existence of multiple high-amplitude peaks in the ME response of the samples. By taking into account the sound velocity for the propagation of longitudinal waves in these crystals, of the order of 6.5×10^5 cm/s [70], and their dimensions we conclude that the observed peaks in the kHz range can be attributed to different types of in-plane contour acoustic modes.

With a bias field applied in the X direction (α_{E31} mode), for the case of the composite with the 41ºY-cut LNO crystal a single and very intense ME peak of up to 249.0 V/(cm·Oe) was observed at a frequency of 323.1 kHz. For the sample with the Y-cut LNO crystal, on the other hand, three different smaller peaks were observed in this range. This clearly illustrates how the anisotropic nature of the material constants takes an important part in the determination of which kinds of EM resonance modes may or may not be excited under certain conditions. Consequently we conclude that the anisotropic nature of the PE crystals is even more noticeable in the resonant regime in relation to the quasi-static. In the structure with the Y-cut LNO crystal, the largest peak occurs at approximately 344.3 kHz and takes the value of 132.9 V/(cm·Oe). The other two peaks appear at 270.1 kHz and 302.3 kHz and reach heights of 101.1 V/(cm·Oe) and 26.8 V/(cm·Oe), respectively. In the GPO sample we observed four different resonance modes associated with comparatively smaller ME coefficients. The largest resonant effect here is of 23.2 V/(cm·Oe), occurring at 199.7 kHz. The other three peaks take values of 12.0 V/(cm·Oe), 5.0 V/(cm·Oe) and 13.0 V/(cm·Oe) and are excited at frequencies of 184.3 kHz, 220.5 kHz and 257.9 kHz, respectively. Furthermore we note that all of the aforementioned peaks are associated with a characteristic sudden decrease in phase by ca. 180º as it can been seen in the inset of Figure 5.4 *a)*. In this case the ME resonance peaks are all followed by a change of phase from 0º down to -180º and therefore the imaginary part of the ME coefficients yield peaks with negative values in resonance. A comparison with the impedance of the crystals in

Figure 5.3 demonstrates that the same number of resonant modes can be identified in both experiments and that the frequencies and amplitudes of the resonant ME effects in the composites are closely related to the frequencies and amplitudes of the anti-resonant EM modes in the PEs. Thus we conclude that they must correspond ca.to the same type of resonance modes. This is the case because, as the impedance of the PE crystals is maximized in the anti-resonant mode, its capacitance and thus longitudinal effective dielectric constant (ε) is consequently minimized which results in a large enhancement of the direct voltage ME effect (i.e. increase in the d/ε ratio) [190].

Having obtained a good agreement between the simulated and experimental values of the anti-resonance frequencies, with relative errors inferior to 4%, the spatial distribution of the relative displacement fields for each mode can then be plotted as shown in Figure 5.4 *c)*. Thus, we see that the three resonance modes observed in the Y-cut LNO crystal correspond to the three contour acoustic modes (where the in-plane components of the displacement fields do not change significantly in the Z direction and the out-of-plane displacement u_3 is null) dubbed as *1)*, *2)* and *3)*. We can identify mode *1)* as an extensional mode closely related to type I, as labeled by the IRE standard [121]. In the 41ºY-cut LNO crystal, the observed single resonance *4)* corresponds to an extensional mode of type III which is a very symmetric almost isotropic mode. This seems to suggest that remarkably strong resonance modes can be excited in PE crystals, whose geometric symmetry coincides in some way with the symmetry of its anisotropic material constants. This is the case for the 41ºY-cut square-shaped crystal, which is associated with almost equal in-plane d_{31} and d_{32} PE coefficients as well as c_{11}^E and c_{22}^E elastic stiffness constants. By comparison with the properties of some bulk tri-layered composites found in the literature with equivalent structures but employing different compounds, we conclude that the 249 V/(cm·Oe) coefficient observed in the 41ºY-cut LNO sample is one of the largest ever found in ME 2-2 bulk tri-layered structures, being even larger than the 175 V/(cm·Oe) value measured in a Permendur/Quartz/Permendur system [135]. It is also remarkably larger than those found in lead-based PMN-PT (70 V/(cm·Oe)) and PZT (110 V/(cm·Oe)) composites with Permendur [137]. In the X-cut GPO piezocrystal, the first two modes at 184.3 kHz and 199.7 kHz and the fourth one at 257.9 kHz were identified as different kinds of contour shear modes. The first two modes, *5)* and *6)*, and the *8)* respectively resemble variations of the modes *1)* and *3)* in the Y-cut crystal with the addition of an in-plane shear component. The third smallest mode at 220.5 kHz, labeled *7)*, is characterized by an oscillatory displacement of the vertexes of the crystal in a way similar to mode *2)* in the Y-cut LNO piezocrystal.

When a bias field of H = 25 Oe was applied in the Y direction instead of X (α_{E32} mode) we obtained the results indicated in Figure 5.4 *b)*. The observed peaks are in general associated with a drop in amplitude in relation to α_{E31} which proves that the ME effects under resonance conditions

are also strongly affected by the direction of the applied bias field. The most noticeable change here is the large decrease in amplitude or even disappearance of some of the resonant modes observed in the previous measurement. This is the case of the modes labelled as *5)*, *7)* and *1)*. In order to explain this we note that these modes are mainly characterized by large elastic displacements in the X direction of the crystals as shown in Figure 5.4 *c)*. Since the Metglas layer tends to expand mainly in the direction of the applied bias field we thus conclude that a magnetic field applied in the Y direction will induce only a small straining of this layer in the X direction. This will thus constrain the capacity of the thin Metglas foil to excite the corresponding EM modes of the PE phases. Additionally we note that the modes labelled as *3)*, *6)* and *8)*, which are characterized by large displacements in the Y direction tend to be less affected by the change in the direction of the applied bias. Nevertheless the reason for the decrease observed in the amplitude of the mode *4)* is not very clear. Furthermore we see that the phase of all of the ME signals still drops by ca. 180º during resonance but now we notice that outside of resonance conditions the phase of the ME effects for the GPO and Y-cut LNO samples is reversed just like in the quasi-static case. Therefore the imaginary part of the ME coefficients have peaks with positive values in resonance. This kind of behavior has also been recently observed e.g. in [191].

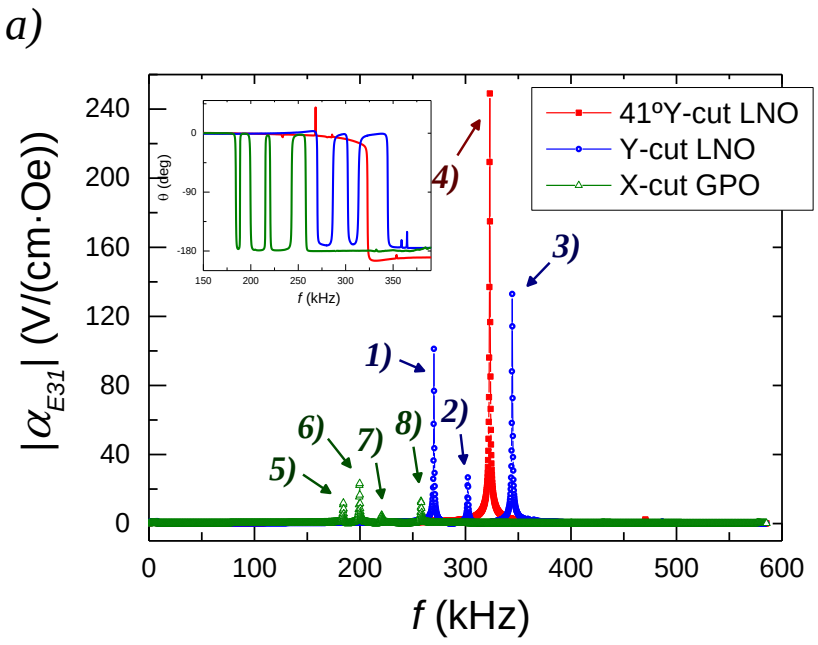

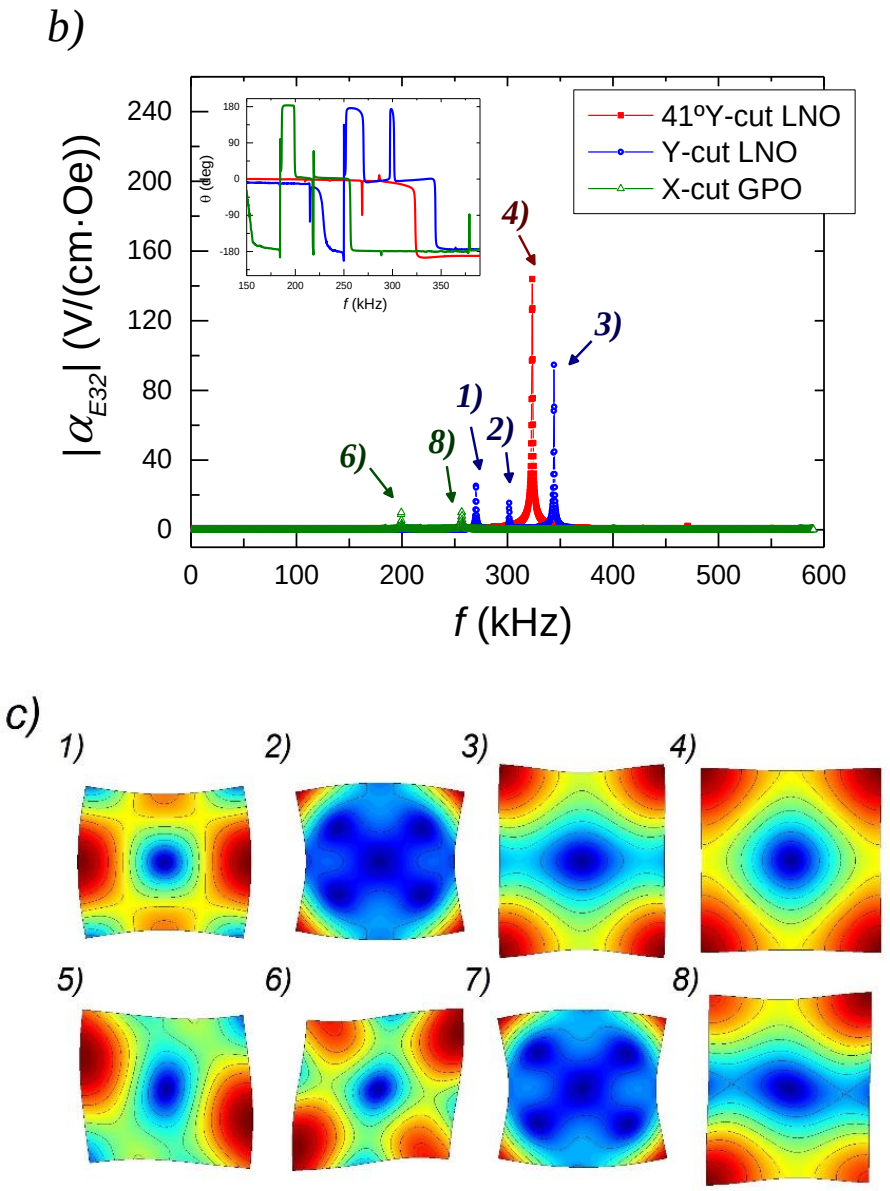

Figure 5.4 *a)* α_{E31} and *b)* α_{E32} direct dynamic ME effect measured in tri-layered composites consisting of Metglas and LNO and GPO as a function of the modulation frequency with H = 25 Oe and δH = 0.1 Oe. The various resonant peaks seen here are labeled *1)–8).* The insets in each graph shows the variation of the phase of the ME voltage coefficients (in degrees) as a function of the frequency. *c)* Spatial distribution of the in-plane relative displacement field and deformation associated with each type of contour EM resonance mode. Here, redder regions correspond to larger relative displacement amplitudes. The deformation of the crystals are largely exaggerated for the sake of clarity.

From a theoretical point of view, considering only the linear elastic properties of the PE crystals and solving their eigenvalue equations of motion under traction-free boundary conditions, several resonance modes in addition to the ones observed in the measurements can be predicted. We therefore conclude that the pattern and natural frequency of these normal modes are mainly determined by the elastic coefficients of the crystals as well as their mass density and geometry. The excitation or not of some of these modes in the ME measurements, under specific mechanical and electrical boundary conditions, is then driven by the PE effect and thus depends on its anisotropic coefficients. While strong ME effects were observed for the extensional EM resonance modes in the samples with LNO, much weaker effects were seen for the asymmetrical shear modes in the one with GPO. These shear modes arise primarily because of non-null stiffness coefficients c_{16}^{E} in the X-cut crystal which couple in-plane normal and shear type stresses and strains. Having seen this, we note that extensional normal modes, similar to the ones identified in the LNO crystals, as well as more symmetrical shear modes can also be solutions of the equations of motion in crystals of GPO e.g. with a Z- or Y-cut, since here we have $c_{16}^{E} = c_{26}^{E} = 0$. Nevertheless, the form of its corresponding PE tensors in principle doesn't permit the ME excitation of the extensional modes in L-T tri-layered composites, since in these cases we have both null d_{31} and d_{32} components. In conclusion, we see that even though a large ME effect may be predicted for a given anisotropic composite under quasi-static conditions, under resonant conditions the picture changes radically. Thus, in this case, a more sophisticated investigation must be carried out taking into account further parameters such as the relation between the crystal orientation and the geometry of the composite.

In summary, in this experimental part we investigated the relation between the cut orientation of the piezocrystals and respective in-plane anisotropic ME response of the corresponding tri-layered composites. By precisely selecting this cut direction, systems with different relations between perpendicular α_{E31} and α_{E32} ME coefficients could be designed, thus finding applications in specific orientation-sensitive devices. A composite with a Y-cut LNO crystal, for example, was shown to operate closely to the anisotropic unipolar regime ($\alpha_{E31} > 0$ and $\alpha_{E32} = 0$), and one with a 41ºY-cut LNO crystal closely to the in-plane isotropic regime ($\alpha_{E31} = \alpha_{E32}$). Figure 5.5 *a)* further illustrates the results of calculated quasi-static α_{E31} and α_{E32} coefficients as a function of the LNO crystal cut angle in the *YZ* plane in relation to the *Y* axis, i.e. the θ angle in the standard notation (*YXl*) θ or $\theta = 90^{o} + \beta$ in the Euler angles scheme. According to the calculations, the anisotropic unipolar regime and the in-plane isotropic regime should be observed for LNO crystals with cut angles of 2ºY and 45ºY, respectively. From this point of view, other cuts could also be interesting, such as the 162.1ºY-cut LNO, corresponding to an anisotropic bipolar regime ($\alpha_{E31} = -\alpha_{E32}$), and the 129ºY-cut LNO, corresponding to the maximum expected ME voltage coefficient as seen in Figure 5.5 *a)*. Also, Figure 5.5 *b)* depicts the calculated ME voltage coefficients as a function of the relative thickness ratio

between the PE and MS phases using the same formalism. This calculation was made for some of the most interesting LNO crystal cuts. From this we see that a decrease in the thickness of the PE layer results in more stress being transferred to it from the MS and, consequently, in an increase of the ME effect. However, since the detected voltage is proportional to the PE layer thickness, the thinner the layer is, the lower the output signal will be. Therefore, taking into account that any measuring circuit has its own input noise, the maximal signal-to-noise ratio should be observed for a finite ferroelectric film thickness.

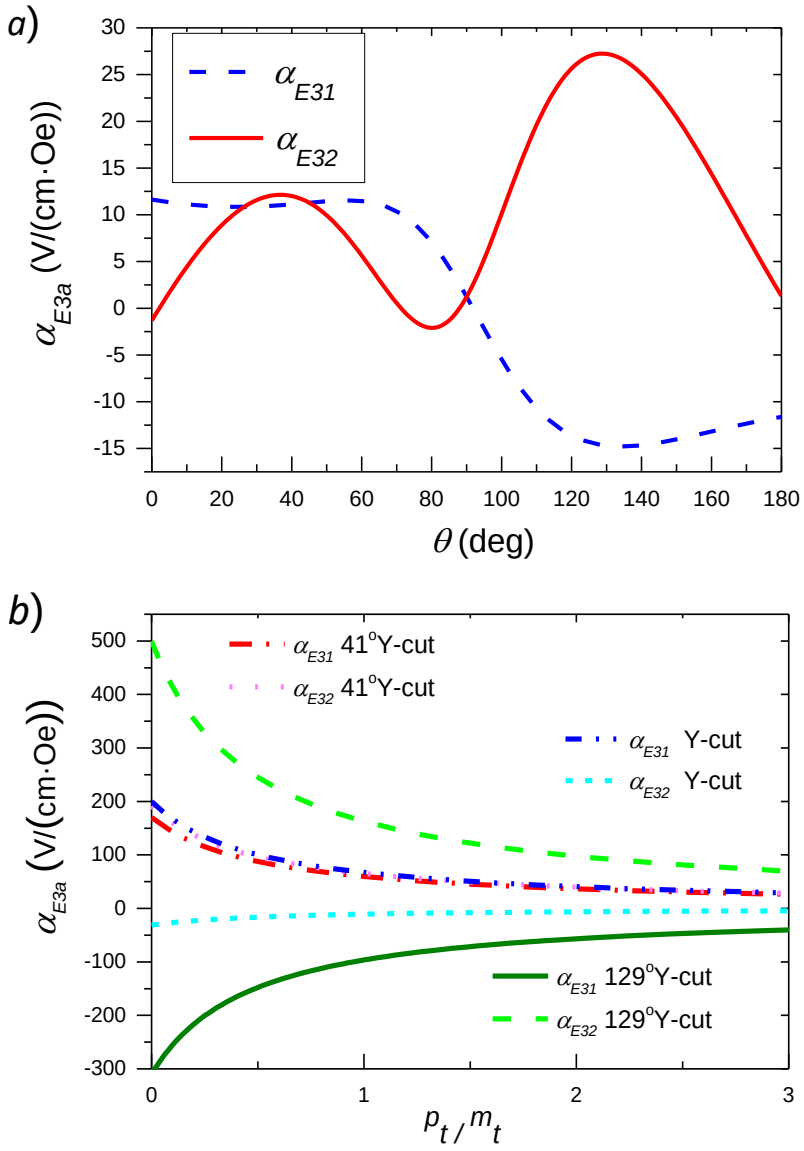

Figure 5.5 *a*) Calculated in-plane quasi-static ME voltage coefficients as a function of the θ piezocrystal cut angle (measured from the Y axis). *b*) ME coefficients for different crystal cuts as a function of the PE/MS relative thickness ratio ($^{p}t/^{m}t$).

5.5. Conclusions

In conclusion, we have conducted a numerical analysis and an experimental study of the ME and EM anisotropic properties of tri-layered composites of Metglas/Piezoelectric/Metglas using differently oriented piezoelectric single crystals of $LiNbO_3$ and $GaPO_4$. The samples consisted of Y- and 41ºY-cut LNO and X-cut GPO substrates bound to Metglas foils using epoxy.

The quasi-static ME measurements have shown a strongly anisotropic response with transversal ME voltage coefficients being dependent on the direction of the applied in-plane magnetic bias field as well as the orientation of the crystal (crystal cut). This is related to the piezoelectric, dielectric and elastic properties of single crystals being extremely anisotropic. As confirmed by some theoretical calculations, this ME behavior was qualitatively correctly predicted by a simple constitutive model, in which the material tensor properties of the piezocrystals were transformed according to their physical orientation. Therefore, we saw that the tri-layered composite with the 41ºY-cut LNO crystal exhibited an almost isotropic in-plane ME response, with $\alpha_{E31} \approx \alpha_{E32}$, whereas the systems with the Y-cut LNO and X-cut GPO substrates demonstrated an approximately in-plane unipolar effect ($\alpha_{E31} > 0$ and $\alpha_{E32} \approx 0$) with the polar axis directed along the X direction. Also, the largest measured ME coefficient here was of 0.95 V/(cm·Oe) for the Y-cut LNO sample in a field of 25 Oe. In the GPO composite, a coupling of up to 0.24 V/(cm·Oe) was obtained.

In the resonant regime, several in-plane contour EM resonant peaks were observed in the ME spectrum. Here we saw how strongly the anisotropic nature of the PE crystals influences the excitation of certain contour acoustic resonance modes. So, e.g., three distinct resonance modes were observed in the system featuring the Y-cut LNO crystal, whereas a single one was observed in the composite with the 41ºY-cut LNO one. A very intense single peak exhibiting a ME coefficient of up to 249 V/(cm·Oe) was detected in the sample with the 41ºY-cut LNO crystal. In order to predict, which kinds of modes could be excited under given conditions and to identify such modes by comparison with simulated results, we employed impedance measurements, thus clarifying the relation between the anisotropic constants and the excitation of such peaks. The aforementioned large symmetric peak was therefore shown to be related to the in-plane isotropic properties of the crystal, so that a very symmetric and high-amplitude resonance mode was generated. In the GPO sample, four weak contour asymmetrical shear modes of resonance were identified, with the largest having a response of up to 23.2 V/(cm·Oe) and appearing at a frequency of 199.7 kHz.

In conclusion, we were able to experimentally identify relatively large anisotropic ME effects in composites based on PE single-crystals which were in good agreement with the theory. In

principle, such ME responses can be further enhanced through the optimization of the volume ratio and the coupling between layers. Finally we showed how the control of the crystal orientation can be used to greatly enhance the anisotropic ME effects in composites. The selection of the crystal orientation should therefore allow one to engineer almost any desired anisotropic properties for some given application.

Chapter 6

6. Equivalent magnetic noise in bi-laminates comprising bidomain $LiNbO_3$ crystals for application as magnetic vector sensors

Abstract

In this chapter, the anisotropic direct magnetoelectric (ME) properties of bi-layered composites comprising magnetostrictive Metglas foils and single-crystalline piezoelectric bidomain plates of 127ºY-cut $LiNbO_3$ (LNO) are studied both theoretically and experimentally. The LNO plates possessed an engineered bidomain structure with opposite spontaneous polarization vectors along the thickness direction (i.e. a "head-to-head" or "tail-to-tail" ferroelectric macrodomain structure). Impedance, ME effect and equivalent magnetic noise density measurements have been performed on the composites operating under quasi-static and resonant conditions. The investigated systems also included single-domain and simple bonded bimorph crystals for comparison. Whereas the anisotropic quasi-static ME effect was found to be only two times stronger in the bidomain samples than in their bimorph and unidomain counterparts, in the bending resonance mode the effect in the bidomain structures was up to one order of magnitude stronger: ME coefficients of up to 578 V/(cm·Oe) were obtained at ca. 30 kHz at the bending resonance using 0.5 mm thick piezoelectric crystals. Equivalent magnetic noise density measurements yielded values down to 153 $pT/Hz^{1/2}$ at 1 kHz (quasi-static mode) and 524 $fT/Hz^{1/2}$ under resonant conditions. A further optimization of the fabrication techniques, laminate geometry and detection circuit is expected to allow reducing these values down to at least 10 $pT/Hz^{1/2}$ and 250 $fT/Hz^{1/2}$, respectively, and the resonance frequency by at least two orders of magnitude. Such systems may thus find use in simple and sensitive, passive and stable, low-frequency and high-temperature vector magnetic field sensors. applications.

6.1. Introduction

Sensitive low-frequency magnetic field variation sensors have recently been largely sought after for applications ranging from biomagnetic to magnetic anomaly detectors [59, 192]. The usefulness of magnetic sensors is determined not only by their output gain but also by their equivalent magnetic noise, both of which are crucial to achieve a high sensitivity and responsivity [59]. Thanks to their large magnetic-to-electric conversion factors, laminate ME composites have been singled out as natural contenders for these applications [59, 192, 193]. Comparatively to other magnetic sensors, a compact size and passive operation at room temperature are additional features that these systems have to offer.

The ME effect is defined as a coupling between electric and magnetic fields in material systems in such a way that an electric polarization (P) might be induced by an applied magnetic field (H), in which case it is denoted the direct effect, or a magnetization (M) induced by an applied electric field (E), denoted the converse effect [8]. Intense efforts have been devoted to the study of the ME effect in systems ranging from the single-phase to the multi-phase and from the bulk to the nano-sized, driven by many promising new applications in multifunctional devices [6, 8, 9, 11, 36]. Up to date, by far the largest ME effects have been obtained in the composite systems where such a phenomenon results from an elastic coupling between mechanically bonded piezoelectric (PE) and magnetostrictive (MS) phases [6, 8]. In this group the most commonly studied structures have been the simple 2-2 type laminates [6, 9, 36]. As the figure of merit, the direct ME voltage coefficient $\alpha_{\mathrm{E}ij} = \delta V_i/(\delta H_j \cdot t_p)$ measured under open circuit conditions has been generally employed. Here, δV_i and δH_j are the dynamic output voltage and input magnetic field amplitudes in the i and j directions, respectively, and t_p is the thickness of the PE phase [6, 9, 36]. As for the operation mode, longitudinally magnetized and transversely polarized (L-T) laminates have been shown to exhibit the largest effects due to small demagnetization fields and a large transfer of stress [6, 7]. ME responses of the order of tens of V/(cm·Oe) have already been observed under quasi-static conditions [61, 194]. Even stronger effects of the order of a few kV/(cm·Oe) have also been obtained under electromechanical resonance (EMR) conditions of the PE plates when the amplitude of the vibrations is largely enhanced [62, 109, 110].

From a practical point of view, the sensitivity of a ME sensor to a minute magnetic field is determined by its conversion factor and by its intrinsic and extrinsic noise floor. The former kind of noise is mainly composed by the Johnson noise and the $1/f$ noise in the composite and by the detection circuit and is determined by material properties such as conductivity and dielectric losses

and the physical structure of the composite [59]. The extrinsic noise, on the other hand, is dominated by the thermal noise, introduced by pyroelectric currents due to small fluctuations of the temperature, and the vibrational noise, introduced by the PE effect due to stray vibrations in the environment [193, 195]. Various strategies have been proposed to mitigate these effects through the optimization of the laminate design and detection circuitry [59, 193]. Currently, the lowest equivalent magnetic noise density values for ME sensors reported in the literature are of the order of a few $pT/Hz^{1/2}$ for frequencies of operation as low as 1 Hz [61, 196-198] and of the order of some tens of $fT/Hz^{1/2}$ under EMR conditions in the kHz range [58, 192, 199]. The frequency of operation has also been made as small as 10 mHz [200]. These values are very respectable when compared to the ones of other well-known magnetic sensors including giant magnetoresistance, flux-gate and superconducting quantum interference based devices which have noise floors of the order of 10^5 $fT/Hz^{1/2}$, 10^3 $fT/Hz^{1/2}$ and 10 $fT/Hz^{1/2}$, respectively, for frequencies between 1 Hz and 1 kHz [192, 198, 201].

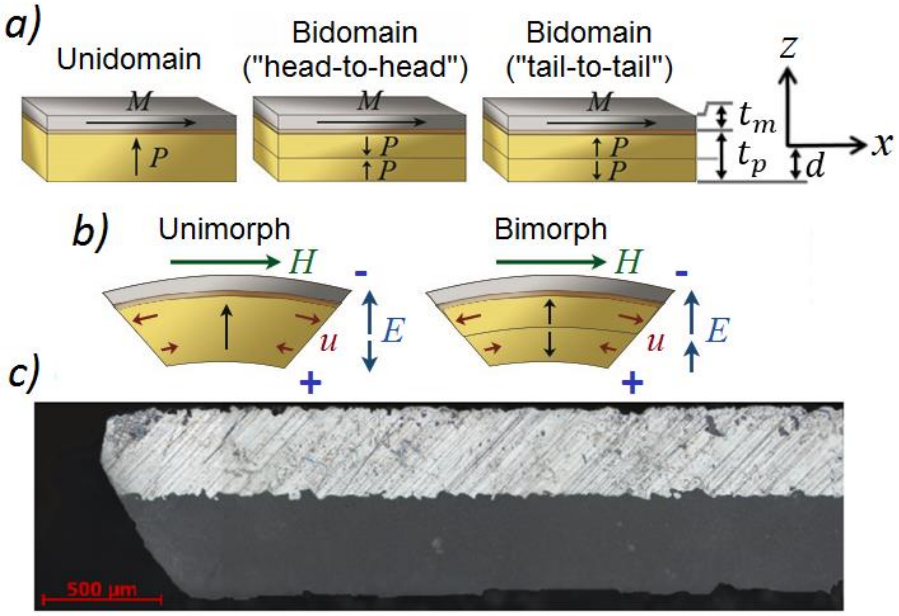

Figure 6.1 *a)* Representation of the various types of bi-layered bending L-T composites studied in this work and the frame of reference. *b)* Operation principle of a ME bimorph under a bending deformation produced by an applied magnetic field. *c)* Optical micrograph of the "head-to-head" bidomain structure in a selectively etched lap of a 127ºY-cut single crystal of LNO obtained by the DA technique.

Unlike the most commonly employed symmetric tri-layered structures, bi-layered bimorph or unimoph configurations with asymmetrical structures are able to produce bending resonant modes

at low frequencies [202]. The bimorphs, having oppositely poled layers (see Figure 6.1 *a)*), tend to generate larger ME effects under a flexural strain as illustrated in Figure 6.1 *b)* [203]. Furthermore, by rejecting deformations confined to the extensional mode, such structures also have an intrinsic ability to partially cancel both extrinsic vibrational and thermal noises [192, 193]. In practice, PE bimorphs are usually obtained by gluing or sintering together oppositely poled lead-based PE plates such as PZT or PMN-PT characterized by large PE and dielectric constants [202]. However, along with the mechanical losses associated with the bonded interfaces and their disruption after repeated straining, these structures are known to suffer from several intrinsic drawbacks which include low Curie temperatures (ca. 100ºC), large creep and ageing effects, hysteretic behavior and high commercial price. Nevertheless, since the ME voltage effect is known to be approximately proportional to the ratio between the PE and dielectric constants, lead-free single-crystalline ferroelectrics, poled and cut along desirable crystallographic directions, have already been shown to exhibit comparable ME effects in composites along with a much more stable performance [135, 137]. Recently we have shown that large ME effects could be obtained in composites containing $LiNbO_3$ (LNO) single crystals [128, 134]. LNO is an uniaxial trigonal ferroelectric (point group *3m*) with a very linear PE behavior and a high Curie temperature of ca. 1210ºC [70]. In the single-crystal form, it also exhibits particularly small dielectric losses and multiple fundamental anisotropic EMR modes [191] with high quality factors [59]. In addition, single-crystalline $LiNbO_3$ and $LiTaO_3$ bidomains with strong linear bending deformations have recently been developed for applications in precision electromechanical actuators [204]. These bidomains consist of plates having two engineered ferroelectric macrodomains with inverted spontaneous polarization vectors along the thickness direction like in the case of a bimorph. This has been achieved using a stationary external heating (SEH) and, more recently, a diffusion annealing (DA) technique. The main advantage of these structures is a more efficient PE and elastic coupling between inverted domains than in the case of a bonded or sintered bimorph due to the absence of an intermediate viscous glue or diffusion interface between macrocrystals.

In present work we propose the use of bidomain LNO single crystals produced by SEH and DA in bi-layered ME composites for applications in vector magnetic field and current sensors, and we study the ME properties of the respective laminate structures. As the MS phase we chose a Fe–Ni-based amorphous Metglas alloy with very large relative magnetic permeability ($\mu_r > 10^4$) and piezomagnetic coefficients and a low saturation field [82, 86]. ME sensors are generally used in conjunction with voltage or charge amplifier schemes [58, 60, 62]. We note that the use of LNO crystals, in principle, will only be attractive in the former case because the latter is strongly favored by PEs with larger PE coefficients, irrespective of their dielectric constants (i.e. larger short-circuit charge ME coefficients in composites), such as PZT or PMN-PT [60, 197, 205]. We believe that such

LNO-based ME bimorphs potentially offer a sensitive, passive, low-frequency and high-temperature operation.

6.2. Theoretical calculations

In order to predict and better understand the behavior of bi-layered composites, as depicted in Figure 6.1 *a)*, we used a low-frequency model based on the linear theory of piezoelectricity, magnetostriction and elastodynamics of thin plates [67, 124, 141, 206-212]. The composites were assumed to vibrate freely and to be formed by flat plates of PE and MS phases connected by means of epoxy and electroded on their top and bottom faces. The plates are also assumed to be perfectly bonded without any sliding interfaces, cracks or imperfections (i.e. the displacement fields are continuous across interfaces). Figure 6.1 *a)* shows the laminate frame of reference used in the calculations. The dimensions of the composites are length (l) × width (w) × thickness (t), such that $l = w$ and $l \gg t$. Here, d represents the position of the neutral plane where the z axis is centered, t_{p-} and t_{p+} are the thickness of the bottom and top domains of the PE plate, respectively, t_{p0} the thickness of the non-PE polydomain region between the domains, t_e the thickness of the epoxy layer, and t_m that of the MS phase. The total thickness of the structure is then $t = t_m + t_p$, where $t_p = t_{p-} + t_{p0} + t_{p+} + t_e$ is the thickness of the PE plus epoxy layer. Starting from thermodynamic considerations, the constitutive equations for the PE phase, using the Einstein summation convention (with i, j, k and l ranging over the integers 1, 2 and 3), are given by [67, 208]:

$$S_{ij} = s^E_{ijkl} T_{kl} + d_{kij} E_k \; ; \tag{6.1}$$

$$D_i = d_{ikl} T_{kl} + \varepsilon^T_{ik} E_k \; , \tag{6.2}$$

where the upper case letters represent the material fields, with S_{ij} being the elastic strain tensor given by $S_{ij} = (1/2) \cdot \left(u_{i,j} + u_{j,i}\right)$, where u_i is the displacement vector, T_{kl} is the elastic stress tensor, D_i the electric displacement vector and E_k is the electric field vector equal to $E_k = -\phi_{,k}$, with ϕ being the electric potential. The lower case letters represent the material constant tensors, with s^E_{ijkl} being the elastic compliance (given in units of 10^{-12} m^2/N), d_{kij} the PE strain coefficient (given in units of pC/N), and ε^T_{ik} the dielectric permittivity (given in terms of relative permeability $\varepsilon^T_{ik}/\varepsilon_0$). The values of the material constants for LNO where obtained from the literature [70]. Equations (6.1, 6.2) apply

to a PE poled in the *z* direction. For the case of the polarization pointing in a reverse direction, the constants are transformed by an inversion matrix, thus leading merely to a change of sign of the PE coefficients $d_{kij} \rightarrow -d_{kij}$. In the non-PE polydomain layer the elastic and dielectric constants are assumed to be preserved, while the PE coefficients are null. For the isotropic epoxy layer, without taking into account the effect of viscosity, we consider the constants: $\varepsilon_{33}^{T}/\varepsilon_0 \approx 2.5\ldots6.0$, $d_{kij} = 0$, $s_{11}^{E} \approx (274\ldots310)\times10^{-12}$ m^2/N, $s_{12}^{E} \approx (-72\ldots-131)\times10^{-12}$ m^2/N and $\rho = 1.164$ g/cm^3 [213].

The constitutive equations for the MS phase may equivalently be given by [124, 141, 209-212]:

$$S_{ij} = s_{ijkl}^{H} T_{kl} + q_{kij} H_k \, ; \tag{6.3}$$

$$B_i = q_{ikl} T_{kl} + \mu_{ik}^{T} H_k \, , \tag{6.4}$$

where H_k is the magnetic field strength, B_i is the magnetic induction, q_{kij} is the piezomagnetic coefficient (given in units of ppm/Oe), and μ_{ik}^{T} is the magnetic permeability. In this equations we assumed a linear pseudo-piezomagnetic approximation parametrized by a bias field (H_0) dependent constant q_{kij}, which is only valid for small variations of the magnetic field H_k around this bias field value. In a traction-free Metglas layer the slope of the magnetostriction curve has a maximum of ca. 4 ppm/Oe for a bias field of ca. 10 Oe, which was therefore taken as our q_{11} coefficient [86]. The remaining constants of this isotropic alloy are $q_{12} = -1.7$ ppm/Oe, $s_{11}^{H} = 10\times10^{-12}$ m^2/N, $s_{12}^{H} = -3.3\times10^{-12}$ m^2/N, and $\rho = 7.9$ g/cm^3 [86, 142, 214]. For simplicity we assume here that the highly conductive MS plate is in electrostatic and magnetostatic equilibrium, so that the electric E_i and displacement D_i fields are null and the magnetic field strength H_i is constant inside it. Thus, the MS plate functions as the top equipotential electrode of the system. The thickness of the plate is also assumed to be small enough, so that the demagnetization effect may be disregarded for magnetic fields H_a applied in the in-plane a direction.

In sufficiently thin plates under null stress loads it is suitable to assume the conditions $T_{31} = T_{32} = T_{33} = 0$ everywhere [67, 206-208]. For fully electroded top and bottom equipotential surfaces, appropriate electrical conditions are $E_1 = E_2 = 0$ [67, 208]. Taking this into account, the constitutive equations for PE plates can therefore be written, using Voigt's notation [208], in a more convenient form:

$$T_m = \overline{c_{mn}^D} S_n - \overline{h_{3m}} D_3 \; ; \tag{6.5}$$

$$E_3 = -\overline{h_{3n}} S_n + \overline{\beta_{33}^S} D_3 \; , \tag{6.6}$$

where m and n range over the integers 1, 2 and 6, and $\overline{c_{mn}^D} = \left(s_{mn}^E - \frac{d_{3m} d_{3n}}{\varepsilon_{33}^T}\right)^{-1}$ with the superscript -1 indicating the inverse of the rank-3 matrix, $\overline{h_{3m}} = \overline{c_{mn}^D} \frac{d_{3n}}{\varepsilon_{33}^T}$ and $\overline{\beta_{33}^S} = \frac{1}{\varepsilon_{33}^T}\left(1 + \overline{h_{3m}} d_{3m}\right)$. For the MS plates from equation (6.3) one has:

$$T_m = \overline{c_{mn}^H} S_n - \overline{q_{am}} H_a \; , \tag{6.7}$$

where $\overline{c_{mn}^H} = (s_{mn}^H)^{-1}$ and $\overline{q_{am}} = \overline{c_{mn}^H} q_{an}$.

According to the Kirchhoff-Love theory for thin flat plates, for small non-shear deformations the displacement fields may be in the first approximation written as linear continuous functions of the *z* coordinate in the form [206, 207]:

$$u_a = u_a^0 - z w_{,a}^0 \; ; \tag{6.8}$$

$$u_3 = w^0 \; , \tag{6.9}$$

where the indexes a and b range over the in-plane 1 and 2 directions. Also, u_a^0 and w^0 are fields which depend only on the in-plane coordinates *x* and *y*. Consequently, the only non-zero strains are the in-plane components $S_{ab} = S_{ab}^{0\,ext} - z S_{ab}^{0\,flex} = (1/2)\left(u_{a,b}^0 + u_{b,a}^0\right) - z w_{,ab}^0$, where $S_{ab}^{0\,ext}$ and $S_{ab}^{0\,flex}$ represent the extensional and flexural strains, respectively. From the balance laws, the dynamical equations of motion for plates then follow [206, 207]:

$$N_{ab,b} = J_1 \ddot{u}_a^0 - J_2 \ddot{w}_{,a}^0 \; ; \tag{6.10}$$

$$M_{ab,ab} = J_1 \ddot{w}^0 + J_2 \ddot{u}_{a,a}^0 - J_3 \ddot{w}_{,aa}^0 \; , \tag{6.11}$$

where $N_{ab} = \int_{-d}^{t-d} T_{ab}\, dz$ is the resultant force, $M_{ab} = \int_{-d}^{t-d} zT_{ab} dz$ is the resultant moment in any vertical section of the plate, and $J_i = \int_{-d}^{t-d} z^{i-1}\rho dz = \langle z^{i-1}\rho \rangle t$ are the averaged densities across the thickness of the composite. In order for the solutions of equations (6.10, 6.11) to be unique, boundary conditions must be imposed on the side surfaces of the plate. For the case of a traction-free composite these are [206, 207]:

$$n_a N_{ab} = 0\ ; \tag{6.12}$$

$$n_a M_{ab} = 0\ ; \tag{6.13}$$

$$n_a M_{ab,b} = 0\ , \tag{6.14}$$

where n_α are unitary vectors normal to the side surfaces. The position of the neutral plane d is generally equated using the equilibrium conditions for the resultant force and resultant moment, $N_m = 0$ and $M_m = 0$, respectively, when the plate is in zero applied D_3 and H_a fields and the solutions $S_n^{0\,ext}$ and $S_n^{0\,flex}$ are non-trivial [209, 215]. To simplify equations (6.10, 6.11), we use a harmonic approximation, where all the fields are assumed to have a harmonic time dependence of the type $u_a = u_a e^{j\omega t}$, where the phasor amplitude u_a may take complex values. The time derivatives $\ddot{u}_a$ thus transform into $-\omega^2 u_a e^{j\omega t}$.

The constant voltage amplitude developed between the bottom and top electrodes of the system, assuming that D_3 does not depend on z and thus is continuous across the PE and epoxy layers, may then be written, taking into account the constitutive equation (6.6) and the displacement fields (6.8) and (6.9), as:

$$V_3 = \int_{-d}^{t_p-d} E_3 dz = -\langle \overline{h_{3n}} \rangle_p t_p S_n^{0\,ext} + \langle z\overline{h_{3n}} \rangle_p t_p S_n^{0\,flex} + \langle \overline{\beta_{33}^S} \rangle_p t_p D_3\ , \tag{6.15}$$

where the symbol $\langle\,\rangle_p$ indicates an averaging across the thickness of the non-conductive layers ($-d < z < t_p - d$) and $\langle\,\rangle_m$ - an averaging across the conductive MS layers ($t_p - d < z < t_m + t_p - d$). Solving this equation together with (6.10, 6.11) and taking into account the fields (6.5-6.9) allows one to obtain the spatial displacements / strains and D_3 written as a linear function of the V_3 and H_α constants. The current flowing through the composite in the z direction is then $I_3 = j\omega \int_0^w \int_0^l D_3 dx\, dy$, thus giving a linear relationship between the three important constants V_3, I_3 and

H_a. Noting that the electrical impedance of the system in the absence of a magnetic field (H_a = 0) is given by $Z = V_3/I_3$ and the ME voltage coefficient under open-circuit conditions (I_3 = 0) is $\alpha_{E3a} = V_3/(H_a \cdot t_p)$, this relationship may then be cast into the form $V_3 = ZI_3 + (\alpha_{E3a} t_p) H_a$, which completely describes the macroscopic electric and magnetic behavior of the composite.

Since our LNO single crystals are highly anisotropic, their PE properties are strongly dependent on their crystallographic orientation (i.e. cut angle). Therefore, the optimization of this orientation as well as of other geometrical parameters may lead to greatly enhanced ME coefficients in composites. In order to estimate the maximum expected magnitude of the ME voltage coefficient for a series of bi-layered plates of Metglas / LNO, an averaging quasi-static model (i.e. at frequencies well below any EMR mode) is used. To the first order, all material fields (T_m, S_n, E_3, D_3 and H_a) are replaced by homogeneous surface-averaged fields in each layer, so that the dependences of the in-plane *x* and *y* coordinates are eliminated. We also neglect the infinitesimal radial frequency ω^2 terms. Consequently, equations (6.10, 6.11, 6.14) are immediately satisfied. The open-circuit condition is also simplified to I_3 = D_3 = 0. What is left is to solve equations (6.12, 6.13) which, in Voigt's notation, transform into $N_m = 0$ and $M_m = 0$. In this case, the resulting ME coefficient and impedance don't depend on the position of the neutral plane d and thus it is convenient to replace this term with $t_p/2$ in the equations via a change of coordinates together with $S_n^{0\,ext}$ being replaced by $S_n^{0\,ext\,\prime} = S_n^{0\,ext} - (t_p/2 - d) S_n^{0\,flex}$. Substituting the stresses given by (6.5) and (6.7) in equations (6.12, 6.13), one then obtains the strain components $S_n^{0\,flex}$ and $S_n^{0\,ext\,\prime}$ written as linear functions of the magnetic field which are subsequently replaced in (6.15) to give the ME coefficient. Finally, we note that the material properties in the crystallographic frame of the PE crystal were transformed into the laminate frame of Figure 6.1 *a)* using a rotation matrix of the type $Z_1X_2Z_3$ described by the Euler angles α, β and γ

The results of the maximum transversal ME coefficient ($|\alpha_{E3a}|$) for a composite with a "tail-to-tail" bidomain crystal with t_{p-} = t_{p+} = $t_p/2$ = 0.25 mm, a Metglas layer with t_m= 29 µm, and without non-PE phases (t_{p0} = t_e = 0), calculated as a function of the crystal orientation, are depicted in Figure 6.2 *a)*.

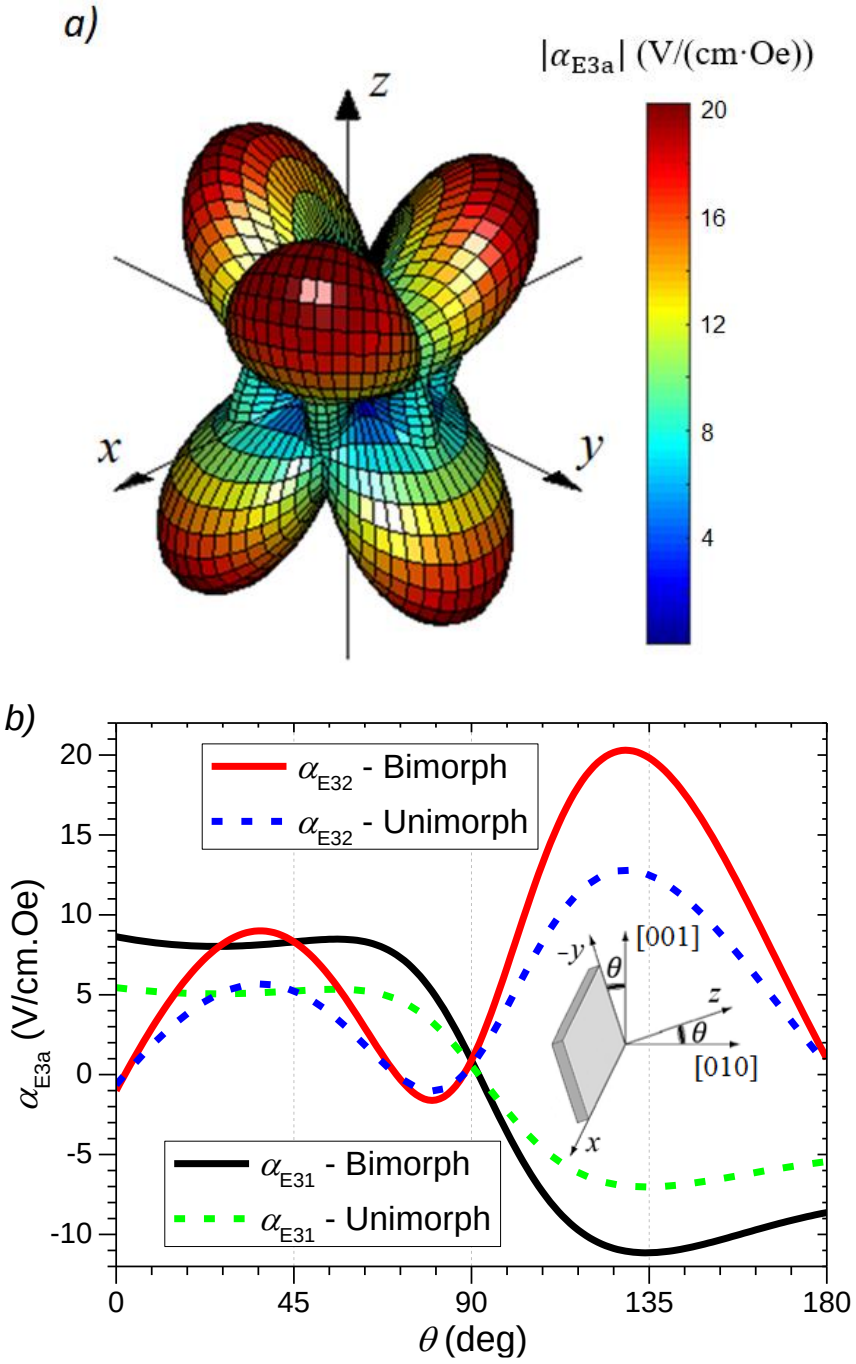
a)
$|\alpha_{E3a}|$ (V/(cm·Oe))
20
16
12
8
4
z
x
y
b)
α_{E32} - Bimorph
α_{E32} - Unimorph
α_{E31} - Bimorph
α_{E31} - Unimorph
α_{E3a} (V/cm.Oe)
θ (deg)
20
15
10
5
0
-5
-10
0
45
90
135
180
-y
[001]
θ
z
θ
[010]
x

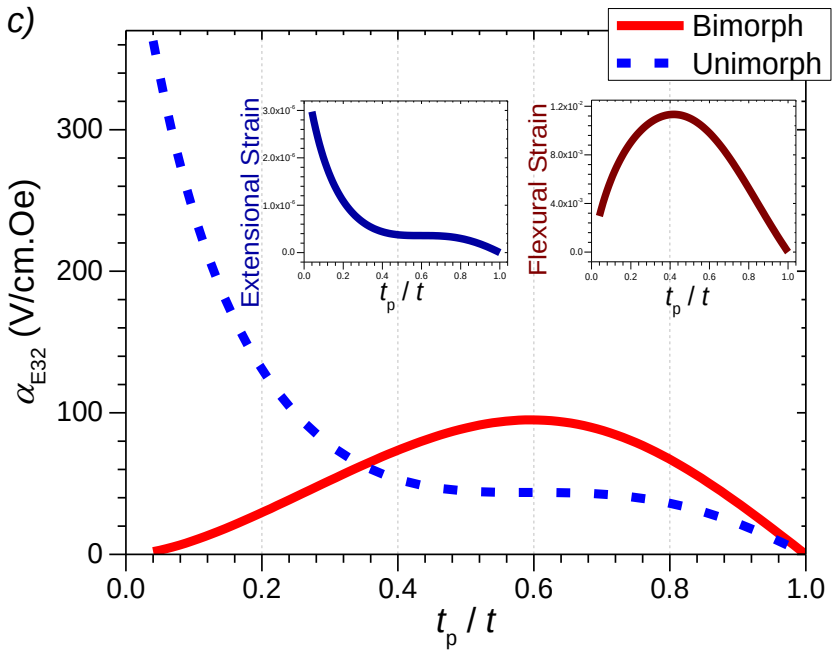

Figure 6.2 *a)* Representation surface of the maximum estimated absolute transversal ME voltage coefficient $|\alpha_{E3a}|$ (across $0 < \gamma < 180^{o}$) as a function of the LNO crystal orientation (α and β angles) for a Metglas/bimorph LNO composite. *b)* Calculated in-plane ME coefficients for composites with unimorph or bimorph LNO crystals as a function of its Y-cut angle θ. *c)* Estimated ME α_{E32} coefficients in systems with 127ºY-cut unimorph and bimorph LNO crystals as a function of the PE thickness ratio t_p/t. The insets show the bending and extensional strains in the *y* direction.

This shows that the ME effect is strongly dependent on the crystal orientation and is maximized for a 129ºY-cut crystal (α = 0º, β = 39º and γ = 90º) and five other cuts equivalent by symmetry. Figure 6.2 *b)* displays the same results for α_{E31} and α_{E32} in the case of bidomain and single-domain (with t_{p-} = 0 and t_{p+} = t_p = 0.5 mm) crystals as a function of the $\theta = 90 + \beta$ cut angle around the *x* axis in relation to the plane parallel to the *y* direction. We see that both ME coefficients are maximized for crystals with approximately 127ºY-cut angle and are, as expected, nearly twice as large in the composite with the bidomain crystal in comparison to the one with the unidomain crystal due to the dominance of the bending strain for this particular PE thickness ratio (t_p/t). The material constants for this important cut are: $\varepsilon_{33}^{T}/\varepsilon_0$ = 49.16, d_{31} = 11.84 pC/N, d_{32} = – 26.70 pC/N, s_{11}^{E} = 5.83×10^{-12} m^2/N, s_{22}^{E} = 6.92×10^{-12} m^2/N, s_{12}^{E} = – 1.74×10^{-12} m^2/N, and ρ = 4.647 g/cm^3 [70]. In addition, we note the existence of several other cuts which may also exhibit interesting relationships between the in-plane α_{E31} and α_{E32} coefficients for various vector-sensitive practical applications.

Figure 6.2 *c)* shows the variation in α_{E32}, for the same bidomain and single-domain systems and a 127°Y-cut crystal, as a function of the thickness ratio of the PE phase t_p/t. The insets of the figure display the *y* directed bending strain ($-S_2^{0\,flex}$) and extensional strain in the midplane of the PE plates ($S_2^{0\,ext\,\prime}$) for an applied H_2 field of 1 Oe. In the bidomain we observe an initial increase in α_{E32} with increasing t_m due to an increase in the bending strain produced by a thicker Metglas layer under the action of the in-plane magnetic field. However, as the thickness of the MS phase approaches that of the PE, the former starts bending less due to a decrease in the constraint produced by the latter which was originally responsible for the bending. Finally, when t_p/t is close to 0, the stress produced by the PE on the MS phase is negligible, and, therefore, the latter is strained in a purely extensional manner, as in the case of a free MS layer under an in-plane magnetic field. Since the voltage developed across the two domains is inverted in the bidomain, this case is associated with a null ME effect whereas a maximum effect is obtained in the single-domain composite. For a certain t_p/t, the thickness ratio of the top PE macrodomain, where the displacement is larger, that maximizes the amplitude of the output voltage in equations (6.15) can be shown to be given by $t_{p+}/t_p = 1/2 - \overline{h_{3n}}S_n^{0\,ext\,\prime}/\overline{h_{3n}}S_n^{0\,flex}t_p$. In this case this optimal thickness ratio takes values between 0.61 and 0.65 for t_p/t between 1 and 0.4. In conclusion, we see that the ME effect in the bidomain composite can be maximized at 95 V/(cm·Oe) for a t_p/t ratio of approximately 0.6, which corresponds to ca. 12 layers of the commercially available 29 μm thick Metglas foil. [139].

Along with the quasi-static case, the study of the ME composites operating under resonance conditions may also provide a useful insight into its behavior. Since, in general, exact analytical solutions to the bi-dimensional equations of motion (6.10, 6.11) are hard to find, we solved them for the special case of traction-free long bars with $l \gg w \gg t$ with the length direction and magnetic field directed along the *x* axis. In this case, it is pertinent for T_{ij} to vanish everywhere except for T_{11} in this direction. Accordingly, the constitutive equations (6.5-6.7), equations of motion (6.10, 6.11) and boundary conditions (6.12-6.14) are reduced to a unidimensional problem (with $m = n = a = b = 1$) [208, 216]. In the case of pure extensional vibrations, we set $u_1 = u_1^0$ in (6.8). Thus, equation (6.10) was solved together with (6.12) and constitutive equations (6.5,6.7) and (6.15) in order to obtain the frequency dependent complex admittance and ME coefficient:

$$Y = j\omega\frac{wl}{t_p\langle\overline{\beta_{33}^S}\rangle_p}\left(1 + t_p\frac{\langle\overline{h_{31}}\rangle_p^2}{\langle\overline{\beta_{33}^S}\rangle_p}\frac{1}{t\langle C_{11}\rangle k\frac{l}{2}\cot\left(k\frac{l}{2}\right)}\right); \tag{6.16}$$

$$\alpha_{E31} = -\frac{t_m\langle\overline{q_{11}}\rangle_m\langle\overline{h_{31}}\rangle_p}{t_p\frac{\langle\overline{h_{31}}\rangle_p^2}{\langle\overline{\beta_{33}^S}\rangle_p} + t\langle C_{11}\rangle k\frac{l}{2}\cot\left(k\frac{l}{2}\right)}, \tag{6.17}$$

where $k = \omega\sqrt{\langle\rho\rangle/\langle C_{11}\rangle}$ is the wave number, and $\langle C_{11}\rangle = \left(\langle\overline{c_{11}^{D}}\rangle_p - \langle\overline{h_{31}}\rangle_p^2/\langle\overline{\beta_{33}^{S}}\rangle_p\right)(t_p/t) + \langle\overline{c_{11}^{H}}\rangle_m(t_m/t)$ is an effective extensional stiffness. These two expressions are valid for the case of a loss-free resonator. Mechanical energy losses may be taken into account through the use of complex elastic constants or a complex frequency $\omega = \omega' - j\omega'' = \omega'\left(1 - j(1/Q)\right)$, where Q is the mechanical quality factor [124, 210, 211, 215]. Dielectric losses ($\varepsilon_{33}^{T''}$) and a non-zero conductivity (σ) of the PE plate can also be introduced through the complex dielectric constant $\varepsilon_{33}^{T} = \varepsilon_{33}^{T'} - j(\varepsilon_{33}^{T''} + \sigma/\omega) = \varepsilon_{33}^{T'}(1 - j\tan(\delta))$, where $\tan(\delta)$ is the loss tangent [190, 217]. For $Q = \infty$ and $\tan(\delta) = 0$, the resonance frequencies are defined as the frequencies at which Y asymptotically approaches $\infty \pm j\infty$ and $\alpha_{\mathrm{E}31}$ tends towards $\left(-t_m\langle\overline{q_{11}}\rangle_m\langle\overline{\beta_{33}^{S}}\rangle_p/t_p\langle\overline{h_{31}}\rangle_p\right)(1 + j0)$ [67, 141]. These frequencies are given by:

$$f_{r_n} = \frac{2n-1}{2l}\sqrt{\frac{\langle C_{11}\rangle}{\langle\rho\rangle}},\ n \in \mathbb{N}\,. \tag{6.18}$$

Likewise the antiresonance frequencies are defined as subsequent frequencies, obtained by setting the denominator of $\alpha_{\mathrm{E}31}$ in equation (6.17) equal to zero, at which the impedance Z tends toward $\infty \pm j\infty$ and $\alpha_{\mathrm{E}31}$ has a critical point tending toward $-\langle\overline{q_{11}}\rangle_m\langle\overline{h_{31}}\rangle_p(\pm\infty - j\infty)$ [67, 141]. At this point the amplitude of the voltage ME effect is thus largely enhanced due to a maximization of the volume averaged strain amplitude across the PE. Equations (6.16, 6.17) show that in the case of a PE bimorph with equally sized domains, since $\langle\overline{h_{31}}\rangle_p = 0$, pure extensional deformations yield no resonant modes in Y and a zero ME effect. In the unimorph, because the amplitude of $\langle\overline{h_{31}}\rangle_p$ is maximized, the resonance frequency in (6.18) is minimized, and the amplitude of the resonant effect is maximized.

As in the previous case, we may also assume pure bending vibrations with $u_1 = -zw_1^0$ in (6.8). Hence, equation (6.11) may be solved together with (6.13,6.14) and constitutive equations (6.5,6.7) and (6.15) in order to yield the admittance and ME coefficient (disregarding the term $J_3\ddot{w}_{,aa}^0$ in (6.11) which is valid for a small enough wave number $k \ll \sqrt{2(J_1/J_3)}$):

$$Y = j\omega\frac{wl}{t_p\langle\overline{\beta_{33}^{S}}\rangle_p}\left(1 + t_p\frac{\langle z\overline{h_{31}}\rangle_p^2}{\langle\overline{\beta_{33}^{S}}\rangle_p}\frac{1}{\frac{1}{2}t^3\langle D_{11}\rangle k\frac{l}{2}\left(\cot\left(k\frac{l}{2}\right)+\coth\left(k\frac{l}{2}\right)\right)}\right); \tag{6.19}$$

$$\alpha_{E31} = -\frac{t_m\langle z\overline{q_{11}}\rangle_m\langle z\overline{h_{31}}\rangle_p}{t_p\frac{\langle z\overline{h_{31}}\rangle_p^2}{\langle\overline{\beta_{33}^S}\rangle_p}+\frac{1}{2}t^3\langle D_{11}\rangle k\frac{l}{2}\left(\cot\left(k\frac{l}{2}\right)+\coth\left(k\frac{l}{2}\right)\right)}, \tag{6.20}$$

where $k = \sqrt{\omega}\left(\langle\rho\rangle/(t^2\langle D_{11}\rangle)\right)^{1/4}$ is the wave number, and $\langle D_{11}\rangle = \left(\langle z^2\overline{c_{11}^D}\rangle_p - \langle z\overline{h_{31}}\rangle_p^2/\langle\overline{\beta_{33}^S}\rangle_p\right)\left(t_p/t^3\right) + \langle z^2\overline{c_{11}^H}\rangle_m(t_m/t^3)$ is an effective flexural stiffness (approximately thickness-independent). The position of the neutral plane is obtained by setting $N_{11} = 0$, with $D_3 = H_1 = 0$, thus giving the expression $d = \sum_{i=1}^{N} {}^i\overline{c_{11}}\left({t_i}^2 + 2t_i\sum_{j=0}^{i-1}t_j\right)/\sum_{i=1}^{N}2\,{}^i\overline{c_{11}}t_i$, where ${}^i\overline{c_{11}}$ and t_i are the effective stiffness and thickness of the i-th material layer, respectively, and N is the total number of layers. When $Q \to \infty$, under resonance conditions Y tends toward $\infty \pm j\infty$ and α_{E31} toward $\left(-t_m\langle z\overline{q_{11}}\rangle_m\langle\overline{\beta_{33}^S}\rangle_p/t_p\langle z\overline{h_{31}}\rangle_p\right)(1 + j0)$. These resonance frequencies can be shown to be given by:

$$f_{r_n} = \frac{2\chi_n^2 t}{\pi l^2}\sqrt{\frac{\langle D_{11}\rangle}{\langle\rho\rangle}},\quad n \in \mathbb{N}, \tag{6.21}$$

where the first n-th χ_n constants are ≈ 2.365, 5.498, 8.639, etc. This expression shows that the bending resonance frequency will be nearly proportional to the thickness of the bar and inversely proportional to the square of its length. Additionally, these resonances are followed by antiresonance modes, obtained by setting the denominator of α_{E31} in equation (6.20) equal to zero, where Z approaches $\infty \pm j\infty$, and α_{E31} has a critical point tending toward $-\langle z\overline{q_{11}}\rangle_m\langle z\overline{h_{31}}\rangle_p(\pm\infty - j\infty)$. Equations (6.19, 6.20) show that in the case of a unimorph with a large PE volume ratio (i.e. with $t_p/t \approx 1$ and thus $d \approx t_p/2$), since $\langle z\overline{h_{31}}\rangle_p = \overline{h_{31}}\left({t_p}^2 - 2dt_p\right) \approx 0$, pure bending deformations yield only weak resonant modes in Y and α_{E31}. Furthermore, the resonance frequency in (6.21) is minimized and the amplitude of the resonant effects are maximized for a PE bimorph with equally sized domains since $\left|\langle z\overline{h_{31}}\rangle_p\right|$ has a local maximum at $t_{p+}/t_p = 1 - d/t_p \approx 1/2$. Another important observation is that the bending resonance frequency may in principle be significantly decreased by using thinner and longer bars as well as a large volume ratio of the Metglas phase because of its comparatively larger density and compliance constants. Equation (6.20) further shows how the ME effect tends to decrease with an increasing thickness ratio of the non-PE phases. For small frequencies, the ME coefficient drops with the thickness ratio of the non-PE polydomain region between PE domains ca. as $1 - (t_{p0}/t_p)^2$ while the frequency of resonance increases slightly. It also

tends to drop very rapidly with the thickness ratio of the epoxy phase t_e/t while the frequency of resonance decreases.

In order to investigate the intrinsic noise characteristics of the aforementioned composite from a theoretical point of view, we consider the equivalent circuit presented in Figure 6.3 *a)*. As described in equation (6.15), the ME laminate can be modelled by its Thévenin equivalent circuit as a magnetically induced voltage source with $\delta V_3 = \left(\alpha_{\mathrm{E}3a} t_p\right)\delta H_a$ in series with its equivalent complex impedance Z [188, 209]. Due to the high-resistance capacitor-like nature of the composite, we may assume that in the frequency range of interest ($10^2 \ldots 10^6$ Hz) the noise is dominated by the thermal Jonhson noise with a current noise spectral density of $i_Z = \sqrt{4k_b T Y'}$ [218, 219]. The Nyquist noise theorem then ascertains that the resultant spectral density of the voltage noise (in units of $\mathrm{V/Hz^{1/2}}$) in the open-circuited output of the ME composite can be given by [219]:

$$e_Z = |Z| i_Z = \sqrt{4k_b T Z'}\,, \tag{6.22}$$

where k_b is the Boltzman constant, T is the temperature, and Z' and Z'' represent the real and imaginary parts of the impedance, respectively.

Sufficiently far away from any EMR frequency we can assume the impedance of the composite to be formed by a capacitor C_p, with the capacitance $C_p = C(1 - j\tan(\delta))$, in parallel with a resistor R_p, with the resistance $R_p = R$, thus taking into account the dielectric loss ($\tan(\delta)$) and *DC* leakage resistance (R). Substituting these parameters in equation (6.22) shows that this circuit behaves as a low-pass filter with a cut-off frequency of $1/2\pi RC\sqrt{1 + \tan(\delta)^2}$ and the output RMS voltage noise ranging between $\sqrt{4k_b T R}$ at very low and $\sqrt{4k_b T \tan(\delta)/(C\tan(\delta)^2 + C)}$ at very high frequencies. Thus, in order to minimize the noise level, one should use laminates with a large capacitance, small loss tangent and large resistance. To include the effects of a single EMR mode, it is common to add an equivalent series RCL circuit composed of a motional resistance (R_m), capacitance (C_m) and inductance (L_m) in parallel with the previous RC circuit [67, 188, 209]. With this, the total noise spectral density of the composite given by (6.22) will additionally have a local maximum at the antiresonance frequency ($f_a = 1/2\pi\sqrt{L_m\left(C_m C/(C_m + C)\right)}$) and a local minimum close to the resonance frequency ($f_r = 1/2\pi\sqrt{L_m C_m}$), the latter being significant only for very small values of R and large values of $\tan(\delta)$.

To take the effects of the detection circuit into account, we assume it to be formed by a generic differential amplifier with a certain gain G associated with a given input impedance (Z_{a1} and Z_{a2}) between each input and the earth and a given current (i_a) and voltage (e_a) input noise spectral densities, as in the equivalent circuit shown in Figure 6.3 *a)*. In this case, the total intrinsic noise spectral density at the output of the detection circuit, with δH_a = 0, is given by the expression:

$$v_n = |G|\sqrt{\left(4k_bTZ'_{eq}\right)^2 + \left(\left|Z_{eq}\right|i_a\right)^2 + e_a^2}\,, \tag{6.23}$$

where Z_{eq} is the equivalent impedance of the circuit equal to $Z\|(Z_{a1}+Z_{a2})$. The equivalent magnetic noise spectral density (given in units of T/Hz$^{1/2}$), generated in this circuit in the absence of a magnetic field, may then be calculated through $v_n/\left(t_p|\alpha_{\mathrm{E}3a}|\right)$. This parameter evaluates the minimum *AC* magnetic field detectable by the sensor and is maximized in structures with a small noise density and a large ME voltage output.

Assuming an ideal detection circuit (i.e. with G = 1, $Z_{a1} = Z_{a2} = \infty$, i_a = 0 and e_a = 0), we can estimate the intrinsic equivalent magnetic noise of a thin bar ME composite using equation (6.22) together with (6.19, 6.20). In this case, for low frequencies, well below any EMR, and for typical values of the material parameters, the equivalent magnetic noise density is approximately given by:

$$\frac{e_Z}{t_p|\alpha_{\mathrm{E}31}|} \approx \sqrt{\frac{4k_bT}{twl}\left(\frac{s_{11}^H}{q_{11}}\right)^2 \frac{\varepsilon_{33}^{T'}}{d_{31}^2}\frac{1}{f}\left(\frac{1}{Q}+\tan(\delta)\left(\frac{s_{11}^E\varepsilon_{33}^{T'}}{s_{11}^E\varepsilon_{33}^{T'}-d_{31}^2}\right)\right)\cdot \mathrm{f}\left(\frac{t_p}{t},\frac{t_{p+}}{t_p},\frac{d_{31}^2}{s_{11}^E\varepsilon_{33}^{T'}},\frac{s_{11}^H}{s_{11}^E}\right)}\,, \tag{6.24}$$

where f( ) is a dimensionless rational function of the thickness ratios between phases and its electrical and elastic constants. This suggests that, in principle, the detection limit of the system can be minimized through the control of its geometry and material parameters by the use of composites with a large volume (twl) and PEs with large PE coefficients and small dielectric constants ($\propto \varepsilon_{33}^{T'}/d_{31}^2$), as well as MS materials with large piezomagnetic and small compliance coefficients. The loss factors ($1/Q$ and $\tan(\delta)$) are responsible for the non-zero real part of the admittance in (6.19), and consequently the intrinsic thermal noise, and should also be small. This theoretical limit can be shown to be minimized when using a volume fraction of the PE LNO phase of ca. 0.65. Under resonant conditions, at a resonance frequency f_{r_n} given by (6.21), the composite behaves somewhat differently, with its equivalent noise density being approximately:

$$\frac{e_Z}{t_p|\alpha_{E31}|} \approx \sqrt{\frac{4k_bT}{twl}\left(\frac{s_{11}^H}{q_{11}}\right)^2 \langle D_{11}\rangle \frac{\chi_n^2}{f_{r_n}}\frac{1}{Q'} \cdot \mathrm{g}\left(\frac{t_p}{t}, \frac{t_{p+}}{t_p}, \frac{d_{31}^2}{s_{11}^E \varepsilon_{33}^{T'}}, \frac{s_{11}^H}{s_{11}^E}, \chi_n^2\right)}, \tag{6.25}$$

where g( ) is a different dimensionless function of the thickness ratios between phases and its electrical and elastic constants, and $1/Q' = 1/Q + \tan(\delta) \cdot \mathrm{h}( )$ is a loss factor with h( ) being another function of the thickness ratios and material constants. For the case of our composites, this function takes values of ca. 0.2 and thus $Q' \approx Q$ and the dielectric losses take a smaller role on the determination of the total energy losses. This expression also differs from the quasi-static case in that the electrical material properties of the PE now have a much smaller influence on the noise and it tends to decrease with increasing resonance frequency given by $(2t/\pi l^2)\sqrt{\langle D_{11}\rangle/\langle\rho\rangle}$. The noise density can furthermore be shown to be minimized for a smaller volume fraction of the PE phase of ca. 0.45. Of note is the fact that this equation, together with equation (6.21), shows that, for a fixed volume ratio between the phases and starting with a reference geometry with length l_0, width w_0 and thickness t_0, geometrically seen the only way to further decrease both the resonance frequency and equivalent magnetic noise is to change the dimensions in such a way that $(t/t_0)^{1/2} < (l/l_0) < (t/t_0)^2(w/w_0)$, mostly by increasing the volume of the composite, while keeping in mind that one should still have $l \gg w \gg t$ in order to preserve the validity of the model.

The relations between various important coefficients at room temperature calculated for a composite thin bar (with l = 10 mm and w = 1 mm) of Metglas (with t_m= 29 μm) and a 127°Y-cut LNO bidomain crystal (with t_p= 0.5 mm and $t_{p-} = t_{p+} = t_p/2$), and introducing typical values of $\tan(\delta)$ = 0.7% and Q = 300, are depicted in Figure 6.3 *b)*. The absolute impedance ($|Z|$) is shown to initially decrease with the frequency as $1/f$ while the thermal noise density (e_Z) and equivalent magnetic noise density (EMND) decrease with $1/\sqrt{f}$. The absolute impedance curve evidences the presence of bending EM resonance and antiresonance modes at frequencies of 30.04 and 31.88 kHz, respectively. The absolute impedance, thermal noise and absolute ME coefficient ($|\alpha_{E32}|$) attain a local maximum of 9.7 MΩ, 400 nV/Hz$^{1/2}$ and 1.6 kV/(cm·Oe), respectively, at the antiresonance frequency. Also, the equivalent magnetic noise evidences a wide minimum, as small as 438 fT/Hz$^{1/2}$, between these two frequencies at 30.20 kHz. This frequency range is thus very interesting from the point of view of magnetic sensors. After this minimum, we see that the magnetic noise level increases with f up to a maximum at 53 kHz, where the ME voltage is minimized and subsequently continues decreasing. Optimizing the volume ratio between phases can also be shown to further decrease the magnetic noise down to 57 pT/Hz$^{1/2}$ at 1 Hz and 73 fT/Hz$^{1/2}$ at resonance. For very low operation

frequency it is also useful to note that, just by decreasing the thickness of the LNO crystal to 0.1 mm and increasing the length and width of the composite to 50 mm and 5 mm, respectively, one may theoretically decrease the resonance frequency by two orders of magnitude down to 263 Hz while maintaining a respectable magnetic noise floor of 481 fT/Hz$^{1/2}$.

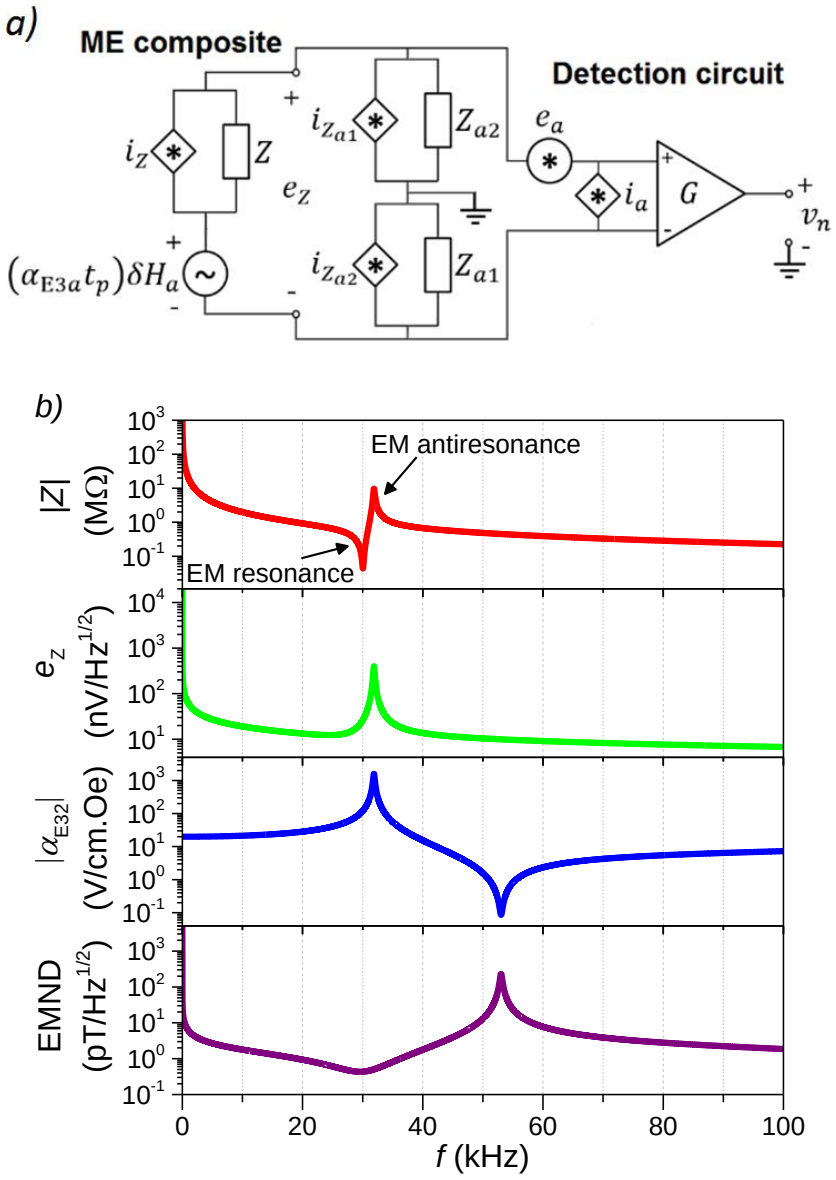

Figure 6.3 *a)* Equivalent circuit of a ME composite and the detection circuit used in the noise analysis. *b)* Calculated frequency dependence of the absolute impedance ($|Z|$), intrinsic thermal noise density (e_Z), absolute ME coefficient ($|\alpha_{E32}|$) and equivalent magnetic noise density (EMND) of a thin-bar composite (with l = 10 mm and w = 1 mm) of Metglas (29 μm thick) and a 127°Y-cut symmetric bidomain LNO crystal (0.5 mm thick).

6.3. Experimental details

A bulk ferroelectric bidomain structure has been formed in commercial (ELAN Company Ltd.) single-crystalline 10×10×0.5 mm^3 plates of congruent 127ºY-cut LNO by SEH and DA methods in the absence of any external electric fields [204]. The structures comprised two equally sized macrodomains with opposite spontaneous polarization vectors and a narrow non-piezoelectric boundary polydomain area in the middle plane. These two methods are recognized for their ability to form macroscopic bidomain structures in plates with large areas (up to 10 cm^2) within relatively small time intervals of less than 3 h and to precisely control the position of the interface between domains through the tuning of specific experimental parameters. In greater detail, the SEH method is based on the creation of a dual-sign temperature gradient distribution throughout the plate thickness, achieved through stationary external light heating in an inert atmosphere of pure nitrogen, required for the controlled formation of two single domains with opposite "head-to-head" polarization vectors [204]. This is based on the fact that projections of the spontaneous polarization vectors will tend to align in the direction opposed to that of the volume temperature gradient following cooling of the sample through its Curie temperature ($T_c \approx 1210$ºC) from the paraelectric to the ferroelectric state [220]. Further experimental details of this method can be found in Ref. [204]. The transition interdomain region produced by this technique in LNO crystals can be visualized by optical microscopy using a technique of selective etching of polished angle laps and by piezoresponse force microscopy having identified irregular shapes with a width between crests of up to 260 μm [221, 222]. The average deformation of this rough region is ca. null under an applied electric field and thus it can be seen as non-PE. In the second, more recently developed technique of DA, appropriate conditions for a directed in- and out-diffusion of Li_2O during high-temperature annealing of the substrates in air near their Curie temperature were created in order to form "tail-to-tail" and "head-to-head" bidomain structures. In this case, one of the domains is gradually reversed from the surface to the bulk in a built-in electric field due to an inhomogeneous distribution of ionized impurities and / or defects that appear during the diffusion process in the single-domain LNO or LTO [203, 223]. Figure 6.1 *c)* shows an optical micrograph of the "head-to-head" bidomain structure obtained in an etched 0.5 mm thick 127ºY-cut LNO crystal produced by DA. The interdomain region here appears to be smoother than in the case of the bidomains fabricated by SEH having a width of only ca. 45 μm.

In order to fabricate the bilayered ME composites, up to 5 layers of commercial 29 μm thick flexible foils of the 2826MB type ($Fe_{0.4–0.5}Ni_{0.4–0.5}Mo_{0.05–0.1}B_{0.01–0.05}$) amorphous Metglas® alloy (Hitachi Metals Europe GmbH) with an area of 10×10 mm^2 were bonded to the top face of single-

domain and bidomain 127ºY-cut LNO crystal plates using an epoxy resin. The structures were subsequently cured at room temperature for 24 h under an applied vertical compressive stress. For comparison, an asymmetric bimorph composite was also obtained by gluing together two oppositely polarized (in a "head-to-head" fashion) 0.25 mm thick 127ºY-cut LNO crystals with epoxy, where one of the crystals was rotated by 180º about its *x* axis (i.e. the [100] crystal direction). To investigate the PE and EM parameters of the crystals, impedance measurements were carried out using a simple I-V circuit in conjunction with a lock-in amplifier (Zurich Instruments®, HF2LI). In order to identify the nature of the EMR modes in the PE plates with a good accuracy, numerical simulations of the impedance spectra were performed by solving equations (6.10-6.15) using a finite element method. To study the ME and noise properties of the composites, measurements of the direct ME effect were performed under quasi-static (@ 1 kHz) and EMR conditions. A dynamic lock-in technique using a home-made setup described elsewhere [128, 224] was employed. Essentially, the samples were placed in the centre of a collinear Helmholtz coil and an electromagnet responsible for the generation of a small amplitude *AC* (δH_a) and a *DC* bias (H) magnetic fields, respectively. The amplitude and phase of the voltage (δV_3) induced across the samples were subsequently measured with the help of the lock-in amplifier, and the ME coefficients were calculated through $\alpha_{E3a} = \delta V_3/(t_p \cdot \delta H_a)$. In order to minimize the effect of the electromotive force appearing in the input due to the Faraday induction in the cables, a shielded balanced line with differential detection was used. The remaining parasitic signal with an amplitude of about 81 mV/(Oe·MHz) and 90º out-of-phase with the applied *AC* field, as measured with a non-ME reference sample, was subtracted from the final results. In the noise measurements, the samples and coils responsible for the generation of the *DC* field were placed inside a home-made Metglas-coated container designed to shield its interior from stray magnetic and electromagnetic fields and external vibrations. The RMS voltage induced between the electrodes of the samples was then measured by the lock-in without an applied *AC* magnetic field.

6.4. Results and discussion

The results of the impedance measurements performed on the 127ºY-cut LNO crystals with a single ferroelectric domain (unidomain), two "head-to-head" domains produced by SEH (bidomain H-H SEH), two "head-to-head" or "tail-to-tail" domains produced by DA (bidomain H-H DA and bidomain H-H DA, respectively) and two LNO crystals glued with epoxy in a "head-to-head" fashion (bimorph H-H) are show in Figure 6.4 *a)*. Some of the most important parameters obtained in this part are summarized in Table 6.1. The values of capacitance (C and dielectric loss tangent $\tan(\delta)$)

of the crystals were determined from the low frequency (f < 1 kHz) part of the spectrum. We note that the obtained capacitance values generally are close to the value predicted by $C = \varepsilon_{33}^T wl/t_p$ = 87 pF. The only exception is the capacitance of 56 pF obtained for the bimorph H-H sample, which is strongly influenced by the intermediate epoxy layer. In fact, using the expression $C = wl/(t_p/\varepsilon_{33}^T + t_e/{}^e\varepsilon_{33}^T)$, where t_e is the thickness and ${}^e\varepsilon_{33}^T$ the dielectric permittivity of the epoxy layer (${}^e\varepsilon_{33}^T/\varepsilon_0 \approx 2.5\ldots6.0$), allows one to estimate the first as $t_e \approx 14\ldots34$ μm. The tan(δ) parameters are about 0.75% in both unidomain and bidomain samples produced by DA and twice as much in the bimorph H-H and bidomain H-H SEH ones, thus demonstrating higher dielectric losses possibly due to a thicker interdomain region of epoxy in the former and a larger conductivity in the latter due to a big amount of intrinsic defects introduced by the SEH technique. Therefore, we conclude that the bidomain crystals produced by DA seem to exhibit more desirable properties in the quasi-static regime.

At higher frequencies we observe, as expected, multiple excited EMR modes in the impedance spectra which differ for the single and bidomain crystals. The latter yields various low-frequency (24…31 kHz) peaks which should be associated with bending-type resonance modes and are absent in the former. The unidomain crystal, on the other hand, exhibits multiple higher-frequency (250…340 kHz) resonances which should be associated with in-plane extensional contour modes of vibration and are mostly absent in the bidoman crystals. To attest this, we compare the resonance frequencies measured experimentally with those calculated with equations (6.18) and (6.21) for long thin bars. Substituting the material constants and geometrical parameters in equation (6.21) yields $\langle D_{11} \rangle$ = 1.30×10^{10} and $\langle D_{22} \rangle$ = 1.16×10^{10}, and thus frequencies of 31.45 kHz and 29.74 kHz for the fundamental pure bending resonances of the bidomains in the *x* and *y* directions, respectively. These values are close to the experimental ones, especially those obtained in the bidomain T-T DA crystal. Deviations between the resonance frequencies of different samples are in part due to small variations in their geometry and thickness ratios between phases. Also, higher overtones of these modes are observed at ca. 5.4, 13.3, … times the fundamental frequency as predicted by equation (6.21). As for the extensional modes in the unidomain crystal, equation (6.18) gives $\langle C_{11} \rangle$ = 1.72×10^{11}, $\langle C_{22} \rangle$ = 1.44×10^{11} and thus fundamental frequencies of 303.75 kHz and 278.75 kHz for resonances in the *x* and *y* directions, respectively, and higher harmonics at odd multiples of these frequencies, which is in agreement with the observations.

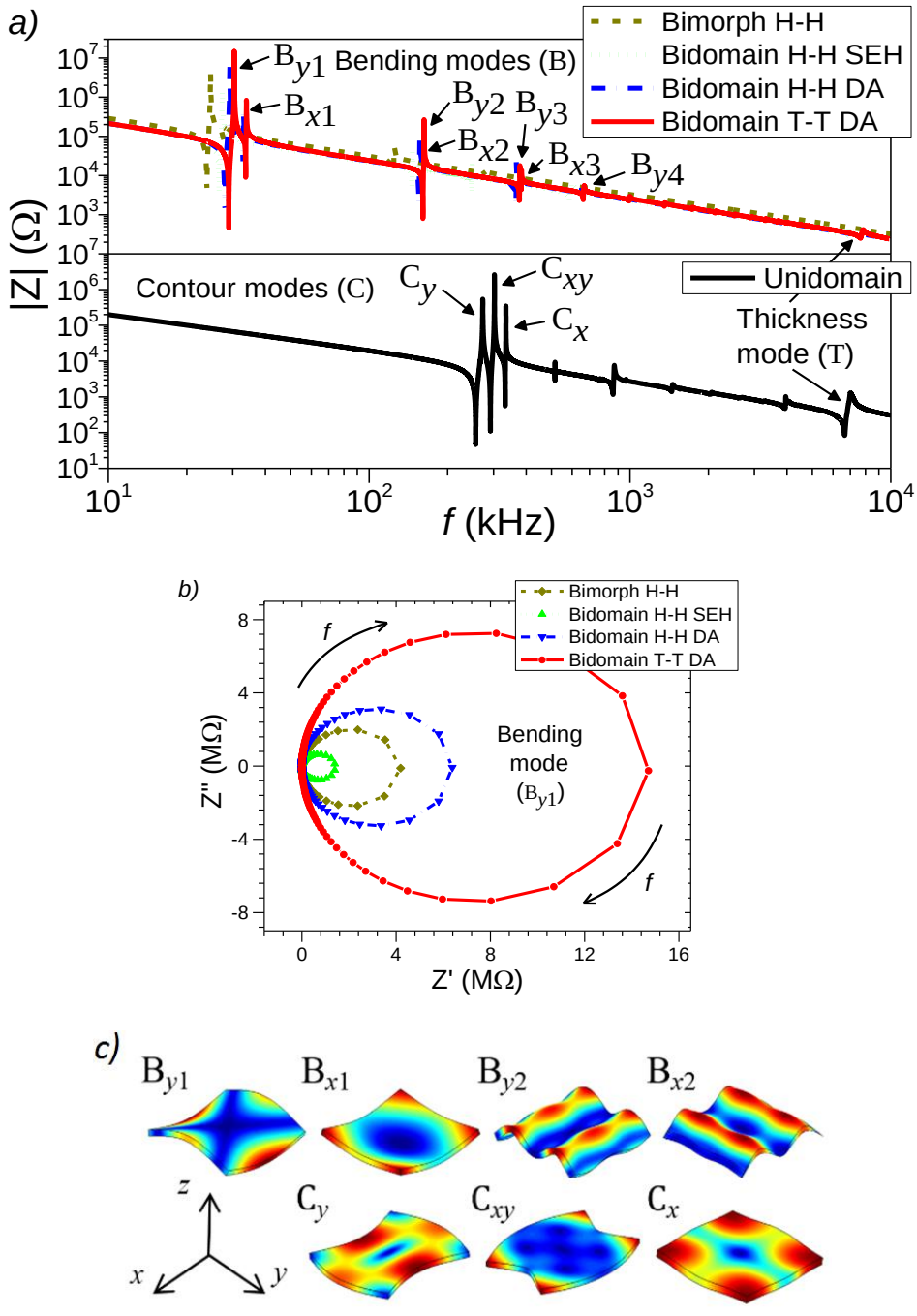

Figure 6.4 *a)* Impedance spectra ($|Z|$ *vs* f) of the unidomain, bimorph and bidomain 127ºY-cut LNO crystals. Some of the observed bending and contour EMR modes are labeled as B_{in} and C_i, respectively. *b)* Nyquist plot (Z'' *vs* Z') for the crystals operating in the range of the fundamental B_{y1} bending mode of antiresonance (23…33 kHz). *c)* Spatial deformation of the crystals associated with some of the EMR modes in the impedance measurements as simulated by the final element method. On the color scale, the red and blue regions correspond to large and small displacement amplitudes ($|u|$), respectively. Note that the displacements shown are largely exaggerated for the sake of clarity.

The resonance modes identified using a finite element method appear labelled in Figure 6.4 *a)*, and some of them are plotted in Figure 6.4 *c)*. We see that in the bidomain crystals the fundamental bending modes are characterized by a saddle-like deformation, which occurs because the in-plane PE coefficients (d_{31} and d_{32}) have different signs. These bending modes appear in pairs, B_{y1} being closely related to the pure bending mode in the *y* direction and B_{x1} with the one in the *x* direction. The amplitudes of the $|Z|$ peaks are larger in the former because $|d_{32}| > |d_{31}|$. The smaller peaks B_{y2}, B_{x2}, etc. correspond to higher harmonics of the fundamental modes in the *y* and *x* directions, respectively.

Table 6.1 Summary of some of the most important experimental impedance properties of the LNO crystals and ME properties of the bilayered composites. Here, C and $\tan(\delta)$ are the parallel capacitance and loss tangent measured at low frequency (< 1 kHz), respectively, f_r and f_a are the resonance and antiresonance frequencies of the fundamental EMR bending mode (B_{y1}), $|Z|$ is the peak impedance amplitude in antiresonance, k_{eff} is an effective electromechanical coupling factor (${k_{eff}}^2 = (f_a^2 - f_r^2)/f_a^2$), Q is the mechanical quality factor, α_{E31} and α_{E32} are the quasi-static ME coefficients, f_a^{ME} is the resonance frequency of the ME effect for the fundamental bending mode, and $|\alpha_{E32}(f_a^{ME})|$ is the amplitude of the ME response under such conditions.

Sample	Unidomain	Bimorph H-H	Bidomain H.H SEH	Bidomain H-H DA	Bidomain T-T DA
C, pF	80.8	56.0	84.1	74.4	76.1
$\tan(\delta)$, %	0.73	1.48	1.49	0.80	0.70
f_r, kHz	–	23.87	26.57	27.96	28.96
f_a, kHz	–	24.65	27.35	29.22	30.40
$\|Z\|$, MΩ	–	4.19	1.41	6.24	14.71
k_{eff}	–	0.250	0.237	0.290	0.305
Q	–	445	365	849	2263
α_{E31}, V/(cm·Oe)	–0.50	0.29	0.30	0.30	–0.41
α_{E32}, V/(cm·Oe)	0.81	–1.06	–0.74	–0.95	1.88
f_a^{ME}, kHz	31.20	25.55	28.20	30.35	30.82
$\|\alpha_{E32}(f_a^{ME})\|$, V/(cm·Oe)	82.8	242.0	131.5	233.2	462.7

Figure 6.4 *b)* shows the Nyquist plots of the active (Z') and reactive (Z'') parts of the impedance near the antiresonance frequency of the fundamental B_{y1} mode measured in the studied bidomain crystals. Comparing the amplitudes of the Z' peaks and the Q factors associated with this mode (see Table 6.1) shows that the larger values are obtained in the T-T DA crystal followed by H-H DA, bimorph and H-H SEH. The unidomain PE is shown to exhibit no bending resonance modes yielding instead three strong fundamental contour modes at frequencies of the order of 300 kHz labelled C_y, C_{xy}, and C_x. From their displacement profile shown in Figure 6.4 *c)* we conclude that C_y and C_x are roughly similar to pure extensional modes in the *y* and *x* directions, respectively, and C_{xy} is a combination of the two. A much weaker version of these modes also seems to be present in the bidomain H-H SEH crystal, which is probably due to some small difference in volume between both domains. Smaller overtones of the fundamental contour modes are also observed in the unidomain sample at approximately odd multiples of their frequencies. Finally, we note in this crystal the presence of a wide EMR peak at a much higher frequency of ca. 7 MHz. This should correspond to the standard thickness extensional mode predicted to occur at around this frequency [67, 203, 208]. In the single-domain crystal, thickness modes are expected at odd multiples of this fundamental frequency, while in a bidomain crystal such modes should only be observed at twice these frequencies [203, 208]. Thus, we conclude that the weak thickness modes observed at ca. 7 MHz in the bidomain and not in the bimorph crystals must be an indication of the roughness or off-centered position of the interdomain boundary.

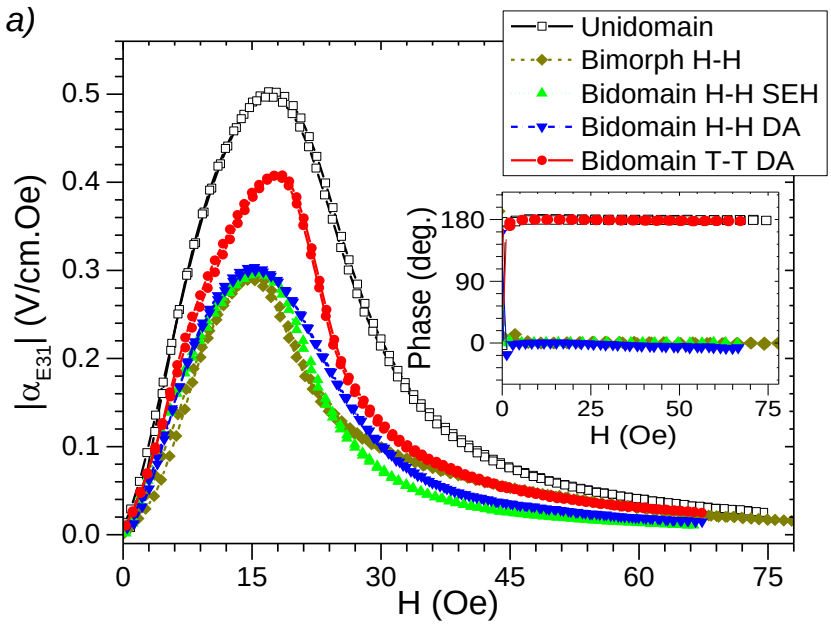

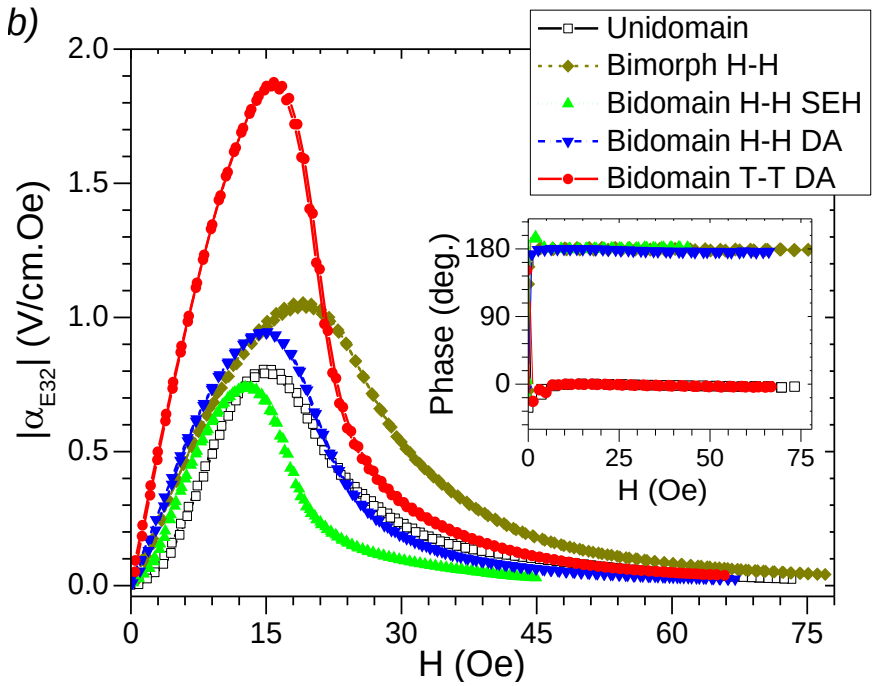

Figure 6.5 Quasi-static in-plane direct ME coefficients *a)* $|\alpha_{E31}|$ and *b)* $|\alpha_{E32}|$ measured as a function of the magnetic bias field in the bi-layered composites with single-domain and bidomain 127°Y-cut LNO crystals (with f = 1 kHz and δH = 1 Oe). The phase of the ME coefficient with respect to the *AC* magnetic field is shown in the inset.

In conclusion, the impedance measurements of the crystals have suggested that the bidomain crystals produced by DA, especially the T-T ones, seem to offer a better PE performance under quasi-static and bending resonance conditions in comparison to the bidomain H-H SEH, bimorph and unidomain crystals.

After measuring the impedance of the crystals, the bilayered ME composites have been prepared and the ME measurements performed. Figure 6.5 shows the results for the quasi-static (with f = 1 kHz and δH = 1 Oe) ME coefficients ($|\alpha_{E3a}|$ and phase) measured as a function of an applied bias field in the x (α_{E31}) and y (α_{E32}) directions. We start the analysis by noting that the observed ME curves follow the typical piezomagnetic $q = \partial S/\partial H$ curves of Metglas which are maximized at ca. 16 Oe and go to zero as the magnetization saturates [82, 87, 92]. We also see that the α_{E31} coefficients differ from the α_{E32} ones, which is a consequence of the anisotropy of the PE crystals. In general, the maximum α_{E32} values are about three times larger than the α_{E31} ones and have different signs because $d_{32} \approx -3d_{31}$. This is qualitatively in agreement with the values predicted in the above calculations. The sign of the coefficients also agrees with that of the unidomain and T-T bidomain samples having an opposite sign as compared to the H-H ones. The large quantitative

difference between the calculated and experimental values can be explained by a far-from-prefect mechanical coupling between the MS and PE phases due to the rough intermediate viscous epoxy layer, a deviation from the assumption of perfectly defined ferroelectric domains with a centered boundary and the fact that the q coefficients of Metglas are in reality strongly non-linear and decrease under a compressive pre-stress from the PE phase in the direction of the applied bias field [56, 161, 225, 226]. Generally we see that the maximum $|\alpha_{E32}|$ coefficients are larger in the bidomain samples as compared to the unidomain ones. In particular $|\alpha_{E32}|$ is ca. twice as large in the T-T DA sample, just as predicted by the calculations. This provides a signature of performance of the T-T sample which should thus be near to the case of the ideal bimorph.

The results of the dynamic ME measurements performed as a function of the frequency of the *AC* field (with δH = 0.1 Oe and f up to 600 kHz) and in a bias field of 16 Oe in the *y* direction are plotted in Figure 6.6. We see that the α_{E32} coefficients yield notable peaks in amplitude corresponding to the EMR of the PE crystals which are closely related to the peaks observed in the impedance measurements. At resonance the ME coefficients are enhanced approximately by the factor Q in relation to their quasi-static counterparts [188, 209]. Because these measurements were made under open-circuit conditions, the peaks in the ME effect should correspond to the antiresonance frequencies of the samples, where the impedance and averaged strains (i.e. overall deformation) are maximized [190, 191, 217]. As predicted, we see that the lower-frequency bending EMR modes are strong in the bidomain samples and almost absent, although very sharp, in the unidomain ones. The reverse is verified in relation to the higher-frequency contour modes. Unlike in the impedance measurements though, only a single fundamental bending mode is excited. This must correspond to a combination of the in-plane modes labelled B_{y1} and B_{x1}, although much closer to the former, because the bias and *AC* fields were applied and the Metglas layers was deformed mostly in the *y* direction (i.e. $\left|\langle\overline{h_{32}}\rangle_p\langle\overline{q_{22}}\rangle_m\right| > \left|\langle\overline{h_{31}}\rangle_p\langle\overline{q_{21}}\rangle_m\right|$). The ME coefficient in the unidomain sample associated with the C_y contour mode is larger than the C_x one, also partially due to the same reason. The presence of weak contour resonant ME effects in the bidomain samples must be due to a small effective off-centering of the interface between domains (i.e. $t_{p+} \neq t_{p-}$), thus resulting in a non-zero averaged coefficient $\langle\overline{h_{31}}\rangle_p$ in equation (6.17).

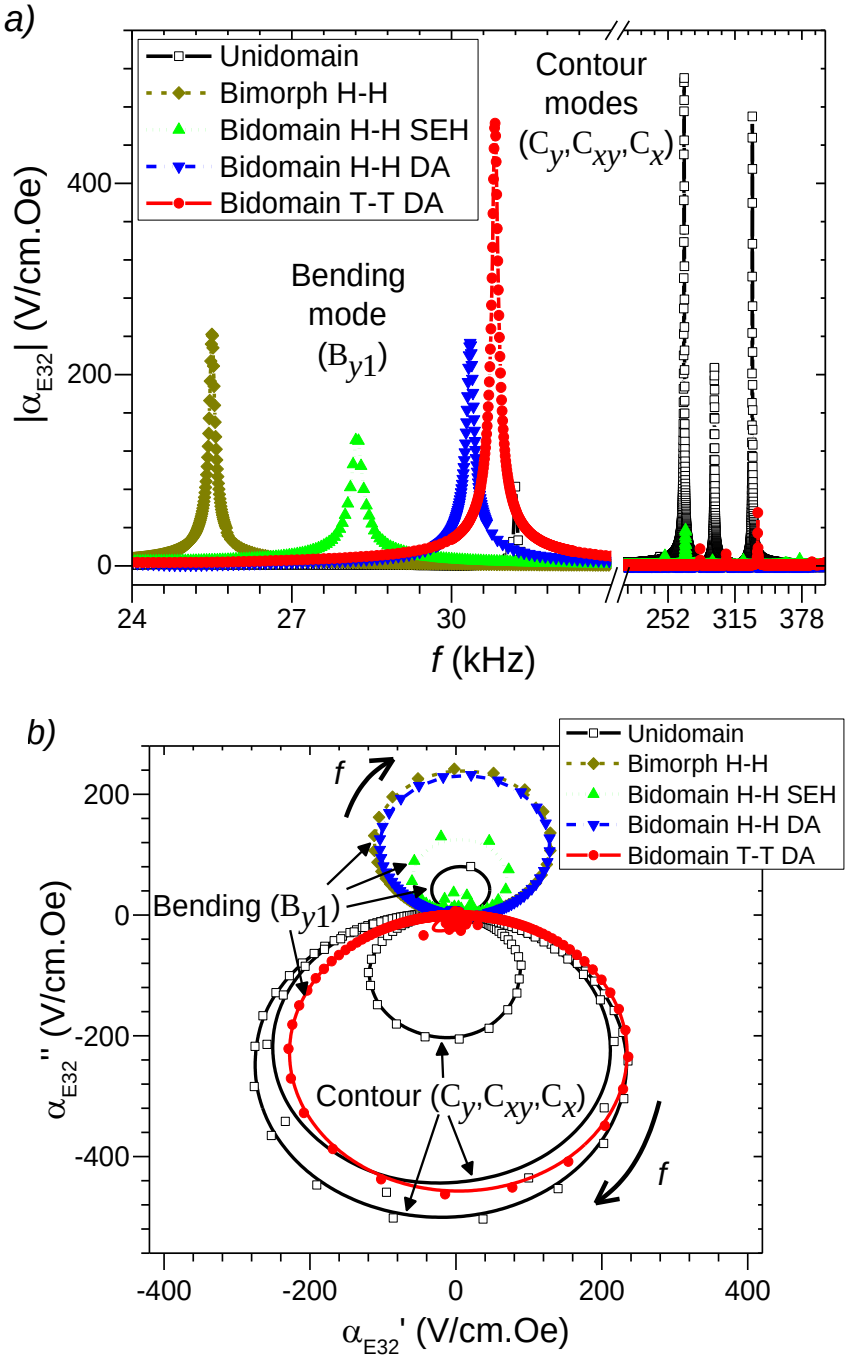

Figure 6.6 Resonant direct ME coefficients (α_{E32}) measured as a function of the frequency of the *AC* magnetic field in the bi-layered composites with single-domain and bidomain 127ºY-cut LNO crystals (with H = 16 Oe and δH = 0.1 Oe). *a)* Results of $|\alpha_{E32}|$ in the range of the fundamental bending and contour EMR modes and *b)* Nyquist plot (α_{E32}'' *vs* α_{E32}') in the range of up to 600 kHz.

Figure 6.6 *b)* shows the Nyquist plot of the ME coefficients separated into the real (α_{E32}') and imaginary (α_{E32}'') parts. As predicted by the theory, we see that close to the antiresonance

frequency these coefficients are approximately proportional to $j\omega Z$, where Z is the complex impedance of the samples which nearly corresponds to the impedance of the crystals plotted in Figure 6.4 *b)* [191, 209]. Furthermore, the sign of the maximum imaginary part of α_{E32} is associated with the sign of $-\langle\overline{h_{31}}\rangle_p$, for the contour modes, and $-\langle z\overline{h_{31}}\rangle_p$, for the bending modes, as shown in equations (6.17, 6.20). These effective extensional and flexural PE coefficients have different signs for one and the same sample when $0 \leq t_{p+}/t \leq 0.5$, thus resulting in ME contour and bending peaks with different signs. As in the case of the quasi-static effects, we see that a large bending resonant coefficient of up to 463 V/(cm·Oe) was obtained in the bidomain T-T DA sample at 30.8 kHz followed by 242 V/(cm·Oe) in the bimorph H-H, 233 V/(cm·Oe) in the bidomain H-H DA, 131 V/(cm·Oe) in the bidomain H-H SEH, and only 83 V/(cm·Oe) in the unidomain sample. The ME effects under contour resonance conditions in the single-domain sample are also shown to be of the same magnitude as the ME effects under the bending resonant condition in the bidomain samples.

It is worth to note the fact that the bending ME effect was found to be nearly twice as large in the bidomain T-T DA sample in contrast to the bimorph one obtained by simply bonding two oppositely poled PE plates, both under quasi-static and resonance conditions. This proves the superiority of the DA technique in the fabrication of the bidomain structure in LNO crystals with a relatively smooth and thin transition region between domains, thus maximizing the elastic coupling between them. The DA technique could therefore be more useful, e.g., in the fabrication of ME-based magnetic field sensors or actuators operating at low frequencies in the bending regime. Also, though from a theoretical point of view one would expect the ME response to be equivalent in H-H and T-T ideal bimorphs, with the exception of a change in sign, in practice we identified a much larger effect in the T-T sample produced by DA. This should be related to a difference in the ferroelectric microstructure of the crystals which originates as a consequence of the different DA processing conditions. The identification of the exact physical mechanisms responsible for the observed effect is outside the scope of this work and requires further investigation. In the group of the composites with two ferroelectric domains, the bimorph produced by SEH yielded smaller effects which are related to the highly irregular interdomain region. Thus, some improvements still have to be made in this technique.

Having found the best low-frequency ME properties in the composite containing the 127ºY-cut bidomain T-T crystal produced by DA, we performed noise measurements in this sample. These were made using the same setup as in the ME measurements while shielding the system from external stray magnetic fields. Figure 6.7 *a)* shows the results of these measurements in the form of the noise spectral density as a function of the frequency (in the 10…100 kHz range) in an optimal applied bias field of 16 Oe in the *y* direction.

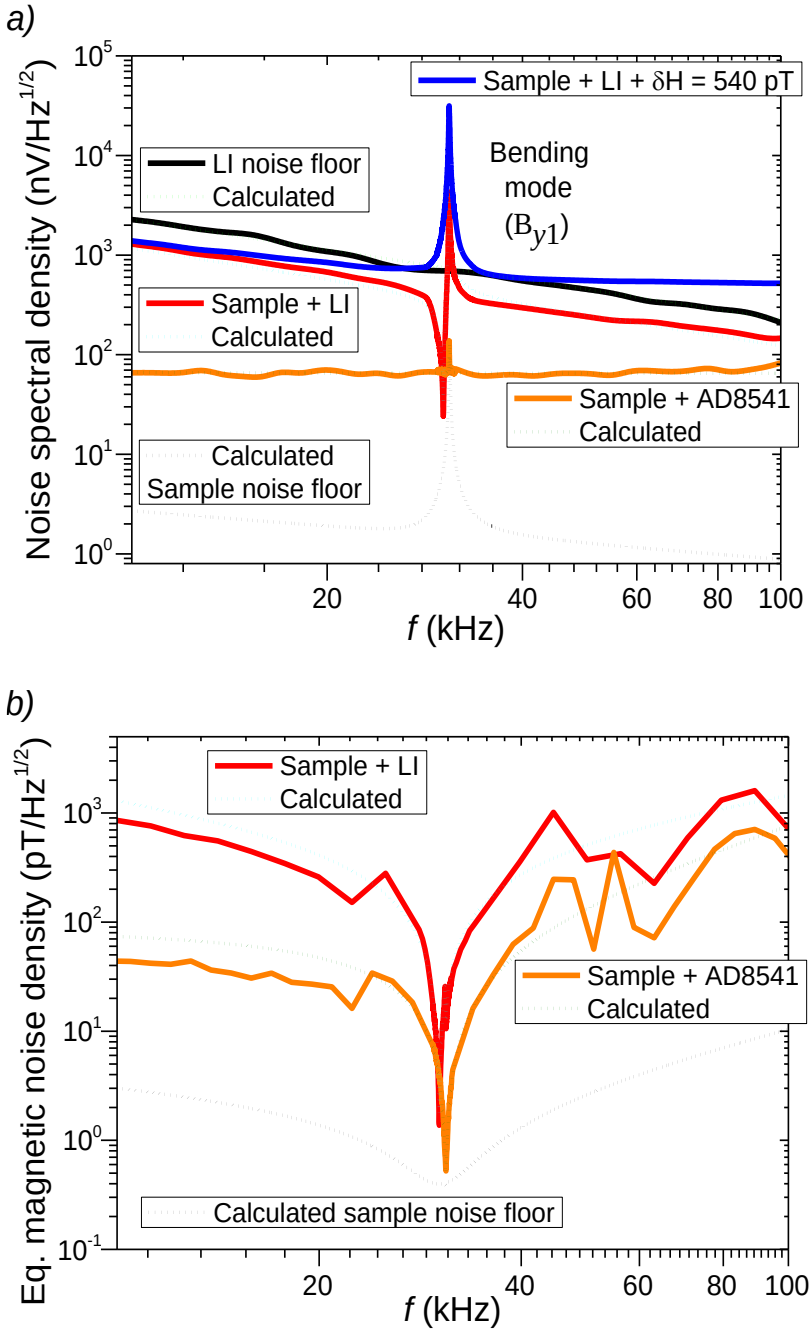

Figure 6.7 *a)* Noise spectral density measured as a function of the frequency in the systems composed of the bi-layered composite with a bidomain T-T 127ºY-cut LNO crystal produced by DA and detection circuits consisting of simply the lock-in amplifier (LI) or AD8541 pre-amplifier plus lock-in (with an applied magnetic bias H = 16 Oe and AC fields δH = 0 and δH = 540 pT). Superimposed are the theoretical noise components originated in the sample and detection circuits calculated using an equivalent circuit model. *b)* Experimental and calculated equivalent magnetic noise spectral density of the samples and detection circuit (LI and AD8541).

First of all, we note that the top line with a constant slope in Figure 6.7 *a)* represents the noise density floor measured at the input of the lock-in amplifier (LI) in the absence of the ME composite (i.e. with $Z \to \infty$). This curve is consistent with the theoretical one calculated using expression (6.23), associated with the equivalent detection circuit shown in Figure 6.3 *a)*, and using the LI parameters G = 1, Z_{a1}= Z_{a2} = 1 MΩ||20 pF, e_a = 1 nV/Hz$^{1/2}$ and i_a = 10 pA/Hz$^{1/2}$.

The noise density measured for the complete system composed of the sample and lock-in is also represented. As predicted in Section 2, we see that the noise drops in this range approximately as $1/f$ and has a local minimum and maximum corresponding to the EM resonance and antiresonance of the impedance of the laminate, respectively. This result is shown to be well fitted with the noise calculated using equation (6.23) and the following equivalent parameters for the ME composite: R = 1 GΩ, C = 60 pF, L_m = 5.0 H, C_m = 5.55 pF, $R_m = (1/Q).\sqrt{L_m/C_m}$, Q = 300 and $\tan(\delta)$ = 0.7%. Therefore, the dominant noise contribution should be attributed to the Johnson noise. As predicted by equation (6.23), the small decrease in the noise density observed between this case and the preceding one should be due to a decrease in the equivalent impedance of the circuit, Z_{eq}= $Z||(Z_{a1} + Z_{a2})$.

The maximum peak noise under antiresonance conditions at f_a = 30.8 kHz is related to the peak in the real part of the impedance of the composite. The pronounced local minimum close to the resonance frequency at f_r = 30.2 kHz, on the other hand, mostly appears as a consequence of the relatively large input current noise density i_a of the lock-in. This current noise flows through the equivalent impedance of the circuit contributing to the total noise with a voltage $|Z_{eq}|i_a$, which is particularly small at resonance, where $|Z|$ is minimized, thus giving rise to the local minimum. In quantitative terms, this spectrum demonstrates a noise density of 11.3 μV/Hz$^{1/2}$ for a low frequency of 1 kHz, 23.8 nV/Hz$^{1/2}$ at EM resonance, and 4.3 μV/Hz$^{1/2}$ at EM antiresonance of the sample. These values are quite large, thus reflecting the strong effect introduced by the circuit of the lock-in amplifier.

To prove this, we plotted in Figure 6.7 *a)* the calculated component of the voltage noise due solely to the ME composite as obtained by equation (6.22). This curve shows a noise level up to three orders of magnitude lower than that measured off resonance. It also exhibits a single peak corresponding to the antiresonance peak of the impedance. The values obtained in this case are 9.8 nV/Hz$^{1/2}$ at 1 kHz, 7.2 nV/Hz$^{1/2}$ at EM resonance, and 95.9 nV/Hz$^{1/2}$ at EM antiresonance. Even so, when applying a field of just δH = 540 pT to the system composed of the ME composite and lock-in, we see that this field is easily detected with a good signal-to-noise ratio for frequencies above ca. 10 kHz.

We note at this point that some commercial operational amplifiers offer input current noises lower than 0.1 fA/Hz$^{1/2}$ and input voltage noises lower than 1 nV/Hz$^{1/2}$ [227]. In order to decrease the noise of the detection circuit we experimented with a readily available CMOS AD8541 operational amplifier with a low reported input bias current of 4 pA and small input current noise density (< 0.1 pA/Hz$^{1/2}$). The amplifier was connected in the non-inverting buffer amplifier configuration, biased with a 10 MΩ resistor between inputs, and the ouput voltage was measured with the lock-in amplifier operating in its 50 Ω input mode. The obtained result is plotted in Figure 6.7 *a)* and depicts a significant reduction of the noise level of the system. This is consistent with the values calculated using the circuit model together with the circuit parameters G = 1, Z_a = 10 MΩ, e_a = 65 nV/Hz$^{1/2}$ and i_a = 0.1 pA/Hz$^{1/2}$. Off resonance the noise level thus dropped by almost two orders of magnitude being limited by the relatively large input voltage noise of the operational amplifier (e_a) for frequencies above ca. 10 kHz. At antiresonance we observe a single small peak in the noise which can be attributed to the peak in the impedance of the composite. In conclusion, using this improved detection circuit we obtained a noise spectral density of just 151 nV/Hz$^{1/2}$ for a low frequency of 1 kHz, 67 nV/Hz$^{1/2}$ at EM resonance, and 152 nV/Hz$^{1/2}$ at EM antiresonance of the sample. Comparing the measurements performed with the low input voltage and current noise detection circuits, of note is the fact that the minimum equivalent magnetic noise of the system operating at EMR conditions is only weakly affected by the noise characteristics of these detection circuits.

Using the expression $\delta H_{min}/\sqrt{\Delta f} = v_n.\sqrt{SNR}/|\alpha_{E32}|.t_p$, where Δf is the detection bandwidth and SNR is the signal-to-noise ratio, allows us estimating the minimum *AC* magnetic field detectable by this system. With SNR = 1 we calculated the spectral density of the equivalent magnetic noise for our sample using the data obtained for the noise density and ME effect. The result is presented in Figure 6.7 *b)*. We see that in the simple system composed of the laminate sample and lock-in amplifier the equivalent magnetic noise initially decreases with increasing frequency, from a value of 11.4 nT/Hz$^{1/2}$ at 1 kHz, attaining then a sharp minimum at the resonance frequency of the impedance when the noise density is minimized, although the ME response is not at its maximum. At this point the noise is shown to be as small as 1.4 pT/Hz$^{1/2}$. However, the ME coefficient here is only of 33 V/(cm·Oe). Operating the composite at antiresonance leads to a large output of 463 V/(cm·Oe), although in this case the magnetic noise increases up to 17.7 pT/Hz$^{1/2}$. Yet again we observe a good correspondence between the experimental results and the ones calculated with the help of the equivalent circuit of Figure 6.3 *a)*.

Thus, we conclude that the input noise of the lock-in is the main contributor to the total noise. Separating the magnetic noise into its components introduced by the sample and the lock-in, with the

help of the equivalent circuit, shows us that, in principle, using an ideal detection circuit, this noise may be suppressed down to 9.8 pT/Hz$^{1/2}$ at 1 kHz and to 397 fT/Hz$^{1/2}$ in a broad minimum around the EMR frequency (see Figure 6.7 *b)*). It is important to note that these values are comparable to those obtained in PZT and PMN-PT based magnetic sensors [58, 61, 192, 196, 197, 199]. Using the low input current noise detection circuit based on the AD8541 operational amplifier allowed us to obtain equivalent magnetic noise density values much closer to the latter. Thus, a noise level down to 153 pT/Hz$^{1/2}$ was measured at a low frequency of 1 kHz and as small as 524 fT/Hz$^{1/2}$ was obtained at the antiresonance frequency of the sample where the ME voltage output is maximized.

At this point we note that the system studied by us could possibly be used to measure not only *AC* but also small *DC* magnetic field variations. To do this, one could apply an *AC* magnetic field with a given amplitude and frequency to the laminate and subsequently measure the ME response as a function of the H bias field, as we did in the quasi-static ME measurements. Thus, using, e.g., the bidomain T-T DA sample, associated with the quasi-static ME response shown in Figure 6.5 *b)* (with f = 1 kHz and δH = 1 Oe), biased in its linear region of operation with H = 4 Oe and corresponding ME effect slope of $\partial|\alpha_{E32}|/\partial H$ = 155 mV/(cm·Oe^2), would permit the detection of a minimum field variation per square root of bandwidth of $H_{min}/\sqrt{\Delta f} = v_n \cdot \sqrt{SNR} \cdot \sqrt{2}/\left((\partial|\alpha_{E32}|/\partial H) \cdot \delta H \cdot t_p\right)$ = 2.6 nT/Hz$^{1/2}$ (for SNR = 1). An up to three orders of magnitude lower value may be expected for the same composite operating at resonance, due to a ca. 10 times smaller voltage noise density and 100 times larger ME effect, or even lower through the optimization of the composite and detection circuit.

From a theoretical point of view, equations (6.19-6.21) show that the optimization of the PE thickness ratio from the current value of $t_p/t \approx 0.95$ to ca. 0.6, maintaining a constant thickness, should allow one to reduce the equivalent magnetic noise of the laminate by ca. one order of magnitude and the resonance frequency down to ca. 25 kHz. Thus, in order to enhance the ME effect and reduce the noise density of the bidomain T-T composite, we stacked up to 4 additional layers of Metglas on top of the original structure. The results of the quasi-static and resonant ME measurements, performed using simply the lock-in as the detection circuit, are depicted in Figure 6.8. In the quasi-static regime we observe a decrease in the maximum $|\alpha_{E32}|$ values accompanied by an increase in $|\alpha_{E31}|$, as the number N of layers is increased. On the other hand, the bias field required to maximize the ME coefficient also increases with N. From the theoretical calculations made above and represented in Figure 6.2 *c)*, one would expect both coefficients to increase with N up to about 12 due to the enhanced bending strain, and to get closer together, since in this case the anisotropy of the crystal contributes less to the properties of the composite as a whole. The decrease in $|\alpha_{E32}|$ and increase in the bias field might be explained by the demagnetization effect which reduces the

effective *H* field inside the MS phase and increases with the thickness of this layer [225]. Another factor is the larger pre-stress produced by the intermediate epoxy layers [161].

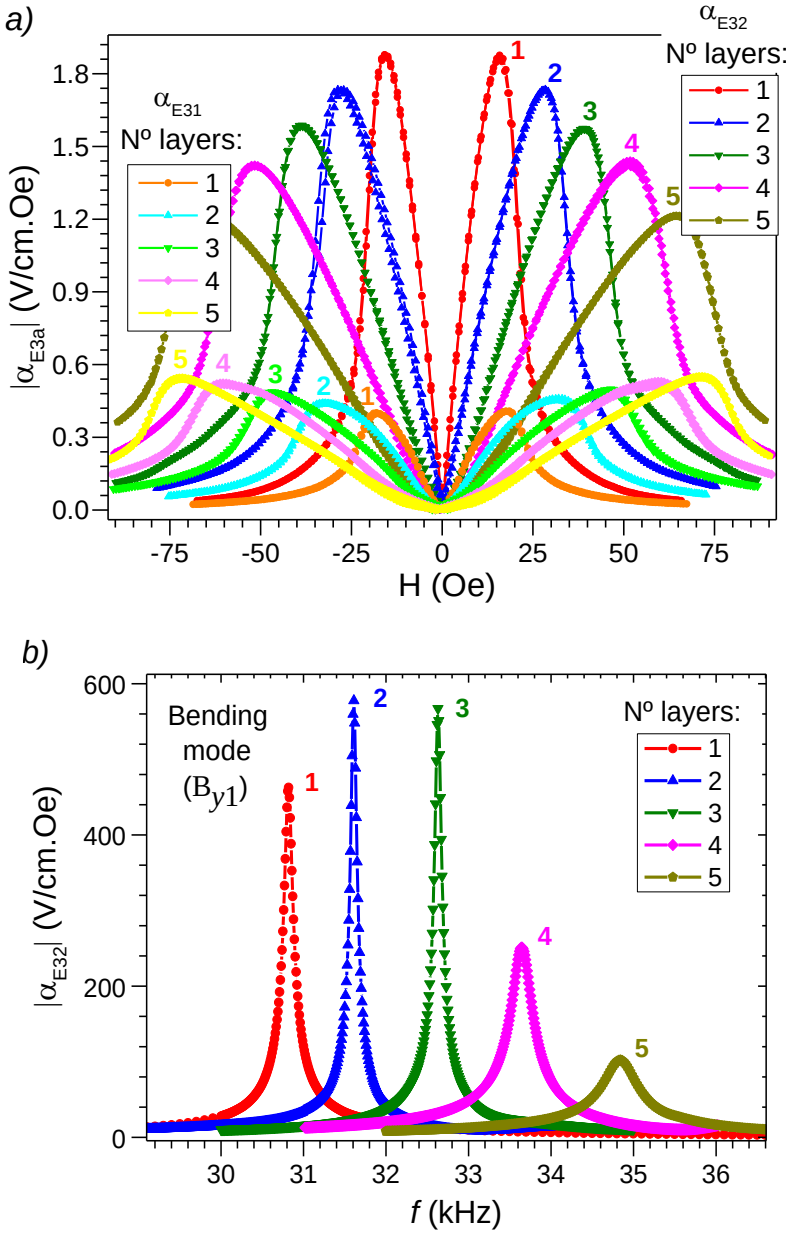

Figure 6.8 Direct ME coefficients ($|\alpha_{E3a}|$) measured in the bi-layered composite with bidomain T-T 127ºY-cut LNO crystals produced by DA and N = 1–5 layers of Metglas. *a)* Quasi-static effect as a function of the applied bias field (with f = 1 kHz and δH = 1 Oe); *b)* Dynamic effect under fundamental bending resonance conditions and in an optimal bias field (H = 16, 28, 39, 52, 65 Oe for N = 1, 2, 3, 4, and 5, respectively, and δH = 0.1 Oe).

Figure 6.8 *b)* shows the α_{E32} ME coefficients measured close to the fundamental bending resonance in optimal bias fields as obtained in the quasi-static measurements. Here we see that the resonance frequency tends to increase by about 1 kHz with the number N of Metglas layers. As predicted by equation (6.21), this is due to the increase in the thickness of the composite, even though the sound velocity $1/\sqrt{\rho s_{22}}$ is smaller in Metglas. Also we note an increase in $|\alpha_{E32}|$ by about 25% of up to 578 V/(cm·Oe) for 2–3 layers of Metglas. Increasing further the number of layers results in a rapid reduction of the ME coefficient and the Q factor. This behavior can be explained by a balance between different phenomena [228]. On the one hand, the increase of the volume ratio of the MS phase up to ca. 0.4 tends to increase the bending deformation and consequently enhance the ME effect, as predicted by the calculations. On the other hand, the demagnetization effect decreases the effective magnetic field inside the MS layer, and the larger volume of intermediate layers of viscous epoxy increases the shear lag and elastic losses, both of which tend to reduce the ME effect [225, 226].

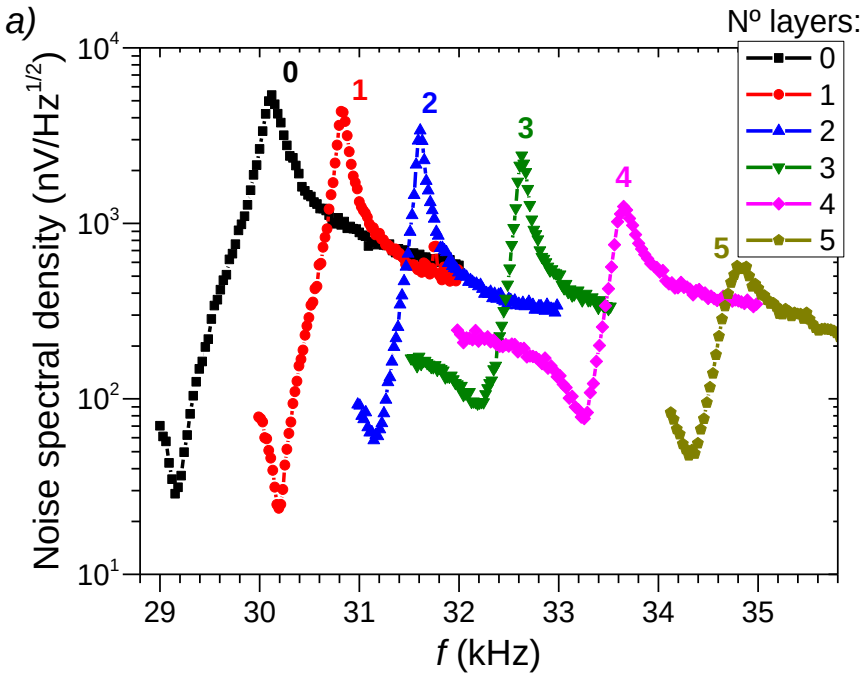

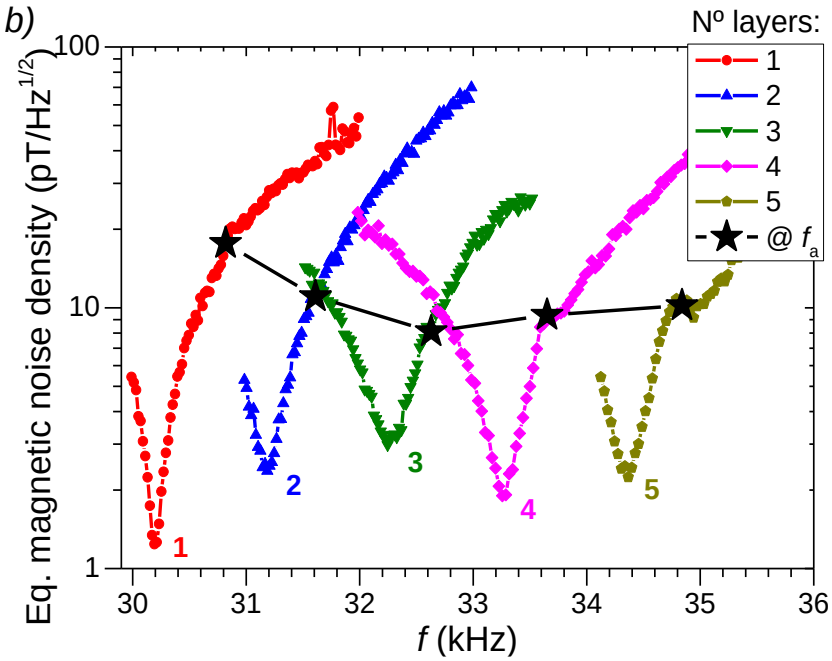

Figure 6.9 *a)* Noise spectral density and *b)* Equivalent magnetic noise spectral density measured in the range of the fundamental bending EMR in the bi-layered composite with bidomain T-T 127ºY-cut LNO crystals produced by DA and N = 1–5 layers of Metglas. The black asterisks indicate the equivalent noise at ME resonance (i.e. at the frequency of the impedance antiresonance).

Figure 6.9 shows the results of the noise measurements performed in the system composed of the laminate and lock-in detection circuit in the range of the fundamental bending mode of resonance and in optimal bias fields. Generally, the peaks in the noise density tend to get less pronounced with an increasing number of Metglas layers, being maximal in a simple bidomain crystal without any layer of Metglas, thus showing that the measured noise is not of magnetic origin. This behavior follows the decrease of the amplitude of the resonance and antiresonance peaks of the impedance, as predicted by equation (6.19), due to the reduction of the relative volume of the PE phase, as well as the decrease of the Q factor. More simply, one can say that the peak noise spectral density continuously decreases with the number of added MS layers because the larger volume of the MS phase produces a larger stress on the PE crystal, thus preventing it from vibrating (resulting in smaller Y' and Z' peaks) under the action of noise sources other than magnetic. The equivalent magnetic noise spectral density of the samples is depicted in Figure 6.9 *b)*. This shows that the noise can be as small as 1.4 pT/Hz$^{1/2}$ at 30.2 kHz in the composite with a single Metglas layer. However, the ME coefficient here is also relatively small, ca. 33 V/(cm·Oe). Increasing further the number of MS layers seems to augment this noise because, as we have seen before, the presence of this minimum at the impedance resonance frequency is mainly a consequence of the noise introduced by

the detection circuit through the term $|Z_{eq}|i_a$. At antiresonance, on the other hand, the ME coefficient is maximized up to 567 V/(cm·Oe) and the magnetic noise minimized down to 8.1 pT/Hz$^{1/2}$ in the sample with an optimal number of 3 Metglas layers (@ 32.6 kHz). By fitting this result with the one calculated using the equivalent circuit model, we can derive the following equivalent parameters for the ME composite: R = 1 GΩ, C = 60 pF, L_m = 7.11 H, C_m = 3.44 pF, $R_m = (1/Q)\sqrt{L_m/C_m}$, Q = 300 and $\tan(\delta)$ = 0.7%. This circuit shows us that in principle the noise density due solely to the ME composite, operating at antiresonance, could potentially be as small as 74 nV/Hz$^{1/2}$ and the corresponding equivalent magnetic noise as low as 247 fT/Hz$^{1/2}$. A detection circuit with a larger input impedance ($Z_{a1} + Z_{a2}$) and smaller input noise (i_a and e_a) is thus expected to allow reducing the values of the experimental magnetic noise by a very large margin.

In future studies it is crucial to make further attempts to reduce the equivalent magnetic noise and the operation frequency of the bidomain composites by various methods [59]. The enhancement of the signal-to-noise ratio should start with the development of a suitable low-noise detection circuit [58, 60]. Its most desirable properties are a large input impedance (Z_a) and small input current (i_a) and voltage (e_a) noise densities. As mentioned above, some commercially available operational amplifiers already offer input current noises lower than 0.1 fA/Hz$^{1/2}$ and input voltage noises lower than 1 nV/Hz$^{1/2}$ [227]. These parameters could in theory offer us a more than one order of magnitude smaller magnetic noise level for the off-resonance conditions. Other desirable characteristics of the circuit are a large common mode rejection ratio and a small input bias current. On the part of the samples, some improvements must still be made in the bidomain fabrication techniques in order to achieve a thinner and smoother interface between the macrodomains. The thickness ratio between the PE and MS phases must also be optimized by increasing the relative volume of the latter, as well as the bonding between the phases by reducing the thickness of the epoxy layer or through the use of an alternative bonding method (e.g. co-firing, thick film printing). In order to decrease the equivalent magnetic noise density, one can simply increase the size of the laminates and the quality factor (i.e. reduce the dielectric, PE and elastic friction losses). Other possibilities include using an asymmetric bias field together with a symmetric structure [195] or an asymmetric structure with two different MS materials on the top and bottom faces having a magnetostriction with opposite signs, such as Metglas and nickel [202]. To further decrease the fundamental frequency of the bending resonance, where the equivalent magnetic noise is minimized, a hypothesis would be the fabrication of composites with a smaller thickness and larger area and a larger relative volume of the MS phase. In this regard, e.g., a long bar of the Metglas / 127ºY-cut LNO laminate with dimensions of 50 ×5 ×0.1 mm^3 could in theory easily have a resonance frequency lower than 300 Hz. Other methods that can be used to tune the resonance frequency comprise variating the applied magnetic bias field [229] or electric bias field [230, 231], adding a certain surface mass to the laminate [228]

or a third long elastic component with a large Q factor [109]. Alternatively, the bidomain composites could also find use for higher-frequency applications allowing in this case a reduction in the size of the devices, while maintaining the same frequency of operation. Some other interesting alternatives to the realization of the magnetic sensors could explore the non-linear MS behavior of Metglas, in order to realize high-sensitivity wide-band frequency-selective sensors [92, 148], or the ME effect originated from a magnetic-torque interaction in cantilever bimorph structures by putting a permanent magnet at the tip [232]. A different operation mode based on measuring the shift in the bending resonance frequency with the applied bias field could also be employed [233].

6.5. Conclusions

We have conducted a study of the applicability of ME bilayered composites containing $10 \times 10 \times 0.5$ mm^3 PE plates of LNO possessing a ferroelectric bidomain structure, formed in single-domain crystals through the use of stationary external heating (SEH) or diffusion annealing (DA) techniques, for applications in low-frequency vector magnetic field and current sensors. Such ME sensors in principle may offer a large sensitivity to minute magnetic fields, an entirely passive operation at room temperature and well above it, and can be made small size, robust, cheap and simple to operate.

Theoretical calculations established the relations between geometric and material parameters of the Metglas / LNO composites and their frequency-dependent ME, impedance and noise properties. The ME effect has been found to be maximized in a LNO crystal with an approximately 127ºY-cut and a thickness ratio of the PE phase of ca. 0.6. The model also predicted the existence of EM resonant bending modes and the possibility to generate a magnetic noise floor down to the pT/Hz$^{1/2}$ range at 1 Hz and sub-pT/Hz$^{1/2}$ range at resonance conditions. For a LNO crystal with dimensions of $50 \times 5 \times 0.1$ mm these resonance modes are expected to appear at frequencies as low as just a few hundred Hz.

From the impedance and ME measurements, the PE properties of the 127ºY-cut LNO crystals have been found to be slightly improved in a bidomain H-H structure produced by the SEH technique in comparison to a unimorph structure and a bimorph one produced by bonding two crystals together. They were also found to be almost twice as large in a bidomain T-T structure fabricated by a newly developed DA method. These results have proven the existence of a more efficient PE and elastic coupling between both ferroelectric macrodomains in these bidomain crystals. Other advantages of the bidomain plates in comparison to sintered or glued ones include lower elastic losses associated

with the viscous glue or diffusion interface between macrocrystals, the easiness to obtain the bidomain structure over large plate areas, the existence of a continuous single-crystalline arrangement across the entire thickness, a high resistance to the creep effect, a high-temperature stability, the absence of the necessity to preliminary prepare the surfaces to be joined and the large simplicity of the employed techniques. A ME effect as large as 1.9 V/(cm·Oe) has been observed in such a crystal glued together with a single 29 μm thick layer of Metglas foil under quasi-static conditions. At higher operation frequencies, multiple distinct ME peaks were identified at frequencies of the order of 30 kHz and of the order of 300 kHz corresponding to EM bending and contour resonance modes of the PE crystals, respectively. The former were found to be very strong in the bidomain and bimorph samples, while the latter were pronounced only in the single-domain ones. A ME effect as large as 578 V/(cm·Oe) has been observed in a T-T bidomain crystal, produced by DA and bonded together with two layers of Metglas, under bending resonant conditions at ca. 31 kHz.

Noise measurements yielded an equivalent magnetic noise spectral density floor of 153 $pT/Hz^{1/2}$ at 1 kHz (quasi-static regime) and down to 524 $fT/Hz^{1/2}$ under resonance conditions in the T-T bidomain sample produced by DA with a single layer of Metglas. A comparison of these values with the ones obtained using an equivalent circuit model has shown that the total noise spectral density observed was dominated by the thermal Johnson noise in the sample and detection circuit. The detection circuit, composed of the input of a lock-in amplifier or an operational amplifier, was also found to make a large contribution to the total noise of the circuit when operating outside the resonance conditions. Some improvements in the detection circuit are expected to allow decreasing the values of the magnetic noise floor down to at least 9.8 $pT/Hz^{1/2}$ at 1 kHz and 397 $fT/Hz^{1/2}$ at resonance, values which are comparable to the ones already obtained in some PZT and PMN-PT based ME sensors [58, 61, 192, 196, 197, 199]. In this case, the advantages of using LNO are, however, undisputable, seeing that they implicate a non-hysteretic PE response, much higher thermal and chemical stability, larger resistance to creep and ageing effects, a lead-free nature, an easy high-quality crystal growth process, well established properties and applications and a much lower commercial price.

Altogether in this part we have thus shown that lead-free bidomain LNO crystals could be useful, e.g., in the fabrication of thermally stable ME-based vector magnetic field sensors operating at low frequencies in the bending mode regime.

Chapter 7

7. Conclusion

In summary, this work aimed at the theoretical and experimental study of the anisotropic ME properties of differently structured composites based on single crystalline piezoelectrics, mainly lead-free $LiNbO_3$, directed towards multiple future applications.

In the first part a theoretical model of the anisotropic quasi-static direct ME effect in tri-layered composites of Metglas and PE single crystals was used in the quantitative estimation of the ME coupling as a function of the crystallographic orientation (i.e. PE cut plane). Initially, a description of the PE and linear MS effects in terms of electric, magnetic and elastic material fields and constants was given. An averaging quasi-static method was subsequently used together with specific boundary conditions in order to derivate the relation between the material constants and the transversal (T-L) direct ME voltage (α_{E3a}) and charge coefficients (α_{Q3a}). The method consisted of the solution of the elastostatic and electrostatic equations taking into account the linear constitutive relations of the two phases. The properties of some common PE and MS materials (the latter with emphasis on the Metglas alloy exhibiting giant magnetostriction) have been discussed, and their influence on the ME coupling has been explored. It has been demonstrated that large ME voltage coefficients tend to be favored by large transversal piezoelectric coefficients, transversal and longitudinal piezomagnetic coefficients and coupling constants as well as small out-of-plane dielectric and compliance constants and the volume ratio between the PE and MS phases. On the other hand, it has also been shown that the ME charge coefficients do not depend on the dielectric constants of the PEs and thus tend to be much larger in lead-based crystals with very large piezoelectric constants such as PMN-PT and PZN-PT. The effects of the demagnetization fields on the attenuation of the ME coefficients were briefly explored. A description of the ME composites as equivalent Thévenin/Norton circuits composed of a magnetically driven voltage/current source in series/parallel with a characteristic impedance of the composite has also been exposed.

After that, we used the phenomenological quasi-static model in the calculation of the maximum expected direct transversal ME voltage coefficients in a series of tri-layered composites of the type Metglas/Piezocrystal/Metglas, as a function of the PE crystal orientation. The PE single crystals studied in this chapter included lead-free lithium niobate, α-galium phosphate, α-quartz, langatate, langasite, aluminum nitride, lithium tantalate and barium titanate, as well as the lead-based

PZT-2, PMN-33%PT ([111] poled), PMN-30%PT ([011] poled), PMN-33%PT ([001] poled), PZN-9%PT ([011] poled) and PZN-8%PT ([001] poled). The estimations revealed a strong dependence of the ME effects on the crystal orientation. They also supported the possibility of generating large quasi-static ME voltage coefficients in composites comprising lead-free PE single-crystals through the optimization of the crystal orientation. These ME effects were found to be particularly attractive for the case of lithium niobate, α-galium phosphate, quartz, [111]-poled PMN-33%PT and [011]-poled PZN-9%PT. The enhanced effects were found to be originated from a particularly good combination of relatively large PE coefficients and low dielectric constants. We thus have revealed that the choice of crystals with an appropriate cut is a vital step in the development of ME composites valuable for practical applications.

In the second part we introduced a comparative study between the direct and converse ME effects in tri-layered composites of the type Metglas/PE/Metglas based on single crystals of $LiNbO_3$ (LNO) and [011]-poled PMN-PT bonded with a cyanoacrylate glue. Due to the simplified preparation method, the amplitude of the observed ME effect was rather modest. In the quasi-static regime, although the highly piezoelectric PMN-PT-based composite exhibited an orders of magnitude stronger converse ME effect, the measurements of the direct ME effect have shown comparable magnitudes for both types of systems, mainly due to comparable ratios between piezoelectric and dielectric coefficients of both crystals. The converse ME effects, on the other hand, were shown to be much stronger in the sample with the PMN-PT crystal since, according to the theory, this effect depends only on the piezoelectric constants which are much larger in this case. We also presented the results of the direct ME measurements in the resonant regime. Here we found an even larger ME effect peak in the composite with the 41ºY-cut LNO than in the one with PMN-PT. The largest direct ME voltage coefficient of about 88 V/(cm·Oe) has been obtained for the 41ºY-cut LNO composite, while this was only of 66 V/(cm·Oe).for the PMN-PT-based structure Therefore, in this study we identified crystalline LNO as a valuable alternative to lead-based PEs in ME applications with the potential to form its own field of ME-based low-cost high-temperature magnetic-field sensors.

In another study we conducted a numerical analysis and an experimental study of the ME and EM anisotropic properties of tri-layered composites of Metglas/Piezoelectric/Metglas using differently oriented piezoelectric single crystals of $LiNbO_3$ and $GaPO_4$. The samples consisted of Y- and 41ºY-cut LNO and X-cut GPO substrates bound to Metglas foils using epoxy. The quasi-static ME measurements have shown a strongly anisotropic response with the transversal ME voltage coefficients being dependent on the direction of the applied in-plane magnetic bias field as well as the orientation of the crystal (crystal cut). This is related to the piezoelectric, dielectric and elastic properties of single crystals which are extremely anisotropic. As confirmed by some theoretical

calculations, this ME behavior was qualitatively correctly predicted by a simple constitutive model, in which the material tensor properties of the piezocrystals were transformed according to their physical orientation. Therefore, we saw that the tri-layered composite with the 41ºY-cut LNO crystal exhibited an almost isotropic in-plane ME response, with $\alpha_{E31} \approx \alpha_{E32}$, whereas the systems with the Y-cut LNO and X-cut GPO substrates demonstrated an approximately in-plane unipolar effect ($\alpha_{E31} > 0$ and $\alpha_{E32} \approx 0$) with the polar axis directed along the X direction. Also, the largest measured ME coefficient here was of 0.95 V/(cm·Oe) for the Y-cut LNO sample in a field of 25 Oe. In the GPO composite, a coupling of up to 0.24 V/(cm·Oe) was obtained.

In the resonant regime, several in-plane contour EM resonant peaks were observed in the ME spectrum. Here we saw how strongly the anisotropic nature of the PE crystals influences the excitation of certain contour acoustic resonance modes. So, e.g., three distinct resonance modes were observed in the system featuring the Y-cut LNO crystal, whereas a single one was observed in the composite with the 41ºY-cut LNO one. A very intense single peak exhibiting a ME coefficient of up to 249 V/(cm·Oe) was detected in the sample with the 41ºY-cut LNO crystal. In order to predict, which kinds of modes could be excited under given conditions and to identify such modes by comparison with simulated results, we employed impedance measurements, thus clarifying the relation between the anisotropic constants and the excitation of such peaks. The aforementioned large symmetric peak was therefore shown to be related to the in-plane isotropic properties of the crystal, so that a very symmetric and high-amplitude resonance mode was generated. In the GPO sample, four weak contour asymmetrical shear modes of resonance were identified, with the largest having a response of up to 23.2 V/(cm·Oe) and appearing at a frequency of 199.7 kHz.

In conclusion, in this part we were able to experimentally identify relatively large anisotropic ME effects in composites based on PE single-crystals which were in good agreement with the theory. In principle, such ME responses can be further enhanced through the optimization of the volume ratio and the coupling between layers. Finally we showed how the control of the crystal orientation can be used to greatly enhance the anisotropic ME effects in composites. The selection of the crystal orientation should therefore allow one to engineer almost any desired anisotropic properties for any given application.

Lastly, we conducted a study of the applicability of ME bilayered composites containing $10 \times 10 \times 0.5$ mm^3 PE plates of LNO possessing a ferroelectric bidomain structure, formed in single-domain crystals through the use of stationary external heating (SEH) or diffusion annealing (DA) techniques, for applications in low-frequency vector magnetic field and current sensors. Theoretical calculations established the relations between geometric and material parameters of the Metglas/LNO composites and their frequency-dependent ME, impedance and noise properties. The

ME effect has been found to be maximized in a LNO crystal with an approximately 127ºY-cut and a thickness ratio of the PE phase of ca. 0.6. The model also predicted the existence of EM resonant bending modes and the possibility to generate a magnetic noise floor down to the pT/Hz$^{1/2}$ range at 1 Hz and sub-pT/Hz$^{1/2}$ range at resonance conditions. For a LNO crystal with dimensions of 50 × 5 ×0.1 mm these resonance modes are expected to appear at frequencies as low as just a few hundred Hz.

From the impedance and ME measurements, the PE properties of the 127ºY-cut LNO crystals have been found to be slightly improved in a bidomain H-H structure produced by the SEH technique in comparison to a unimorph structure and a bimorph one produced by bonding two crystals together. They were also found to be almost twice as large in a bidomain T-T structure fabricated by a newly developed DA method. These results have proven the existence of a more efficient PE and elastic coupling between both ferroelectric macrodomains in these bidomain crystals. Other advantages of the bidomain plates in comparison to sintered or glued ones include lower elastic losses associated with the viscous glue or diffusion interface between macrocrystals, the relative ease to obtain the bidomain structure over large plate areas, the existence of a continuous single-crystalline arrangement across the entire thickness, a high resistance to the creep effect, a high-temperature stability, the absence of the necessity to preliminary prepare the surfaces to be joined and the large simplicity of the employed techniques. A ME effect as large as 1.9 V/(cm·Oe) has been observed in such a crystal glued together with a single 29 μm thick layer of Metglas foil under quasi-static conditions. At higher operation frequencies, multiple distinct ME peaks were identified at frequencies of the order of 30 kHz and of the order of 300 kHz corresponding to EM bending and contour resonance modes of the PE crystals, respectively. The former were found to be very strong in the bidomain and bimorph samples, while the latter were pronounced only in the single-domain ones. A ME effect as large as 578 V/(cm·Oe) has been observed in a T-T bidomain crystal, produced by DA and bonded together with two layers of Metglas, under bending resonant conditions at ca. 31 kHz.

Noise measurements yielded an equivalent magnetic noise spectral density floor of 153 pT/Hz$^{1/2}$ at 1 kHz (quasi-static regime) and down to 524 fT/Hz$^{1/2}$ under resonance conditions in the T-T bidomain sample produced by DA with a single layer of Metglas. A comparison of these values with the ones obtained using an equivalent circuit model has shown that the total noise spectral density observed was dominated by the thermal Johnson noise in the sample and detection circuit. The detection circuit, composed of the input of a lock-in amplifier or an operational amplifier, was also found to make a large contribution to the total noise of the circuit when operating outside the resonance conditions. Some improvements in the detection circuit are expected to allow decreasing the values of the magnetic noise floor down to at least 9.8 pT/Hz$^{1/2}$ at 1 kHz and 397 fT/Hz$^{1/2}$ at

resonance which are comparable to the ones already obtained in some PZT and PMN-PT based ME sensors [58, 61, 192, 196, 197, 199]. In this case, the advantages of using LNO are, however, undisputable, seeing that they include a non-hysteretic PE response, much higher thermal and chemical stability, larger resistance to creep and ageing effects, lead-free nature, easy high-quality crystal growth process, well established properties and applications and a much lower commercial price.

All in all, in this thesis we have shown that lead-free unidomain and bidomain LNO single-crystals could be useful, e.g., in the fabrication of thermally stable ME-based vector magnetic field sensors operating at low frequencies in the bending or extensional resonant regimes. According to the theory, the ME effect in our laminates may still be improve by more than one order of magnitude through various means. Therefore, future studies shall include the optimization of the thickness ratio between PE and MS layers, e.g. by stacking multiple layers of Metglas, and the improvement of the bounding method, e.g. through the use of wafer bonding techniques, electron or laser beam welding, sputtering or pulsed laser deposition of Metglas. In order to decrease the magnetic noise we shall improve the bidomain formation methods and employ very low input noise pre-amplifiers such as the ADA4530-1 component. To further decrease the resonant frequency, long bars of $50 \times 5 \times 0.2$ mm with bidomain LNO will be produced. To this end the non-linear magnetostrictive properties of Metglas may also be explored in greater detail. The ME effect experimental setup shall also be improved in order to better allow the measurement of single-phase and thin-film ME systems. Thus, two new independent *DC* and *AC* Helmholtz coils will be developed with a wider magnetic field uniformity and connected through balanced lines in order to achieve lower input noise and inductive coupling. We conclude by noting that ultimately there is still a lot of room for future improvements and the range of possibilities for this kind of ME systems thus seems to be immensely vast.

References

[1] P. Debye, "Bemerkung zu einigen neuen Versuchen über einen magneto-elektrischen Richteffekt", *Z. Phys.*, **36**(4), 300-301, (1926). http://dx.doi.org/10.1007/BF01557844

[2] T. H. O'Dell, "The Electrodynamics of Continuous Media", North-Holland, Amsterdan, 1970.

[3] L. D. Landau, L. P. Pitaevskii, E. M. Lifshitz, "Electrodynamics of continuous media, Second Edition: Volume 8 (Course of Theoretical Physics)", Butterworth-Heinemann, 1984.

[4] M. Fiebig, N. A. Spaldin, "Current trends of the magnetoelectric effect", *Eur. Phys. J. B*, **71**(3), 293-297, (2009). http://dx.doi.org/10.1140/epjb/e2009-00266-4

[5] W. Eerenstein, N. D. Mathur, J. F. Scott, "Multiferroic and magnetoelectric materials", *Nature*, **442**(7104), 759-765, (2006). http://dx.doi.org/10.1038/nature05023

[6] C.-W. Nan, M. I. Bichurin, S. Dong, D. Viehland, G. Srinivasan, "Multiferroic magnetoelectric composites: Historical perspective, status, and future directions", *J. Appl. Phys.*, **103**(3), 031101-031135, (2008). http://dx.doi.org/10.1063/1.2836410

[7] J. Zhai, Z. Xing, S. Dong, J. Li, D. Viehland, "Magnetoelectric Laminate Composites: An Overview", *J. Am. Ceram. Soc.*, **91**(2), 351-358, (2008). http://dx.doi.org/10.1111/j.1551-2916.2008.02259.x

[8] M. Fiebig, "Revival of the magnetoelectric effect", *J. Phys. D: Appl. Phys.*, **38**(8), R123-R152, (2005). http://dx.doi.org/10.1088/0022-3727/38/8/R01

[9] J. Ma, J. Hu, Z. Li, C.-W. Nan, "Recent Progress in Multiferroic Magnetoelectric Composites: from Bulk to Thin Films", *Adv. Mater.*, **23**(9), 1062-1087, (2011). http://dx.doi.org/10.1002/adma.201003636

[10] M. Bichurin, D. Viehland, G. Srinivasan, "Magnetoelectric interactions in ferromagnetic-piezoelectric layered structures: Phenomena and devices", *J. Electroceram.*, **19**(4), 243-250, (2007). http://dx.doi.org/10.1007/s10832-007-9058-x

[11] G. Srinivasan, "Magnetoelectric Composites", *Annu. Rev. Mater. Res.*, **40** 153-178, (2010). http://dx.doi.org/10.1146/annurev-matsci-070909-104459

[12] S. Priya, R. Islam, S. Dong, D. Viehland, "Recent advancements in magnetoelectric particulate and laminate composites", *J. Electroceram*, **19**(1), 149-166, (2007). http://dx.doi.org/10.1007/s10832-007-9042-5

[13] M. Bichurin, V. Petrov, A. Zakharov, D. Kovalenko, S. C. Yang, D. Maurya, V. Bedekar, S. Priya, "Magnetoelectric Interactions in Lead-Based and Lead-Free Composites", *Materials*, **4**(4), 651-702, (2011). http://dx.doi.org/10.3390/ma4040651

[14] J. Ryu, S. Priya, K. Uchino, H.-E. Kim, "Magnetoelectric Effect in Composites of Magnetostrictive and Piezoelectric Materials", *J. Electroceram.*, **8**(2), 107-119, (2002). http://dx.doi.org/10.1023/a:1020599728432

[15] D. C. Lupascu, H. Wende, M. Etier, A. Nazrabi, I. Anusca, H. Trivedi, V. V. Shvartsman, J. Landers, S. Salamon, C. Schmitz-Antoniak, "Measuring the magnetoelectric effect across scales", *GAMM-Mitt.*, **38**(1), 25-74, (2015). http://dx.doi.org/10.1002/gamm.201510003

[16] R. C. Kambale, D.-Y. Jeong, J. Ryu, "Current Status of Magnetoelectric Composite Thin/Thick Films", *Adv. Cond. Matter Phys.*, **2012** 824643-824657, (2012). http://dx.doi.org/10.1155/2012/824643

[17] M. Vopsaroiu, J. Blackburn, M. G. Cain, "Emerging Technologies and Opportunities Based on the Magneto-Electric Effect in Multiferroic Composites", *MRS Proceedings*, **1161** 1161-I05-04, (2009). http://dx.doi.org/10.1557/PROC-1161-I05-04

[18] Y. Wang, J. Hu, Y. Lin, C.-W. Nan, "Multiferroic magnetoelectric composite nanostructures", *NPG Asia Mater.*, **2**(2), 61-68, (2010). http://dx.doi.org/10.1038/asiamat.2010.32

[19] R. A. Islam, S. Priya, "Progress in Dual (Piezoelectric-Magnetostrictive) Phase Magnetoelectric Sintered Composites", *Adv. Cond. Matter Phys.*, **2012** 1-29, (2012). http://dx.doi.org/10.1155/2012/320612

[20] L. W. Martin, R. Ramesh, "Multiferroic and magnetoelectric heterostructures", *Acta Mater.*, **60**(6–7), 2449-2470, (2012). http://dx.doi.org/10.1016/j.actamat.2011.12.024

[21] S.-W. Cheong, M. Mostovoy, "Multiferroics: a magnetic twist for ferroelectricity", *Nat. Mater.*, **6**(1), 13-20, (2007). http://dx.doi.org/10.1038/nmat1804

[22] G. Lawes, G. Srinivasan, "Introduction to magnetoelectric coupling and multiferroic films", *J. Phys. D: Appl. Phys.*, **44**(24), 243001, (2011). http://dx.doi.org/10.1088/0022-3727/44/24/243001

[23] Ü. Özgür, Y. Alivov, H. Morkoç, "Microwave ferrites, part 2: passive components and electrical tuning", *J. Mater. Sci. Mater. Electron.*, **20**(10), 911-951, (2009). http://dx.doi.org/10.1007/s10854-009-9924-1

[24] M. M. Vopson, "Fundamentals of Multiferroic Materials and Their Possible Applications", *Crit. Rev. Solid State Mater. Sci.*, **40**(4), 223-250, (2015). http://dx.doi.org/10.1080/10408436.2014.992584

[25] N. X. Sun, G. Srinivasan, " Voltage Control of Magnetism in Multiferroic Heterostructures and Devices", *Spin*, **02**(03), 12240004, (2012). http://dx.doi.org/10.1142/S2010324712400048

[26] N. A. Spaldin, M. Fiebig, "The Renaissance of Magnetoelectric Multiferroics", *Science*, **309**(5733), 391-392, (2005). http://dx.doi.org/10.1126/science.1113357

[27] R. Ramesh, N. A. Spaldin, "Multiferroics: progress and prospects in thin films", *Nat. Mater.*, **6**(1), 21-29, (2007). http://dx.doi.org/10.1038/nmat1805

[28] R. Ramesh, "Materials science: Emerging routes to multiferroics", *Nature*, **461**(7268), 1218-1219, (2009). http://dx.doi.org/10.1038/4611218a

[29] S. Picozzi, C. Ederer, "First principles studies of multiferroic materials ", *J. Phys.: Condens. Matter*, **21**(30), 303201-303237, (2009). http://dx.doi.org/10.1088/0953-8984/21/30/303201

[30] R. Grössinger, G. V. Duong, R. Sato-Turtelli, "The physics of magnetoelectric composites", *J. Mag. Mag. Mat.*, **320**(14), 1972-1977, (2008). http://dx.doi.org/10.1016/j.jmmm.2008.02.031

[31] Y. Zhou, D. Maurya, Y. Yan, G. Srinivasan, E. Quandt, S. Priya, "Self-Biased Magnetoelectric Composites: An Overview and Future Perspectives", *Energy Harvesting Syst.*, **3**(1), 1-42, (2015). http://dx.doi.org/10.1515/ehs-2015-0003

[32] W. Junling, "Multiferroic Materials

Properties, Techniques, and Applications", CRC Press, 2016. http://dx.doi.org/10.1201/9781315372532

[33] M. Fiebig, T. Lottermoser, D. Meier, M. Trassin, "The evolution of multiferroics", *Nat. Rev. Mater.*, **1** 16046-16059, (2016). http://dx.doi.org/10.1038/natrevmats.2016.46

[34] L. W. Martin, S. P. Crane, Y. H. Chu, M. B. Holcomb, M. Gajek, M. Huijben, C. H. Yang, N. Balke, R. Ramesh, "Multiferroics and magnetoelectrics: thin films and nanostructures", *J. Phys.: Condens. Matter*, **20**(43), 434220-434232, (2008). http://dx.doi.org/10.1088/0953-8984/20/43/434220

[35] C. A. F. Vaz, J. Hoffman, C. H. Ahn, R. Ramesh, "Magnetoelectric Coupling Effects in Multiferroic Complex Oxide Composite Structures", *Adv. Mater.*, **22**(26-27), 2900-2918, (2010). http://dx.doi.org/10.1002/adma.200904326

[36] H. Palneedi, V. Annapureddy, S. Priya, J. Ryu, "Status and Perspectives of Multiferroic Magnetoelectric Composite Materials and Applications", *Actuators*, **5**(1), 9-39, (2016). http://dx.doi.org/10.3390/act5010009

[37] F. Matsukura, Y. Tokura, H. Ohno, "Control of magnetism by electric fields", *Nat. Nano.*, **10**(3), 209-220, (2015). http://dx.doi.org/10.1038/nnano.2015.22

[38] S. Dong, J.-M. Liu, S.-W. Cheong, Z. Ren, "Multiferroic materials and magnetoelectric physics: symmetry, entanglement, excitation, and topology", *Adv. Phys.*, **64**(5-6), 519-626, (2015). http://dx.doi.org/10.1080/00018732.2015.1114338

[39] M. I. Bichurin, V. M. Petrov, R. V. Petrov, "Direct and inverse magnetoelectric effect in layered composites in electromechanical resonance range: A review", *J. Mag. Mag. Mat.*, **324**(21), 3548-3550, (2012). http://dx.doi.org/10.1016/j.jmmm.2012.02.086

[40] M. I. Bichurin, V. M. Petrov, S.Priya, *Chapter 12 Magnetoelectric Multiferroic Composites*. In: M. Lallart, editor. *Ferroelectrics - Physical Effects*: InTech; (2011) http://dx.doi.org/10.5772/16415

[41] K.-H. Cho, M. I. Bichurin, V. M. Petrov, A. Bhalla, S. Priya, "Magnetoelectric Laminate Composite: Effect of Piezoelectric Layer on Magnetoelectric Properties", *Ferroelectrics*, **473**(1), 110-128, (2014). http://dx.doi.org/10.1080/00150193.2014.923670

[42] T. H. O'Dell, "The field invariants in a magneto-electric medium", *Phil. Mag.*, **8**(87), 411-418, (1963). http://dx.doi.org/10.1080/14786436308211142

[43] M. I. Bichurin, V. M. Petrov, D. A. Filippov, G. Srinivasan, "Magnetoelectric effect in composite materials *(em russo)*," Veliki Noogorod, 2005.

[44] W. F. B. Jr., R. M. Hornreich, S. Shtrikman, "Upper Bound on the Magnetoelectric Susceptibility", *Phys. Rev.*, **168**(2), 574-577, (1968). http://dx.doi.org/10.1103/PhysRev.168.574

[45] N. A. Spaldin, R. Ramesh, "Electric-Field Control of Magnetism in Complex Oxide Thin Films", *MRS Bull.* , **33** 1047-1050, (2008). http://dx.doi.org/10.1557/mrs2008.224

[46] G. A. Gehring, "On the microscopic theory of the magnetoelectric effect", *Ferroelectrics*, **161**(1), 275-285, (1994). http://dx.doi.org/10.1080/00150199408213376

[47] N. A. Hill, "Why Are There so Few Magnetic Ferroelectrics?", *J. Phys. Chem. B*, **104**(29), 6694-6709, (2000). http://dx.doi.org/10.1021/jp000114x

[48] J.-P. Rivera, "A short review of the magnetoelectric effect and related experimental techniques on single phase (multi-) ferroics ", *Eur. Phys. J. B*, **71**(3), 299-313, (2009). http://dx.doi.org/10.1140/epjb/e2009-00336-7

[49] J. P. Rivera, "On definitions, units, measurements, tensor forms of the linear magnetoelectric effect and on a new dynamic method applied to Cr-Cl boracite", *Ferroelectrics*, **161**(1), 165-180, (1994). http://dx.doi.org/10.1080/00150199408213365

[50] H. Grimmer, "The forms of tensors describing magnetic, electric and toroidal properties", *Ferroelectrics*, **161**(1), 181-189, (1994). http://dx.doi.org/10.1080/00150199408213366

[51] J. V. Suchtelen, "Product properties: a new application of composite materials", *Philips Res. Rep.*, **27**(1), 28-37, (1972).

[52] J. v. d. Boomgard, A. M. J. G. v. Run, J. V. Suchtelen, "Piezoelectric-piezomagnetic composites with magnetoelectric effect", *Ferroelectrics*, **14**(1), 727-728, (1976). http://dx.doi.org/10.1080/00150197608236711

[53] C.-W. Nan, "Magnetoelectric effect in composites of piezoelectric and piezomagnetic phases", *Phys. Rev. B*, **50**(9), 6082-6088, (1994). http://dx.doi.org/10.1103/PhysRevB.50.6082

[54] C.-W. Nan, "Physics of inhomogeneous inorganic materials", *Prog. Mater. Sci.*, **37**(1), 1-116, (1993). http://dx.doi.org/10.1016/0079-6425(93)90004-5

[55] M. I. Bichurin, V. M. Petrov, G. Srinivasan, "Theory of low-frequency magnetoelectric effects in ferromagnetic-ferroelectric layered composites ", *J. Appl. Phys.*, **92**(12), 7681-7683, (2002). http://dx.doi.org/10.1063/1.1522834

[56] M. I. Bichurin, V. M. Petrov, G. Srinivasan, "Theory of low-frequency magnetoelectric coupling in magnetostrictive-piezoelectric bilayers", *Phys. Rev. B*, **68**(5), 054402-054414, (2003). http://dx.doi.org/10.1103/PhysRevB.68.054402

[57] G. V. Duong, R. Groessinger, M. Schoenhart, D. Bueno-Basques, "The lock-in technique for studying magnetoelectric effect", *J. Mag. Mag. Mat.*, **316**(2), 390-393, (2007). http://dx.doi.org/10.1016/j.jmmm.2007.03.185

[58] X. Zhuang, M. L. C. Sing, C. Cordier, S. Saez, C. Dolabdjian, J. Das, J. Gao, J. Li, D. Viehland, "Analysis of Noise in Magnetoelectric Thin-Layer Composites Used as Magnetic Sensors", *IEEE Sens. J.*, **11**(10), 2183-2188, (2011). http://dx.doi.org/10.1109/JSEN.2011.2114648

[59] Y. J. Wang, J. Q. Gao, M. H. Li, Y. Shen, D. Hasanyan, J. F. Li, D. Viehland, "A review on equivalent magnetic noise of magnetoelectric laminate sensors", *Phil. Trans. R. Soc. A*, **372**(2009), 20120455-20120467, (2014). http://dx.doi.org/10.1098/rsta.2012.0455

[60] Z. P. Xing, J. Y. Zhai, S. X. Dong, J. F. Li, D. Viehland, W. G. Odendaal, "Modeling and detection of quasi-static nanotesla magnetic field variations using magnetoelectric laminate sensors", *Meas. Sci. Technol.*, **19**(1), 015206-015214, (2008). http://dx.doi.org/10.1088/0957-0233/19/1/015206

[61] Y. Wang, D. Gray, D. Berry, J. Gao, M. Li, J. Li, D. Viehland, "An Extremely Low Equivalent Magnetic Noise Magnetoelectric Sensor", *Adv. Mater.*, **23**(35), 4111–4114, (2011). http://dx.doi.org/10.1002/adma.201100773

[62] R. Jahns, H. Greve, E. Woltermann, E. Quandt, R. H. Knochel, "Noise Performance of Magnetometers With Resonant Thin-Film Magnetoelectric Sensors", *IEEE T. Instrum. Meas.*, **60**(8), 2995-3001, (2011). http://dx.doi.org/10.1109/TIM.2011.2122410

[63] R. E. Newnham, D. P. Skinner, L. E. Cross, "Connectivity and piezoelectric-pyroelectric composites", *Mater. Res. Bull.*, **13**(5), 525-536, (1978). http://dx.doi.org/10.1016/0025-5408(78)90161-7

[64] S. N. Babu, T. Bhimasankaram, S. V. Suryanarayana, "Magnetoelectric effect in metal-PZT laminates", *Bull. Mater. Sci.*, **28**(5), 419-422, (2004). http://dx.doi.org/10.1007/BF02711230

[65] C. P. Zhao, F. Fang, W. Yang, "A dual-peak phenomenon of magnetoelectric coupling in laminated Terfenol-D/PZT/Terfenol-D composites", *Smart Mater. Struct.*, **19**(12), 125004-125010, (2010). http://dx.doi.org/10.1088/0964-1726/19/12/125004

[66] J. Ryu, A. V. Carazo, K. Uchino, H.-E. Kim, "Magnetoelectric Properties in Piezoelectric and Magnetostrictive Laminate Composites", *Jpn. J. Appl. Phys.*, **40**(8), 4948-4951, (2001). http://dx.doi.org/10.1143/JJAP.40.4948

[67] A. H. Meitzler, H. F. Tiersten, A. W. Warner, D. Berlincourt, G. A. Coquin, F. S. Welsh, "IEEE Standard on Piezoelectricity", *ANSI/IEEE Std 176-1987*, 1-74, (1988). http://dx.doi.org/10.1109/IEEESTD.1988.79638

[68] M. Zgonik, P. Bernasconi, M. Duelli, R. Schlesser, P. Günter, M. H. Garrett, D. Rytz, Y. Zhu, X. Wu, "Dielectric, elastic, piezoelectric, electro-optic, and elasto-optic tensors of BaTiO_{3} crystals", *Phys. Rev. B*, **50**(9), 5941-5949, (1994). http://dx.doi.org/10.1103/PhysRevB.50.5941

[69] H. Xiao-Kang, Z. Li-Bo, W. Qiong-Shui, Z. Li-Yan, Z. Ke, L. Yu-Long, "Determination of elastic, piezoelectric, and dielectric constants of an R:BaTiO3 single crystal by Brillouin scattering ", *Chin. Phys. B*, **21**(6), 067801, (2012). http://dx.doi.org/10.1088/1674-1056/21/6/067801

[70] R. S. Weis, T. K. Gaylord, "Lithium niobate: Summary of physical properties and crystal structure", *Appl. Phys. A: Mater. Sci. Process.*, **37**(4), 191-203, (1985). http://dx.doi.org/10.1007/bf00614817

[71] P. Davulis, J. A. Kosinski, M. P. da Cunha, "GaPO4 Stiffness and Piezoelectric Constants Measurements using the Combined Thickness Excitation and Lateral Field Technique", *Int. Freq. Control Symposium and Expo., 2006 IEEE*, 664-669, (2006). http://dx.doi.org/10.1109/FREQ.2006.275466

[72] W. Wallnöfer, P. W. Krempl, A. Asenbaum, "Determination of the elastic and photoelastic constants of quartz-type GaPO4 by Brillouin scattering", *Phys. Rev. B*, **49**(15), 10075-10080, (1994). http://dx.doi.org/10.1103/PhysRevB.49.10075

[73] M. Šulca, J. Erharta, J. Noseka, "Interferometric Measurement of the Temperature Dependence of Piezoelectric Coefficients for PZN-8%PT Single Crystals", *Ferroelectrics*, **293**(1), 283-290, (2003). http://dx.doi.org/10.1080/00150190390238612

[74] D.-S. Paik, S.-E. Park, T. R. Shrout, W. Hackenberger, "Dielectric and piezoelectric properties of perovskite materials at cryogenic temperatures", *J. Mater. Sci.*, **34**(3), 469-473, (1999). http://dx.doi.org/10.1023/A:1004578225228

[75] M. Shanthi, L. C. Lim, K. K. Rajan, J. Jin, "Complete sets of elastic, dielectric, and piezoelectric properties of flux-grown [011]-poled Pb(Mg1⁄3Nb2⁄3)O3-(28–32)%PbTiO3 single crystals", *Appl. Phys. Lett.*, **92**(14), 142906, (2008). http://dx.doi.org/10.1063/1.2907702

[76] S. Priya, S. Nahm, "Lead-Free Piezoelectrics", Springer-Verlag New York, 2012. http://dx.doi.org/10.1007/978-1-4419-9598-8

[77] S. S. Guo, S. G. Lu, Z. Xu, X. Z. Zhao, S. W. Or, "Enhanced magnetoelectric effect in Terfenol-D and flextensional cymbal laminates ", *Appl. Phys. Lett.*, **88**(18), 182906-182908, (2006). http://dx.doi.org/10.1063/1.2200389

[78] J. G. Wan, Z. Y. Li, Y. Wang, M. Zeng, G. H. Wang, J.-M. Liu, "Strong flexural resonant magnetoelectric effect in Terfenol-D⁄epoxy-Pb(Zr,Ti)O3 bilayer ", *Appl. Phys. Lett.*, **86**(20), 202504-202506, (2005). http://dx.doi.org/10.1063/1.1935040

[79] S. Dong, J.-F. Li, D. Viehland, "Longitudinal and transverse magnetoelectric voltage coefficients of magnetostrictive/piezoelectric laminate composite: theory ", *IEEE Trans. Ultrason. Ferroelectr. Freq. Control*, **50**(10), 1253-1261 (2003). http://dx.doi.org/10.1109/TUFFC.2003.1244741

[80] S. Dong, J.-F. Li, D. Viehland, "Ultrahigh magnetic field sensitivity in laminates of TERFENOL-D and Pb(Mg1/3Nb2/3)O3–PbTiO3 crystals ", *Appl. Phys. Lett.*, **83**(11), 2265-2267, (2003). http://dx.doi.org/10.1063/1.1611276

[81] S. Dong, J. Cheng, J. F. Li, D. Viehland, "Enhanced magnetoelectric effects in laminate composites of Terfenol-D/Pb(Zr,Ti)O3 under resonant drive ", *Appl. Phys. Lett.*, **83**(23), 4812-4814, (2003). http://dx.doi.org/10.1063/1.1631756

[82] J. Zhai, S. Dong, Z. Xing, J. Li, D. Viehland, "Giant magnetoelectric effect in Metglas/polyvinylidene-fluoride laminates ", *Appl. Phys. Lett.*, **89**(8), 083507-083509, (2006). http://dx.doi.org/10.1063/1.2337996

[83] Y. Yang, J. Gao, Z. Wang, M. Li, J.-F. Li, J. Das, D. Viehland, "Effect of heat treatment on the properties of Metglas foils, and laminated magnetoelectric composites made thereof", *Mater. Res. Bull.*, **46**(2), 266-270, (2011). http://dx.doi.org/10.1016/j.materresbull.2010.10.015

[84] U. Laletsin, N. Padubnaya, G. Srinivasan, C. P. DeVreugd, "Frequency dependence of magnetoelectric interactions in layered structures of ferromagnetic alloys and piezoelectric oxides ", *Appl. Phys. A*, **78**(1), 33-36, (2004). http://dx.doi.org/10.1007/s00339-003-2293-3

[85] http://www.Metglas.com/products/magnetic_materials/,

[86] S. Dong, J. Zhai, J. Li, D. Viehland, "Near-ideal magnetoelectricity in high-permeability magnetostrictive/piezofiber laminates with a (2-1) connectivity.", *Appl. Phys. Lett.*, **89**(25), 252904-252906, (2006). http://dx.doi.org/10.1063/1.2420772

[87] G. Sreenivasulu, S. K. Mandal, S. Bandekar, V. M. Petrov, G. Srinivasan, "Low-frequency and resonance magnetoelectric effects in piezoelectric and functionally stepped ferromagnetic layered composites", *Phys. Rev. B*, **84**(14), 144426-144431, (2011). http://dx.doi.org/10.1103/PhysRevB.84.144426

[88] J. Wang, Y. Zhang, J. Ma, Y. Lin, C. W. Nan, "Magnetoelectric behavior of BaTiO3 films directly grown on CoFe2O4 ceramics ", *J. Appl. Phys.*, **104**(1), 014101-014105, (2008). http://dx.doi.org/10.1063/1.2949256

[89] T. Kiyomiya, Y. Yamada, Y. Matsuo, H. Wakiwaka, Y. Torii, M. Makimura, "Magnetostrictive properties of Tb-Fe and Tb-Fe-Co films", *Electron. Comm. Jpn.*, **91**(5), 49-55, (2008). http://dx.doi.org/10.1002/ecj.10115

[90] G. Sreenivasulu, U. Laletin, V. M. Petrov, V. V. Petrov, G. Srinivasan, "A permendur-piezoelectric multiferroic composite for low-noise ultrasensitive magnetic field sensors", *Appl. Phys. Lett.*, **100**(17), 173506-173510, (2012). http://dx.doi.org/10.1063/1.4705305

[91] M. Matsumoto, T. Kubota, M. Yokoyama, T. Okazaki, Y. Furuya, A. Makino, M. Shimada, "Magnetic Properties of Rapidly Solidified Ribbon of Fe49Co49V2 and Spark-Plasma-Sintered Pellet of Its Powder", *Mater. Trans.*, **51**(10), 1883-1886, (2010). http://dx.doi.org/10.2320/matertrans.M2010047

[92] D. A. Burdin, D. V. Chashin, N. A. Ekonomov, L. Y. Fetisov, Y. K. Fetisov, G. Sreenivasulu, G. Srinivasan, "Nonlinear magneto-electric effects in ferromagnetic-piezoelectric composites", *J. Mag. Mag. Mat.*, **358–359** 98-104, (2014). http://dx.doi.org/10.1016/j.jmmm.2014.01.062

[93] A. E. Clark, M. Wun-Fogle, J. B. Restorff, T. A. Lograsso, J. R. Cullen, "Effect of quenching on the magnetostriction on Fe_{1-x}Ga _x (0.13x<0.21)", *IEEE Trans. Magn.*, **37**(4), 2678-2680, (2001). http://dx.doi.org/10.1109/20.951272

[94] A. E. Clark, M. Wun-Fogle, J. B. Restorff, T. A. Lograsso, "Magnetostrictive Properties of Galfenol Alloys Under Compressive Stress", *Mater. Trans.*, **43**(5), 881-886, (2002). http://dx.doi.org/10.2320/matertrans.43.881

[95] S. Dong, J.-F. Li, D. Viehland, "Magnetoelectric coupling, efficiency, and voltage gain effect in piezoelectric-piezomagnetic laminate composites ", *J. Mater. Sci.*, **41**(1), 97-106, (2006). http://dx.doi.org/10.1007/s10853-005-5930-8

[96] G. Srinivasan, I. V. Zavislyak, A. S. Tatarenko, "Millimeter-wave magnetoelectric effects in bilayers of barium hexaferrite and lead zirconate titanate ", *Appl. Phys. Lett.*, **89**(15), 152508-152510, (2006). http://dx.doi.org/10.1063/1.2360901

[97] G. Srinivasan, E. T. Rasmussen, J. Gallegos, R. Srinivasan, Y. I. Bokhan, V. M. Laletin, "Magnetoelectric bilayer and multilayer structures of magnetostrictive and piezoelectric oxides", *Phys. Rev. B*, **64**(21), 214408-214413, (2001). http://dx.doi.org/10.1103/PhysRevB.64.214408

[98] G. Srinivasan, C. P. DeVreugd, C. S. Flattery, V. M. Laletsin, N. Paddubnaya, "Magnetoelectric interactions in hot-pressed nickel zinc ferrite and lead zirconante titanate composites ", *Appl. Phys. Lett.*, **85**(13), 2550-2552, (2004). http://dx.doi.org/10.1063/1.1795365

[99] G. Liu, C.-W. Nan, N. Cai, Y. Lin, "Calculations of giant magnetoelectric effect in multiferroic composites of rare-earth-iron alloys and PZT by finite element method", *Int. J. Solids Struct.*, **41**(16-17), 4423-4434, (2004). http://dx.doi.org/10.1016/j.ijsolstr.2004.03.022

[100] S. Dong, J. Zhai, F. Bai, J.-F. Li, D. Viehland, "Push-pull mode magnetostrictive/piezoelectric laminate composite with an enhanced magnetoelectric voltage coefficient ", *Appl. Phys. Lett.*, **87**(6), 062502-062504, (2005). http://dx.doi.org/10.1063/1.2007868

[101] D. R. Tilley, J. F. Scott, "Frequency dependence of magnetoelectric phenomena in BaMnF4", *Phys. Rev. B*, **25**(5), 3251-3260, (1982). http://dx.doi.org/10.1103/PhysRevB.25.3251

[102] M. I. Bichurin, V. M. Petrov, O. V. Ryabkov, S. V. Averkin, G. Srinivasan, "Theory of magnetoelectric effects at magnetoacoustic resonance in single-crystal ferromagnetic-ferroelectric heterostructures", *Phys. Rev. B*, **72**(6), 060408-060411, (2005). http://dx.doi.org/10.1103/PhysRevB.72.060408

[103] M. I. Bichurin, V. M. Petrov, Y. V. Kiliba, G. Srinivasan, "Magnetic and magnetoelectric susceptibilities of a ferroelectric/ferromagnetic composite at microwave frequencies", *Phys. Rev. B*, **66**(13), 134404-134413, (2002). http://dx.doi.org/10.1103/PhysRevB.66.134404

[104] S. Timoshenko, "Vibration Problems in Engineering", D. Van Nostrand,New York, 1961.

[105] U. Laletsin, N. Padubnaya, G. Srinivasan, C. P. DeVreugd, "Frequency dependence of magnetoelectric interactions in layered structures of ferromagnetic alloys and piezoelectric oxides", *Appl. Phys. A*, **78**(1), 33-36, (2004). http://dx.doi.org/10.1007/s00339-003-2293-3

[106] Y. K. Fetisov, K. E. Kamentsev, A. Y. Ostashchenko, G. Srinivasan, "Wide-band magnetoelectric characterization of a ferrite-piezoelectric multilayer using a pulsed magnetic field", *Solid State Commun.*, **132**(1), 13-17, (2004). http://dx.doi.org/10.1016/j.ssc.2004.07.019

[107] N. Cai, C.-W. Nan, J. Zhai, Y. Lin, "Large high-frequency magnetoelectric response in laminated composites of piezoelectric ceramics, rare-earth iron alloys and polymer ", *Appl. Phys. Lett.*, **84**(18), 3516-3518, (2004). http://dx.doi.org/10.1063/1.1739277

[108] H. Greve, E. Woltermann, H.-J. Quenzer, B. Wagner, E. Quandt, "Giant magnetoelectric coefficients in (Fe90Co10)78Si12B10-AlN thin film composites", *Appl. Phys. Lett.*, **96**(18), 182501-182503, (2010). http://dx.doi.org/10.1063/1.3377908

[109] G. Liu, X. Li, J. Chen, H. Shi, W. Xiao, S. Dong, "Colossal low-frequency resonant magnetomechanical and magnetoelectric effects in a three-phase ferromagnetic/elastic/piezoelectric composite", *Appl. Phys. Lett.*, **101**(14), 142904-142907, (2012). http://dx.doi.org/10.1063/1.4756919

[110] H. Greve, E. Woltermann, R. Jahns, S. Marauska, B. Wagner, R. Knöchel, M. Wuttig, E. Quandt, "Low damping resonant magnetoelectric sensors", *Appl. Phys. Lett.*, **97**(15), 152503-152505, (2010). http://dx.doi.org/10.1063/1.3497277

[111] Y. Zhang, G. Liu, H. Shi, W. Xiao, Y. Zhu, M. Li, M. Li, J. Liu, "Enhanced magnetoelectric effect in ferromagnetic–elastic–piezoelectric composites", *J. Alloy. Compd.*, **613** 93-95, (2014). http://dx.doi.org/10.1016/j.jallcom.2014.06.035

[112] C. Kirchhof, M. Krantz, I. Teliban, R. Jahns, S. Marauska, B. Wagner, R. Knöchel, M. Gerken, D. Meyners, E. Quandt, "Giant magnetoelectric effect in vacuum", *App. Phys. Lett.*, **102**(23), 232905-232908, (2013). http://dx.doi.org/10.1063/1.4810750

[113] M. Liu, O. Obi, J. Lou, Y. Chen, Z. Cai, S. Stoute, M. Espanol, M. Lew, X. Situ, K. S. Ziemer, V. G. Harris, N. X. Sun, "Giant Electric Field Tuning of Magnetic Properties in Multiferroic

Ferrite/Ferroelectric Heterostructures", *Adv. Funct. Mater.*, **19**(11), 1826-1831, (2009). http://dx.doi.org/10.1002/adfm.200801907

[114] S. Sherrit, B. K. Mukherjee, "Characterization of Piezoelectric Materials for Transducers", *arXiv*, (2007).

[115] W. P. Mason, "Physical Acoustics and the Properties of Solids (The Bell Telephone Laboratories Series)", Van Nostrand, 1958.

[116] T. Ikeda, "Fundamentals of Piezoelectricity", Oxford Science Publications, 1990.

[117] J. W. Morris, "Notes on the Thermodynamics of Solids (Chapter 15: Tensors and Tensor Properties)", Department of Materials Science & Engineering, University of Califormia, Berkeley, 2008.

[118] D. Damjanovic, "Ferroelectric, dielectric and piezoelectric properties of ferroelectric thin films and ceramics ", *Rep. Prog. Phys.*, **61**(9), 1267, (1998). http://dx.doi.org/10.1088/0034-4885/61/9/002

[119] R. F. Tinder, "Tensor Properties of Solids: Phenomenological Development of the Tensor Properties of Crystals", Morgan & Claypool Publishers, 2008.

[120] J. F. Nye, "Physical Properties of Crystals: Their Representation by Tensors and Matrices", Oxford University Press, 1985.

[121] "IRE Standards on Piezoelectric Crystals: Determination of the Elastic, Piezoelectric, and Dielectric Constants-The Electromechanical Coupling Factor, 1958", *Proceedings of the IRE*, **46**(4), 764-778, (1958). http://dx.doi.org/10.1109/JRPROC.1958.286778

[122] H.-Y. Kuo, A. Slinger, K. Bhattacharya, "Optimization of magnetoelectricity in piezoelectric–magnetostrictive bilayers", *Smart Mater. Struct.*, **19**(12), 125010-125022, (2010). http://dx.doi.org/10.1088/0964-1726/19/12/125010

[123] D. A. Burdin, D. V. Chashin, N. A. Ekonomov, L. Y. Fetisov, Y. K. Fetisov, G. Sreenivasulu, G. Srinivasan, "Nonlinear magneto-electric effects in ferromagnetic-piezoelectric composites", *J. Mag. Mag. Mat.*, **358-359** 98-104, (2014). http://dx.doi.org/10.1016/j.jmmm.2014.01.06

[124] M. Bichurin, V. Petrov, "Modeling of Magnetoelectric Effects in Composites", Springer Netherlands, 2014. http://dx.doi.org/10.1007/978-94-017-9156-4

[125] Y. Benveniste, "Magnetoelectric effect in fibrous composites with piezoelectric and piezomagnetic phases", *Phys. Rev. B*, **51**(22), 16424-16427, (1995). http://dx.doi.org/10.1103/PhysRevB.51.16424

[126] C. W. Nan, M. Li, J. H. Huang, "Calculations of giant magnetoelectric effects in ferroic composites of rare-earth–iron alloys and ferroelectric polymers", *Phys. Rev. B*, **63**(14), 144415, (2001). http://dx.doi.org/10.1103/PhysRevB.63.144415

[127] J. A. Osborn, "Demagnetizing Factors of the General Ellipsoid", *Phys. Rev.*, **67**(11-12), 351-357, (1945). http://dx.doi.org/10.1103/PhysRev.67.351

[128] A. A. Timopheev, J. V. Vidal, A. L. Kholkin, N. A. Sobolev, "Direct and converse magnetoelectric effects in Metglas/LiNbO3/Metglas trilayers", *J. Appl. Phys.*, **114**(4), 044102-044108, (2013). http://dx.doi.org/10.1063/1.4816400

[129] Y. Wang, S. W. Or, H. L. W. Chan, X. Zhao, H. Luo, "Enhanced magnetoelectric effect in longitudinal-transverse mode Terfenol-D/Pb(Mg1/3Nb2/3)O3–PbTiO3 laminate composites with optimal crystal cut", *J. Appl. Phys.*, **103**(12), 124511, (2008). http://dx.doi.org/10.1063/1.2943267

[130] C.-S. Park, K.-H. Cho, M. A. Arat, J. Evey, S. Priya, "High magnetic field sensitivity in Pb(Zr,Ti)O3–Pb(Mg1/3Nb2/3)O3 single crystal/Terfenol-D/Metglas magnetoelectric laminate composites", *J. Appl. Phys.*, **107**(9), 094109, (2010). http://dx.doi.org/10.1063/1.3406142

[131] J. Lou, M. Liu, D. Reed, Y. Ren, N. X. Sun, "Giant Electric Field Tuning of Magnetism in Novel Multiferroic FeGaB/Lead Zinc Niobate–Lead Titanate (PZN-PT) Heterostructures", *Adv. Mater.*, **21**(46), 4711-4715, (2009). http://dx.doi.org/10.1002/adma.200901131

[132] H. F. Tian, T. L. Qu, L. B. Luo, J. J. Yang, S. M. Guo, H. Y. Zhang, Y. G. Zhao, J. Q. Li, "Strain induced magnetoelectric coupling between magnetite and BaTiO3", *Appl. Phys. Lett.*, **92**(6), 063507-063509, (2008). http://dx.doi.org/10.1063/1.2844858

[133] P. Yang, K. Zhao, Y. Yin, J. G. Wan, J. S. Zhu, "Magnetoelectric effect in magnetostrictive/piezoelectric laminate composite Terfenol-D⁄LiNbO3 [(zxtw)−129°⁄30°]", *Appl. Phys. Lett.*, **88**(17), 172903-172905, (2006). http://dx.doi.org/10.1063/1.2198486

[134] J. V. Vidal, A. A. Timopheev, A. L. Kholkin, N. A. Sobolev, "Anisotropy of the magnetoelectric effect in tri-layered composites based on single-crystalline piezoelectrics", *Vacuum*, **122, Part B** 286-292, (2015). http://dx.doi.org/10.1016/j.vacuum.2015.06.022

[135] G. Sreenivasulu, V. M. Petrov, L. Y. Fetisov, Y. K. Fetisov, G. Srinivasan, "Magnetoelectric interactions in layered composites of piezoelectric quartz and magnetostrictive alloys", *Phys. Rev. B*, **86**(21), 214405-214411, (2012). http://dx.doi.org/10.1103/PhysRevB.86.214405

[136] R. Viswan, D. Gray, Y. Wang, Y. Li, D. Berry, J. Li, D. Viehland, "Strong magnetoelectric coupling in highly oriented ZnO films deposited on Metglas substrates", *Phys. Status Solidi-R*, **5**(10-11), 391-393, (2011). http://dx.doi.org/10.1002/pssr.201105357

[137] G. Sreenivasulu, L. Y. Fetisov, Y. K. Fetisov, G. Srinivasan, "Piezoelectric single crystal langatate and ferromagnetic composites: Studies on low-frequency and resonance magnetoelectric effects", *Appl. Phys. Lett.*, **100**(5), 052901-052904, (2012). http://dx.doi.org/10.1063/1.3679661

[138] G. Sreenivasulu, P. Qu, E. Piskulich, V. M. Petrov, Y. K. Fetisov, A. P. Nosov, H. Qu, G. Srinivasan, "Shear strain mediated magneto-electric effects in composites of piezoelectric lanthanum gallium silicate or tantalate and ferromagnetic alloys", *App. Phys. Lett.*, **105**(3), 032409-032412, (2014). http://dx.doi.org/10.1063/1.4891536

[139] R. Tinder, "Tensor Properties of Solids", Morgan & Claypool, 2007. http://dx.doi.org/10.2200/S00057ED1V01Y200712ENG04

[140] F. Fang, C. Zhao, W. Yang, "Thickness effects on magnetoelectric coupling for Metglas/PZT/Metglas laminates", *Sci. China Phys. Mech. Astron.*, **54**(4), 581-585, (2011). http://dx.doi.org/10.1007/s11433-011-4268-2

[141] D. Hasanyan, J. Gao, Y. Wang, R. Viswan, Y. S. M. Li, J. Li, D. Viehland, "Theoretical and experimental investigation of magnetoelectric effect for bending-tension coupled modes in magnetostrictive-piezoelectric layered composites", *J. Appl. Phys.*, **112**(1), 013908-013918, (2012). http://dx.doi.org/10.1063/1.4732130

[142] Y. Wang, D. Hasanyan, M. Li, J. Gao, J. Li, D. Viehland, H. Luo, "Theoretical model for geometry-dependent magnetoelectric effect in magnetostrictive/piezoelectric composites", *J. Appl. Phys.*, **111**(12), 124513-124518, (2012). http://dx.doi.org/10.1063/1.4729832

[143] http://bostonpiezooptics.com/crystal-quartz,

[144] R. T. Smith, F. S. Welsh, "Temperature Dependence of the Elastic, Piezoelectric, and Dielectric Constants of Lithium Tantalate and Lithium Niobate", *J. Appl. Phys.*, **42**(6), 2219-2230, (1971). http://dx.doi.org/10.1063/1.1660528

[145] A. Balatto, "Basic Material Quartz and Related Innovations", *Springer Series in Materials Science*, **114** 9-35, (2008). http://dx.doi.org/10.1007/978-3-540-68683-5_2

[146] J. Kushibiki, I. Takanaga, S. Nishiyama, "Accurate measurements of the acoustical physical constants of synthetic /spl alpha/-quartz for SAW devices ", *IEEE Trans. Ultrason., Ferroelectr., Freq. Control.*, **49**(1), 125 - 135 (2002). http://dx.doi.org/10.1109/58.981390

[147] P. M. Davulis, M. P. d. Cunha, "A full set of langatate high-temperature acoustic wave constants: elastic, piezoelectric, dielectric constants up to 900°C.", *IEEE Trans. Ultrason., Ferroelectr., Freq. Control.*, **60**(4), 824-33, (2013). http://dx.doi.org/10.1109/TUFFC.2013.2631

[148] Y. K. Fetisov, D. A. Burdin, D. V. Chashin, N. A. Ekonomov, "High-Sensitivity Wideband Magnetic Field Sensor Using Nonlinear Resonance Magnetoelectric Effect", *Sens. J., IEEE*, **14**(7), 2252-2256, (2014). http://dx.doi.org/10.1109/JSEN.2014.2309718

[149] M. Adachi, T. Kimura, W. Miyamoto, Z. Chen, A. Kawabata, "Dielectric, Elastic and Piezoelectric Properties of La3Ga5SiO14 (LANGASITE) Single Crystals", *J. Korean Phys. Soc.*, **32** S1274-S1277, (1998). http://dx.doi.org/10.3938/jkps.32.1274

[150] R. Tarumi, H. Nitta, H. Ogi, M. Hirao, "Low-temperature elastic constants and piezoelectric coefficients of langasite (La3Ga5SiO14)", *Philos. Mag.*, **91**(16), 2140-2153, (2011). http://dx.doi.org/10.1080/14786435.2010.549095

[151] A. Sotnikov, H. Schmidt, M. Weihnacht, E. Smirnova, T. Chemekova, Y. Makarov, "Elastic and piezoelectric properties of AlN and LiAlO2 single crystals.", *IEEE Trans. Ultrason., Ferroelectr., Freq. Control.*, **57**(4), 808-11, (2010). http://dx.doi.org/10.1109/TUFFC.2010.1485

[152] G. Bu, D. Ciplys, M. Shur, L. J. Schowalter, S. Schujman, R. Gaska, "Electromechanical coupling coefficient for surface acoustic waves in single-crystal bulk aluminum nitride", *Appl. Phys. Lett.*, **84**(23), 4611-4613, (2004). http://dx.doi.org/10.1063/1.1755843

[153] http://www.roditi.com/SingleCrystal/Lithium-Tantalate/LiTaO3-Properties.html,

[154] R. T. Smith, F. S. Welsh, "Temperature Dependence of the Elastic, Piezoelectric, and Dielectric Constants of Lithium Tantalate and Lithium Niobate", *Journal of Applied Physics*, **42**(6), 2219-2230, (1971). http://dx.doi.org/10.1063/1.1660528

[155] A. W. Warner, M. Onoe, G. A. Coquin, "Determination of Elastic and Piezoelectric Constants for Crystals in Class (3m)", *The Journal of the Acoustical Society of America*, **42**(6), 1223-1231, (1967). http://dx.doi.org/10.1121/1.1910709

[156] "Technical Publication TP-226 - Properties of Piezoelectricity Ceramics", Morgan Electro Ceramics,

[157] R. Zhang, B. Jiang, W. Cao, "Single-domain properties of 0.67Pb(Mg1/3Nb2/3)O3–0.33PbTiO3 single crystals under electric field bias", *Appl. Phys. Lett.*, **82**(5), 787-789, (2003). http://dx.doi.org/10.1063/1.1541937

[158] R. Zhang, B. Jiang, W. Cao, "Elastic, piezoelectric, and dielectric properties of multidomain 0.67Pb(Mg1/3Nb2/3)O3–0.33PbTiO3 single crystals", *J. Appl. Phys.*, **90**(7), 3471-3475, (2001). http://dx.doi.org/10.1063/1.1390494

[159] C. He, J. Weiping, W. Feifei, K. Zhu, Q. Jinhao, "Full tensorial elastic, piezoelectric, and dielectric properties characterization of [011]-poled PZN-9%PT single crystal", *IEEE Trans. Ultrason., Ferroelectr., Freq. Control.*, **58**(6), 1127-1130, (2011). http://dx.doi.org/10.1109/TUFFC.2011.1921

[160] R. Zhang, B. Jiang, W. Jiang, W. Cao, "Complete set of properties of 0.92Pb(Zn1/3Nb2/3)O3–0.08PbTiO3 single crystal with engineered domains", *Mater. Lett.*, **57**(7), 1305-1308, (2003). http://dx.doi.org/10.1016/S0167-577X(02)00976-X

[161] H.-M. Zhou, Y.-H. Zhou, X.-J. Zheng, Q. Ye, J. Wei, "A general 3-D nonlinear magnetostrictive constitutive model for soft ferromagnetic materials", *J. Mag. Mag. Mat.*, **321**(4), 281–290, (2009). http://dx.doi.org/10.1016/j.jmmm.2008.09.012

[162] P. Han, W. Yan, J. Tian, X. Huang, H. Pan, "Cut directions for the optimization of piezoelectric coefficients of lead magnesium niobate–lead titanate ferroelectric crystals", *Appl. Phys. Lett.*, **86**(5), 052902-052904, (2005). http://dx.doi.org/10.1063/1.1857085

[163] Y. Shen, K. L. McLaughlin, J. Gao, M. Li, J. Li, D. Viehland, "Effective optimization of magnetic noise for a Metglas/Pb(Zr,Ti)O3 magnetoelectric sensor array in an open environment", *Mater. Lett.*, **91**(0), 307-310, (2013). http://dx.doi.org/10.1016/j.matlet.2012.10.003

[164] Y. Wang, D. Gray, J. Gao, D. Berry, M. Li, J. Li, D. Viehland, H. Luo, "Improvement of magnetoelectric properties in Metglas/Pb(Mg1/3Nb2/3)O3–PbTiO3 laminates by poling optimization", *J. Alloys Compd.*, **519**(0), 1-3, (2012). http://dx.doi.org/10.1016/j.jallcom.2011.12.093

[165] M. M. Kumar, A. Srinivas, S. V. Suryanarayana, G. S. Kumar, T. Bhimasankaram, "An experimental setup for dynamic measurement of magnetoelectric effect", *Bull. Mater. Sci.*, **21**(3), 251-255, (1998). http://dx.doi.org/10.1007/BF02744978

[166] J. More-Chevalier, C. Cibert, R. Bouregba, G. Poullain, "Eddy currents: A misleading contribution when measuring magnetoelectric voltage coefficients of thin film devices", *J. Appl. Phys.*, **117**(15), 154104-154110, (2015). http://dx.doi.org/10.1063/1.4917534

[167] Y. Chen, S. M. Gillette, T. Fitchorov, L. Jiang, H. Hao, J. Li, X. Gao, A. Geiler, C. Vittoria, V. G. Harris, "Quasi-one-dimensional miniature multiferroic magnetic field sensor with high sensitivity at zero bias field ", *Appl. Phys. Lett.*, **99**(4), 042505, (2011). http://dx.doi.org/10.1063/1.3617434

[168] J. Gao, Z. Wang, Y. Shen, M. Li, Y. Wang, P. Finkel, J. Li, D. Viehland, "Self-powered low noise magnetic sensor", *Mater. Lett.*, **82**(0), 178-180, (2012). http://dx.doi.org/10.1016/j.matlet.2012.05.067

[169] J. Gao, Y. Shen, P. Finkel, J. Blottman, J. Li, D. Viehland, "Geomagnetic field tuned frequency multiplication in Metglas/Pb(Zr, Ti)O3 heterostructure", *Mater. Lett.*, **88**(0), 47-50, (2012). http://dx.doi.org/10.1016/j.matlet.2012.08.062

[170] C. A. Vaz, "Electric field control of magnetism in multiferroic heterostructures.", *J. Phys.: Cond. Matt.*, **24**(33), 333201, (2012). http://dx.doi.org/10.1088/0953-8984/24/33/333201

[171] M. Li, Y. Wang, D. Hasanyan, J. Li, D. Viehland, "Giant converse magnetoelectric effect in multi-push-pull mode Metglas/Pb(Zr,Ti)O3/Metglas laminates ", *Appl. Phys. Lett.*, **100**(13), 132904-132906, (2012). http://dx.doi.org/10.1063/1.3698114

[172] S.-E. Park, T. R. Shrout, "Ultrahigh strain and piezoelectric behavior in relaxor based ferroelectric single crystals ", *J. Appl. Phys.*, **82**(4), 1804, (1997). http://dx.doi.org/10.1063/1.365983

[173] M. Yachi, M. Ono, "The third overtone resonator using 36° rotated Y cut LiNbO3 crystal", *Ultrasonics Symposium, 1995. Proceedings., 1995 IEEE*, **2** 1003, (1995). http://dx.doi.org/10.1109/ULTSYM.1995.495732

[174] L. E. Myers, R. C. Eckardt, M. M. Fejer, R. L. Byer, W. R. Bosenberg, J. W. Pierce, "Quasi-phase-matched optical parametric oscillators in bulk periodically poled LiNbO3", *J. Opt. Soc. Am. B*, **12**(11), 2102-2116, (1995). http://dx.doi.org/10.1364/JOSAB.12.002102

[175] A. Heinrich, A. L. Hörner, A. Wixforth, B. Stritzker, "Pulsed laser deposition of La0.67Ca0.33MnO3 thin films on LiNbO3 and surface acoustic wave studies", *Thin Solid Films*, **510**(1-2), 77-81, (2006). http://dx.doi.org/10.1016/j.tsf.2005.12.165

[176] A. Kawamata, H. Hosaka, T. Morita, "Non-hysteresis and perfect linear piezoelectric performance of a multilayered lithium niobate actuator", *Sens. Actuators A Phys.*, **135**(2), 782-786, (2007). http://dx.doi.org/10.1016/j.sna.2006.08.025

[177] G. Matsunami, A. Kawamata, H. Hosaka, T. Morita, "Multilayered LiNbO3 actuator for XY-stage using a shear piezoelectric effect", *Sens. Actuators A Phys.*, **144**(2), 337-340, (2008). http://dx.doi.org/10.1016/j.sna.2008.02.006

[178] L. Dreher, M. Weiler, M. Pernpeintner, H. Huebl, R. Gross, M. S. Brandt, S. T. B. Goennenwein, "Surface acoustic wave driven ferromagnetic resonance in nickel thin films: Theory and experiment", *Phys. Rev. B*, **86**(13), 134415, (2012). http://dx.doi.org/10.1103/PhysRevB.86.134415

[179] N. Obata, T. Kawahata, R. Suzuki, K. Nishimura, H. Uchida, M. Inoue, "Fabrication and properties of InSb films with ion-beam sputtering for use in the amplification of magneto-surface-acoustic waves", *Phys. Stat. Sol. (a)*, **201**(8), 1973-1975, (2004). http://dx.doi.org/10.1002/pssa.200304681

[180] T. Wu, A. Bur, J. L. Hockel, K. Wong, T.-K. Chung, G. P. Carman, "Electrical and Mechanical Manipulation of Ferromagnetic Properties in Polycrystalline Nickel Thin Film", *IEEE Magn. Lett.*, **2** 6000104-6000104, (2011). http://dx.doi.org/10.1109/LMAG.2010.2100810

[181] A. W. Warner, M. Onoe, G. A. Coquin, "Determination of Elastic and Piezoelectric Constants for Crystals in Class (3m) ", *J. Acoust. Soc. Am.*, **42**(6), 1223-1231, (1967). http://dx.doi.org/10.1121/1.1910709

[182] W. Yue, J. Yi-jian, "Crystal orientation dependence of piezoelectric properties in LiNbO3 and LiTaO3", *Opt. Mater.*, **23**(1-2), 403-408, (2003). http://dx.doi.org/10.1016/s0925-3467(02)00328-2

[183] C. Zhang, W. Chen, J. Li, J. Yang, "Two-dimensional analysis of magnetoelectric effects in multiferroic laminated plates", *IEEE Trans. Ultrason. Ferroelectr. Freq. Control.*, **56**(5), 1046-1053 (2009). http://dx.doi.org/10.1109/TUFFC.2009.1137

[184] C. Zhang, W. Chen, C. Zhang, "Two-dimensional theory of piezoelectric plates considering surface effect", *Eur. J. Mech. - A/Solid.*, **41**(0), 50-57, (2013). http://dx.doi.org/10.1016/j.euromechsol.2013.02.005

[185] R. Zhang, B. Jiang, W. Cao, "Elastic, piezoelectric, and dielectric properties of multidomain 0.67Pb(Mg[sub 1/3]Nb[sub 2/3])O[sub 3]--0.33PbTiO[sub 3] single crystals", *J. Appl. Phys.*, **90**(7), 3471-3475, (2001). http://dx.doi.org/10.1063/1.1390494

[186] Z. Huang, "Theoretical modeling on the magnetization by electric field through product property", *J. Appl. Phys.*, **100**(11), 114104-114108, (2006). http://dx.doi.org/10.1063/1.2388125

[187] G. Wu, T. Nan, R. Zhang, N. Zhang, S. Li, N. X. Sun, "Inequivalence of direct and converse magnetoelectric coupling at electromechanical resonance", *Appl. Phys. Lett.*, **103**(18), 182905-182909, (2013). http://dx.doi.org/10.1063/1.4827875

[188] J.-P. Zhou, Y.-J. Ma, G.-B. Zhang, X.-M. Chen, "A uniform model for direct and converse magnetoelectric effect in laminated composite", *Appl. Phys. Lett.*, **104**(20), 202904-202908, (2014). http://dx.doi.org/10.1063/1.4878559

[189] M. Cochez, J. D. Foulon, A. Ibanez, A. Goiffon, E. Philippot, B. Capelle, A. Zarka, J. Schwartzel, J. Detaint, "Crystal growth and characterizations of a quartz-like material : GaPO4", *J. Phys. IV France*, **04** C2-183-C2-188, (1994). http://dx.doi.org/10.1051/jp4:1994222

[190] K.-H. Cho, S. Priya, "Direct and converse effect in magnetoelectric laminate composites", *Appl. Phys. Lett.*, **98**(23), 232904-232906, (2011). http://dx.doi.org/10.1063/1.3584863

[191] D. Rajaram Patil, Y. Chai, R. C. Kambale, B.-G. Jeon, K. Yoo, J. Ryu, W.-H. Yoon, D.-S. Park, D.-Y. Jeong, S.-G. Lee, J. Lee, J.-H. Nam, J.-H. Cho, B.-I. Kim, K. Hoon Kim, "Enhancement of resonant and non-resonant magnetoelectric coupling in multiferroic laminates with anisotropic piezoelectric properties", *Appl. Phys. Lett.*, **102**(6), 062909-062912, (2013). http://dx.doi.org/10.1063/1.4792590

[192] J. Zhai, Z. Xing, S. Dong, J. Li, D. Viehland, "Detection of pico-Tesla magnetic fields using magneto-electric sensors at room temperature", *Appl. Phys. Lett.*, **88**(6), 062510-062512, (2006). http://dx.doi.org/10.1063/1.2172706

[193] Z. Xing, J. Zhai, J. Li, D. Viehland, "Investigation of external noise and its rejection in magnetoelectric sensor design", *J. Appl. Phys.*, **106**(2), 024512-024519, (2009). http://dx.doi.org/10.1063/1.3176500

[194] Z. Fang, S. G. Lu, F. Li, S. Datta, Q. M. Zhang, M. El Tahchi, "Enhancing the magnetoelectric response of Metglas/polyvinylidene fluoride laminates by exploiting the flux concentration effect", *Appl. Phys. Lett.*, **95**(11), 112903-112905, (2009). http://dx.doi.org/10.1063/1.3231614

[195] J. Zhai, Z. Xing, S. Dong, J. Li, D. Viehland, "Thermal noise cancellation in symmetric magnetoelectric bimorph laminates", *Appl. Phys. Lett.*, **93**(7), 072906-072909, (2008). http://dx.doi.org/10.1063/1.2969794

[196] Y. Wang, M. Li, D. Hasanyan, J. Gao, J. Li, D. Viehland, "Geometry-induced magnetoelectric effect enhancement and noise floor reduction in Metglas/piezofiber sensors", *Appl. Phys. Lett.*, **101**(9), 092905-092908, (2012). http://dx.doi.org/10.1063/1.4737906

[197] F. Cong, J. Jie, M. Jiashuai, L. Di, X. Haiqing, Z. Xiangyong, L. Haosu, "Significant reduction of equivalent magnetic noise by in-plane series connection in magnetoelectric Metglas/Mn-doped Pb(Mg1/3Nb 2/3)O3 -PbTiO3 laminate composites", *J. Phys. D: Appl. Phys.*, **48**(46), 465002-465007, (2015). http://dx.doi.org/10.1088/0022-3727/48/46/465002

[198] J. Gao, J. Das, Z. Xing, J. Li, D. Viehland, "Comparison of noise floor and sensitivity for different magnetoelectric laminates", *J. Appl. Phys.*, **108**(8), 084509-084511, (2010). http://dx.doi.org/10.1063/1.3486483

[199] J. Gao, Y. Shen, Y. Wang, P. Finkel, J. Li, D. Viehland, "Magnetoelectric bending-mode structure based on Metglas/Pb(Zr,Ti)O(3) fiber laminates", *IEEE Trans. Ultrason. Ferroelectr. Freq. Control.*, **58**(8), 1545-1549, (2011). http://dx.doi.org/10.1109/tuffc.2011.1981

[200] J. Gao, Y. Wang, M. Li, Y. Shen, J. Li, D. Viehland, "Quasi-static ($f<10^{-2}$ Hz) frequency response of magnetoelectric composites based magnetic sensor", *Mater. Lett.*, **85** 84-87, (2012). http://dx.doi.org/10.1016/j.matlet.2012.06.100

[201] Y. Shen, J. Gao, L. Shen, D. Gray, J. Li, P. Finkel, D. Viehland, X. Zhuang, S. Saez, C. Dolabdjian, "Analysis of the environmental magnetic noise rejection by using two simple magnetoelectric sensors", *Sens. Actuators A Phys.*, **171**(2), 63-68, (2011). http://dx.doi.org/10.1016/j.sna.2011.08.013

[202] L. Y. Fetisov, N. S. Perov, Y. K. Fetisov, G. Srinivasan, V. M. Petrov, "Resonance magnetoelectric interactions in an asymmetric ferromagnetic-ferroelectric layered structure", *J. Appl. Phys.*, **109**(5), 053908-053911, (2011). http://dx.doi.org/10.1063/1.3553640

[203] V. D. Kugel, G. Rosenman, D. Shur, "Piezoelectric properties of bidomain LiNbO3 crystals", *J. Appl. Phys.*, **78**(9), 5592-5596, (1995). http://dx.doi.org/10.1063/1.359681

[204] A. S. Bykov, S. G. Grigoryan, R. N. Zhukov, D. A. Kiselev, S. V. Ksenich, I. V. Kubasov, M. D. Malinkovich, Y. N. Parkhomenko, "Formation of bidomain structure in lithium niobate plates by the stationary external heating method", *Russ. Microlectron.*, **43**(8), 536-542, (2014). http://dx.doi.org/10.1134/s1063739714080034

[205] Y. Wang, D. Hasanyan, M. Li, J. Gao, J. Li, D. Viehland, "Equivalent magnetic noise in multi-push-pull configuration magnetoelectric composites: model and experiment", *IEEE Trans. Ultrason. Ferroelectr. Freq. Control.*, **60**(6), 1227-1233, (2013). http://dx.doi.org/10.1109/TUFFC.2013.2686

[206] J. N. Reddy, "Theory and Analysis of Elastic Plates and Shells", CRC Press, Taylor and Francis, 2006.

[207] S. Timoshenko, S. Woinowsky-Krieger, "Theory of plates and shells", McGraw-Hill, 1959.

[208] H. F. Tiersten, "Linear Piezoelectric Plate Vibrations", Springer US, 1969. http://dx.doi.org/10.1007/978-1-4899-6453-3

[209] M. Guo, S. Dong, "A resonance-bending mode magnetoelectric-coupling equivalent circuit", *IEEE Trans. Ultrason. Ferroelectr. Freq. Control*, **56**(11), 2578-2586, (2009). http://dx.doi.org/10.1109/tuffc.2009.1346

[210] M. I. Bichurin, V. M. Petrov, S. V. Averkin, E. Liverts, "Present status of theoretical modeling the magnetoelectric effect in magnetostrictive-piezoelectric nanostructures. Part I: Low frequency and electromechanical resonance ranges", *J. Appl. Phys.*, **107**(5), 053904-053915, (2010). http://dx.doi.org/doi:http://dx.doi.org/10.1063/1.3313919

[211] V. M. Petrov, M. I. Bichurin, V. V. Zibtsev, S. K. Mandal, G. Srinivasan, "Flexural deformation and bending mode of magnetoelectric nanobilayer", *J. Appl. Phys.*, **106**(11), 113901-113906, (2009). http://dx.doi.org/10.1063/1.3264638

[212] C. Zhang, J. Yang, W. Chen, "Theoretical modeling of frequency-dependent magnetoelectric effects in laminated multiferroic plates", *IEEE Trans. Ultrason. Ferroelectr. Freq. Control*, **56**(12), 2750-2759, (2009). http://dx.doi.org/10.1109/TUFFC.2009.1366

[213] I. Oral, "Determination of elastic constants of epoxy resin/biochar composites by ultrasonic pulse echo overlap method", *Polym. Compos.*, 1-9, (2015). http://dx.doi.org/10.1002/pc.23488

[214] C. Liang, S. Morshed, B. C. Prorok, "Correction for longitudinal mode vibration in thin slender beams", *Appl. Phys. Lett.*, **90**(22), 221912-221914, (2007). http://dx.doi.org/10.1063/1.2745262

[215] V. M. Petrov, G. Srinivasan, M. I. Bichurin, T. A. Galkina, "Theory of magnetoelectric effect for bending modes in magnetostrictive-piezoelectric bilayers", *J. Appl. Phys.*, **105**(6), 063911-063916, (2009). http://dx.doi.org/10.1063/1.3087766

[216] G.-L. Yu, H.-W. Zhang, F.-M. Bai, Y.-X. Li, J. Li, "Theoretical investigation of magnetoelectric effect in multilayer magnetoelectric composites", *Compos. Struct.*, **119** 738-748, (2015). http://dx.doi.org/10.1016/j.compstruct.2014.09.049

[217] K.-H. Cho, C.-S. Park, S. Priya, "Effect of intensive and extensive loss factors on the dynamic response of magnetoelectric laminates", *Appl. Phys. Lett.*, **97**(18), 182902-182904, (2010). http://dx.doi.org/10.1063/1.3511285

[218] Z. Xing, J. Li, D. Viehland, "Noise and scale effects on the signal-to-noise ratio in magnetoelectric laminate sensor/detection units", *Appl. Phys. Lett.*, **91**(18), 182902-182904, (2007). http://dx.doi.org/10.1063/1.2804118

[219] C. D. Motchenbacher, J. A. Connelly, "Low noise electronic system design", J. Wiley & Sons, 1993.

[220] M. Tasson, H. Legal, J. C. Gay, J. C. Peuzin, F. C. Lissalde, "Piezoelectric study of poling mechanism in lithium niobate crystals at temperature close to the curie point", *Ferroelectrics*, **13**(1), 479-481, (1976). http://dx.doi.org/10.1080/00150197608236646

[221] I. V. Kubasov, M. S. Timshina, D. A. Kiselev, M. D. Malinkovich, A. S. Bykov, Y. N. Parkhomenko, "Interdomain region in single-crystal lithium niobate bimorph actuators produced by

light annealing", *Crystallogr. Rep.*, **60**(5), 700-705, (2015). http://dx.doi.org/10.1134/S1063774515040136

[222] I. V. Kubasov, A. M. Kislyuk, A. S. Bykov, M. D. Malinkovich, R. N. Zhukov, D. A. Kiselev, S. V. Ksenich, A. A. Temirov, N. G. Timushkin, Y. N. Parkhomenko, "Bidomain structures formed in lithium niobate and lithium tantalate single crystals by light annealing", *Crystallogr. Rep.*, **61**(2), 258-262, (2016). http://dx.doi.org/10.1134/s1063774516020115

[223] Z.-Y. Zhang, Y.-y. Zhu, H.-f. Wang, L.-c. Wang, S.-n. Zhu, N.-b. Ming, "Domain inversion in LiNbO3 and LiTaO3 induced by proton exchange", *Physica B Condens. Matter*, **398**(1), 151-158, (2007). http://dx.doi.org/10.1016/j.physb.2007.05.011

[224] J. V. Vidal, A. A. Timopheev, A. L. Kholkin, N. A. Sobolev, *Dynamic Measurements of Magnetoelectricity in Metglas-Piezocrystal Laminates*. In: I. Tiginyanu, P. Topala, V. Ursaki, editors. *Nanostructures and Thin Films for Multifunctional Applications: Technology, Properties and Devices*. Cham: Springer International Publishing; (2016). p. 227-265. http://dx.doi.org/10.1007/978-3-319-30198-3_7

[225] C.-M. Chang, G. P. Carman, "Modeling shear lag and demagnetization effects in magneto-electric laminate composites", *Phys. Rev. B*, **76**(13), 134116-134122, (2007).

[226] D. Hasanyan, Y. Wang, J. Gao, M. Li, Y. Shen, J. Li, D. Viehland, "Modeling of resonant magneto-electric effect in a magnetostrictive and piezoelectric laminate composite structure coupled by a bonding material", *J. Appl. Phys.*, **112**(6), 064109-064116, (2012). http://dx.doi.org/10.1063/1.4752271

[227] U. Tietze, C. Schenk, C. Schenk, E. Gamm, "Electronic circuits: handbook for design and application, Volume 1", Springer, 2008.

[228] C. Lu, P. Li, Y. Wen, A. Yang, C. Yang, D. Wang, W. He, J. Zhang, "Magnetoelectric Composite Metglas/PZT-Based Current Sensor", *IEEE Trans. Magn.*, **50**(11), 1-4, (2014). http://dx.doi.org/10.1109/TMAG.2014.2326193

[229] L. Chen, P. Li, Y.-M. Wen, Y. Zhu, "Tunable characteristics of bending resonance frequency in magnetoelectric laminated composites", *Chin. Phys. B*, **22**(7), 077505-077509, (2013). http://dx.doi.org/10.1063/1.3560055

[230] Y. Wang, D. Hasanyan, M. Li, J. Gao, R. Viswan, J. Li, D. Viehland, "Electric-field tuning of magnetoelectric properties in Metglas/piezofiber composites", *Phys. Stat. Sol. RRL*, **6**(5), 265–267, (2012). http://dx.doi.org/10.1002/pssr.201206159

[231] P. Finkel, J. Bonini, E. Garrity, K. Bussman, J. Gao, J. F. Li, S. E. Lofland, D. Viehland, "Enhanced resonant magnetoelectric coupling in frequency-tunable composite multiferroic bimorph structures", *Appl. Phys. Lett.*, **98**(9), 092905-092907, (2011). http://dx.doi.org/10.1063/1.3560055

[232] Z. Xing, J. Li, D. Viehland, "Giant magnetoelectric effect in Pb(Zr,Ti)O3-bimorph/NdFeB laminate device", *Appl. Phys. Lett.*, **93**(1), 013505-013506, (2008). http://dx.doi.org/10.1063/1.2956676

[233] G. Hatipoglu, S. Tadigadapa, "Micromachined magnetoflexoelastic resonator based magnetometer", *Appl. Phys. Lett.*, **107**(19), 192406-192410, (2015). http://dx.doi.org/10.1063/1.4935790

[234] Y. Shen, K. L. McLaughlin, J. Gao, D. Gray, L. Shen, Y. Wang, M. Li, D. Berry, J. Li, D. Viehland1, "AC magnetic dipole localization by a magnetoelectric sensor ", *Smart Mater. Struct.*, **21**(6), 065007, (2012). http://dx.doi.org/10.1088/0964-1726/21/6/065007

Appendix

A.1. Tables of material constants

Listing of the linear material constants: relative dielectric constant ε_{ij}^{T}, piezoelectric coefficient d_{ij} (pC/N), piezomagnetic coefficient q_{ij} (ppm/Oe) and elastic compliance s_{ij}^{E} (10^{-12} m^2/N) for the studied compounds.

Metglas 2826 MB

Symmetry: Isotropic
ρ = 7.9 g/cm^3

Parameter	q_{11}	q_{12}	s_{11}^{E}	s_{12}^{E}	s_{44}^{E}
Value	4	-1.7	10	-3.3	26.6
Ref.	[82, 86, 141, 142]	[142]	[140-143]	[143, 214]	
Note	For Metglas 2605 SA1		Y=100GPa from the supplier (s_{11} =1/Y, for an isotropic media)	ν = 0.33 from the supplier (s_{12} =-ν /Y, for an isotropic media)	s_{44} =2(1+ν) /Y, for an isotropic media

$LiNbO_3$

Point group: *3m*
ρ = 4.647 g/cm^3

Parameter	ε_{11}^{T}	ε_{33}^{T}	d_{15}	d_{22}	d_{31}	d_{33}
Value	85.2	28.7	69.2	20.8	-0.85	6
Ref.	[70]					

Parameter	s_{11}^{E}	s_{12}^{E}	s_{13}^{E}	s_{14}^{E}	s_{33}^{E}	s_{44}^{E}
Value	5.831	-1.150	-1.452	-1.000	5.026	17.10
Ref.	[70]					

PMN-30%PT ([011] poled)

Point group: *mm2*
ρ = 8.150 g/cm^3

Parameter	ε_{11}^{T}	ε_{22}^{T}	ε_{33}^{T}	d_{31}	d_{32}	d_{33}	d_{15}	d_{24}
Value	8783	5233	6966	813	-2116	1916	3262	289
Ref.	[75]							

Parameter	s_{11}^E	s_{22}^E	s_{33}^E	s_{12}^E	s_{13}^E	s_{23}^E	s_{44}^E	s_{55}^E	s_{66}^E
Value	23.3	97.5	72.8	-33.4	9.26	-69.0	13.7	151.1	20.2
Ref.	[75]								

α-$GaPO_4$

Point group: *32*

ρ = 3.571 g/cm^3

Parameter	ε_{11}^T	ε_{33}^T	d_{11}	d_{14}
Value	5.38	5.82	4.37	-1.58
Ref.	[71, 189]		[71, 72]	

Parameter	s_{11}^E	s_{12}^E	s_{13}^E	s_{14}^E	s_{33}^E	s_{44}^E
Value	18.055	-4.371	-3.753	2.697	11.674	26.731
Ref.	[71, 72]					

α-Quartz

Point group: *32*

ρ = 2.6485 g/cm^3

Parameter	ε_{11}^T	ε_{33}^T	d_{11}	d_{14}
Value	4.507	4.628	2.331	0.776
Ref.	[145, 146]		[143, 145, 146]	

Parameter	s_{11}^E	s_{12}^E	s_{13}^E	s_{14}^E	s_{33}^E	s_{44}^E
Value	12.779	-1.807	-1.238	-4.525	9.733	19.983
Ref.	[145, 146]					

Langatate ($La_3Ga_{5.5}Ta_{0.5}SiO_{14}$, LGT)

Point group: *32*

ρ = 6.130 g/cm^3

Parameter	ε_{11}^T	ε_{33}^T	d_{11}	d_{14}
Value	19.62	80.44	-5.736	6.343
Ref.	[147]			

Parameter	s_{11}^E	s_{12}^E	s_{13}^E	s_{14}^E	s_{33}^E	s_{44}^E
Value	9.043	-4.559	-1.747	-3.684	5.148	21.607
Ref.	[147]					

Langasite ($La_3Ga_5SiO_{14}$, LGS)

Point group: *32*

$\rho = 5.754$ g/cm^3

Parameter	ε_{11}^T	ε_{33}^T	d_{11}	d_{14}
Value	18.9	51.2	-5.94	4.99
Ref.	[149, 150]			

Parameter	s_{11}^E	s_{12}^E	s_{13}^E	s_{14}^E	s_{33}^E	s_{44}^E
Value	8.75	-4.34	-1.61	-3.43	5.26	19.2
Ref.	[149, 150]					

AlN

Point group: *6mm*

$\rho = 3.260$ g/cm^3

Parameter	ε_{11}^T	ε_{33}^T	d_{15}	d_{31}	d_{33}
Value	9.09	10.44	-2.60	-1.96	4.48
Ref.	[151, 152]				

Parameter	s_{11}^E	s_{12}^E	s_{13}^E	s_{33}^E	s_{44}^E
Value	2.903	-0.843	-0.537	2.860	8.137
Ref.	[151, 152]				

$LiTaO_3$

Point group: *3m*

$\rho = 7.465$ g/cm^3

Parameter	ε_{11}^T	ε_{33}^T	d_{15}	d_{22}	d_{31}	d_{33}
Value	53.53	43.37	26.4	7.5	-3.0	5.7
Ref.	[153-155]					

Parameter	s_{11}^E	s_{12}^E	s_{13}^E	s_{14}^E	s_{33}^E	s_{44}^E
Value	4.930	-0.519	-1.280	0.588	4.317	10.46
Ref.	[153-155]					

$BaTiO_3$

Point group: *4mm*

$\rho = 6.020\ g/cm^3$

Parameter	ε_{11}^T	ε_{33}^T	d_{15}	d_{31}	d_{33}
Value	4366	132	560.7	-33.72	93.95
Ref.	[68, 69]				

Parameter	s_{11}^E	s_{12}^E	s_{13}^E	s_{33}^E	s_{44}^E	s_{66}^E
Value	7.38	-1.39	-4.41	13.1	16.4	7.46
Ref.	[68, 69]					

PMN-33%PT ([111] poled)

Point group: *3m*

$\rho = 8.060\ g/cm^3$

Parameter	ε_{11}^T	ε_{33}^T	d_{15}	d_{22}	d_{31}	d_{33}
Value	3950	640	4100	1340	-90	190
Ref.	[157]					

Parameter	s_{11}^E	s_{12}^E	s_{13}^E	s_{14}^E	s_{33}^E	s_{44}^E
Value	62.16	-53.85	-5.58	-166.24	13.34	510.98
Ref.	[157]					

PMN-33%PT ([001] poled)

Point group: *4mm*

$\rho = 8.060\ g/cm^3$

Parameter	ε_{11}^T	ε_{33}^T	d_{15}	d_{31}	d_{33}
Value	1600	8200	146	-1330	2820
Ref.	[158]				

Parameter	s_{11}^E	s_{12}^E	s_{13}^E	s_{33}^E	s_{44}^E	s_{66}^E
Value	69.0	-11.1	-55.7	119.6	14.5	15.2
Ref.	[158]					

PZN-8%PT ([001] poled)

Point group: *4mm*

$\rho = 8.315$ g/cm^3

Parameter	ε_{11}^T	ε_{33}^T	d_{15}	d_{31}	d_{33}
Value	2900	7700	159	-1455	2890
Ref.	[160]				

Parameter	s_{11}^E	s_{12}^E	s_{13}^E	s_{33}^E	s_{44}^E	s_{66}^E
Value	87.0	-13.1	-70.0	141	15.8	15.4
Ref.	[160]					

PZN-9%PT ([011] poled)

Point group: *mm2*

$\rho = 8.316$ g/cm^3

Parameter	ε_{11}^T	ε_{22}^T	ε_{33}^T	d_{31}	d_{32}	d_{33}	d_{15}	d_{24}
Value	8740	2075	3202	476.0	-1705	1237	2012	118.7
Ref.	[159]							

Parameter	s_{11}^E	s_{22}^E	s_{33}^E	s_{12}^E	s_{13}^E	s_{23}^E	s_{44}^E	s_{55}^E	s_{66}^E
Value	73.07	125.6	67.49	-63.98	4.256	-68.04	15.12	299.3	16.54
Ref.	[159]								

PZT-2

Point group: ∞mm

$\rho = 7.600$ g/cm^3

Parameter	ε_{11}^T	ε_{33}^T	d_{15}	d_{31}	d_{33}
Value	990	450	440	-60.2	152
Ref.	[156]				

Parameter	s_{11}^E	s_{12}^E	s_{13}^E	s_{33}^E	s_{44}^E
Value	11.6	-3.33	-4.97	14.8	45.0
Ref.	[156]				

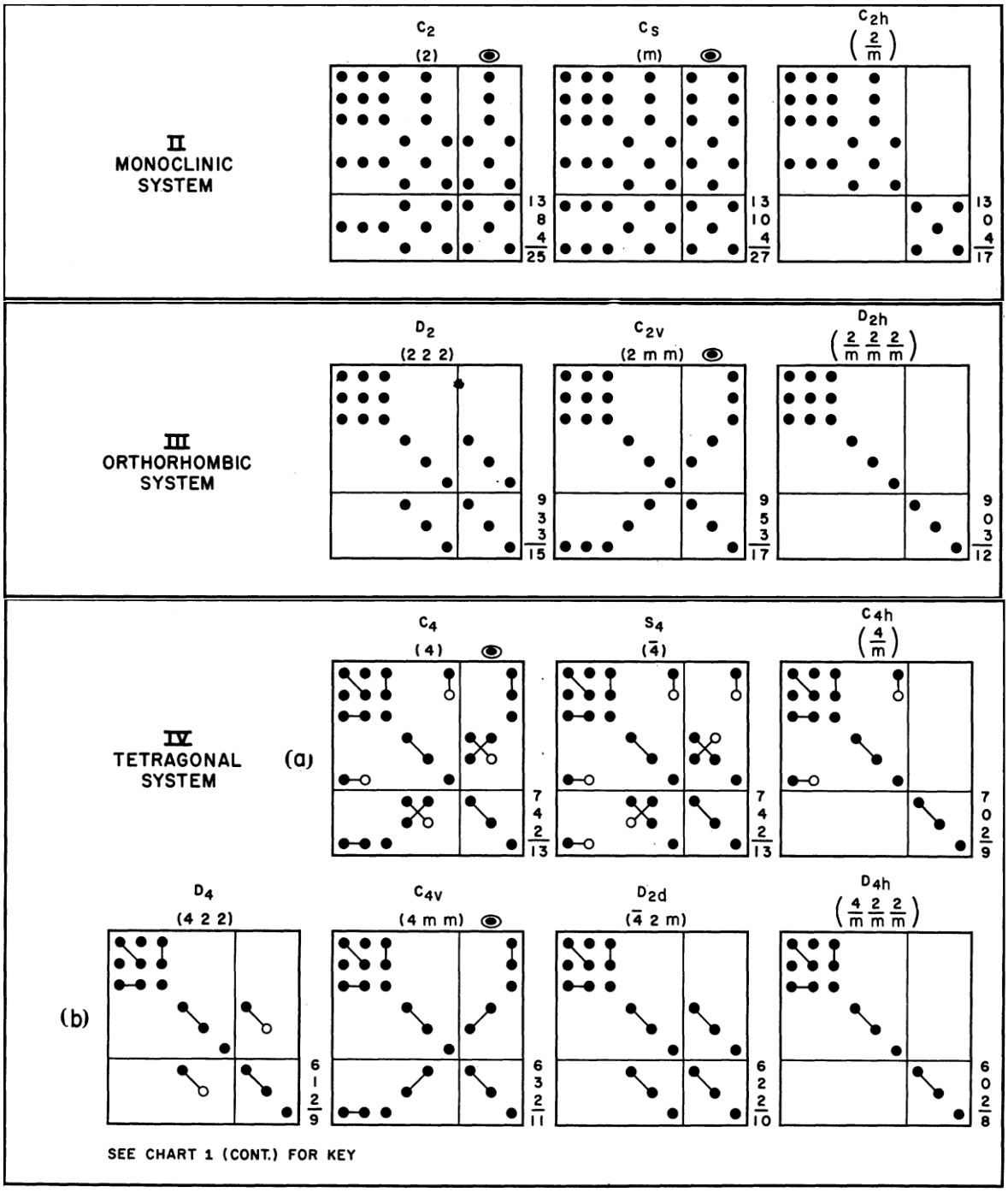
II
MONOCLINIC
SYSTEM
C2
(2)
Cs
(m)
C2h
(2/m)
13 8 4 25
13 10 4 27
13 0 4 17
III
ORTHORHOMBIC
SYSTEM
D2
(2 2 2)
C2v
(2 m m)
D2h
(2/m 2/m 2/m)
9 3 3 15
9 5 3 17
9 0 3 12
IV
TETRAGONAL
SYSTEM
(a)
C4
(4)
S4
(4̄)
C4h
(4/m)
7 4 2 13
7 4 2 13
7 0 2 9
(b)
D4
(4 2 2)
C4v
(4 m m)
D2d
(4̄ 2 m)
D4h
(4/m 2/m 2/m)
6 1 2 9
6 3 2 11
6 2 2 10
6 0 2 8
SEE CHART 1 (CONT.) FOR KEY

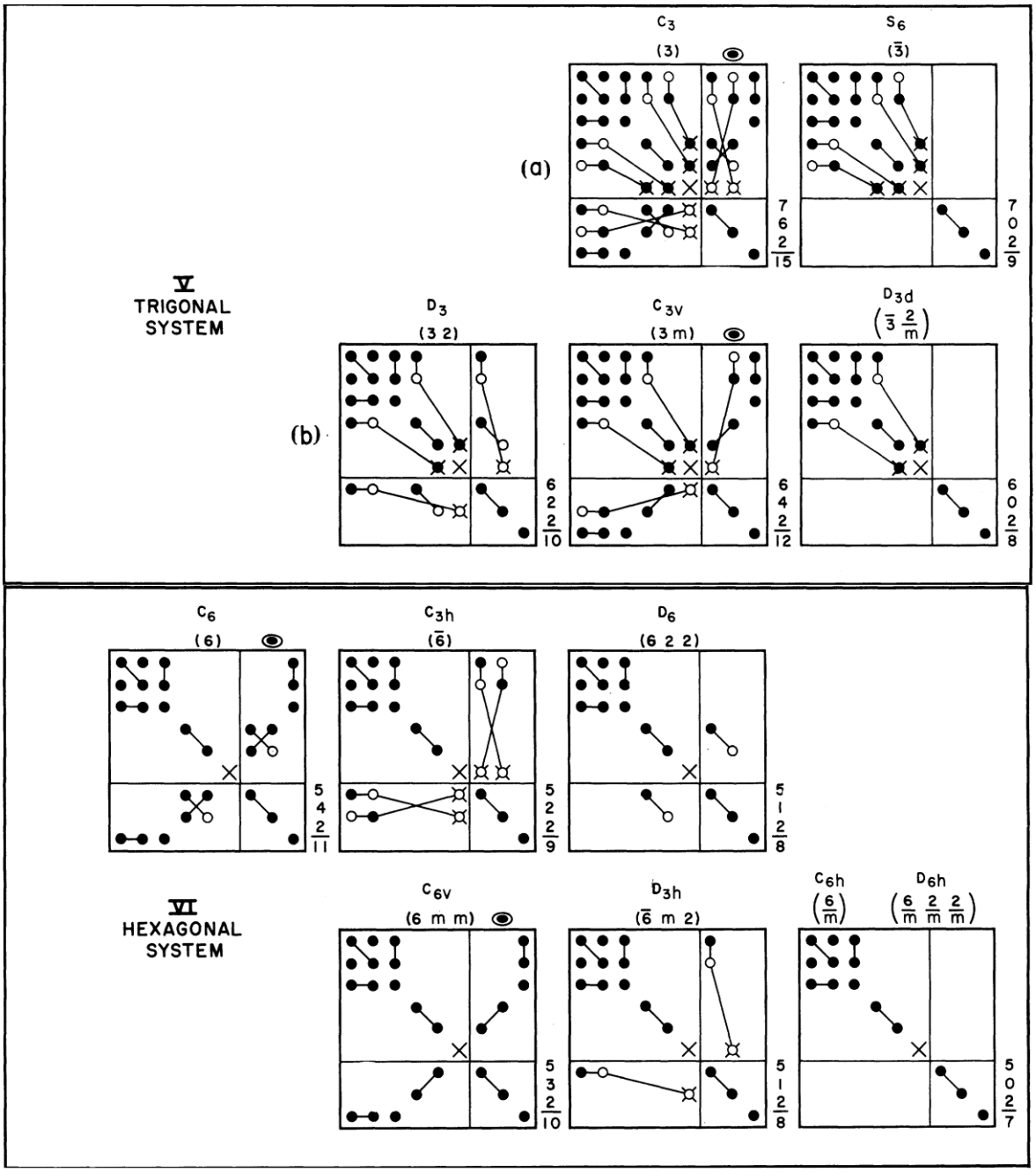
V
TRIGONAL
SYSTEM
(a)
C3
(3)
S6
(3̄)
7 6 2 15
7 0 2 9
(b)
D3
(3 2)
C3v
(3 m)
D3d
(3̄ 2/m)
6 2 2 10
6 4 2 12
6 0 2 8
VI
HEXAGONAL
SYSTEM
C6
(6)
C3h
(6̄)
D6
(6 2 2)
5 4 2 11
5 2 2 9
5 1 2 8
C6v
(6 m m)
D3h
(6̄ m 2)
C6h
(6/m)
D6h
(6/m 2/m 2/m)
5 3 2 10
5 1 2 8
5 0 2 7

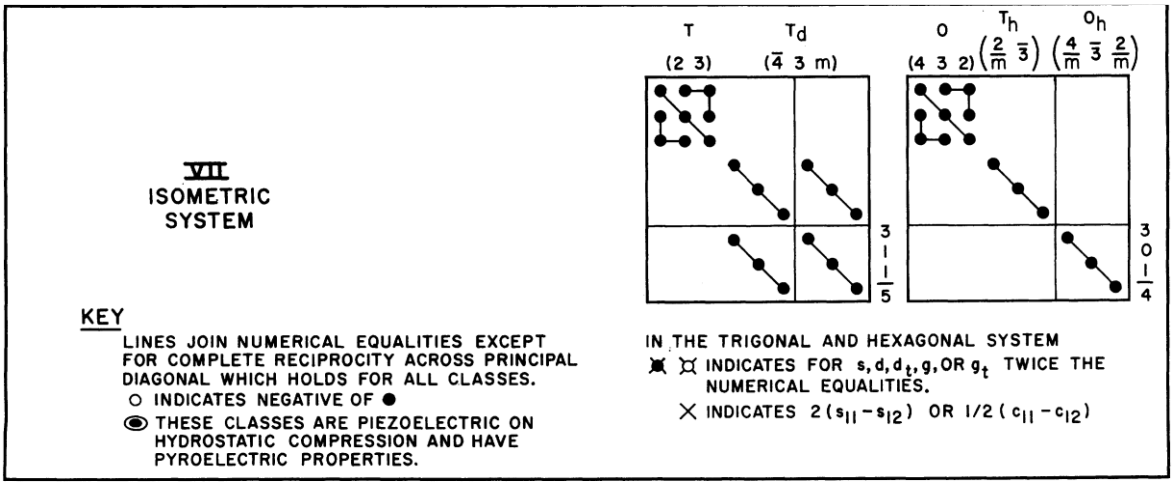

Figure A.1.1 Elasto-piezo-dielectric matrix form for various crystal classes. Adapted from [121].

A.2. Developed components of the ME measurement setup

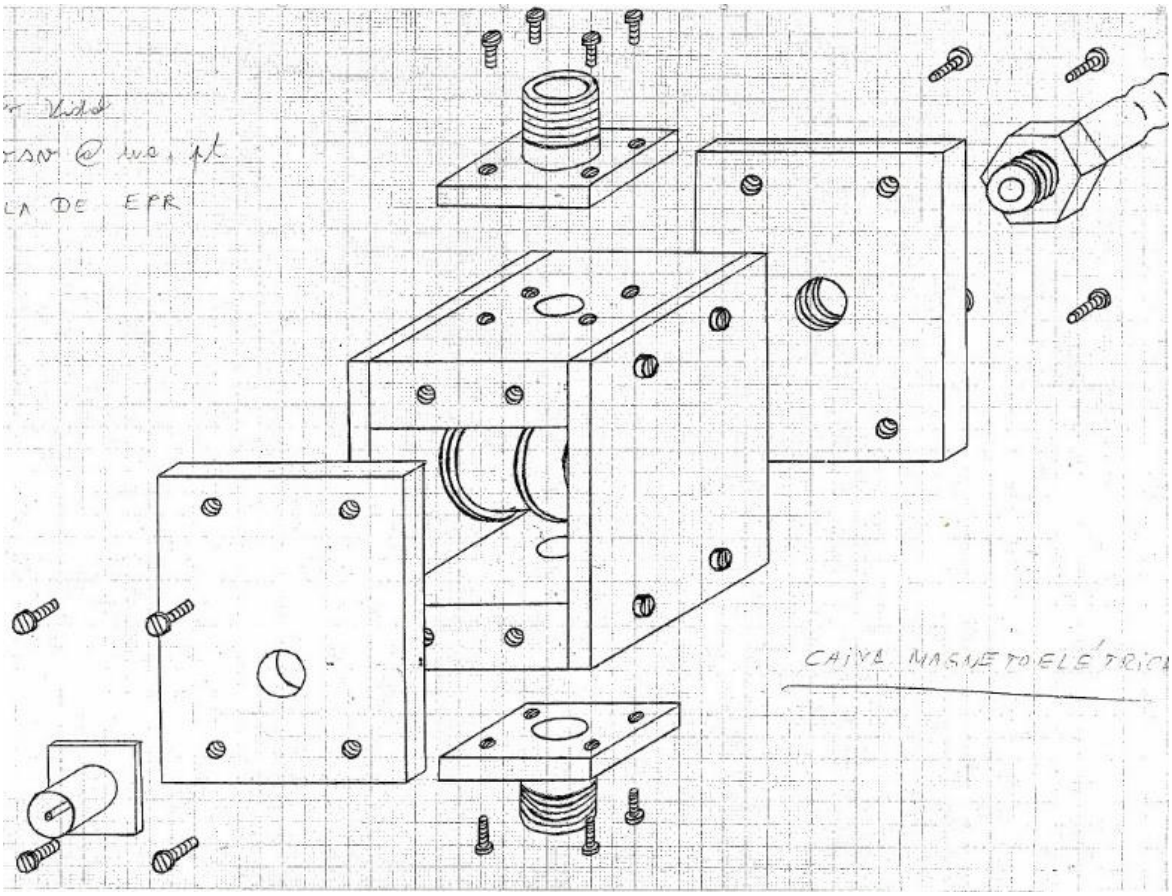

Figure A.2.2 Technical drawing of the developed box containing the Helmholtz Coil in isometric projection.

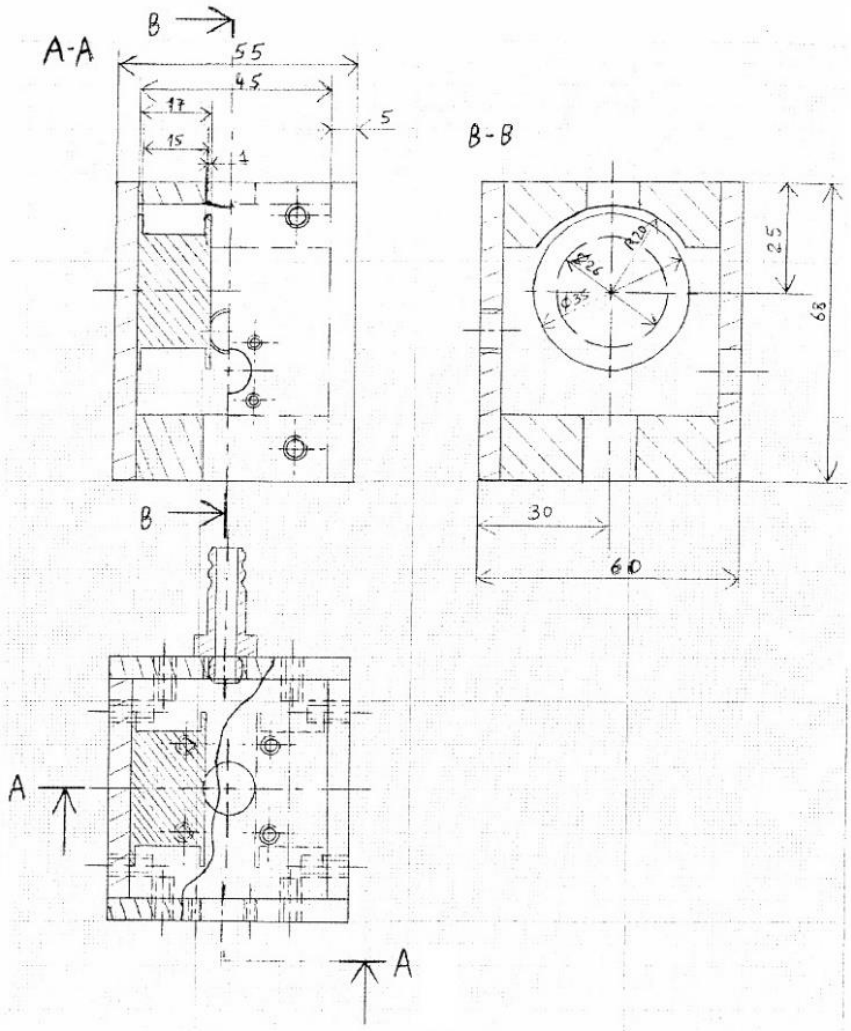

Figure A.2.3 Technical drawing of the developed box containing the Helmholtz Coil in multiview orthographic projection.

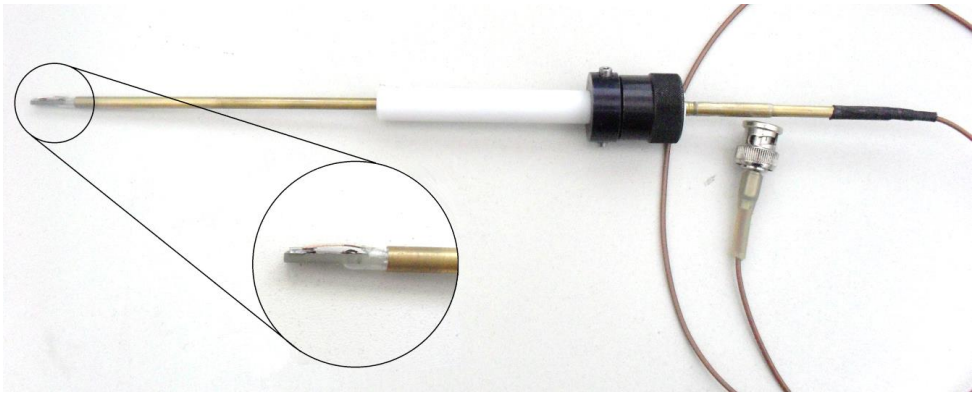

Figure A.2.4 One of the sample supports developed during the investigation consisting of a top and bottom electrical contacts passing through a grounded brass tube thus acting as an electromagnetic shield.

A.3. LabVIEW based programs used for data acquisition and processing

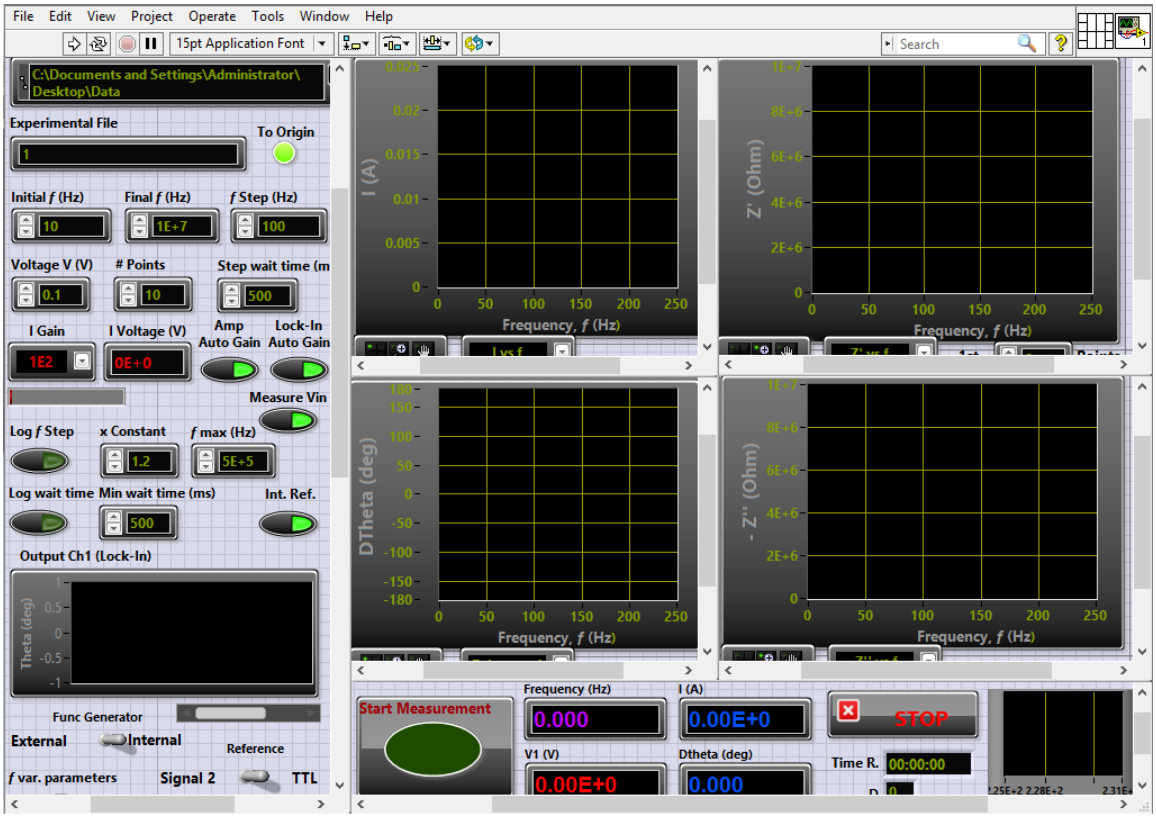

Figure A.3.1 Impedance (*Z*) measurements as a function of the frequency (*f*). Controlled equipment: lock-in amplifier (Zurich Instruments®, model HF2LI); current pre-amplifier.(Zurich Instruments®, model TA); function generator (SRS®, model DS345).

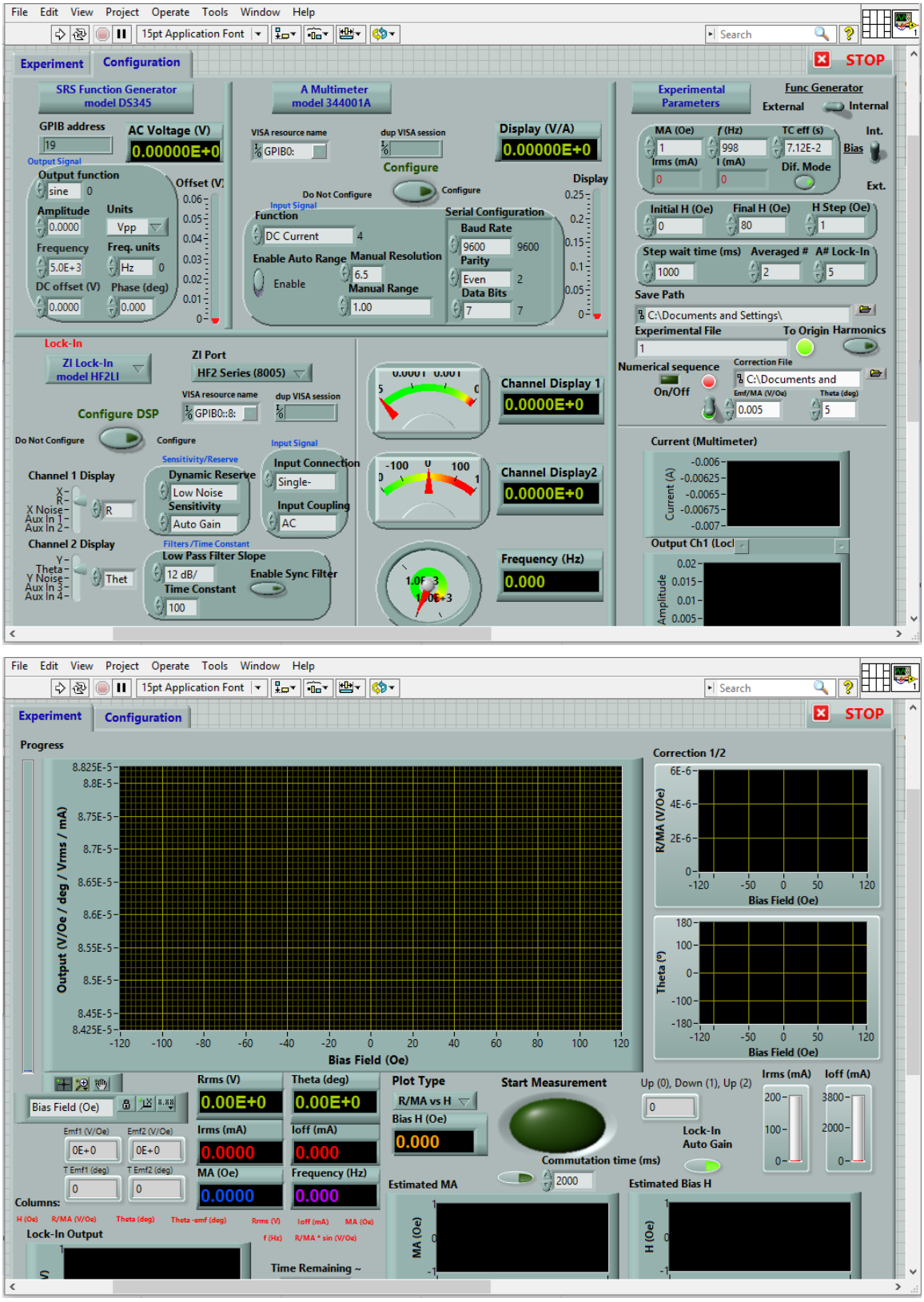

Figure A.3.2 ME effect (a_E) measurements as a function of the bias field (H). Controlled equipment: lock-in amplifier; function generator; power amplifier (AE Techron®, model 7224); multimeter (Agilent®, model 34401A).

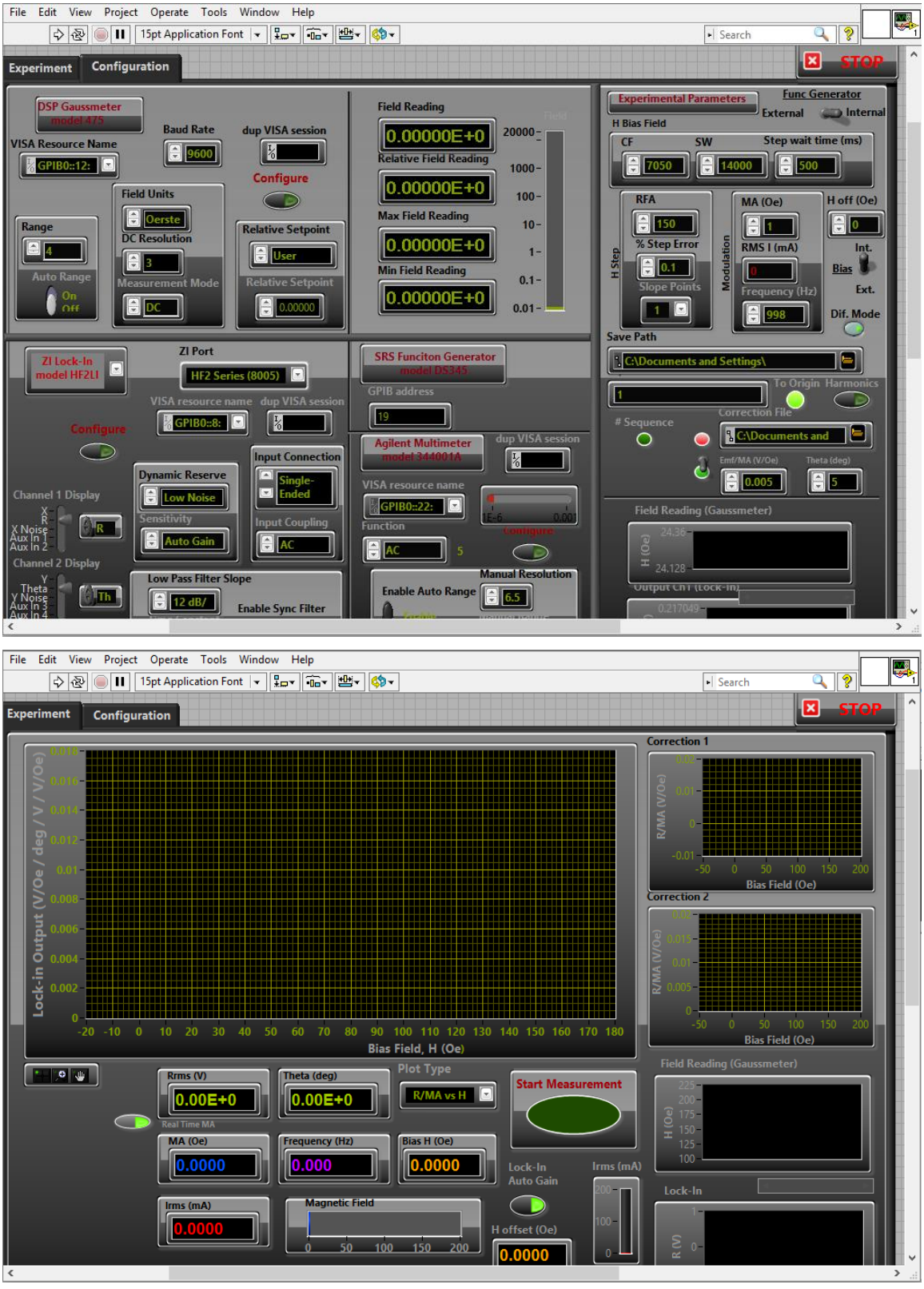

Figure A.3.3 ME effect (a_E) measurements as a function of the bias field (H). Controlled equipment: lock-in amplifier; function generator; power amplifier; multimeter; external electromagnet (Bruker® ESP 300E); gaussmeter (DSP®, model 475).

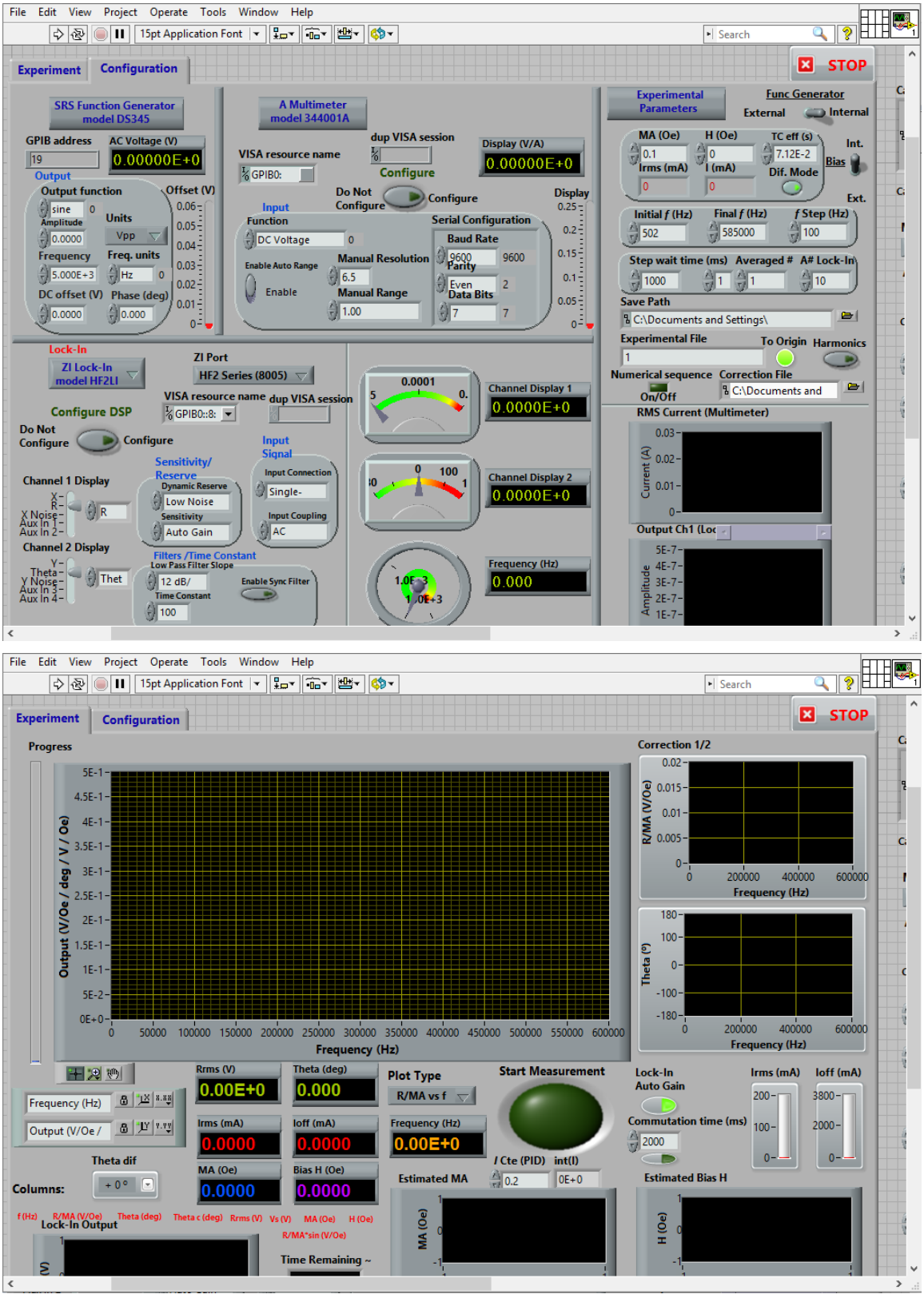

Figure A.3.4 ME effect (a_E) measurements as a function of the frequency of the modulated magnetic field (f). Controlled equipment: lock-in amplifier; function generator; power amplifier; multimeter.

A.4. Matlab based programs used in theoretical calculations

Code A.4.1. Transformation of the piezoelectric (*d* and *e*), dielectric (ε^T and ε^S) and elastic (s^E and c^E) material constants from the crystalline frame into the laminate frame of reference associated with the Euler angles Alfa, Beta and Gamma.

```
%LiNbO3


%density (kg/m3)
P=4647;

%dielectric coefficients (F/m)
e0=8.854187817E-12;
e11T=85.2*e0;
e33T=28.7*e0;
e22T=e11T;
eT=[e11T 0 0;0 e22T 0;0 0 e33T];

%piezoelectric coefficients (C/N)

d15=69.2E-12;
d22=20.8E-12;
d31=-0.85E-12;
d33=6E-12;
d11=0;d12=0;d13=0;d14=0;d23=0;d25=0;d26=0;d34=0;d35=0;d36=0;
d16=-2*d22;
d21=-d22;
d24=d15;
d32=d31;
D=[d11 d12 d13 d14 d15 d16;d21 d22 d23 d24 d25 d26; d31 d32 d33 d34 d35 d36];

%compliance coefficients (m^2/N)
s11E=5.831E-12;
s12E=-1.15E-12;
s13E=-1.452E-12;
s14E=-1E-12;
s33E=5.026E-12;
s44E=17.1E-12;
s15E=0;s16E=0;s25E=0;s26E=0;s34E=0;s35E=0;s36E=0;s43E=0;s45E=0;s46E=0;s51E=0;s52E=0;s53E=0;s54E=0;s61E=0;s62E=0;s63E=0;s64
E=0;
s21E=s12E;
s22E=s11E;
s23E=s13E;
s24E=-s14E;
s31E=s13E;
s32E=s13E;
s41E=s14E;
s42E=-s14E;
s55E=s44E;
s56E=2*s14E;
s65E=2*s14E;
s66E=2*(s11E-s12E);
sE=[s11E s12E s13E s14E s15E s16E;s21E s22E s23E s24E s25E s26E;s31E s32E s33E s34E s35E s36E;s41E s42E s43E s44E s45E
s46E;s51E s52E s53E s54E s55E s56E;s61E s62E s63E s64E s65E s66E];

A=[-sE zeros(6,3);-D eye(3)];
B=[-eye(6) D';zeros(3,6) eT];
C=inv(A)*B;

E=C(7:9,1:6)
cE=C(1:6,1:6)
eS=C(7:9,7:9)

%%%%%%%%%%%%%%%%%%%%%%%%%%%%%%%%%%%%%%%%%%%%%%%%%%%%%%%%%%%%%%%%%%%%%%%%%%%%%%%%%%%%%%%%%%%%%%%%%%%%%%%%%%%%%%%%%%%%


%Euler angles (deg)
Alfa=0;
Gamma=0;
Sigma=0;

alfa=Alfa*(pi/180);
gamma=Gamma*(pi/180);
sigma=Sigma*(pi/180);

%Transformation matrix

a(1,1)=cos(sigma)*cos(alfa)-cos(gamma)*sin(alfa)*sin(sigma);
a(1,2)=cos(sigma)*sin(alfa)+cos(gamma)*cos(alfa)*sin(sigma);
a(1,3)=sin(sigma)*sin(gamma);
a(2,1)=-sin(sigma)*cos(alfa)-cos(gamma)*sin(alfa)*cos(sigma);
a(2,2)=-sin(sigma)*sin(alfa)+cos(gamma)*cos(alfa)*cos(sigma);
a(2,3)=cos(sigma)*sin(gamma);
a(3,1)=sin(gamma)*sin(alfa);
a(3,2)=-sin(gamma)*cos(alfa);
a(3,3)=cos(gamma);
```

```
%D/E to 3D

for i=1:3
    for j=1:3
        for k=1:3
            if k==j
                D1(i,j,k)=D(i,j);
                E1(i,j,k)=E(i,j);
            else
                D1(i,j,k)=D(i,9-j-k)/2;
                E1(i,j,k)=E(i,9-j-k);
            end
        end
    end
end

%sE/cE to 3D

for i=1:3
    for j=1:3
        for k=1:3
            for l=1:3
                if i==j&k==l
                    sE1(i,j,k,l)=sE(i,k);
                    cE1(i,j,k,l)=cE(i,k);
                else if i==j&k~=l
                        sE1(i,j,k,l)=sE(i,9-k-l)/2;
                        cE1(i,j,k,l)=cE(i,9-k-l);
                    else if i~=j&k==l
                            sE1(i,j,k,l)=sE(9-i-j,k)/2;
                            cE1(i,j,k,l)=cE(9-i-j,k);
                        else if i~=j&k~=l
                                sE1(i,j,k,l)=sE(9-i-j,9-k-l)/4;
                                cE1(i,j,k,l)=cE(9-i-j,9-k-l);
                            end
                        end
                    end
                end
            end
        end
    end
end

%Rotate eT/eS

eT1Y(1:3,1:3)=0;
eS1Y(1:3,1:3)=0;
for i=1:3
    for j=1:3
        for m=1:3
            for n=1:3
                eT1Y(i,j)=eT1Y(i,j)+a(i,m)*a(j,n)*eT(m,n);
                eS1Y(i,j)=eS1Y(i,j)+a(i,m)*a(j,n)*eS(m,n);
            end
        end
    end
end

%Rotate D/E

D1Y(1:3,1:3,1:3)=0;
E1Y(1:3,1:3,1:3)=0;
for i=1:3
    for j=1:3
        for k=1:3
            for m=1:3
                for n=1:3
                    for o=1:3
                        D1Y(i,j,k)=D1Y(i,j,k)+a(i,m)*a(j,n)*a(k,o)*D1(m,n,o);
                        E1Y(i,j,k)=E1Y(i,j,k)+a(i,m)*a(j,n)*a(k,o)*E1(m,n,o);
                    end
                end
            end
        end
    end
end

%Rotate sE/cE

sE1Y(1:3,1:3,1:3,1:3)=0;
cE1Y(1:3,1:3,1:3,1:3)=0;
for i=1:3
    for j=1:3
        for k=1:3
            for l=1:3
                for m=1:3
                    for n=1:3
                        for o=1:3
                            for p=1:3
                                sE1Y(i,j,k,l)=sE1Y(i,j,k,l)+a(i,m)*a(j,n)*a(k,o)*a(l,p)*sE1(m,n,o,p);
                                cE1Y(i,j,k,l)=cE1Y(i,j,k,l)+a(i,m)*a(j,n)*a(k,o)*a(l,p)*cE1(m,n,o,p);
                            end
                        end
                    end
                end
            end
```

```
        end
    end
end

%D/E to 2D

for i=1:3
    for j=1:3
        for k=1:3
            if j==k
                DY(i,j)=D1Y(i,j,k);
                EY(i,j)=E1Y(i,j,k);
            else
                DY(i,9-j-k)=2*D1Y(i,j,k);
                EY(i,9-j-k)=E1Y(i,j,k);
            end
        end
    end
end

%sE/cE to 2D

for i=1:3
    for j=1:3
        for k=1:3
            for l=1:3
                if i==j&k==l
                    sEY(i,k)=sE1Y(i,j,k,l);
                    cEY(i,k)=cE1Y(i,j,k,l);
                else if i==j&k~=l
                        sEY(i,9-k-l)=2*sE1Y(i,j,k,l);
                        cEY(i,9-k-l)=cE1Y(i,j,k,l);
                    else if i~=j&k==l
                            sEY(9-i-j,k)=2*sE1Y(i,j,k,l);
                            cEY(9-i-j,k)=cE1Y(i,j,k,l);
                        else if i~=j&k~=l
                                sEY(9-i-j,9-k-l)=4*sE1Y(i,j,k,l);
                                cEY(9-i-j,9-k-l)=cE1Y(i,j,k,l);
                            end
                        end
                    end
                end
            end
        end
    end
end
```

Code A.4.2. Calculation of the maximum transversal extensional quasi-static ME coefficients (α_{E31} and α_{E32}) for a series of tri-layered plates of Metglas/piezoelectric/Metglas as a function of the crystalline orientation of the piezoelectric and geometry of the composite.

```
clearvars -except P eS eT D E cE sE
close all

%Parameters:

%Coupling parameter

Kc=1;%0.00011;


%Metglas

%geometry (m)
tt=29E-6;

%piezomagnetic coefficient (1/Oe)

q11=4E-6;
q12=-1.7E-6;
q16=0E-6;
q=[q11 q12 q12 0 0 q16;q12 q11 q12 0 0 q16;q12 q12 q11 0 0 q16];

%compliance coefficients (m^2/N)
s11H=10E-12;
s12H=-3.3E-12;
s44H=2*13.3E-12;
sH=[s11H s12H s12H 0 0 0;s12H s11H s12H 0 0 0;s12H s12H s11H 0 0 0;0 0 0 s44H 0 0;0 0 0 0 s44H 0;0 0 0 0 0 s44H];

%geometry (m)
t=0.5E-3;
l=10E-3;

f=(t/(2*tt));
v=(t/(t+2*tt));
%%%%%%%%%%%%%%%%%%%%%%%%%%%%%%%%%%%%%%%%%%%%%%%%%%%%%%%%%%%%%%%%%%%%%%%%%%%%%%%

%D/E to 3D

for i=1:3
```

```
    for j=1:3
        for k=1:3
            if k==j
                D1(i,j,k)=D(i,j);
                E1(i,j,k)=E(i,j);
            else
                D1(i,j,k)=D(i,9-j-k)/2;
                E1(i,j,k)=E(i,9-j-k);
            end
        end
    end
end

%sE/cE to 3D

for i=1:3
    for j=1:3
        for k=1:3
            for l=1:3
                if i==j&&k==l
                    sE1(i,j,k,l)=sE(i,k);
                    cE1(i,j,k,l)=cE(i,k);
                else if i==j&&k~=l
                        sE1(i,j,k,l)=sE(i,9-k-l)/2;
                        cE1(i,j,k,l)=cE(i,9-k-l);
                    else if i~=j&&k==l
                            sE1(i,j,k,l)=sE(9-i-j,k)/2;
                            cE1(i,j,k,l)=cE(9-i-j,k);
                        else if i~=j&&k~=l
                                sE1(i,j,k,l)=sE(9-i-j,9-k-l)/4;
                                cE1(i,j,k,l)=cE(9-i-j,9-k-l);
                            end
                        end
                    end
                end
            end
        end
    end
end


%%%%%%%%%%%%%%%%%%%%%%%%%%%%%%%%%%%%%%%%%%%%%%%%%%%%%%%%%%%%%%%%%%%%%%%%%%%%%%%

cpu=cputime;
%Euler angles
Al=0;
Be=0;
Sig=0;

Alfa=0;
Beta=0;
Gamma=0;

for Alfa=0:1:180
    Al=Al+1;
    Be=0;
    for Beta=0:1:180
        Be=Be+1;
        Sig=0;
        for Gamma=0:1:180
            Sig=Sig+1;

alfa=Alfa*(pi/180);
beta=Beta*(pi/180);
gamma=Gamma*(pi/180);

%Transformation matrix

a(1,1)=cos(gamma)*cos(alfa)-cos(beta)*sin(alfa)*sin(gamma);
a(1,2)=cos(gamma)*sin(alfa)+cos(beta)*cos(alfa)*sin(gamma);
a(1,3)=sin(gamma)*sin(beta);
a(2,1)=-sin(gamma)*cos(alfa)-cos(beta)*sin(alfa)*cos(gamma);
a(2,2)=-sin(gamma)*sin(alfa)+cos(beta)*cos(alfa)*cos(gamma);
a(2,3)=cos(gamma)*sin(beta);
a(3,1)=sin(beta)*sin(alfa);
a(3,2)=-sin(beta)*cos(alfa);
a(3,3)=cos(beta);

%%%%%%%%%%%%%%%%%%%%%%%%%%%%%%%%%%%%%%%%%%%%%%%%%%%%%%%%%%%%%%%%%%%%%%%%%%%%%%%

%Rotated eT/eS

eT1Y(1:3,1:3)=0;
eS1Y(1:3,1:3)=0;
for i=1:3
    for j=1:3
        for m=1:3
            for n=1:3
                eT1Y(i,j)=eT1Y(i,j)+a(i,m)*a(j,n)*eT(m,n);
                eS1Y(i,j)=eS1Y(i,j)+a(i,m)*a(j,n)*eS(m,n);
            end
        end
    end
end

%Rotated D/E

D1Y(1:3,1:3,1:3)=0;
```

```
E1Y(1:3,1:3,1:3)=0;
for i=1:3
    for j=1:3
        for k=1:3
            for m=1:3
                for n=1:3
                    for o=1:3
                        D1Y(i,j,k)=D1Y(i,j,k)+a(i,m)*a(j,n)*a(k,o)*D1(m,n,o);
                        E1Y(i,j,k)=E1Y(i,j,k)+a(i,m)*a(j,n)*a(k,o)*E1(m,n,o);
                    end
                end
            end
        end
    end
end

%Rotated sE/cE

sE1Y(1:3,1:3,1:3,1:3)=0;
cE1Y(1:3,1:3,1:3,1:3)=0;
for i=1:3
    for j=1:3
        for k=1:3
            for l=1:3
                for m=1:3
                    for n=1:3
                        for o=1:3
                            for p=1:3
                                sE1Y(i,j,k,l)=sE1Y(i,j,k,l)+a(i,m)*a(j,n)*a(k,o)*a(l,p)*sE1(m,n,o,p);
                                cE1Y(i,j,k,l)=cE1Y(i,j,k,l)+a(i,m)*a(j,n)*a(k,o)*a(l,p)*cE1(m,n,o,p);
                            end
                        end
                    end
                end
            end
        end
    end
end

%D/E to 2D

for i=1:3
    for j=1:3
        for k=1:3
            if j==k
                DY(i,j)=D1Y(i,j,k);
                EY(i,j)=E1Y(i,j,k);
            else
                DY(i,9-j-k)=2*D1Y(i,j,k);
                EY(i,9-j-k)=E1Y(i,j,k);
            end
        end
    end
end

%sE/cE to 2D

for i=1:3
    for j=1:3
        for k=1:3
            for l=1:3
                if i==j&&k==l
                    sEY(i,k)=sE1Y(i,j,k,l);
                    cEY(i,k)=cE1Y(i,j,k,l);
                else if i==j&k~=l
                        sEY(i,9-k-l)=2*sE1Y(i,j,k,l);
                        cEY(i,9-k-l)=cE1Y(i,j,k,l);
                    else if i~=j&k==l
                            sEY(9-i-j,k)=2*sE1Y(i,j,k,l);
                            cEY(9-i-j,k)=cE1Y(i,j,k,l);
                        else if i~=j&k~=l
                                sEY(9-i-j,9-k-l)=4*sE1Y(i,j,k,l);
                                cEY(9-i-j,9-k-l)=cE1Y(i,j,k,l);
                            end
                        end
                    end
                end
            end
        end
    end
end

%%%%%%%%%%%%%%%%%%%%%%%%%%%%%%%%%%%%%%%%%%%%%%%%%%%%%%%%%%%%%%%%%%%%%%%%%%%%%%%%


AY=[sEY(1,1)+f*Kc*sH(1,1) sEY(1,2)+f*Kc*sH(1,2) sEY(1,6)+f*Kc*sH(1,6) 0 0 DY(3,1)*Kc;sEY(2,1)+f*Kc*sH(2,1)
sEY(2,2)+f*Kc*sH(2,2) sEY(2,6)+f*Kc*sH(2,6) 0 0 DY(3,2)*Kc;sEY(6,1)+f*Kc*sH(6,1) sEY(6,2)+f*Kc*sH(6,2)
sEY(6,6)+f*Kc*sH(6,6) 0 0 DY(3,6)*Kc;DY(1,1) DY(1,2) DY(1,6) -1 0 eT1Y(1,3);DY(2,1) DY(2,2) DY(2,6) 0 -1 eT1Y(2,3);DY(3,1)
DY(3,2) DY(3,6) 0 0 eT1Y(3,3)];

%Transversal ME coefficients

MY=AY\[q(1,1)*Kc q(1,2)*Kc q(1,6)*Kc 0 0 0]';

alfaE31A=(MY(6)/100)

MY2=AY\[q(2,1)*Kc q(2,2)*Kc q(2,6)*Kc 0 0 0]';
```

```
alfaE32A=(MY2(6)/100)

alfaE31(Al,Be,Sig)=alfaE31A;
alfaE32(Al,Be,Sig)=alfaE32A;

        end
    end
    Alfa
end
```

Code A.4.3. Representation of the maximum transversal ME coefficients (α_{E31} and α_{E32}) as a function of the crystalline orientation of the piezoelectric and geometry of the composite.

```
for k=1:181
    if k<=91
        alfaE32(:,:,k)=alfaE31(:,:,k+90);
    else
        alfaE32(:,:,k)=alfaE31(:,:,k-90);
    end
end
alfaE3132=alfaE31-alfaE32;
for i=1:181
    for j=1:181
        [alfaE31max(i,j),Imax(i,j)]=max(alfaE31(i,j,:));
        [alfaE31min(i,j),Imin(i,j)]=min(alfaE31(i,j,:));
        [alfaE31absmax(i,j),Iabsmax(i,j)]=max(abs(alfaE31(i,j,:)));
        [alfaE3132absmin(i,j),Iabsmin(i,j)]=min(abs(alfaE3132(i,j,:)));
        alfaE3132absmax(i,j)=abs(alfaE31(i,j,Iabsmin(i,j))./(alfaE3132absmin(i,j)+0.1);
    end
end
[X,Y]=meshgrid(0:180);

figure
contourf(X,Y,alfaE31absmax,100,'linecolor','none')
shading flat
colorbar
xlabel('\beta (deg)','FontSize',12)
ylabel('\alpha (deg)','FontSize',12)
title('PZN-8%PT ([001] poled)  Maximum  |\alphaE| (V/cm-Oe)')
grid on
figure
subplot(2,2,1)
contourf(X,Y,alfaE31max,100,'linecolor','none')
shading flat
colorbar
xlabel('\beta (deg)')
ylabel('\alpha (deg)')
title('Maximum  \alphaE (V/cm-Oe)')
subplot(2,2,2)
contourf(X,Y,alfaE31min,100,'linecolor','none')
shading flat
colorbar
xlabel('\beta (deg)')
ylabel('\alpha (deg)')
title('Minimum  \alphaE (V/cm-Oe)')
subplot(2,2,3)
contourf(X,Y,alfaE31(1:181,1:181,1),100,'linecolor','none')
shading flat
colorbar
xlabel('\beta (deg)')
ylabel('\alpha (deg)')
title(' \alphaE31 (V/cm-Oe)')
subplot(2,2,4)
contourf(X,Y,alfaE32(1:181,1:181,1),100,'linecolor','none')
shading flat
colorbar
xlabel('\beta (deg)')
ylabel('\alpha (deg)')
title('  \alphaE32 (V/cm-Oe)')

figure
contourf(X,Y,alfaE3132absmin,'linecolor','none')
shading flat
colorbar
xlabel('\beta (deg)','FontSize',12)
ylabel('\alpha (deg)','FontSize',12)
title('  \alphaE31-\alphaE32 (V/cm-Oe)')
contourf(X,Y,alfaE3132absmax,'linecolor','none')
shading flat
colorbar
xlabel('\beta (deg)','FontSize',12)
ylabel('\alpha (deg)','FontSize',12)
title('  \alphaE31 (V/cm-Oe)')

Alfa=alfaE31absmax;
figure
XX1=sin(X*(pi/180)).*sin(Y*(pi/180)).*Alfa;
YY1=-sin(X*(pi/180)).*cos(Y*(pi/180)).*Alfa;
ZZ1=cos(X*(pi/180)).*Alfa;
n=5;
XX=XX1(1:n:end,1:n:end);
YY=YY1(1:n:end,1:n:end);
ZZ=ZZ1(1:n:end,1:n:end);
```

```
surf(XX,YY,ZZ,sqrt(XX.^2+YY.^2+ZZ.^2))
colormap jet
hold on
surf(-XX,YY,ZZ,sqrt(XX.^2+YY.^2+ZZ.^2))
colormap jet
% shading interp
xlabel('X')
ylabel('Y')
zlabel('Z')
title('Maximum  |\alphaE| (V/cm-Oe)')
colorbar
Arw=max(max(Alfa))*1.2;
quiver3([-Arw 0 0],[0 -Arw 0],[0 0 -Arw],[1 0 0],[0 1 0],[0 0 1],2,'k')
axis equal
view([135,30])
camlight headlight

[Max,a]=max(alfaE31);
[Max,b]=max(Max);
[Max,s]=max(Max);
Max
s=s-1
b=b(1,1,s+1)-1
a=a(1,b+1,s+1)-1
[Min,a]=min(alfaE31);
[Min,b]=min(Min);
[Min,s]=min(Min);
Min
s=s-1
b=b(1,1,s+1)-1
a=a(1,b+1,s+1)-1
```

Code A.4.4. Calculation of the maximum transversal extensional and flexural quasi-static ME coefficients (α_{E31} and α_{E32}) for a series of bi-layered plates of Metglas/piezoelectric, containing a unidomain or bidomain piezoelectric crystal, as a function of its crystalline orientation and geometry of the composite.

```
clearvars -except P eS eT D E cE sE
close all
clc

Bidomain=1;

%Parameters:

%geometry (m)
tp=0.5E-3;
xbid=0.5;    %up polarization fraction
l=10E-3;

%Coupling parameter

Kc=1;%0.00011;

%Metglas
Pm=7900;

%geometry (m)
tm1=29E-6;

%piezomagnetic coefficient (1/Oe)

q11=4E-6;
q12=-1.7E-6;
q16=0E-6;
q=[q11 q12 q12 0 0 q16;q12 q11 q12 0 0 q16;q12 q12 q11 0 0 q16];

%compliance coefficients (m^2/N)
s11H=10E-12;
s12H=-3.3E-12;
s44H=2*13.3E-12;
sH=[s11H s12H s12H 0 0 0;s12H s11H s12H 0 0 0;s12H s12H s11H 0 0 0;0 0 0 s44H 0 0;0 0 0 0 s44H 0;0 0 0 0 0 s44H];


%%%%%%%%%%%%%%%%%%%%%%%%%%%%%%%%%%%%%%%%%%%%%%%%%%%%%%%%%%%%%%%%%%%%%%%%%%%%

%D/E to 3D

for i=1:3
    for j=1:3
        for k=1:3
            if k==j
                D1(i,j,k)=D(i,j);
                E1(i,j,k)=E(i,j);
            else
                D1(i,j,k)=D(i,9-j-k)/2;
                E1(i,j,k)=E(i,9-j-k);
            end
        end
    end
end
```

```
%sE/cE to 3D

for i=1:3
    for j=1:3
        for k=1:3
            for l=1:3
                if i==j&&k==l
                    sE1(i,j,k,l)=sE(i,k);
                    cE1(i,j,k,l)=cE(i,k);
                else if i==j&&k~=l
                        sE1(i,j,k,l)=sE(i,9-k-l)/2;
                        cE1(i,j,k,l)=cE(i,9-k-l);
                    else if i~=j&&k==l
                            sE1(i,j,k,l)=sE(9-i-j,k)/2;
                            cE1(i,j,k,l)=cE(9-i-j,k);
                        else if i~=j&&k~=l
                                sE1(i,j,k,l)=sE(9-i-j,9-k-l)/4;
                                cE1(i,j,k,l)=cE(9-i-j,9-k-l);
                            end
                        end
                    end
                end
            end
        end
    end
end


%%%%%%%%%%%%%%%%%%%%%%%%%%%%%%%%%%%%%%%%%%%%%%%%%%%%%%%%%%%%%%%%%%%%%%%%%%%%%%%

cpu=cputime;

%Euler angles
Al=1;
Be=0;
Sig=1;

Alfa=0;
Beta=0;
Gamma=0;

for Alfa=0:1:180
    Al=Al+1;
    Be=0;
    for Beta=0:1:180
        Be=Be+1;
        Sig=0;
        for Gamma=0:1:180
            Sig=Sig+1;

            alfa=Alfa*(pi/180);
            beta=Beta*(pi/180);
            gamma=Gamma*(pi/180);

            %Transformation matrix

            a(1,1)=cos(gamma)*cos(alfa)-cos(beta)*sin(alfa)*sin(gamma);
            a(1,2)=cos(gamma)*sin(alfa)+cos(beta)*cos(alfa)*sin(gamma);
            a(1,3)=sin(gamma)*sin(beta);
            a(2,1)=-sin(gamma)*cos(alfa)-cos(beta)*sin(alfa)*cos(gamma);
            a(2,2)=-sin(gamma)*sin(alfa)+cos(beta)*cos(alfa)*cos(gamma);
            a(2,3)=cos(gamma)*sin(beta);
            a(3,1)=sin(beta)*sin(alfa);
            a(3,2)=-sin(beta)*cos(alfa);
            a(3,3)=cos(beta);

            %Top layer material coefficients

            if Bidomain==1
                abot=[1 0 0;0 -1 0;0 0 -1]*a;
            else
                abot=a;
            end

            %%%%%%%%%%%%%%%%%%%%%%%%%%%%%%%%%%%%%%%%%%%%%%%%%%%%%%%%%%%%%%%%%%%%%%%%%%%%%%%

            %Rotated eT/eS

            eT1Y(1:3,1:3)=0;
            eS1Y(1:3,1:3)=0;
            eT1Ybot(1:3,1:3)=0;
            eS1Ybot(1:3,1:3)=0;
            for i=1:3
                for j=1:3
                    for m=1:3
                        for n=1:3
                            eT1Y(i,j)=eT1Y(i,j)+a(i,m)*a(j,n)*eT(m,n);
                            eS1Y(i,j)=eS1Y(i,j)+a(i,m)*a(j,n)*eS(m,n);
                            eT1Ybot(i,j)=eT1Ybot(i,j)+abot(i,m)*abot(j,n)*eT(m,n);
                            eS1Ybot(i,j)=eS1Ybot(i,j)+abot(i,m)*abot(j,n)*eS(m,n);
                        end
                    end
                end
            end


            %Rotated D/E
```

```
            D1Y(1:3,1:3,1:3)=0;
            E1Y(1:3,1:3,1:3)=0;
            D1Ybot(1:3,1:3,1:3)=0;
            E1Ybot(1:3,1:3,1:3)=0;
            for i=1:3
                for j=1:3
                    for k=1:3
                        for m=1:3
                            for n=1:3
                                for o=1:3
                                    D1Y(i,j,k)=D1Y(i,j,k)+a(i,m)*a(j,n)*a(k,o)*D1(m,n,o);
                                    E1Y(i,j,k)=E1Y(i,j,k)+a(i,m)*a(j,n)*a(k,o)*E1(m,n,o);
                                    D1Ybot(i,j,k)=D1Ybot(i,j,k)+abot(i,m)*abot(j,n)*abot(k,o)*D1(m,n,o);
                                    E1Ybot(i,j,k)=E1Ybot(i,j,k)+abot(i,m)*abot(j,n)*abot(k,o)*E1(m,n,o);
                                end
                            end
                        end
                    end
                end
            end

            %Rotated sE/cE

            sE1Y(1:3,1:3,1:3,1:3)=0;
            cE1Y(1:3,1:3,1:3,1:3)=0;
            sE1Ybot(1:3,1:3,1:3,1:3)=0;
            cE1Ybot(1:3,1:3,1:3,1:3)=0;
            for i=1:3
                for j=1:3
                    for k=1:3
                        for l=1:3
                            for m=1:3
                                for n=1:3
                                    for o=1:3
                                        for p=1:3
                                            sE1Y(i,j,k,l)=sE1Y(i,j,k,l)+a(i,m)*a(j,n)*a(k,o)*a(l,p)*sE1(m,n,o,p);
                                            cE1Y(i,j,k,l)=cE1Y(i,j,k,l)+a(i,m)*a(j,n)*a(k,o)*a(l,p)*cE1(m,n,o,p);

sE1Ybot(i,j,k,l)=sE1Ybot(i,j,k,l)+abot(i,m)*abot(j,n)*abot(k,o)*abot(l,p)*sE1(m,n,o,p);

cE1Ybot(i,j,k,l)=cE1Ybot(i,j,k,l)+abot(i,m)*abot(j,n)*abot(k,o)*abot(l,p)*cE1(m,n,o,p);
                                        end
                                    end
                                end
                            end
                        end
                    end
                end
            end

            %D/E to 2D

            for i=1:3
                for j=1:3
                    for k=1:3
                        if j==k
                            DY(i,j)=D1Y(i,j,k);
                            EY(i,j)=E1Y(i,j,k);
                            DYbot(i,j)=D1Ybot(i,j,k);
                            EYbot(i,j)=E1Ybot(i,j,k);
                        else
                            DY(i,9-j-k)=2*D1Y(i,j,k);
                            EY(i,9-j-k)=E1Y(i,j,k);
                            DYbot(i,9-j-k)=2*D1Ybot(i,j,k);
                            EYbot(i,9-j-k)=E1Ybot(i,j,k);
                        end
                    end
                end
            end

            %sE/cE to 2D

            for i=1:3
                for j=1:3
                    for k=1:3
                        for l=1:3
                            if i==j&&k==l
                                sEY(i,k)=sE1Y(i,j,k,l);
                                cEY(i,k)=cE1Y(i,j,k,l);
                                sEYbot(i,k)=sE1Ybot(i,j,k,l);
                                cEYbot(i,k)=cE1Ybot(i,j,k,l);
                            else if i==j&k~=l
                                    sEY(i,9-k-l)=2*sE1Y(i,j,k,l);
                                    cEY(i,9-k-l)=cE1Y(i,j,k,l);
                                    sEYbot(i,9-k-l)=2*sE1Ybot(i,j,k,l);
                                    cEYbot(i,9-k-l)=cE1Ybot(i,j,k,l);
                                else if i~=j&k==l
                                        sEY(9-i-j,k)=2*sE1Y(i,j,k,l);
                                        cEY(9-i-j,k)=cE1Y(i,j,k,l);
                                        sEYbot(9-i-j,k)=2*sE1Ybot(i,j,k,l);
                                        cEYbot(9-i-j,k)=cE1Ybot(i,j,k,l);
                                    else if i~=j&k~=l
                                            sEY(9-i-j,9-k-l)=4*sE1Y(i,j,k,l);
                                            cEY(9-i-j,9-k-l)=cE1Y(i,j,k,l);
                                            sEYbot(9-i-j,9-k-l)=4*sE1Ybot(i,j,k,l);
                                            cEYbot(9-i-j,9-k-l)=cE1Ybot(i,j,k,l);
                                        end
                                    end
                                end
                            end
                        end
                    end
                end
            end
```

```
                        end
                    end
                end
            end
        end
    end

    %%%%%%%%%%%%%%%%%%%%%%%%%%%%%%%%%%%%%%%%%%%%%%%%%%%%%%%%%%%%%%%%%%%%%%%%%%%%
    inveT1Y=zeros(3);

    % inveT1Y=inv(eT1Y);                        %D1, D2 = 0
    inveT1Y(3,3)=1/eT1Y(3,3);                   %E1, E2 = 0

    DY1=DY(:,[1 2 6]);
    DYbot1=DYbot(:,[1 2 6]);
    sEY1=sEY([1 2 6],[1 2 6]);


    sEYbot1=sEYbot([1 2 6],[1 2 6]);

    sEff=sEY1-DY1'*(inveT1Y*DY1);

    sEffbot=sEYbot1-DYbot1'*(inveT1Y*DYbot1);

    sEffinv=inv(sEff);
    sEffbotinv=inv(sEffbot);

    dEff=-(inveT1Y*DY1)*sEffinv;
    dEffbot=-(inveT1Y*DYbot1)*sEffbotinv;

    sHinv=inv(sH([1 2 6],[1 2 6]));
    sqinv=sHinv*(q(1,[1 2 6])');
    sqinvaE32=sHinv*(q(2,[1 2 6])');

    %%%%%%%%%%%%%%%%%%%%%%%%%%%%%%%%%%%%%%%%%%%%%%%%%%%%%%%%%%%%%%%%%%%%%%%%%%%%

    tm=tm1;


    vp=tp/(tp+tm);

    A=zeros(6);
    A11=(tm)*sHinv + (-(-tp*xbid))*sEffinv + (-tp*xbid - (-tp))*sEffbotinv;
    A12=((tm^2)/2)*sHinv + (-((-tp*xbid)^2)/2)*sEffinv + (((-tp*xbid)^2)/2 - ((-tp)^2)/2)*sEffbotinv;
    A21=A12;
    A22=((tm^3)/3)*sHinv + (-((-tp*xbid)^3)/3)*sEffinv + (((-tp*xbid)^3)/3 - ((-tp)^3)/3)*sEffbotinv;
    A=[A11 A12;A21 A22];

    B=zeros(6,1);
    B1=(tm)*sqinv;
    B2=((tm^2)/2)*sqinv;
    B31=[B1;B2];


    %%%%%%%%%%%%%%%%%%%%%%%%%%%%%%%%%%%%%%%%%%%%%%%%%%%%%%%%%%%%%%%%%%%%%%%%%%%%

    C1=(-(-tp*xbid1))*dEff(3,:) + (-tp*xbid1 - (-tp))*dEffbot(3,:);
    C2=(-((-tp*xbid1)^2)/2)*dEff(3,:) + (((-tp*xbid1)^2)/2 - ((-tp)^2)/2)*dEffbot(3,:);
    C=[C1 C2];

    aE31=(C*(A\B31))/(100*tp);

    B1=(tm)*sqinvaE32;
    B2=((tm^2)/2)*sqinvaE32;
    B32=[B1;B2];

    aE32=(C*(A\B32))/(100*tp);

    aE31extensional=([C1 0 0 0]*(A\B31))/(100*tp);
    aE32extensional=([C1 0 0 0]*(A\B32))/(100*tp);
    aE31flexural=([0 0 0 C2]*(A\B31))/(100*tp);
    aE32flexural=([0 0 0 C2]*(A\B32))/(100*tp);

    alfaE31(Al,Be,Sig)=aE31;
    alfaE32(Al,Be,Sig)=aE32;
    alfaE31ext(Al,Be,Sig)=aE31extensional;
    alfaE32ext(Al,Be,Sig)=aE32extensional;
    alfaE31flex(Al,Be,Sig)=aE31flexural;
    alfaE32flex(Al,Be,Sig)=aE32flexural;

  end
 end
 Alfa
end
```

Code A.4.5. Calculation of the maximum analytical transversal dynamic flexural ME coefficients (α_{E31} and α_{E32}), electrical impedance (Z) and intrinsic thermal spectral noise density (e_n) for a series of bi-layered long bars of Metglas/piezoelectric, containing a unidomain or bidomain piezoelectric crystal, as a function of the frequency of the applied modulated magnetic field, crystalline orientation of the piezoelectric, geometry of the

composite and loss factors due to internal friction and intermediate layers of epoxy or a non-piezoelectric dielectric.

```
clearvars -except P eS1Y eT1Y DY EY cEY sEY
close all
clc

Bidomain=1;

Kb=1.287158974E-10;    % sqrt(4*kb*T),  T=300K
e0=8.8541878176E-12; %F/m

i=0;
for x=linspace(0.01,0.99,101)
    i=i+1;
    xl(i)=x;

    %Parameters:

    %geometry (m)

    l=10E-3;
    w=1E-3;

    %Metglas
    Pm=7900;

    %piezomagnetic coefficient (1/Oe)

    q11=4E-6;
    q12=-1.7E-6;
    q16=0E-6;
    q=[q11 q12 q12 0 0 q16;q12 q11 q12 0 0 q16;q12 q12 q11 0 0 q16];

    %compliance coefficients (m^2/N)
    s11H=10E-12;
    s12H=-3.3E-12;
    s44H=2*13.3E-12;
    sH=[s11H s12H s12H 0 0 0;s12H s11H s12H 0 0 0;s12H s12H s11H 0 0 0;0 0 0 s44H 0 0;0 0 0 0 s44H 0;0 0 0 0 0 s44H];


    %Epoxy

    PE=1164;

    %compliance coefficients (m^2/N)
    s11E=292E-12;
    s12E=-101.5E-12;
    s44E=2*(s11E-s12E);
    sE=[s11E s12E s12E 0 0 0;s12E s11E s12E 0 0 0;s12E s12E s11E 0 0 0;0 0 0 s44E 0 0;0 0 0 0 s44E 0;0 0 0 0 0 s44E];

    %dielectric coefficients
    eTE=(4.25)*e0*eye(3);

    %Effective parameters

    % cD11=1/(sEY(1,1)-DY(3,1)*DY(3,1)/eT1Y(3,3));
    % h31=cD11*DY(3,1)/eT1Y(3,3);
    % b331=(1/eT1Y(3,3))*(1+h31*DY(3,1));

    tgloss=0.007;
    eT1Yloss=(eT1Y(3,3)*(1-1i*tgloss));
    cD22=(1)/(sEY(2,2)-DY(3,2)*DY(3,2)/(eT1Yloss));
    h32=cD22*DY(3,2)/(eT1Yloss);
    b332=(1/(eT1Yloss))*(1+h32*DY(3,2));

    cH22=1/(sH(2,2));
    qH22=cH22*q(2,2);

    cD22E=(1)/(sE(2,2));
    h32E=0;
    b332E=(1/(eTE(3,3)*(1-1i*tgloss)));


    %geometry (m)

    tpm=((0.5E-3)+(29E-6));

    te=0;%1000E-6;
    X=(0.5E-3)/tpm;
    Xnp=0;
    % X=0.6
    tp=X*tpm;
    xbid=0.5;    %up polarization fraction
    if Bidomain == 0
        xbid=1;
    end

    t1=(1-xbid)*(1-Xnp)*tp;
    t2=Xnp*tp;
    t3=xbid*(1-Xnp)*tp;
    t4=te;
    t5=(1-X)*tpm;

    tp=tp+te;
```

```
    tm=t5;
    ti=[t1 t2 t3 t4 t5];
    t=sum(ti);

    c22t=[cD22 cD22 cD22 cD22E cH22];
    h32t=[-h32 0 h32 0 0];
    b33t=[b332 b332 b332 b332E 0];
    q22t=[0 0 0 0 qH22];

    tc=cumsum(ti);
    tc=[0 tc];

    d221=0;
    d222=0;
    for I=1:length(ti)
        d222=d222+2*c22t(I)*ti(I);
        d221=d221+c22t(I)*((ti(I)^2)+2*ti(I)*tc(I));
    end
    d22=d221/d222;
    % 1-(d22/tp)
    % 1-0.5*(t/tp)

    B332=0;
    H32=0;
    D22p=0;
    for I=1:4
        B332=B332+b33t(I)*(ti(I)/tp);
        H32=H32+h32t(I)*(((tc(I+1)-d22)^2)-((tc(I)-d22)^2))/(2*tp);
        D22p=D22p+c22t(I)*(((tc(I+1)-d22)^3)-((tc(I)-d22)^3))/(3*tp);
    end
    Q22=q22t(5)*(((tc(5+1)-d22)^2)-((tc(5)-d22)^2))/(2*tm);
    D22m=c22t(5)*(((tc(5+1)-d22)^3)-((tc(5)-d22)^3))/(3*tm);
    D22=(D22p-((H32^2)/B332))*(tp/(t^3))+(D22m)*(tm/(t^3));
    Pmed=(P*(t1+t2+t3)+PE*t4+Pm*t5)/t;

    Q=300;
    f=linspace(0.001,100E3,100000);
    W=2*pi*f;
    W=W.*(1-1i*(1/Q));
    K=((Pmed/(D22*(t^2)))^(1/4))*sqrt(W)*(1/2);

    fk=K.*(cot(K)+coth(K));
    Y=((1i*W*w*l)./(tp*B332)).*(1+(2*tp*(H32^2)./(B332*t*(D22*(t^2))*fk)));
    aE32=-(tm*Q22*H32)./(((tp*((H32^2)./B332))+t*(D22*(t^2))*0.5*fk));
    fr=real((2*(2.365^2)/(pi*(l^2)))*sqrt((D22*(t^2))/Pmed))
    Nmin(i)=min((1E-4)*Kb*sqrt(real(1./Y))./(abs(aE32).*tp));

    W=2*pi*0.00001*(1-1i*(1/Q));
    K=((Pmed/(D22*(t^2)))^(1/4))*sqrt(W)*(1/2);
    fk=K.*(cot(K)+coth(K));
    Ylowf(i)=((1i*W*w*l)./(tp*B332)).*(1+(2*tp*(H32^2)./(B332*t*(D22*(t^2))*fk)));
    aE32lowf(i)=-(tm*Q22*H32)./((tp*((H32^2)./B332))+t*(D22*(t^2))*0.5*fk);
    Noilowf(i)=(1E-4)*Kb*sqrt(real(1./Ylowf(i))).*(abs(aE32lowf(i)).*tp);
    aElowf(i)=abs(aE32lowf(i)*tp);

    W=2*pi*fr*(1-1i*(1/Q));
    K=((Pmed/(D22*(t^2)))^(1/4))*sqrt(W)*(1/2);
    fk=K.*(cot(K)+coth(K));
    Yres(i)=((1i*W*w*l)./(tp*B332)).*(1+(2*tp*(H32^2)./(B332*t*(D22*(t^2))*fk)));
    aE32res(i)=-(tm*Q22*H32)./((tp*((H32^2)./B332))+t*(D22*(t^2))*0.5*fk);
    Noires(i)=(1E-4)*Kb*sqrt(real(1./Yres(i))).*(abs(aE32res(i)).*tp);
    aEres(i)=abs(aE32res(i)*tp);

    Fr(i)=fr;

    semilogy(f,(1E12)*(1E-4)*Kb*sqrt(real(1./Y)).*(abs(aE32).*tp),f,(1E-
6)*abs(1./Y),f,abs(aE32)/100,f,(1E9)*Kb*sqrt(real(1./Y)))
    hold on
end

figure
plot((xl).^(1),Noilowf,'.-')
polyfit(log(xl),log(real(Noilowf)),1)
figure
plot((xl).^(1),Noires,'.-')
polyfit(log(xl),log(Noires),1)
figure
plot((xl).^(1),Nmin,'.-')
polyfit(log(xl),log(Nmin),1)
```

Code A.4.6. Numerical calculation of the dynamic electrical impedance (Z) and displacement fields (u_i) in a series of unidomain or bidomain piezoelectric crystal plates as a function of the frequency of the applied voltage, crystalline orientation of the piezoelectric, geometry of the plate and damping factors, using a finite element method (FEM) realized with the help of Matlab's (version R2014b) partial differential equation and parallel computing toolboxes.

```
clearvars -except P E1Y EY cE1Y cEY eS1Y
close all hidden
```

```
clc

% Parameters

Parallel=0;             % Parallel computing - 1 true; 0 false.
GalCol=1;               % 1 - Galerkin; 0 - Colocation method
LinPot=1;               % Linear potential - 1 true; 0 false; 2 true + equations
ZContInt=0;             % 0 - Z continuous integration; 1 - Top/Bot half integration; 2 - U=UtopIZtopI + UbotIZbotI
Top/Bot half integration;

Bidomain=1;             % 1 - Bidomain; 0 - Unidomain
T3jl=1;                 % Set T3j|h1-0 / T3j|0-h2 in system of eqs - 1 true; 0 false.
T3j0topbot=0;           % Impose T3j(0+)=T3j(0-) - 1 true; 0 false (LinPot = 0).
Ttopboteqs=1;           % Impose Ttop Tbot - 1 true; 0 false.

N = 3;
Neq = 4*(N+1);          % Number of equations 4*(N+1)
I1=N-1;                 % Substituted equations
I2=N;

Ttop3=zeros(3,1);       % T3j top/bot
Tbot3=zeros(3,1);
Vtop=0.1;                 % V.exp(iwt) top/bot
Vbot=0;

%Frequency interval

Fmin=1E3;
Fmax=500E3;
Fstep=50;
Freq=Fmin:Fstep:Fmax;

%Damping

Damp=0;
Dampv=0;    %1E7
Dampv2=2;   %37/2
Dampv3=0;

%Geometry

Hl=0.5E-3;
h1=Hl/2;
h2=h1-Hl;

L1=5E-3;
L2=5E-3;
L=(L1+L2)/2;

gd=[3;4;-L1;L1;L1;-L1;L2;L2;-L2;-L2];
sf='R1';
ns=[82;49];

dl=decsg(gd,sf,ns);
pdegplot(dl,'edgelabels','on','subdomainlabels','on')
axis square
axis([-L*1.1,L*1.1,-L*1.1,L*1.1])

%FEM Mesh

[p,e,t]=initmesh(dl,'Hmax',L/15,'MesherVersion','R2013a');
% [p,e,t]=refinemesh(dl,p,e,t,'regular');
% [p,e,t]=refinemesh(dl,p,e,t,'regular');
% [p,e,t]=refinemesh(dl,p,e,t,'regular');
% [p,e,t]=refinemesh(dl,p,e,t,'longest');
p=jigglemesh(p,e,t,'opt','mean','iter',inf);
figure
pdemesh(p,e,t)
axis square
axis([-L*1.1,L*1.1,-L*1.1,L*1.1])


%Top layer material coefficients

if Bidomain==1
    a=[1 0 0;0 -1 0;0 0 -1];
else
    a=eye(3);
end

%Rotated eS

eS1Ytop(1:3,1:3)=0;
for i=1:3
    for j=1:3
        for m=1:3
            for n=1:3
                eS1Ytop(i,j)=eS1Ytop(i,j)+a(i,m)*a(j,n)*eS1Y(m,n);
            end
        end
    end
end

%Rotated E

E1Ytop(1:3,1:3,1:3)=0;
for i=1:3
    for j=1:3
```

```
        for k=1:3
            for m=1:3
                for n=1:3
                    for o=1:3
                        E1Ytop(i,j,k)=E1Ytop(i,j,k)+a(i,m)*a(j,n)*a(k,o)*E1Y(m,n,o);
                    end
                end
            end
        end
    end
end

%Rotated cE

cE1Ytop(1:3,1:3,1:3,1:3)=0;
for i=1:3
    for j=1:3
        for k=1:3
            for l=1:3
                for m=1:3
                    for n=1:3
                        for o=1:3
                            for q=1:3
                                cE1Ytop(i,j,k,l)=cE1Ytop(i,j,k,l)+a(i,m)*a(j,n)*a(k,o)*a(l,q)*cE1Y(m,n,o,q);
                            end
                        end
                    end
                end
            end
        end
    end
end


% Number of triangles
nt = size(t,2);
% Triangle point indices
it1=t(1,:);
it2=t(2,:);
it3=t(3,:);
% Find centroids of triangles
xpts=(p(1,it1)+p(1,it2)+p(1,it3))/3;
ypts=(p(2,it1)+p(2,it2)+p(2,it3))/3;
% Triangle geometries:
[Area,g1x,g1y,g2x,g2y,g3x,g3y]=pdetrg(p,t);

np = size(p,2); % number of mesh points
u0 = zeros(np,Neq); % allocate initial matrix
u0 = u0(:); % convert to column form

% Define vIvJ ...

vI0=zeros(1,N+1); vI0(1)=1;                                                 % vI z=0
vI01=zeros(1,N+1); vI01(2)=1;                                               % vI' z=0
for tb=1:2
    if tb==1
        h=h1;
    else
        h=h2;
    end
    signh=-(-1)^tb;
    for I=0:N
        vI(I+1,tb)=signh*(1/(I+1))*(h^(I+1)-0^(I+1));                           % <vI> t/b
        vItb(I+1,tb)=h^I;                                                       % vI t/b
        vI1tb(I+1,tb)=I*(h^(I-1));                                              % vI't/b
        if I>0
            vI1(I+1,tb)=signh*(h^I-0^I);                                        % <vI'> t/b
        else
            vI1(I+1,tb)=0;
        end
        for J=0:N
            if GalCol==1
                vIvJ(I+1,J+1,tb)=signh*(1/(I+J+1))*(h^(I+J+1)-0^(I+J+1));    % <vI,vJ> t/b
                vIvJt(I+1,J+1,tb)=signh*(h^(I+J)-0^(I+J));                   % vI.vJ t/-b
                if I+J>0
                    vI1vJ(I+1,J+1,tb)=signh*(I/(I+J))*(h^(I+J)-0^(I+J));    % <vI',vJ> t/b
                    vIvJ1(I+1,J+1,tb)=signh*(J/(I+J))*(h^(I+J)-0^(I+J));    % <vI,vJ'> t/b
                    vIvJ1t(I+1,J+1,tb)=signh*J*(h^(I+J-1)-0^(I+J-1));        % vI.vJ' t/-b
                else
                    vI1vJ(I+1,J+1,tb)=0;
                    vIvJ1(I+1,J+1,tb)=0;
                    vIvJ1t(I+1,J+1,tb)=0;
                end
                if I+J-1>0
                    vI1vJ1(I+1,J+1,tb)=signh*((I*J)/(I+J-1))*(h^(I+J-1)-0^(I+J-1));  % <vI',vJ'> t/b
                else
                    vI1vJ1(I+1,J+1,tb)=0;
                end
            else
                if J==I
                    vIvJ(I+1,J+1,tb)=1;
                elseif J==I+1
                    vIvJ1(I+1,J+1,tb)=I+1;
                    vI1vJ(I+1,J+1,tb)=-(I+1);
                elseif J==I+2
                    vI1vJ1(I+1,J+1,tb)=-(I+1)*(I+2);
                else
                    vIvJ(I+1,J+1,tb)=0;
```

```
                    vIvJ1(I+1,J+1,tb)=0;
                    vI1vJ(I+1,J+1,tb)=0;
                    vI1vJ1(I+1,J+1,tb)=0;
                    vIvJt(I+1,J+1,tb)=0;
                    vIvJ1t(I+1,J+1,tb)=0;
                end
            end
        end
    end
end

% Define material matrices

for tb=1:2
    for j=1:4
        for k=1:4
            for a=1:3
                for b=1:3
                    if j==4&&k==4
                        if tb==1
                            Mjk(j,k,a,b,tb)=-eS1Ytop(a,b);
                        else
                            Mjk(j,k,a,b,tb)=-eS1Y(a,b);
                        end
                    elseif j==4
                        if tb==1
                            Mjk(j,k,a,b,tb)=E1Ytop(a,k,b);
                        else
                            Mjk(j,k,a,b,tb)=E1Y(a,k,b);
                        end
                    elseif k==4
                        if tb==1
                            Mjk(j,k,a,b,tb)=E1Ytop(b,a,j);
                        else
                            Mjk(j,k,a,b,tb)=E1Y(b,a,j);
                        end
                    else
                        if tb==1
                            Mjk(j,k,a,b,tb)=cE1Ytop(a,j,k,b);
                        else
                            Mjk(j,k,a,b,tb)=cE1Y(a,j,k,b);
                        end
                    end
                end
            end
        end
    end
end

Tjk=Mjk; Tjk(4,:,:,:,:)=0;
Djk=Mjk; Djk(1:3,:,:,:,:)=0;
dTjk=eye(4,4); dTjk(4,4)=0;
dDjk=zeros(4,4); dDjk(4,4)=1;


% C coefficients

C1=zeros(Neq,Neq,2,2,2);
Cbc=zeros(4,Neq,2,2,2);
CT3j0=zeros(4,Neq,2,2,2);
for tb=1:2
    for I=0:N
        for J=0:N
            for j=1:4
                for k=1:4
                    for a=1:2
                        for b=1:2
                            C1(4*I+j,4*J+k,a,b,tb) = Mjk(j,k,a,b,tb)*vIvJ(I+1,J+1,tb);
                        end
                    end
                end
            end
        end
    end
end

%A coefficients -W

A11=zeros(Neq,Neq,2);
A21=zeros(Neq,Neq,2);
A1bc=zeros(4,Neq,2);
A2bc=zeros(4,Neq,2);
AT3j01=zeros(4,Neq,2);
AT3j02=zeros(4,Neq,2);

for tb=1:2
    for I=0:N
        for J=0:N
            for j=1:4
                for k=1:4
                    A1bc(j,4*J+k,tb) = Tjk(j,k,3,3,tb)*vI1tb(J+1,tb) + dDjk(j,k)*vItb(J+1,tb);
                    A2bc(j,4*J+k,tb) = 0;
                    if T3jl==1
                        signh=-(-1)^tb;
                        A11(4*I+j,4*J+k,tb) = Mjk(j,k,3,3,tb)*vI1vJ1(I+1,J+1,tb) - Djk(j,k,3,3,tb)*vIvJ1t(I+1,J+1,tb) +
signh*Tjk(j,k,3,3,tb)*vI0(I+1)*vI01(J+1);
                    else
                        A11(4*I+j,4*J+k,tb) = Mjk(j,k,3,3,tb)*vI1vJ1(I+1,J+1,tb) - Mjk(j,k,3,3,tb)*vIvJ1t(I+1,J+1,tb);
```

```
                    end
                    A21(4*I+j,4*J+k,tb) = dTjk(j,k)*vIvJ(I+1,J+1,tb);
                    if J==1
                        AT3j01(j,4*J+k,tb) = Tjk(j,k,3,3,tb);
                    end
                end
            end
        end
    end
end


% f coeficients

F1=zeros(Neq,2);
Fbc=zeros(4,2);
FT3j0=zeros(4,2);
TDtop=[Ttop3;Vtop];
TDbot=[Tbot3;Vbot];
TDtopbot=[TDtop,TDbot];
Ttop31=[Ttop3;0];
Tbot31=[Tbot3;0];
Ttopbot=[Ttop31,-Tbot31];
for tb=1:2
    for I=0:N
        for j=1:4
            Fbc(j,tb)=TDtopbot(j,tb);
            if T3jl==1
                signh=-(-1)^tb;
                F1(4*I+j,tb)=signh*Ttopbot(j,tb)*vItb(I+1,tb);
            else
                F1(4*I+j,tb)=0;
            end
        end
    end
end


% O coefficients

O1=zeros(Neq,Neq,2,2);
Obc=zeros(4,Neq,2,2);
OT3j0=zeros(4,Neq,2,2);
for tb=1:2
    for I=0:N
        for J=0:N
            for j=1:4
                for k=1:4
                    for b=1:2
                        Obc(j,4*J+k,b,tb) = Tjk(j,k,3,b,tb)*vItb(J+1,tb);
                        if T3jl==1
                            signh=-(-1)^tb;
                            O1(4*I+j,4*J+k,b,tb) = -vIvJ1(I+1,J+1,tb)*Mjk(j,k,b,3,tb) + vI1vJ(I+1,J+1,tb)*Mjk(j,k,3,b,tb)
- vIvJt(I+1,J+1,tb)*Djk(j,k,3,b,tb) + signh*Tjk(j,k,3,b,tb)*vI0(I+1)*vI0(J+1);
                        else
                            O1(4*I+j,4*J+k,b,tb) = -vIvJ1(I+1,J+1,tb)*Mjk(j,k,b,3,tb) + vI1vJ(I+1,J+1,tb)*Mjk(j,k,3,b,tb)
- vIvJt(I+1,J+1,tb)*Mjk(j,k,3,b,tb);
                        end
                        if J==0
                            OT3j0(j,4*J+k,b,tb) = Tjk(j,k,3,b,tb);
                        end
                    end
                end
            end
        end
    end
end


% Boundary conditions

pg = pdeGeometryFromEdges(dl);
Q1=zeros(Neq,Neq,2);
Qbc=zeros(4,Neq,2);
Q1ed=zeros(Neq,Neq,4,2);
Qbced=zeros(4,Neq,4,2);
QT3j0ed=zeros(4,Neq,4,2);

na(1,:)=[0,1,0,-1];
na(2,:)=[1,0,-1,0];
for tb=1:2
    for ed=1:4;
        for I=0:N
            for J=0:N
                for j=1:4
                    for k=1:4
                        Q1(4*I+j,4*J+k,tb) = 0;
                        for b=1:2
                            Qbc(j,4*J+k,tb) = 0;
                            Q1(4*I+j,4*J+k,tb) = Q1(4*I+j,4*J+k,tb) + na(b,ed)*(Mjk(j,k,b,3,tb)*vIvJ1(I+1,J+1,tb));
                        end
                        Qbced(j,4*J+k,ed,tb) = Qbc(j,4*J+k,tb);
                        Q1ed(4*I+j,4*J+k,ed,tb) = Q1(4*I+j,4*J+k,tb);
                    end
                end
            end
        end
```

```
    end
end


%Material matrices (top + bot)

if ZContInt==0
    C = C1(:,:,:,:,1) + C1(:,:,:,:,2);
    A1 = A11(:,:,1) + A11(:,:,2);
    A2 = A21(:,:,1) + A21(:,:,2);
    F = F1(:,1) + F1(:,2);
    O = O1(:,:,:,1) + O1(:,:,:,2);
    Qed = Q1ed(:,:,:,1) + Q1ed(:,:,:,2);
elseif ZContInt==1
    for I=0:N
        ind=1.5-0.5*(-1)^I;
        C(4*I+(1:4),:,:,:) = C1(4*I+(1:4),:,:,:,ind);
        A1(4*I+(1:4),:) = A11(4*I+(1:4),:,ind);
        A2(4*I+(1:4),:) = A21(4*I+(1:4),:,ind);
        F(4*I+(1:4),1) = F1(4*I+(1:4),ind);
        O(4*I+(1:4),:,:) = O1(4*I+(1:4),:,:,ind);
        Qed(4*I+(1:4),:,:) = Q1ed(4*I+(1:4),:,:,ind);
    end
else
    C=zeros(2*Neq,2*Neq,2,2);
    C(1:Neq,1:Neq,:,:) = C1(:,:,:,:,1);
    C(Neq+1:2*Neq,1:4,:,:) = C1(:,1:4,:,:,2);
    C(Neq+1:2*Neq,Neq+5:2*Neq,:,:) = C1(:,5:end,:,:,2);
    C(:,Neq+1:Neq+4,:,:) = [];
    A1=zeros(2*Neq,2*Neq);
    A1(1:Neq,1:Neq) = A11(:,:,1);
    A1(Neq+1:2*Neq,1:4) = A11(:,1:4,2);
    A1(Neq+1:2*Neq,Neq+5:2*Neq) = A11(:,5:end,2);
    A1(:,Neq+1:Neq+4) = [];
    A2=zeros(2*Neq,2*Neq);
    A2(1:Neq,1:Neq) = A21(:,:,1);
    A2(Neq+1:2*Neq,1:4) = A21(:,1:4,2);
    A2(Neq+1:2*Neq,Neq+5:2*Neq) = A21(:,5:end,2);
    A2(:,Neq+1:Neq+4) = [];
    O=zeros(2*Neq,2*Neq,2);
    O(1:Neq,1:Neq,:) = O1(:,:,:,1);
    O(Neq+1:2*Neq,1:4,:) = O1(:,1:4,:,2);
    O(Neq+1:2*Neq,Neq+5:2*Neq,:) = O1(:,5:end,:,2);
    O(:,Neq+1:Neq+4,:) = [];
    Qed=zeros(2*Neq,2*Neq,4);
    Qed(1:Neq,1:Neq,:) = Q1ed(:,:,:,1);
    Qed(Neq+1:2*Neq,1:4,:) = Q1ed(:,1:4,:,2);
    Qed(Neq+1:2*Neq,Neq+5:2*Neq,:) = Q1ed(:,5:end,:,2);
    Qed(:,Neq+1:Neq+4,:) = [];
    F=zeros(2*Neq,1);
    F(1:Neq,1) = F1(:,1);
    F(Neq+1:2*Neq,1) = F1(:,2);
end

%Substitute top/bot boundary conditions

if Ttopboteqs==1
    J=1;
else
    J=4;
end
if ZContInt~=2
    for I=0:N
        if I==I1
            C(4*I+J:4*I+4,:,:,:) = Cbc(J:4,:,:,:,1);
            A1(4*I+J:4*I+4,:) = A1bc(J:4,:,1);
            A2(4*I+J:4*I+4,:) = A2bc(J:4,:,1);
            F(4*I+J:4*I+4) = Fbc(J:4,1);
            O(4*I+J:4*I+4,:,:) = Obc(J:4,:,:,1);
            Qed(4*I+J:4*I+4,:,:) = Qbced(J:4,:,:,1);
        elseif I==I2
            C(4*I+J:4*I+4,:,:,:) = Cbc(J:4,:,:,:,2);
            A1(4*I+J:4*I+4,:) = A1bc(J:4,:,2);
            A2(4*I+J:4*I+4,:) = A2bc(J:4,:,2);
            F(4*I+J:4*I+4) = Fbc(J:4,2);
            O(4*I+J:4*I+4,:,:) = Obc(J:4,:,:,2);
            Qed(4*I+J:4*I+4,:,:) = Qbced(J:4,:,:,2);
        end
    end
else
    C(Neq-4+J:Neq,1:Neq,:,:) = Cbc(J:4,:,:,:,1);
    C(2*Neq-4+J:2*Neq,1:4,:,:) = Cbc(J:4,1:4,:,:,2);
    C(2*Neq-4+J:2*Neq,Neq+1:2*Neq-4,:,:) = Cbc(J:4,5:end,:,:,2);
    A1(Neq-4+J:Neq,1:Neq) = A1bc(J:4,:,1);
    A1(2*Neq-4+J:2*Neq,1:4) = A1bc(J:4,1:4,2);
    A1(2*Neq-4+J:2*Neq,Neq+1:2*Neq-4) = A1bc(J:4,5:end,2);
    A2(Neq-4+J:Neq,1:Neq) = A2bc(J:4,:,1);
    A2(2*Neq-4+J:2*Neq,1:4) = A2bc(J:4,1:4,2);
    A2(2*Neq-4+J:2*Neq,Neq+1:2*Neq-4) = A2bc(J:4,5:end,2);
    F(Neq-4+J:Neq,1) = Fbc(J:4,1);
    F(2*Neq-4+J:2*Neq,1) = Fbc(J:4,2);
    O(Neq-4+J:Neq,1:Neq,:) = Obc(J:4,:,:,1);
    O(2*Neq-4+J:2*Neq,1:4,:) = Obc(J:4,1:4,:,2);
    O(2*Neq-4+J:2*Neq,Neq+1:2*Neq-4,:) = Obc(J:4,5:end,:,2);
    Qed(Neq-4+J:Neq,1:Neq,:) = Qbced(J:4,:,:,1);
    Qed(2*Neq-4+J:2*Neq,1:4,:) = Qbced(J:4,1:4,:,2);
    Qed(2*Neq-4+J:2*Neq,Neq+1:2*Neq-4,:) = Qbced(J:4,5:end,:,2);
```

```
    % -1 Line
    C(Neq-3-4:Neq-4,:,:,:) = C(Neq-3-4:Neq-4,:,:,:) + C(2*Neq-3-4:2*Neq-4,:,:,:);
    C(2*Neq-3-4:2*Neq-4,:,:,:) = [];
    A1(Neq-3-4:Neq-4,:,:,:) = A1(Neq-3-4:Neq-4,:) + A1(2*Neq-3-4:2*Neq-4,:);
    A1(2*Neq-3-4:2*Neq-4,:,:,:) = [];
    A2(Neq-3-4:Neq-4,:,:,:) = A2(Neq-3-4:Neq-4,:) + A2(2*Neq-3-4:2*Neq-4,:);
    A2(2*Neq-3-4:2*Neq-4,:,:,:) = [];
    F(Neq-3-4:Neq-4,1) = F(Neq-3-4:Neq-4,1) + F(2*Neq-3-4:2*Neq-4,1);
    F(2*Neq-3-4:2*Neq-4) = [];
    O(Neq-3-4:Neq-4,:,:,:) = O(Neq-3-4:Neq-4,:,:) + O(2*Neq-3-4:2*Neq-4,:,:);
    O(2*Neq-3-4:2*Neq-4,:,:) = [];
    Qed(Neq-3-4:Neq-4,:,:) = Qed(Neq-3-4:Neq-4,:,:) + Qed(2*Neq-3-4:2*Neq-4,:,:);
    Qed(2*Neq-3-4:2*Neq-4,:,:) = [];
end

% Impose T3j(0+)=T3j(0-)

if T3j0topbot==1;
    if ZContInt~=2
        NN=0:N;
        NN([I1+1 I2+1])=[];
        I=max(NN);
        C(4*I+1:4*I+3,:,:,:) = CT3j0(1:3,:,:,:,1) - CT3j0(1:3,:,:,:,2);
        A1(4*I+1:4*I+3,:) = AT3j01(1:3,:,1) - AT3j01(1:3,:,2);
        A2(4*I+1:4*I+3,:) = AT3j02(1:3,:,1) - AT3j02(1:3,:,2);
        F(4*I+1:4*I+3) = FT3j0(1:3,1) - FT3j0(1:3,2);
        O(4*I+1:4*I+3,:,:) = OT3j0(1:3,:,:,1) - OT3j0(1:3,:,:,2);
        Qed(4*I+1:4*I+3,:,:) = QT3j0ed(1:3,:,:,1) - QT3j0ed(1:3,:,:,2);
    else
        C(Neq-3-4:Neq-5,1:4,:,:) = CT3j0(1:3,1:4,:,:,1) - CT3j0(1:3,1:4,:,:,2);
        C(Neq-3-4:Neq-5,5:Neq,:,:) = CT3j0(1:3,5:end,:,:,1);
        C(Neq-3-4:Neq-5,Neq+1:end,:,:) = - CT3j0(1:3,5:end,:,:,2);
        A1(Neq-3-4:Neq-5,1:4,:,:) = AT3j01(1:3,1:4,1) - AT3j01(1:3,1:4,2);
        A1(Neq-3-4:Neq-5,5:Neq,:,:) = AT3j01(1:3,5:end,1);
        A1(Neq-3-4:Neq-5,Neq+1:end,:,:) = - AT3j01(1:3,5:end,2);
        A2(Neq-3-4:Neq-5,1:4,:,:) = AT3j02(1:3,1:4,1) - AT3j02(1:3,1:4,2);
        A2(Neq-3-4:Neq-5,5:Neq,:,:) = AT3j02(1:3,5:end,1);
        A2(Neq-3-4:Neq-5,Neq+1:end,:,:) = - AT3j02(1:3,5:end,2);
        F(Neq-3-4:Neq-5,1) = FT3j0(1:3,1) - FT3j0(1:3,2);
        O(Neq-3-4:Neq-5,1:4,:) = OT3j0(1:3,1:4,:,1) - OT3j0(1:3,1:4,:,2);
        O(Neq-3-4:Neq-5,5:Neq,:) = OT3j0(1:3,5:end,:,1);
        O(Neq-3-4:Neq-5,Neq+1:end,:) = - OT3j0(1:3,5:end,:,2);
        Qed(Neq-3-4:Neq-5,1:4,:) = QT3j0ed(1:3,1:4,:,1) - QT3j0ed(1:3,1:4,:,2);
        Qed(Neq-3-4:Neq-5,5:Neq,:) = QT3j0ed(1:3,5:end,:,1);
        Qed(Neq-3-4:Neq-5,Neq+1:end,:) = - QT3j0ed(1:3,5:end,:,2);
    end
end

% Linear potential(simplification)

NJ=0;
if LinPot==1
    if ZContInt~=2
        Uo = zeros(Neq,1);
        Uo(4,1) = (Vtop+Vbot)/2;
        Uo(8,1) = (Vtop-Vbot)/Hl;
        Neq = 3*(N+1);
    else
        Uo = zeros(size(C,1),1);
        Uo(4,1) = (Vtop+Vbot)/2;
        Uo(8,1) = (Vtop-Vbot)/Hl;
        Uo(Neq+4,1) = (Vtop-Vbot)/Hl;
    end
    F = F - A1*Uo;
    C(4:4:end,:,:,:) = [];
    C(:,4:4:end,:,:) = [];
    A1(4:4:end,:) = [];
    A1(:,4:4:end) = [];
    A2(4:4:end,:) = [];
    A2(:,4:4:end) = [];
    O(4:4:end,:,:) = [];
    O(:,4:4:end,:) = [];
    Qed(4:4:end,:,:) = [];
    Qed(:,4:4:end,:) = [];
    F(4:4:end) = [];
elseif LinPot==2
    if ZContInt~=2
        NI=4:4:Neq;
        NI([I1+1,I2+1])=[];
        NJ=4:4:Neq;
        NJ(1:2)=[];
        C(NI,:,:,:)=[];
        C(:,NJ,:,:)=[];
        A1(NI,:)=[];
        A1(:,NJ)=[];
        A2(NI,:)=[];
        A2(:,NJ)=[];
        O(NI,:,:)=[];
        O(:,NJ,:)=[];
        Qed(NI,:,:)=[];
        Qed(:,NJ,:)=[];
        F(NI)=[];
    else
        C(Neq-4,:,:,:) = zeros(1,size(C,2),2,2);
        A1(Neq-4,:) = zeros(1,size(C,2));
        A1(Neq-4,8) = 1;
        A1(Neq-4,Neq+4) = -1;
        A2(Neq-4,:) = zeros(1,size(C,2));
```

```
        C(Neq-4,:,:) = zeros(1,size(C,2),2);
        Qed(Neq-4,:,:) = zeros(1,size(C,2),4);
        F(Neq-4)=0;
        NI=4:4:size(C,1);
        NI([Neq/4 Neq/4-1 Neq/2-1])=[];
        NJ=4:4:size(C,1);
        NJ([1 2 Neq/4+1])=[];
        C(NI,:,:,:)=[];
        C(:,NJ,:,:)=[];
        A1(NI,:)=[];
        A1(:,NJ)=[];
        A2(NI,:)=[];
        A2(:,NJ)=[];
        O(NI,:,:)=[];
        O(:,NJ,:)=[];
        Qed(NI,:,:)=[];
        Qed(:,NJ,:)=[];
        F(NI)=[];
    end
end

% Material matrices - line form

Neq=size(C,1);
II=0;
c=zeros((Neq^2)*4,1);
for I=1:Neq
    for J=1:Neq
        for a=1:2
            for b=1:2
                II=II+1;
                c(II,:) = C(J,I,b,a);      %C(j,i,l,k);
            end
        end
    end
end

a1=A1(:);
a2=A2(:);
a2=repmat(a2,1,nt);

f=F;

II=0;
o=zeros((Neq^2)*2,nt);
for I=1:Neq
    for J=1:Neq
        for b=1:2
            II=II+1;
            o(II,:) = O(J,I,b);      %O(j,i,k);
        end
    end
end

for ed=1:4;
    q = Qed(:,:,ed);
    bc(ed) = pdeBoundaryConditions(pg.Edges(ed),'q',q);
end
problem = pde(Neq);
problem.BoundaryConditions = bc;


%Assemble coefficients/boundary FEM matrices

[K,M1,F]=assema(p,t,c,a1,f);
[Q,G,H,R]=assemb(problem,p,e);

%Assemble M2 matrix

m=1;
M2=sparse(Neq*np,Neq*np);
for l=1:Neq,
    for k=1:Neq,
        aod=a2(m,:).*Area/12; % Off diagonal element
        ad=2*aod; % Diagonal element

        M21=sparse(it1,it2,aod,np,np);
        M21=M21+sparse(it2,it3,aod,np,np);
        M21=M21+sparse(it3,it1,aod,np,np);
        M21=M21+M21.';
        M21=M21+sparse(it1,it1,ad,np,np);
        M21=M21+sparse(it2,it2,ad,np,np);
        M21=M21+sparse(it3,it3,ad,np,np);

        [ii,jj,kmm]=find(M21);
        M2=M2+sparse(ii+(k-1)*np,jj+(l-1)*np,kmm,Neq*np,Neq*np);
        m=m+1;
    end
end

%Assemble O matrix

Ar=((p(1,it2)-p(1,it1)).*(p(2,it3)-p(2,it1))-(p(2,it2)-p(2,it1)).*(p(1,it3)-p(1,it1)))/2;
G1x=g1x.*sign(Ar);
G2x=g2x.*sign(Ar);
G3x=g3x.*sign(Ar);
G1y=g1y.*sign(Ar);
G2y=g2y.*sign(Ar);
```

```
G3y=g3y.*sign(Ar);

m=1;
O=sparse(Neq*np,Neq*np);
for l=1:Neq,
    for k=1:Neq,

        oo1=o(m,:);
        oo2=o(m+1,:);

        o12=((oo1.*G2x+oo2.*G2y).*Area/3);
        o21=((oo1.*G1x+oo2.*G1y).*Area/3);
        o13=((oo1.*G3x+oo2.*G3y).*Area/3);
        o31=o21;
        o23=o13;
        o32=o12;
        o11=o21;
        o22=o12;
        o33=o13;

        O1=sparse(it1,it2,o12,np,np);
        O1=O1+sparse(it2,it3,o23,np,np);
        O1=O1+sparse(it3,it1,o31,np,np);
        O1=O1+sparse(it2,it1,o21,np,np);
        O1=O1+sparse(it3,it2,o32,np,np);
        O1=O1+sparse(it1,it3,o13,np,np);
        O1=O1+sparse(it1,it1,o11,np,np);
        O1=O1+sparse(it2,it2,o22,np,np);
        O1=O1+sparse(it3,it3,o33,np,np);

        [ii,jj,koo]=find(O1);
        O=O+sparse(ii+(k-1)*np,jj+(l-1)*np,koo,Neq*np,Neq*np);
        m=m+2;
    end
end


% Parallel Computing

NumWorkers=1;
if Parallel==1
    distcomp.feature( 'LocalUseMpiexec', false )
    pool = gcp
    NumWorkers=pool.NumWorkers;

    spmd(NumWorkers)
        assignin('base', 'K',K);
        assignin('base', 'M1',M1);
        assignin('base', 'M2',M2);
        assignin('base', 'F',F);
        assignin('base', 'O',O);
        assignin('base', 'Q',Q);
        assignin('base', 'G',G);
        assignin('base', 'H',H);
        assignin('base', 'R',R);
        assignin('base', 'N',N);
        assignin('base', 'p',p);
        assignin('base', 't',t);
        assignin('base', 'Hl',Hl);
        assignin('base', 'Djk',Djk);
        assignin('base', 'vI',vI);
        assignin('base', 'vI1',vI1);
        assignin('base', 'Area',Area);
        assignin('base', 'Vtop',Vtop);
        assignin('base', 'Vbot',Vbot);
        assignin('base', 'LinPot',LinPot);
        assignin('base', 'ZContInt',ZContInt);
        assignin('base','NJ',NJ);
    end
end

Nwork=floor(length(Freq)/NumWorkers);
Z=zeros(0,5);
nI=0;
hwb=waitbar(0,'waitbar','position',[375 100 270 50]);
figure

for III=1:Nwork
    tic
    for II=1:NumWorkers

        nI=NumWorkers*(III-1)+II;

        W=Freq(nI)*2*pi;
        WW{II}v=W;
        Wcoef{II}=(-P*(W^2)+1i*(Damp + Dampv*W + Dampv2*(W^2) + Dampv3*(W^3)));

    end

    % PDE problem

    if Parallel==1
        if nI==NumWorkers*Nwork;
            spmd(NumWorkers)
                [Z1,u]=assempde2(WW{labindex},Wcoef{labindex});
            end
        else
            spmd(NumWorkers)
```

```
                Z1=assempde2(WW{labindex},Wcoef{labindex});
            end
        end
    else
        if nI==NumWorkers*Nwork;
            [Z1[234],u[234]]=assempde2(WW{labindex},Wcoef{labindex});
        else
            Z1[234]=assempde2(WW{labindex},Wcoef{labindex});
        end
    end

    %Results

    for j=1:NumWorkers
        Z=[Z;Z1{j}];
    end
    plot(Z(:,1),Z(:,5),'.-');
    xlabel('f (Hz)')
    ylabel('|Y|/f (S/Hz)')
    drawnow
    toc;
    TimeRemaining=datestr((Nwork-III)*toc/(3600*24), 'DD:HH:MM:SS')
    waitbar(III/Nwork,hwb,TimeRemaining);
end
close(hwb)

%Countour plots

if Parallel==0

    Neq = 4*(N+1);
    ztop=linspace(0,h1,50);
    zbot=linspace(h2,0,50);
    u=u{NumWorkers};
    u0x1=u(1:np,1);
    u0y1=u((np+1):2*np,1);
    u0z1=u((2*np+1):3*np,1);
    o0=u((3*np+1):4*np,1);
    utopx1=zeros(np,1); utopy1=zeros(np,1); utopz1=zeros(np,1); otop=zeros(np,1); ubotx1=zeros(np,1); uboty1=zeros(np,1);
ubotz1=zeros(np,1); obot=zeros(np,1);
    oztop=zeros(1,length(ztop));
    ozbot=zeros(1,length(zbot));
    if ZContInt~=2
        utop = u;
        ubot = u;
    else
        utop = u(1:Neq*np,:);
        ubot = u([1:np*4 Neq*np+1:(2*Neq-4)*np],:);
    end

    for I=0:N
        nCol=4*np*I;
        utopx1 = utopx1 + utop(nCol+1:nCol+np,1)*vItb(I+1,1);
        utopy1 = utopy1 + utop(nCol+1+np:nCol+2*np,1)*vItb(I+1,1);
        utopz1 = utopz1 + utop(nCol+1+2*np:nCol+3*np,1)*vItb(I+1,1);
        otop = otop + utop(nCol+1+3*np:nCol+4*np,1)*vItb(I+1,1);
        ubotx1 = ubotx1 + ubot(nCol+1:nCol+np,1)*vItb(I+1,2);
        uboty1 = uboty1 + ubot(nCol+1+np:nCol+2*np,1)*vItb(I+1,2);
        ubotz1 = ubotz1 + ubot(nCol+1+2*np:nCol+3*np,1)*vItb(I+1,2);
        obot = obot + ubot(nCol+1+3*np:nCol+4*np,1)*vItb(I+1,2);
        oztop = oztop + ((pdeintrp(p,t,utop(nCol+1+3*np:nCol+4*np,1))*Area')/sum(Area))*(ztop.^I);
% (Int(o)dA)(z)
        ozbot = ozbot + ((pdeintrp(p,t,ubot(nCol+1+3*np:nCol+4*np,1))*Area')/sum(Area))*(zbot.^I);
    end

    p0=[u0x1;u0y1;u0z1;utopx1;utopy1;utopz1;ubotx1;uboty1;ubotz1];
    [p0m,p0i]=max(abs(p0));
    theuRef=conj(p0(p0i))/abs(p0(p0i))
    % theuRef=1         %u Real part
    % theuRef=-1i       %u Imag part
    ctb=3;

    u0x=u0x1*theuRef; u0y=u0y1*theuRef; u0z=u0z1*theuRef; utopx=utopx1*theuRef; utopy=utopy1*theuRef;
utopz=utopz1*theuRef; ubotx=ubotx1*theuRef; uboty=uboty1*theuRef; ubotz=ubotz1*theuRef;
    p0max=max([abs(max(real(utopz))) abs(min(real(ubotz))) abs(max(real(utopx))) abs(max(real(ubotx))) abs(max(real(u0x)))
abs(max(real(utopy))) abs(max(real(uboty))) abs(max(real(u0y)))]);

    pmax=ctb*Hl/p0max;
    y0x=p(1,:)+pmax*real(u0x)';
    y0y=p(2,:)+pmax*real(u0y)';
    y0z=pmax*real(u0z)';
    ytopx=p(1,:)+pmax*real(utopx)';
    ytopy=p(2,:)+pmax*real(utopy)';
    ytopz=h1+pmax*real(utopz)';
    ybotx=p(1,:)+pmax*real(ubotx)';
    yboty=p(2,:)+pmax*real(uboty)';
    ybotz=h2+pmax*real(ubotz)';

    figure
    plot([zbot ztop],[ozbot oztop],[zbot ztop],(Vtop-Vbot)*([zbot ztop]/Hl)+(Vtop+Vbot)/2)
    title('\phi vs z')
    xlabel('z (m)')
    ylabel('\phi (V)')

    figure
    pdeplot(p,e,t,'xydata',sqrt(real(u0x).^2+real(u0y).^2),'colormap','jet','contour','on','flowdata',[real(u0x)
real(u0y)])
    axis equal
```

```
    axis off
    title('ux/uy Middle')
    figure
    pdeplot([y0x;y0y],e,t,'xydata',sqrt(real(u0x).^2+real(u0y).^2),'colormap','jet','contour','on','flowdata',[real(u0x)
real(u0y)])
    axis equal
    axis off
    title('ux/uy Middle')
    figure
    pdeplot(p,e,t,'xydata',real(u0z),'colormap','jet','contour','on')
    axis equal
    axis off
    title('uz Middle')


    figure('position',[10 50 1350 635])
    subplot(1,3,1)
    pdeplot(p,e,t,'xydata',real(obot),'colormap','jet','contour','on')
    axis equal
    axis off
    title('Bottom')
    subplot(1,3,2)
    pdeplot(p,e,t,'xydata',real(o0),'colormap','jet','contour','on')
    axis equal
    axis off
    title('Middle')
    subplot(1,3,3)
    pdeplot(p,e,t,'xydata',real(otop),'colormap','jet','contour','on')
    axis equal
    axis off
    title('Top')
    MyBox2 = uicontrol('style','text');
    set(MyBox2,'String','V');
    set(MyBox2,'Position',[50,300,50,50])
    set(MyBox2,'FontSize',15)


    cminxy=min([min(sqrt(real(ubotx).^2+real(uboty).^2)) min(sqrt(real(utopx).^2+real(utopy).^2))
min(sqrt(real(u0x).^2+real(u0y).^2))]);
    cminz=min([min(real(utopz)) min(real(ubotz)) min(real(u0z))]);
    cmaxxy=max([max(sqrt(real(ubotx).^2+real(uboty).^2)) max(sqrt(real(utopx).^2+real(utopy).^2))
max(sqrt(real(u0x).^2+real(u0y).^2))]);
    cmaxz=max([max(real(utopz)) max(real(ubotz)) max(real(u0z))]);
    cmax=max([cmaxxy-cminxy cmaxz-cminz]);
    figure('position',[10 50 1350 635])
    subplot(2,3,1)

pdeplot([ybotx;yboty],e,t,'xydata',sqrt(real(ubotx).^2+real(uboty).^2),'colormap','jet','contour','on','flowdata',[real(ub
otx) real(uboty)])
    % caxis([cminxy cminxy+cmax])
    axis equal
    axis off
    title('Bottom')
    subplot(2,3,2)
    pdeplot([y0x;y0y],e,t,'xydata',sqrt(real(u0x).^2+real(u0y).^2),'colormap','jet','contour','on','flowdata',[real(u0x)
real(u0y)])
    % caxis([cminxy cminxy+cmax])
    axis equal
    axis off
    title('Middle')
    subplot(2,3,3)

pdeplot([ytopx;ytopy],e,t,'xydata',sqrt(real(utopx).^2+real(utopy).^2),'colormap','jet','contour','on','flowdata',[real(ut
opx) real(utopy)])
    % caxis([cminxy cminxy+cmax])
    axis equal
    axis off
    title('Top')
    subplot(2,3,4)
    pdeplot([ybotx;yboty],e,t,'xydata',real(ubotz),'colormap','jet','contour','on')
    % caxis([cminz cminz+cmax])
    axis equal
    axis off
    subplot(2,3,5)
    pdeplot([y0x;y0y],e,t,'xydata',real(u0z),'colormap','jet','contour','on')
    % caxis([cminz cminz+cmax])
    axis equal
    axis off
    subplot(2,3,6)
    pdeplot([ytopx;ytopy],e,t,'xydata',real(utopz),'colormap','jet','contour','on')
    % caxis([cminz cminz+cmax])
    axis equal
    axis off
    MyBox = uicontrol('style','text');
    set(MyBox,'String','ux/uy');
    set(MyBox,'Position',[50,450,50,50])
    set(MyBox,'FontSize',15)
    MyBox1 = uicontrol('style','text');
    set(MyBox1,'String','uz');
    set(MyBox1,'Position',[50,150,50,50])
    set(MyBox1,'FontSize',15)

    figure
    hold on
    for j=1:nt
        Xy(1,1)=ytopx(1,t(1,j)); Xy(1,2)=ytopx(1,t(2,j)); Xy(2,2)=ytopx(1,t(3,j)); Xy(2,1)=Xy(1,1);
        Yy(1,1)=ytopy(1,t(1,j)); Yy(1,2)=ytopy(1,t(2,j)); Yy(2,2)=ytopy(1,t(3,j)); Yy(2,1)=Yy(1,1);
        Zy(1,1)=ytopz(1,t(1,j)); Zy(1,2)=ytopz(1,t(2,j)); Zy(2,2)=ytopz(1,t(3,j)); Zy(2,1)=Zy(1,1);
```

```
        C1=sqrt(real(utopx(t(1,j))).^2+real(utopy(t(1,j))).^2+real(utopz(t(1,j))).^2);
        C2=sqrt(real(utopx(t(2,j))).^2+real(utopy(t(2,j))).^2+real(utopz(t(2,j))).^2);
        C3=sqrt(real(utopx(t(3,j))).^2+real(utopy(t(3,j))).^2+real(utopz(t(3,j))).^2);
        surf(Xy,Yy,Zy,[C1 C2;C1 C3])
        Xy1(1,1)=ybotx(1,t(1,j)); Xy1(1,2)=ybotx(1,t(2,j)); Xy1(2,2)=ybotx(1,t(3,j)); Xy1(2,1)=Xy1(1,1);
        Yy1(1,1)=yboty(1,t(1,j)); Yy1(1,2)=yboty(1,t(2,j)); Yy1(2,2)=yboty(1,t(3,j)); Yy1(2,1)=Yy1(1,1);
        Zy1(1,1)=ybotz(1,t(1,j)); Zy1(1,2)=ybotz(1,t(2,j)); Zy1(2,2)=ybotz(1,t(3,j)); Zy1(2,1)=Zy1(1,1);
        C1=sqrt(real(ubotx(t(1,j))).^2+real(uboty(t(1,j))).^2+real(ubotz(t(1,j))).^2);
        C2=sqrt(real(ubotx(t(2,j))).^2+real(uboty(t(2,j))).^2+real(ubotz(t(2,j))).^2);
        C3=sqrt(real(ubotx(t(3,j))).^2+real(uboty(t(3,j))).^2+real(ubotz(t(3,j))).^2);
        surf(Xy1,Yy1,Zy1,[C1 C2;C1 C3])
    end
    edge=0;
    for j=1:length(e)
        Xy(1,1)=ytopx(1,e(1,j)); Xy(1,2)=ytopx(1,e(2,j)); Xy(2,2)=y0x(1,e(2,j)); Xy(2,1)=y0x(1,e(1,j));
        Yy(1,1)=ytopy(1,e(1,j)); Yy(1,2)=ytopy(1,e(2,j)); Yy(2,2)=y0y(1,e(2,j)); Yy(2,1)=y0y(1,e(1,j));
        Zy(1,1)=ytopz(1,e(1,j)); Zy(1,2)=ytopz(1,e(2,j)); Zy(2,2)=y0z(1,e(2,j)); Zy(2,1)=y0z(1,e(1,j));
        C1=sqrt(real(utopx(e(1,j))).^2+real(utopy(e(1,j))).^2+real(utopz(e(1,j))).^2);
        C2=sqrt(real(utopx(e(2,j))).^2+real(utopy(e(2,j))).^2+real(utopz(e(2,j))).^2);
        C4=sqrt(real(u0x(e(1,j))).^2+real(u0y(e(1,j))).^2+real(u0z(e(1,j))).^2);
        C3=sqrt(real(u0x(e(2,j))).^2+real(u0y(e(2,j))).^2+real(u0z(e(2,j))).^2);
        surf(Xy,Yy,Zy,[C1 C2;C4 C3])
        Xy1(1,1)=ybotx(1,e(1,j)); Xy1(1,2)=ybotx(1,e(2,j)); Xy1(2,2)=y0x(1,e(2,j)); Xy1(2,1)=y0x(1,e(1,j));
        Yy1(1,1)=yboty(1,e(1,j)); Yy1(1,2)=yboty(1,e(2,j)); Yy1(2,2)=y0y(1,e(2,j)); Yy1(2,1)=y0y(1,e(1,j));
        Zy1(1,1)=ybotz(1,e(1,j)); Zy1(1,2)=ybotz(1,e(2,j)); Zy1(2,2)=y0z(1,e(2,j)); Zy1(2,1)=y0z(1,e(1,j));
        C1=sqrt(real(ubotx(e(1,j))).^2+real(uboty(e(1,j))).^2+real(ubotz(e(1,j))).^2);
        C2=sqrt(real(ubotx(e(2,j))).^2+real(uboty(e(2,j))).^2+real(ubotz(e(2,j))).^2);
        C4=sqrt(real(u0x(e(1,j))).^2+real(u0y(e(1,j))).^2+real(u0z(e(1,j))).^2);
        C3=sqrt(real(u0x(e(2,j))).^2+real(u0y(e(2,j))).^2+real(u0z(e(2,j))).^2);
        surf(Xy1,Yy1,Zy1,[C1 C2;C4 C3])
        plot3(Xy(1,:),Yy(1,:),Zy(1,:),'k')
        plot3(Xy1(1,:),Yy1(1,:),Zy1(1,:),'k')
        if e(5,j)~=edge
            edge=e(5,j);
            plot3([Xy(1,1) Xy1(1,1)],[Yy(1,1) Yy1(1,1)],[Zy(1,1) Zy1(1,1)],'k')
        end
    end

    colormap jet
    view([135,30])
    axis equal
    axis off
    colorbar
    shading interp
    xlabel('X'); ylabel('Y'); zlabel('Z');
    material metal

end
```

……

```
function [Z,u]=assempde2(W,Wcoef);

K=evalin('base', 'K');
M1=evalin('base', 'M1');
M2=evalin('base', 'M2');
F=evalin('base', 'F');
O=evalin('base', 'O');
Q=evalin('base', 'Q');
G=evalin('base', 'G');
H=evalin('base', 'H');
R=evalin('base', 'R');
N=evalin('base', 'N');
p=evalin('base', 'p');
t=evalin('base', 't');
Hl=evalin('base', 'Hl');
Djk=evalin('base', 'Djk');
vI=evalin('base', 'vI');
vI1=evalin('base', 'vI1');
Area=evalin('base', 'Area');
Vtop=evalin('base', 'Vtop');
Vbot=evalin('base', 'Vbot');
LinPot=evalin('base','LinPot');
ZContInt=evalin('base','ZContInt');
NJ=evalin('base','NJ');

% M Matrix
M = M1 + Wcoef*M2;


KK=K+M+Q+O;
FF=F+G;

u=KK\FF;

Neq = 4*(N+1);          % Number of equations 4*(N+1)
nt = size(t,2);
np = size(p,2);

% Linear potential(simplification)
if LinPot==1
    u1=u;
    u=[];
    N1=size(u1,1)/(np*3);
    for I=0:N1-1
        if I==0
```

```
            u=cat(1,u,[u1(3*I*np+1:3*(I+1)*np,1);ones(np,1)*(Vtop+Vbot)/2]);
        elseif I==1
            u=cat(1,u,[u1(3*I*np+1:3*(I+1)*np,1);ones(np,1)*(Vtop-Vbot)/Hl]);
        elseif I==N+1
            u=cat(1,u,[u1(3*I*np+1:3*(I+1)*np,1);ones(np,1)*(Vtop-Vbot)/Hl]);
        else
            u=cat(1,u,[u1(3*I*np+1:3*(I+1)*np,1);zeros(np,1)]);
        end
    end
elseif LinPot==2
    u1=u;
    u=[];
    II=1;
    III=1;
    if ZContInt~=2
        N1=Neq;
    else
        N1=2*Neq-4;
    end
    for I=1:N1
        if I==NJ(II)
            u=cat(1,u,zeros(np,1));
            II=II+1;
        else
            u=cat(1,u,u1((III-1)*np+1:III*np,1));
            III=III+1;
        end
    end
end



U=pdeintrp(p,t,u);
[dUx,dUy]=pdegrad(p,t,u);
if ZContInt~=2
    Utop=U;
    Ubot=U;
    dUtop=[dUx;dUy];
    dUbot=[dUx;dUy];
else
    Utop=U(1:Neq,:);
    Ubot=U([1:4 Neq+1:2*Neq-4],:);
    dUtop=[dUx(1:Neq,:);dUy(1:Neq,:)];
    dUbot=[dUx([1:4 Neq+1:2*Neq-4],:);dUy([1:4 Neq+1:2*Neq-4],:)];
end
D3av=zeros(1,nt);

for J=0:N
    for k=1:4
        D3av1=zeros(1,nt);
        for a=1:2
            D3av1=D3av1 + (vI(J+1,1)*Djk(4,k,3,a,1))*dUtop(4*J+k+(a-1)*Neq,:) + (vI(J+1,2)*Djk(4,k,3,a,2))*dUbot(4*J+k+(a-
1)*Neq,:);
        end
        D3av=D3av + (1/Hl)*(D3av1 + (vI1(J+1,1)*Djk(4,k,3,3,1))*Utop(4*J+k,:) +
(vI1(J+1,2)*Djk(4,k,3,3,2))*Ubot(4*J+k,:));
    end
end


Usumtop=sum((dUx+dUy)*Area')-(Vtop-Vbot)*sum(Area);
Charge3=D3av*Area';
Y=-1i*W*(Charge3)/(Vtop-Vbot);
Z=[W./(2*pi) real(Y) imag(Y) abs(Y) (abs(Y)*(2*pi))./W real(Usumtop) imag(Usumtop) abs(Usumtop)];
```